UNIVERSITY OF STRATHCLYDE
DEPARTMENT OF PHYSICS

Optimisation and Control of Ion Acceleration in Intense Laser-Foil Interactions

by

Adam Higginson

in partial fulfilment of the requirements for the degree of Doctor of Philosophy in Physics

2018

Copyright Declaration

Signed:

Date:

Abstract

This thesis reports on experimental and numerical investigations of ion acceleration driven by the interaction of short, ultra-intense ($> 10^{20}$ Wcm^{-2}), linearly polarised pulses of laser light with thin foil targets. Four investigations were performed to explore various aspects of the acceleration and the physics underpinning potential applications of these sources.

The first investigation explores a hybrid scheme of radiation pressure-sheath acceleration, enhanced by relativistic transparency at an optimum foil thickness. Efficient proton acceleration with energies exceeding 94 MeV is achieved. The range of parameters over which this hybrid scenario occurs is discussed, and implications for ion acceleration driven by next-generation, multi-PW laser facilities are explored.

The second investigation concerns the diagnosis of the highly transient electric field responsible for ion acceleration in the target normal sheath acceleration (TNSA) regime. High resolution, temporally-resolved measurements of the field evolution are obtained using proton deflectometry.

In the third investigation, a laser generated proton beam is used to heat and pre-expand the rear-surface of a secondary foil. This target is then irradiated by a second laser pulse, with the resultant proton beam spatial-intensity distribution measured. For an increasingly expanded target the maximum proton energy, overall number of accelerated protons and the size of the proton beam consistently decreases. A simple analytical model describing the expansion behaviour is developed.

In the final investigation, initial steps towards proton focusing for the purposes of proton fast ignition (PFI) using novel conical targets are addressed. Clear focusing is observed for an open-tipped conical target. These beams are used to isochorically heat copper, with the X-ray emission imaged. Finally, in order to close in on a realistic PFI scenario, the effects of an external plasma surrounding the cone is explored.

Acknowledgements

The work presented in this thesis is the result of over three years of research, with numerous individuals involved that deserve my utmost gratitude. Firstly, I would like to thank my funders, EPSRC and AWE plc, for providing financial support in order to allow me to undertake this project. Secondly, I would like to thank my PhD supervisor, Prof. Paul McKenna, for his constant support, guidance, and for the numerous opportunities he has given me throughout my PhD. He has encouraged me to expand my research horizons and to develop new ideas, without which the work detailed in this thesis would not have been possible. I cannot thank you enough.

Secondly, a big thank you goes to my officemates - Sam Williamson and Zoë Davidson. The endless banter, both in the office and on experiment, helped keep my sanity in-check. Next, to all my friends and colleagues in the group with whom I've had the pleasure of working with over the years, Ross Gray, Martin King, Bruno Gonzalez Izquierdo, Nick Butler, Robbie Wilson, Matthew Duff, Remi Capdessus, Rachel Dance, Jonathan Jarrett, Timothy Frazer, Chris Armstrong and Dean Rusby. Thank you to all of you.

I would like to thank the staff at the Central Laser Facility, in particular David Carroll and Prof. David Neely, for their dedication, professionalism, and invaluable help on experimental campaigns. I would also like to extend my thanks to the staff of the Orion laser facility, AWE plc.

I would like to give thanks to my parents, Bernadette and Derek, for their encouragement and support throughout my time at University, without which I likely would not have pursued a PhD, and also to my brother Cameron and sister Lucy. Lastly, to Hilary: the endless patience you had for me and the support you gave me during the writing of this thesis helped make this work possible. Thank you.

Publications

1. **Near-100 MeV protons via a laser-driven transparency-enhanced hybrid acceleration scheme**

   A. Higginson, R. J. Gray, M. King, R. J. Dance, S. D. R. Williamson, N. M. H. Butler, R. Wilson, R. Capdessus, C. Armstrong, J. S. Green, S. J. Hawkes, P. Martin, W. Q. Wei, S. R. Mirfayzi, X. H. Yuan, S. Kar, M. Borghesi, R. J. Clarke, D. Neely and P. McKenna, Nature Communications, **9**, 724 (2018).

2. **Dual ion species plasma expansion from isotopically layered cryogenic targets**

   G. G. Scott, D. C. Carroll, S. Astbury, R. J. Clarke, C. Hernandez-Gomez, M. King, A. Alejo, I. Y. Arteaga, R. J. Dance, **A. Higginson**, S. Hook, G. Liao, H. Liu, S. R. Mirfayzi, D. R. Rusby, M. P. Selwood, C. Spindloe, M. K. Tolley, F. Wagner, E. Zemaityte, M. Borghesi, S. Kar, Y. Li, M. Roth, P. McKenna and D. Neely, Physical Review Letters, **120**, 204801 (2018).

3. **Transverse Expansion of the electron sheath during laser acceleration of protons**

   K. Svensson, F. Mackenroth, L. Senje, A. Gonoskov, C. Harvey, B. Aurand, M. Hansson, **A. Higginson**, M. Dalui, O. Lundh, P. McKenna, A. Persson, M. Marklund and C.-G Wahlström, Physics of Plasmas, **24**, 123109 (2017).

4. **Experimental demonstration of a compact epithermal neutron source based on a high power laser**

   S. R. Mirfayzi, A. Alejo, H. Ahmed, D. Raspino, S. Ansell, L. A. Wilson, C. Armstrong, N. M. H. Butler, R. J. Clarke, **A. Higginson**, J. Kelleher, C. Murphy, M. Notely, D. R. Rusby, E. Schooneveld, M. Borghesi, P. McKenna, N. J. Rhodes, D. Neely, C. M. Brenner and S. Kar, Applied Physics Letters, **111**, 044101 (2017).

5. **Pulsed X-ray imaging of high-density objects using a ten picosecond high-intensity laser driver**

   D. R. Rusby, C. M. Brenner, C. Armstrong, L. A. Wilson, R. J. Clarke, A. Alejo, H. Ahmed, N. M. H. Butler, D. Haddock, **A. Higginson**, A. McClymont, S. R. Mirfayzi, C. Murphy, M. Notely, P. Oliver, R. Allott, C. Hernandez-Gomez, S. Kar, P. McKenna and D. Neely, SPIE Proceedings – Emerging Imaging and Sensing Technologies **9992**, 99920E (2016).

6. **Detector for imaging and dosimetry of laser-driven epithermal neutrons by alpha conversion**

   S. R. Mirfayzi, A. Alejo, H. Ahmed, L. A. Wilson, S. Ansell, C. Armstrong, N. M. H. Butler, R. J. Clarke, **A. Higginson**, M. Notely, D. Raspino, D. R. Rusby, M. Borghesi, N. J. Rhodes, P. McKenna, D. Neely, C. M. Brenner and S. Kar, Journal of Instrumentation **11**, C10008 (2016).

7. **High resolution Thomson Parabola Spectrometer for full spectral capture of multi-species ion beams**

   A. Alejo, S. Kar, A. Tebartz, H. Ahmed, S. Astbury, D. C. Carroll, J. Ding, D. Doria, **A. Higginson**, P. McKenna, N. Neumann, G. G. Scott, F. Wagner, M. Roth and M. Borghesi, Review of Scientific Instruments, **87**, 083304 (2016).

8. **Evaluating laser-driven Bremsstrahlung radiation sources for imaging and analysis of nuclear waste packages**

   C. P. Jones, C. M. Brenner, C. A. Stitt, C. Armstrong, D. R. Rusby, S. R. Mirfayzi, L. A. Wilson, A. Alejo, H. Ahmed, R. Allott, N. M. H. Butler, R. J. Clarke, D. Haddock, C. Hernandez-Gomez, **A. Higginson**, C. Murphy, M. Notley, C. Paraskevoulakos, J. Jowsey, P. McKenna, D. Neely, S. Kar and T. B. Scott, Journal of Hazardous Materials **318**, 694-701 (2016).

9. **Manipulation of the spatial distribution of laser-accelerated proton beams by varying the laser intensity distribution**

   B. Aurand, L. Senje, K. Svensson, M. Hansson, **A. Higginson**, A. Gonoskov, M. Marklund, A. Persson, O. Lundh, D. Neely, P. McKenna and C.-G Wahlström, Physics of Plasmas **23**, 023113 (2016).

10. **Laser-driven x-ray and neutron source development for industrial ap-**

plications of plasma accelerators

C. M. Brenner, S. R. Mirfayzi, D. R. Rusby, C. Armstrong, A. Alejo, L. A. Wilson, R. J. Clarke, H. Ahmed, N. M. H. Butler, **A. Higginson**, A. McClymont, C. Murphy, M. Notley, P. Oliver, R. Allott, C. Hernandez-Gomez, S. Kar, P. McKenna and D. Neely, Plasma Physics and Controlled Fusion, **58**, 014039 (2016).

Role of the author

The research presented in this thesis is the work of the author, and was conducted in collaboration with a team of researchers. The experimental results were obtained over three campaigns led by Prof. Paul McKenna, University of Strathclyde, who provided overall supervision of the work. These experiments involved the use of two high-power laser facilities: the Vulcan laser system at the Central Laser Facility (CLF) and the Orion laser, AWE plc. In addition to the presented work, the author contributed to multiple other experiments, acting as Deputy Target Area Operator on the two most recent campaigns. The role of the author in the measurements and analysis of results present in the four main results chapters is discussed below.

Chapter 5: The experiment, performed using Target Area Petawatt in the Vulcan laser system, took place during the author's second year as a PhD student. The author played a key role in all aspects of the experimental campaign. He was responsible for designing the configuration of the main diagnostic, stacks of dosimetry film (RCF), used as a proton beam diagnostic, in addition to all of the other main diagnostics detailed in Chapter 5. These included the operation and planning involved with the nuclear activation measurements; the building, setup and operation of the multi-wavelength imaging system, and; assembling and running the backscatter diagnostic. Additionally, the author was responsible for recording and summarising all of the experimental data, and maintaining the details of each laser-shot. Post-experiment, the author digitised the RCF data, with assistance from Mr S.D.R. Williamson, University of Strathclyde. All of the presented experimental data was analysed by the author. The author performed the analytical modelling, with assistance from Dr M. King, Unversity of Strathclyde, which led to further investigations using 2-D particle-in-cell (PIC) simulations. M. King performed the simulations and processed and analysed the results.

Chapters 6 and 7: Both of these chapters resulted from data obtained during the one experimental campaign, using Target Area West in the Vulcan laser system. This

experiment was undertaken during the author's first year as a PhD student. The author was responsible for building the primary diagnostic, RCF stacks, and summarising the experimental data on the campaign. The author performed all of the data analysis, analytical modelling and radiation-hydrodynamic simulations. Dr M. King performed the 2-D PIC simulations featured in Chapter 6 and Appendix B, and developed the particle-tracking algorithm used in Chapter 6.

Chapter 8: The experiment, performed on the Orion laser system, was undertaken during the author's third year as a PhD student. The author was heavily involved in the planning of the experiment, and participated in the majority of the experimental planning meetings for the campaign over a two-year period. The author performed the radiation-hydrodynamic simulations used to help plan the experiment. During the experiment, the author was responsible for aligning the targets and liasing shot information with the facility staff. The author was responsible for coordinating the diagnostic team, consisting of both staff and scientific collaborators, and designing the RCF stacks. The author analysed all of the experimental data presented in this thesis. The hybrid-PIC simulations were performed by Dr J. Kim, University of California San Diego.

Contents

List of Figures

List of Tables

Chapter 1

Introduction

Particle acceleration provides scientists with the tools necessary to investigate the structure of the atomic world. Outside of the laboratory, real-world applications have been realised, including proton beam therapy for cancer treatment; an alternative approach to X-ray therapy.

The first purpose-built particle accelerator, built by Wideröe in 1928 [1], was a linear accelerator (Linac); accelerating charged particles using a series of oscillating electric potentials. One of the largest Linacs used for proton acceleration, LANSCE [2], is located at Los Alamos National Laboratory (LANL). At over 1 km long, this accelerator is capable of accelerating protons to energies exceeding 800 MeV with a narrow energy spread.

The largest particle accelerator has a circumference of over 27 km and is capable of accelerating protons with a maximum energy between 7 and 8 TeV. Known as the Large Hadron Collider (LHC), this synchrotron accelerator is one of the most expensive scientific instruments ever built, at a cost of over £6bn. Further increases in the maximum energy achievable using radio-frequency (RF) accelerators require even larger acceleration lengths.

Laser-driven ion acceleration is a different approach. An ultra-high intensity laser pulse irradiates an initially solid density target, with a typical thickness in the range 10 nm - 100 µm. The first energetic ions accelerated by a laser-plasma interaction were reported by Linor *et al.* [3], achieving ion energies of ~ 1 keV for a laser intensity of 5×10^9 Wcm^{-2} and a pulse duration of 40 ns (full-width at half-maximum, FWHM). Since then, multiple advances (such as the chirped pulse amplification technique [4]) have enabled the peak laser intensity to exceed 10^{21} Wcm^{-2}, with maximum proton

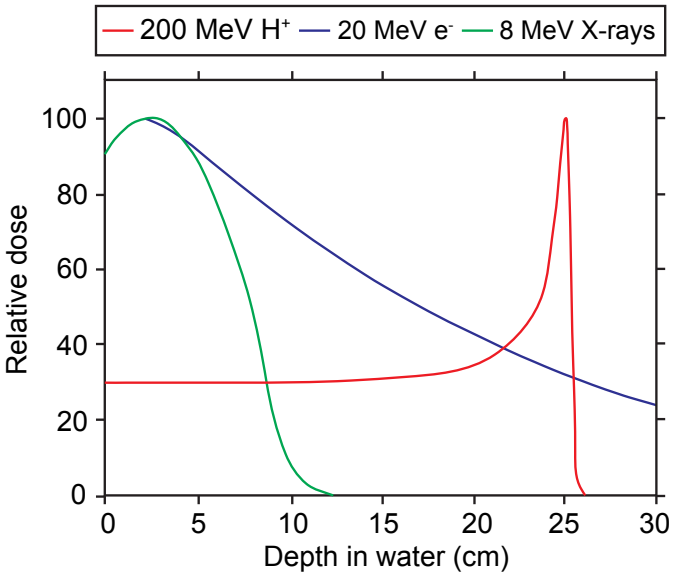

Figure 1.1: Deposition profile of protons (H^+), electrons (e^-) and X-rays, with the labelled energy, in water. The quantity plotted is the relative dose. Figure adapted from [6].

energy (at the time of writing) in excess of 94 MeV, as recorded in this thesis [5].

Due to their potential low cost and size, laser-accelerated ions may become a viable alternative to RF-based accelerators. Laser-driven ion beams also possess unique properties, including an ultra-short bunch duration and an ultra-low emittance. Additionally, the beam of accelerated ions is less prone to space charge effects, due to the co-moving electrons - an inherent advantage. Such an ion beam may be well-suited for a range of potential applications, as discussed in the following section.

1.1 Applications

Hadron therapy

Cancer therapy using ion beams offers a better-suited dose deposition profile when compared to other forms of radiation (i.e. X-rays) for the treatment of certain types of cancer, resulting in less damage to the surrounding healthy tissue. This is illustrated in Fig. 1.1. Energetic protons for use in radiology was first proposed by Wilson [7] in 1946, and later demonstrated by Lawrence [8] in 1957. A recent review article concerning the state of the art of ion beam therapy can be found in Ref. [9]. Ions that penetrate a material deposit most of their kinetic energy near the position where they are fully stopped, with this slope known as the Bragg peak. The depth at which the Bragg peak

occurs can be easily controlled by changing the initial energy of the ions. For proton radiography, the energy window of therapeutical interest lies between 60 and 250 MeV; dependent on the location of the tumour. Current facilities that employ conventional RF particle accelerators have proved effective at removing a number of types of tumours. These facilities, however, have a cost in the range £60 - £250 million - depending on the type of ions used and the number of patient irradiation stations. This high cost motivates interest to develop alternative methods for the production of high energy ion beams.

Laser-driven particle accelerators have been proposed as an alternative to RF-based accelerators for treating cancer [10], with potential advantages in terms of size and cost. They could potentially be directly used to treat a patient, with the levels required for such a scheme detailed in the review article by Linz and Alonso [11]. They may potentially also be used as injectors into RF-accelerators [12], which further accelerate the laser-driven ion beams to the energies required. Further research is required to make laser-driven ion beams a viable and competitive option, with several key issues that must be resolved. The highest published maximum proton energy driven by a laser-plasma interaction is reported in this thesis and in Ref. [5], and is between 94 and 101 MeV. This, however, is still a factor of two too low to treat the deepest-seated tumours. Another issue concerns the spectral profile of the generated proton beam, which is inherently broadband. Further, for the laser systems required (at the time of writing) to accelerate protons with maximum proton energies in excess of $\sim$60 MeV, the laser shot rate is typically 1/hr. A full treatment may require thousands of proton pulses, thus the repetition rate needs to be increased. Avenues to address some of these key problems are discussed in Chapter 4.

Ion fast ignition

The fast ignition (FI) approach to inertial confinement fusion (ICF) is another potential application for laser-driven ion sources. The traditional form of ICF uses multiple long pulse laser beams to irradiate and compress a pellet of deuterium and tritium, with ignition occuring in a central hot spot following compression [13]. This scheme of ICF requires a very high degree of spherical symmetry, and is prone to hydrodynamic instabilities, making efficient fusion very difficult to achieve.

In FI-ICF, the compression and ignition stages are separate. Initially proposed by

Tabak *et al.* [14], the fusion pellet is first compressed by multiple long pulse beams, similar to conventional ICF, however differs in that fusion does not occur solely due to this compression - the degree of compression is lower. Instead, an ignitor beam consisting of either electrons (such as that in the original work [14]), protons or heavy ions, generated by a laser-plasma interaction, initiates the burn. This approach relaxes the irradiation symmetry requirements and reduces the laser energy requirement needed for ignition.

The initial measurements of multi-MeV proton beams from PW experiments [15] stimulated the proton fast ignition (PFI) concept [16]. The fundamental advantage that protons have over electrons in a FI context is their localised energy deposition profile and that they are less susceptible to transport instabilities. However, laser-driven proton beams are generally divergent, which poses a problem if the aim is to generate a localised, heated spot. By using a curved as opposed to planar foil, it is possible to exert some degree of control on the focusability of the resulting proton beam [17]. Additionally, by integrating a conical attachment to the curved foil, an even greater degree of focusing may be achieved – as investigated in Chapter 7. A detailed review regarding PFI can be found in Ref. [18]

Proton deflectometry

Laser-driven proton beams have several radiographic applications, with deflectometry being one of the most useful for the probing of transient electromagnetic fields. Protons accelerated using a laser-driven approach have extremely good emittance, and are particularly well-suited for this task. Additionally, the short bunch length and broad energy spectrum enable high resolution temporally resolved measurements to be made, due to the time-of-flight spreading of protons with different spectral components.

With this technique, a probe proton beam acts to backlight some sample material with a surrounding field structure, with this field structure often induced by a laser-plasma interaction. The protons are deflected by these fields by an amount corresponding to the integrated field strength experienced by the protons. The technique has been pioneered by M. Borghesi at Queen's University Belfast and others. In the work by Borghesi *et al.* [19], a proton beam is used to backlight a wire mesh, where deflections (due to charging of the material by the preceding electrons) of the proton beam cause local modulations in the beam dose profile across the beam cross-section. The proton

probing technique has provided detailed information on multiple nonlinear phenomena in laser-plasma physics, with a detailed review found in Macchi *et al.* [20].

Production of warm dense matter

Ion beams driven by laser-plasma interactions have been used to heat initially solid density matter, isochorically, to states of warm dense matter. This state is characterised as near solid density (or slightly higher), with temperatures between 0.1 eV and 100 eV [21]. It is also short-lived, and after some tens of picoseconds (depending on the material temperature and density) the ions begin to exhibit significant motion and the matter transitions to the plasma state. A brief outline concerning WDM can be found in the review article by Riley [22].

WDM studies are of relevance to several areas of science, including material and planetary studies [23]. These states of matter can be reached using other methods, such as X-ray heating [24] or shock compression [25]. Ions beams are advantageous however, as they are able to create large volumes of heated matter; provided the correct initial energy spread is used. Laser-driven ion beams are especially attractive, with bunch durations of the order of one picosecond at the source (for the laser parameters used in this thesis). Compared to a bunch duration of up to 10 ns from conventional accelerators, the WDM states do not exhibit significant hydrodynamic expansion over the duration of the proton pulse.

Patel *et al.* [17] first demonstrated that by irradiating a thin-foil target with ~ 1.5 MeV laser-accelerated protons, accelerated from the rear of a second foil following its interaction with an intense laser pulse, the target foil was heated to several eV over the duration of the proton beam. By using curved targets, such that the proton beam was focused (similar to those used in Chapter 7 for the same purpose), the matter reached temperatures approaching 20 eV.

1.2 Thesis outline

The work presented in this thesis focuses on furthering the field of laser-driven ion acceleration, with several key issues of importance addressed. These include investigations into increasing the maximum achievable proton energy and laser-to-proton conversion efficiency, and demonstrating control over the beam spatial-intensity distribution. The

thesis is structured as follows. Firstly, the underpinning physics necessary to understand the results presented are discussed in Chapter 2. This is followed by a brief summary of the methods used in Chapter 3, describing the experimental methodology in addition to the simulation tools used.

The first results chapter (Chapter 4) details an experimental and simulation study concerning a hybrid proton acceleration scheme, with the target thickness optimised for the efficient acceleration of high energy protons. Using the Vulcan laser, proton energies in excess of 94 MeV are accelerated from thin ($\sim$ 100 nm) plastic targets – the highest published to date. These results demonstrate the importance of utilising hybrid schemes of ion acceleration, with predictions made for its possible implication using next generation, multi-PW laser facilities [26–29]. This is followed by Chapter 5, where the electrodynamic sheath field driving ion acceleration from micrometer-thick targets is investigated. Proton deflectometry is the tool used to provide this measurement.

In Chapter 6, target expansion dynamics are investigated by measuring the protons accelerated from a pre-expanded target, with expansion induced by proton heating. Implications of this work in the fields of PFI and WDM studies are discussed. Finally, in Chapter 7, the physics underpinning proton focusing via curved and conical targets is investigated using the Orion laser facility. Like in the previous chapter, implications range from PFI to WDM studies, with key aspects crucial to PFI tested, for this first time, on this experimental campaign.

Chapter 2

Fundamental physics underpinning laser-matter interactions

The key physics underpinning laser-matter interactions is described in this chapter. From the initial creation of a plasma to the acceleration of multi-MeV ions, the fundamental physical concepts are discussed. A more thorough description of many of these concepts can be found in the various textbooks that exist on the subject. These include a detailed account of atoms in an intense laser field by Suter [30], nonlinear wave propagation in underdense plasmas by Borovsky *et al.* [31], the classic work by Kruer [32] and the more recent textbook by Gibbon [33]. The latter two provide a well-rounded discussion of most of the basic physics involved in this thesis.

When a short pulsed ($\sim$ps), high intensity ($> 10^{18}$ Wcm^{-2}) laser beam irradiates a solid target material, the rising edge of the pulse is strong enough to ionise the initially-solid front surface, resulting in the creation of a plasma on this surface. A description of a plasma, and the ionisation processes which result in the creation of a plasma, are presented in the following two sections.

2.1 Plasma

Plasma is often called the fourth state of matter, and comprises the vast majority of matter in the observable universe. Formally, a plasma is described as a quasi-neutral collection of particles which exhibit collective behaviour. Macroscopically, a plasma

is charge neutral. However, on a microscopic scale, the individual charged particles are constantly moving. This results in the creation of localised electric fields, driving currents and generating magnetic fields. A plasma has the following defining features:

- The collisional rate in the system must be small compared to the frequency of plasma oscillations.
- Many particles must exist within a sphere with a radius equal to the Debye length.
- The system must be much larger than the Debye length.

The Debye length, which is the distance at which the local electric field of one particle drops by a factor of $1/e_N$, where e_N is Euler's number, is given by:

$$\lambda_D = \sqrt{\frac{\epsilon_0 k_B T_e}{e^2 n_e}} \tag{2.1}$$

where ϵ_0 is the permittivity of free space, k_B is Boltzmann's constant, T_e is the plasma temperature, e is the electronic charge and n_e is the electron density.

Another defining feature of a plasma is the dominance of collective effects over collisional. The most pertinent collective interaction is known as the plasma oscillation, resulting from local charge imbalances in the plasma. Due to the dynamic nature of a plasma, electrons are continually in motion. This motion results in a strong electric field around their displacement. In the time scales relevant to laser plasma physics, the ions are unaffected on the time scale of the electron behaviour. This is due to their lower charge to mass ratio, allowing them to be considered immobile. The electrons move back to their original position, in order to restore neutrality, however overshoot this location and oscillate around their equilibrium position, as a consequence of the local charge imbalance. This oscillation is named the plasma frequency, and is given by:

$$\omega_p = \sqrt{\frac{n_e e^2}{\gamma m_e \epsilon_0}}, \tag{2.2}$$

where m_e is the electron rest mass and $\gamma = 1/\sqrt{(1 - v^2/c^2)}$ is the relativistic Lorentz factor, where v is the velocity of the oscillating electrons and c is the speed of light.

In the following section, the mechanisms that lead to the creation of a plasma by the rising edge of the laser pulse are outlined.

2.2 Laser-induced ionisation

When incident on a solid material, an electromagnetic wave of a sufficiently high intensity can induce ionisation on the surface of the material, liberating electrons from their constituent atom. This results in the formation of a plasma on the front surface of the solid. For ionisation to occur, the laser electric field must be high enough to overcome the Coulombic forces binding the electrons to their constituent atom. In the context of the Bohr model, which describes the atomic behaviour of a hydrogen atom, the electric field binding an electron to the hydrogen nuclei is given by:

$$E_a = \frac{e}{4\pi\epsilon_0 a_B^2}, \tag{2.3}$$

where a_B is the Bohr radius, which is the mean radius of orbit of an electron around the nucleus of a hydrogen atom in its ground state. This distance is given by

$$a_B = \frac{4\pi\epsilon_0\hbar^2}{m_e e^2} = 0.053 \text{ nm}, \tag{2.4}$$

where $\hbar = h/2\pi$ is the reduced Planck's constant. The minimum laser intensity, I_a, required to overcome the binding energy can be found by averaging the magnitude of the Poynting vector over one laser period:

$$I_a = \frac{1}{\mu_0}\langle|\mathbf{E}\times\mathbf{B}|\rangle = \frac{\epsilon_0 c}{2}E_a^2 \simeq 4\times10^{16} \text{ Wcm}^{-2}, \tag{2.5}$$

where $\mathbf{E}$ and $\mathbf{B}$ are the laser electric and magnetic fields, respectively, and μ_0 is the permeability of free space. For a laser intensity, I_L, greater than I_a, ionisation will occur. Intensity levels far higher than this are used in ion acceleration experiments, with typical values of I_L at the peak of the pulse $> 10^{20}$ Wcm^{-2}.

When describing an ultra-intense laser pulse, a useful parameter to define is the peak normalised vector potential, a_0. This is proportional to the peak electric field, E_0, and is given by

$$a_0 = \frac{eE_0}{m_e c\omega_L}. \tag{2.6}$$

For $a_0 > 1$, electrons will be quivering in the laser field at a velocity approaching c. In this intensity regime, the interaction may be referred to as relativistic. The laser

intensity can be related to a_0 through the expression:

$$I_L \lambda_L^2 = a_0^2 \cdot 1.39 \times 10^{18} \text{ Wcm}^{-2} \mu\text{m}^2, \tag{2.7}$$

where λ_L is the laser wavelength. For a typical laser intensity of $I_L = 10^{20}$ Wcm^{-2}, $a_0 \simeq 10$. a_0 can be related to γ through the expression $\gamma = \sqrt{1 + a_0^2/2}$ for linearly polarised light and $\gamma = \sqrt{1 + a_0^2}$ for circularly polarised. Polarisation refers to the plane in which the electric field of a light wave is oscillating. In the case of p-polarisation, which is the polarisation state used for all of the work presented in this thesis, the plane of polarisation is perpendicular to the material surface (i.e. pointing into the material). For s-polarisation the plane of polarisation is parallel to the surface. For cirular polarisation, the direction of the electric field rotates in time at a steady rate, in a plane perpendicular to the direction of the wave. The magnitude of the field is constant in the case of circular polarisation as it rotates.

This intensity threshold is not the minimum intensity required to ionise a material, but is the case for which field ionisation is highly probable. Due to non-linear processes, laser intensities far below this value may still induce ionisation. This is an important consideration. While the peak of the laser pulse in the work presented in this thesis is often $> 10^{20}$ Wcm^{-2}, and therefore many orders of magnitude higher than I_a, the Gaussian (in time and space) laser pulse is first preceded by a low intensity ($> 10^{12}$ Wcm^{-2}) pedestal. This can be present up to a nanosecond prior to the arrival of the main pulse, which in this work is around 1 picosecond long (full width at half-maximum, FWHM). This pedestal is known as amplified spontaneous emission (ASE) and is described in more detail in Chapter 3. Even though many orders of magnitude lower than I_a, the ASE is still capable of ionising the target front surface and pre-expanding the material. There are three main ionisation mechanisms which are relevant to laser-matter interactions, as illustrated in Fig. 2.1. These are known as multi-photon, tunnelling and barrier-suppression ionisation. Which mechanism is dominant depends on the incident laser intensity. The dominant regime of ionisation, for a given value of I_L, can be found from the Keldysh parameter (γ_K). γ_K compares the electron oscillation energy in the electric field of the laser to the ionisation energy of the material, and is given by [34]:

$$\gamma_K = \omega_L \sqrt{\frac{2\varepsilon_a}{I_L}}, \tag{2.8}$$

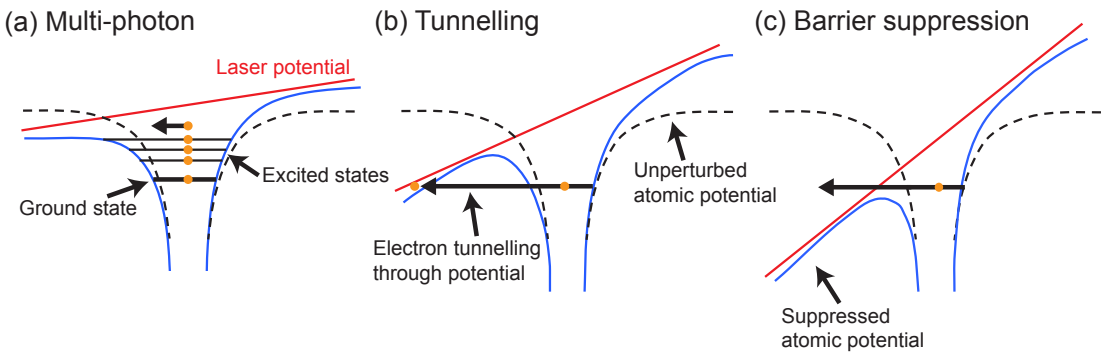

Figure 2.1: Schematics illustrating the main ionisation mechanisms relevant to laser-plasma physics. (a) Multi-photon ionisation; (b) Tunnelling ionisation and; (c) Barrier suppression ionisation. Each process is explained in the main text.

where ω_L is the laser angular frequency and ε_a is the ionisation energy. For $\gamma_K > 1$ (i.e. weak laser intensities) multiphoton ionisation will dominate. For $\gamma_K < 1$, either one of the other two mechanisms will dominate.

Multi-photon ionisation, as the name suggests, requires multiple photons to be absorbed by a single electron within a certain time period, in order for it to gain a sufficient amount of energy to escape from the potential well, as illustrated in Fig. 2.1. Each photon has an energy $E_\gamma = \hbar\omega_L$, which, when absorbed, acts to raise the electron into an excited state. If enough photons are absorbed, such that the electron has a higher energy than that binding it to the nucleus, it will escape with some kinetic energy. For shorter wavelength lasers, fewer photons are required to liberate the electron from its parent nucleus. In the case of a hydrogen atom, for a laser wavelength of $\lambda_L = 1.054\,\mu\text{m}$ (as used in this work), 12 photons are required to liberate the electron from a hydrogen nucleus. This mechanism is important early-on in the interaction, and can occur for laser intensities as low as $I_L \sim 10^{12}$ Wcm^{-2}.

For $\gamma_K < 1$, the electric field of the laser is sufficiently high to begin suppressing the Coulomb potential of the atom. Quantum mechanically, the electron may tunnel through the potential barrier with some finite probability. For $\gamma_K < 1$, tunnelling ionisation rates become significant. For a laser intensity of $I_L \sim 10^{14}$ Wcm^{-2} this mechanism is dominant.

For $\gamma_K \ll 1$, ionisation through barrier suppression dominates. This occurs when the laser's electric field distorts the Coulomb barrier enough such that it falls below the binding energy. This is also known as over the barrier suppression or field ionisation, and was the mechanism initially discussed at the beginning of this section.

The intensities quoted for these mechanisms are based on the dynamics of the hydrogen atom. In the case of atoms with a larger nucleus, as more electrons are stripped from the nucleus, more energy is required to liberate successive electrons. To put this into context, one of the most commonly used target materials for ion acceleration experiments is aluminium. For typical laser intensities used on a laser-solid interaction experiment in this work, it is not expected that an appreciable number of aluminium ions will be fully stripped of electrons, and it is assumed that the inner shell always remains. The ADK model, as described in Ref. [35], accounts for larger ions with a higher number of charge states, thereby providing a more accurate model of the ionisation dynamics expected for a typical target.

As mentioned previously, a relatively weak ($I_L \simeq 10^{12}$ Wcm^{-2}) laser field is enough to ionise the target front surface. The peak of the laser pulse is many orders of magnitude higher, which acts on the electrons in the plasma created predominantly by the leading edge of the pulse. The electron dynamics, from a single electron to a collection of them, due to this external laser field is discussed in the following section.

2.3 Electron dynamics in a laser field

As discussed previously, the ASE preceding the peak of the laser pulse acts to ionise the target front surface during the laser-solid interaction. This results in the creation of a plasma with a scale length L_s. L_s is characterised as the distance over which the electron density falls by a factor of $1/e_N$. The density profile of the plasma can often be locally approximated by a single exponential, taking the form

$$n_e(x) = n_0 \exp\left(\frac{-x}{L_s}\right), \tag{2.9}$$

where $n_e(x)$ is the electron density at a distance x from the front of the target and n_0 is the solid (i.e. initial) electron density.

2.3.1 Single electron motion

When an electromagnetic field interacts with an electron, the strong fields present act to accelerate the particle. With presently achievable laser intensities ($I_L \simeq 10^{21}$ Wcm^{-2}), such a laser field would result in negligible direct displacement of the ions over a single laser period. A laser intensity equal to $I_L \simeq 10^{24}$ Wcm^{-2} would be required before the

displacement of a proton, for example, would become non-negligible and therefore the ion behaviour due to the laser field on the time-scale of the laser period is assumed to be static. The motion of a charged particle in the presence of an electric or magnetic field is described by the Lorentz force,

$$\mathbf{F} = e(\mathbf{E} + \mathbf{v} \times \mathbf{B}), \tag{2.10}$$

where $\mathbf{v}$ is the particle velocity. In the case of an electromagnetic wave, the $\mathbf{v} \times \mathbf{B}$ term only becomes significant when the electron momentum, $\mathbf{p}$, becomes comparable to the rest mass of the electron (as $\mathbf{E}$ is a factor of c larger than $\mathbf{B}$). For a value of $a_0 \ll 1$, electron motion will almost exclusively be a consequence of the electric field – oscillating linearly for a linearly polarised pulse along the direction of the electric field at a frequency equal to ω_L. The quiver velocity in the transverse plane relative to the laser propagation axis, v_y, due to an applied electric field is given by

$$v_y = a_0 c \sin(\omega_L t). \tag{2.11}$$

For $a_0 > 1$, the magnetic field of the laser gives rise to a force in the direction of the laser propagation, accelerating electrons in this direction to a velocity

$$v_x = \frac{a_0^2}{4} \cos(2\omega_L t). \tag{2.12}$$

For a relativistic laser pulse, the combination of Eqs 2.11 and 2.12 results in a figure-of-eight trajectory in the electron rest frame.

2.3.2 Laser propagation in a plasma

When considering the interaction of a laser pulse with a collection of particles, collective effects play a key role. The interaction is recursive, in that the laser acts on the plasma, while the plasma acts on the laser.

From Maxwell's equations, the dispersion relation for the propagation of an electromagnetic wave in a plasma is given as

$$w^2 = k^2 c^2 + \omega_p^2, \tag{2.13}$$

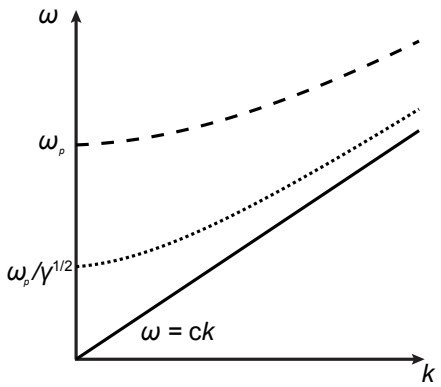

Figure 2.2: The dispersion relation of an electromagnetic wave in a plasma, illustrating how the relativistic increase in the electron mass can result in target transparency. If the wave's frequency is above the plasma frequency, the wave can propagate. The dashed line shows a cold (i.e. classical) plasma wave and the dotted line shows a plasma wave with the electrons oscillating with a Lorentz factor $\gamma \sim 5$. The dispersion relation in vacuum is shown for reference as a solid line.

where $k = 2\pi/\lambda_L$ is the wavenumber. Considering an applied electromagnetic field with a frequency $\omega = \omega_L$. If $\omega_L < \omega_p$, the field cannot penetrate the plasma, due to the more rapid electron response acting to neutralise the field. For $\omega_L > \omega_p$, the electromagnetic wave can propagate through the plasma. The threshold density at which the laser is just able to propagate (when $\omega_L = \omega_p$) is defined as the critical density. This is given by:

$$n_c = \frac{m_e \epsilon_0 \omega_L^2}{e^2} \simeq 1.1 \times 10^{21} \Big(\frac{\lambda_L}{\mu\text{m}}\Big) (\text{cm})^{-3}. \tag{2.14}$$

For $n_e < n_c$ the plasma is described as underdense, while if $n_e > n_c$ it is considered overdense. It should be noted that, for an overdense plasma, the laser field can penetrate beyond n_c, evanescently decaying up to the skin depth. The skin depth is defined as the position where the field magnitude will have dropped by a value equal to $1/e_N$.

For sufficiently high laser intensities, the electron quiver velocity becomes relativistic and the γ term reduces the plasma frequency, allowing lower frequency electromagnetic waves to propagate in the plasma. This depth is known as the relativistic critical density, and is defined as:

$$n_{crit}^{'} = \gamma n_c. \tag{2.15}$$

Recall that if $n_e < n_c$, the target is transparent to the laser field. If $n_c^{'} > n_e > n_c$, then the target becomes transparent because of this relativistic increase of the electron mass. This phenomenon is known as relativistic induced transparency (RIT) [36] and is

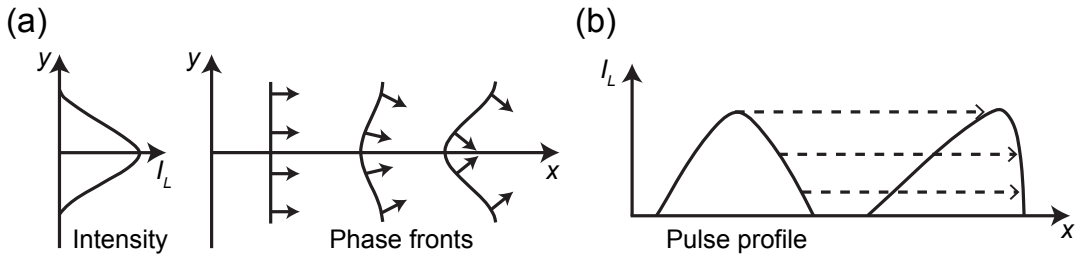

Figure 2.3: (a) Schematic illustrating relativistic self-focusing. A pulse with a transverse intensity profile induces a transverse refractive index profile, peaking at $y = 0$ (i.e. the peak of the laser pulse). This results in the laser pulse at $y = 0$ lagging behind the fringes, leading to a focusing effect. (b) Schematic illustrating profile steepening. The position of the peak intensity moves with a higher group velocity than the pulse leading edge, resulting in a steepening of the pulse.

illustrated in Fig. 2.2. Investigations concerning the onset of this phenomenon in the context of laser-plasma interactions are detailed in the work by Vshivkov *et al.* [37] and Palaniyappan *et al.* [38, 39]. Another effect that contributes to increasing the depth to which the laser pulse will propagate concerns target expansion. As the laser heats and displaces electrons from the front surface, this leads to expansion of the target and a reduction of the electron density n_e. Therefore, RIT is a combination of both a relativistic increase of the electron mass and target expansion. This is critical to the physics underpinning Chapter 4. In Chapter 4, the interaction is initially in the overdense regime. However, for sufficiently thin (< 200 nm) target, the laser pulse can propagate through the target due to RIT. This has several implications on the acceleration of ions, and is detailed in section 2.6.3.

By conservation of momentum, rapid thermal expansion gives rise to a shock wave, directed into the target along the laser propagation axis. For typical ASE intensities of $\sim 10^{12}$ Wcm^{-2}, the shock velocity is of the order $\mu\text{m}\,\text{ns}^{-1}$. If the shock reaches the target rear surface before arrival of the main pulse, the interaction dynamics can change drastically. It can lead to expansion of the target rear, which negatively impacts the acceleration of ions, as investigated in Chapter 6. Specific implications of an electrostatic shock are also discussed in Chapter 7, and was an important consideration when selecting the long pulse laser beam parameters used on the experiment detailed in that chapter.

Two other relativistic effects may occur during the interaction. The first is known as relativistic self-focusing, and is illustrated in Fig. 2.3a. The value of ω_p decreases along the axis of laser propagation, leading to a refractive index profile maximised along the laser axis. This acts like a positive lens, focusing the laser pulse further which results in

an increased laser intensity. The second effect is profile steepening, shown schematically in Fig. 2.3b. This is caused by the finite temporal width of the pulse, with the central regions of the pulse (where the high intensity components are located) moving with a larger group velocity than the surrounding regions. This leads to the position of the pulse peak moving closer to the leading edge, resulting in a steepening of the pulse profile.

2.3.3 Ponderomotive force

According to the Lawson-Woodward theorem [40], an electron experiencing a slowly varying (in time), spatially infinite plane wave cannot extract any energy from the wave. In reality, however, the beam has a Gaussian spatial and temporal profile, and therefore features intensity gradients across its transverse profile. When an electron oscillates in such a field, the electron moves between regions of different intensities. If an electron moves to a region of lower intensity during the first half of the laser period, the return force exerted by this lower intensity region will be smaller than the initial force from the high intensity region. Therefore, during the return cycle, the electron does not return to its original position. Multiple iterations of this result in the electron extracting energy from the laser pulse, and moving away from regions with a higher laser intensity. The pondermotive force is the resultant force experienced by the particle in the gradient of the field.

In the non-relativistic case, the ponderomotive force can be written as

$$\mathbf{F}_p = \frac{e^2}{4m_e\omega_L^2}\nabla\mathbf{E}^2. \tag{2.16}$$

In this case, for $a_0 \ll 1$, only the laser electric field exerts a force on the electrons, resulting in the electrons being ejected perpendicular to the laser propagation axis. In the relativistic case, $\mathbf{F}_p$ is written as

$$\mathbf{F}_p = -m_e c^2 \nabla\gamma, \tag{2.17}$$

The kinetic energy an electron gains as it oscillates in a laser field is converted from the ponderomotive potential:

$$\phi_p = m_e c^2(\gamma - 1). \tag{2.18}$$

This is particularly important for $a_0 \gg 1$, where the electron motion is considerably affected by the $\mathbf{v} \times \mathbf{B}$ term. For a typical I_L corresponding to a value of $a_0 = 10$, the electron will gain a kinetic energy $\varepsilon_e \simeq 3$ MeV.

In the relativistic case, some of the electron motion will be perpendicular to the field-lines. As energy is transferred from n number of photons to the single electron, momentum in the parallel direction is conserved:

$$p_{\parallel} = n\hbar k = \frac{n\hbar\omega_L}{c} = \frac{\phi_p}{c} = m_e c(\gamma - 1) \tag{2.19}$$

The perpendicular component of the momentum is related to $p_{\parallel}$ through

$$p_{\parallel} = \frac{p_{\perp}^2}{2m_e c}, \tag{2.20}$$

which results in an ejection angle relative to the laser propagation axis:

$$\tan\theta = \frac{p_{\perp}}{p_{\parallel}} \quad \Rightarrow \quad \cos\theta = \sqrt{\frac{\gamma - 1}{\gamma + 1}}. \tag{2.21}$$

As I_L increases, the ejection angle θ approaches the laser propagation axis. The depletion of the electron population in the location of the laser focus will continue until ϕ_p is cancelled by space-charge effects.

Depending on the plasma and laser parameters, other mechanisms of energy absorption into electrons may occur instead of the scheme discussed in this section. All of these heating mechanisms are described in the following section.

2.4 Laser absorption mechanisms

This section outlines the processes through which laser energy is coupled to the plasma electrons, which in most cases acts to accelerate the electrons through the target. In overdense plasmas, ponderomotive acceleration is the most important mechanism for the acceleration of electrons through the target. The electron beam is divergent (half-angle equal to $\simeq 30^\circ$ for the laser intensities studied in this thesis), and has an energy ~ 3 MeV. It is these accelerated electrons that lead to ion acceleration in the case of laser-solid interactions, with their acceleration playing a critical role in the parameters of the resultant ion beam.

Two broad categories exist for laser energy absorption by electrons in an overdense plasma: collisional and collisionless. A detailed summary can be found in the review article by Davies [41]. For $a_0 > 1$ electron motion is relativistic, resulting in a low collisional cross-section. For such parameters, collisionless processes dominate. These collisionless process are illustrated in Fig. 2.4, and are described in sections 2.4.2-2.4.4. For low laser intensities, collisional processes may instead dominate. A detailed study of the scaling as a function of laser intensity can be found in the work by Ping *et al.* [42]. A more recent study, investigating the effects due to focal spot size and laser pulse energy, is detailed in Gray *et al.* [43].

In the following section, the most prominent collisional process is discussed.

2.4.1 Inverse Bremsstrahlung

The term 'Bremsstrahlung' is used to describe the electromagnetic radiation produced by the deceleration of a charged particle. The moving particle loses kinetic energy, which is converted into a photon (by law of conservation of energy). Inverse Bremsstrahlung implies the opposite, where an electron gains kinetic energy from a photon. This is a collisional process and dominates for low laser intensities ($\sim 10^{15}$ Wcm^{-2}) where the probability of collision is high, resulting from the lower particle velocities.

For these intensity levels, the oscillating electrons normally do not contribute to damping of the laser field. Due to the background ion plasma, however, there is a probability that an oscillating electron will collide with an ion, thereby enabling the transfer of energy from the laser to the plasma. The heating spectrum is continuous (i.e. thermal), with collisions between the electrons and ions happening, on average, at the electron-ion collisional frequency. This mechanism is important for the transference of energy during the ASE phase of the laser pulse.

2.4.2 Resonance absorption

Resonance absorption occurs when energy is coupled to electrons at the critical surface via the excitation of resonant plasma waves. For this process, the plasma scale length, L_s, must be greater than the laser wavelength, with an electric field component parallel to the density gradient. Therefore, in order to drive the electrons in this direction, the incident pulse must be p-polarised and angled oblique to the target.

As the laser pulse propagates through the plasma, it continually experiences refraction

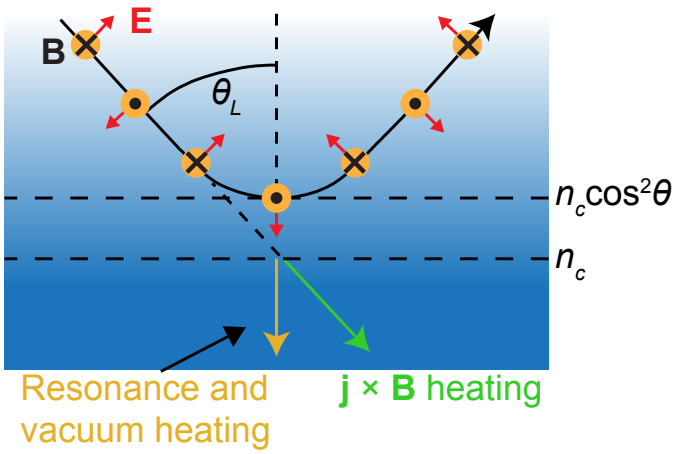

Figure 2.4: Schematic illustrating the three main collisionless absorption processes, described in the main text. The laser is p-polarised and is incident at an oblique angle of incidence, θ_L.

in the increasing electron density. This is the same effect that leads to relativistic self-focusing, described in section 2.3.2. Due to the oblique angle of incidence, the point of reflection occurs at $n_c\cos^2(\theta_L)$ as opposed to n_c. This modified critical density surface is explained with reference to the dispersion relation in Eq. 2.13. The laser k-vector has both a transverse and longitudinal component, resulting in a dispersion relation that accounts for the incidence angle θ_L being given by:

$$\omega^2 = \omega_p^2 + k_x^2 c^2 + \omega_L^2 \sin^2\theta_L. \tag{2.22}$$

Note that x is the longitudinal dimension. If $k_x < 0$ the laser pulse is reflected, which occurs when $n_e > n_c \cos^2\theta_L$.

At the point of reflection, the electric field component oscillates normal to the modified critical surface (i.e. parallel to the density gradient). The electric field evanescently decays beyond $n_c\cos^2(\theta_L)$, resulting in a weak restoring force acting on the oscillating electrons. This resonantly drives a plasma wave with a frequency equal to ω_L at the critical surface. The generation of the plasma wave is most efficient when $\omega_p = \omega_L$ (i.e. at resonance).

This mechanism tends to be the dominant collisionless scheme for $I_L < 10^{17}$ Wcm^{-2}. For higher laser intensities this process still exists, however due to profile steepening (outlined in section 2.3.2), L_s reduces due to the modified scale length.

2.4.3 Vacuum heating

For $L_s < \lambda_L$, vacuum heating [44] may become dominant. In this scheme, electron oscillations are driven in a plasma with a very sharp density gradient. For such a gradient, the electron oscillation amplitude is greater than L_s. Electrons are pulled from the plasma/target during the first half of the laser cycle, and are driven through the target during the return oscillation. Due to the sharp density gradient, the electrons oscillate beyond the critical density surface, thus extracting energy from the laser field.

2.4.4 $\mathbf{j} \times \mathbf{B}$ heating

For relativistic intensities ($a_0 > 1$) $\mathbf{j} \times \mathbf{B}$ heating [45] dominates. $\mathbf{j} \times \mathbf{B}$ heating is the only presently known electron acceleration mechanism where the laser magnetic field is responsible for the energy coupling, as it depends on the field driven by the oscillating component of the ponderomotive force (outlined in section 2.3.3), when the $\mathbf{v} \times \mathbf{B}$ component of the Lorentz force becomes comparable to, or greater than, the electric field contribution. The force acts to ponderomotively drive electrons from regions of high intensity, while also accelerating them along the laser propagation axis. Some of these electrons oscillate near the critical density surface, resulting in some being driven into the overdense target. The force in the direction of the laser k-vector is:

$$\mathbf{F} = \frac{-m_e}{4}\frac{\partial \mathbf{v}_o}{\partial x}(1 - \frac{1 - e_l^2}{1 + e_l^2}\cos(2\omega_L t)) \tag{2.23}$$

where $\mathbf{v}_o$ is the electron quiver velocity and e_l is the ellipticity of the laser pulse. Note that linear and circular polarisation correspond to a value of $e_l = 0$ and $e_l = 1$, respectively. The first term is the ponderomotive force, which acts to drive electrons away from regions of the highest laser intensity. The second terms is the $\mathbf{j} \times \mathbf{B}$ component, which drives electrons at a frequency equal to $2\omega_L$ along the laser axis. Oscillation near n_c results in some being injected into the overdense target and away from the influence of the laser, resulting in energy being extracted by the laser.

$\mathbf{j} \times \mathbf{B}$ heating is most effective for high electron densities and normal incidence. This mechanism works for both s and p-polarisation, but not for circular. In the case of circular polarisation, where $e_l = 1$, the $\mathbf{j} \times \mathbf{B}$ term vanishes. Measurements made by Santala *et al.* [46] demonstrate the change in direction of the accelerated electrons as a function of density scale-length, suggesting a transition from vacuum to $\mathbf{j} \times \mathbf{B}$ heating.

In this study, $\lambda_L = 1\,\mu\text{m}$ and $I_L > 10^{19}$ Wcm^{-2} ($a_0 > 1$) – resulting in $\mathbf{j} \times \mathbf{B}$ heating likely being the dominant heating mechanism at the peak of the pulse.

In the following section, the transport of these accelerated fast electrons is discussed.

2.5 Fast electron transport

The previous section described the mechanisms by which laser energy is coupled to the plasma electrons, which are accelerated through the target. In the context of laser-driven ion acceleration, the electrons are the mediator between the laser pulse and the accelerated ions. Fast (MeV) electrons are accelerated with a peak current on the order of a mega-Ampere (MA), with a Boltzmann-like energy distribution and temperature dependent on the laser intensity. The energy coupled to the electrons varies, depending on the laser and target parameters. Measurements on the total energy absorbed were initially made by Ping *et al.* [42], with laser intensities from $I_L = 10^{18} - 10^{20}$ Wcm^{-2} used. The conversion efficiency from laser to plasma was $\sim 30\%$ for the lower intensity limit and as high as 80% for the upper limit. Gray *et al.* [43] reported similar results. It should be noted that this is the total energy absorbed, including energy resulting in plasma expansion in addition to electron kinetic energy.

Around 10^{13} electrons are injected into the target for the laser systems used in this work, with most propagating through the target. Of critical importance to the transit of this fast electron beam is the concept of current neutrality [47]. For a laser pulse with $I_L = 10^{18}$ Wcm^{-2}, the magnetic energy contained within the electron beam is of the order 10^3 times higher than the energy absorbed by the plasma. A magnetic field of this strength would stop the transport of the fast electrons within several micrometers. The maximum current that can propagate, for an infinitely wide beam, without generating a magnetic field that would change the trajectory of the beam is given by the Alfvén limit [48],

$$I_{max} = 1.7 \times 10^4 \beta\gamma, \tag{2.24}$$

where $\beta = v/c$. For a 2 MeV electron beam, according to Eq. 2.24, the maximum current that can propagate is equal to 82 kA. In a typical laser-solid experiment, currents > 10 MA are regularly achieved; vastly exceeding this limit. Bell *et al.* [47] hypothesised that a return current, $\mathbf{j}_r$, must be supplied in order to inhibit this magnetic field growth,

with a magnitude roughly equal to the fast electron current, $\mathbf{j}_f$, such that:

$$\mathbf{j}_r + \mathbf{j}_f = 0 \tag{2.25}$$

The vast majority of target heating occurs due to this return current. The velocity of the fast electrons is relativistic, leading to a relatively small collisional cross-section and a mean-free path that is larger than the thickness of the target. The return current is much slower, and consequently must have a much higher population of electrons in order to satisfy Eq. 2.25, which in turn leads to heating of the solid material.

Most of these electrons propagate through the target bulk, with the most energetic of these electrons ($< 1\%$ of the population) escaping into vacuum. This leaves the target positively charged. Subsequent fast electrons arrive at the target-vacuum boundary, and are either reflected or confined in an electron cloud on the target rear. This charge differential results in the generation of an electric potential of the order TVm^{-1} on the target rear. The Debye length of the sheath field is around $\lambda_D = 1\,\mu\mathrm{m}$. Most of the electrons in the cloud are confined here during the course of the interaction, due to the net-positive charge of the target acting to pull them back. Therefore, it can be considered static during the course of the interaction. This cloud is characterised in Chapter 5, and is shown in Fig. 5.3a

The subsequent fast electrons that are reflected at the target-vacuum boundary travel back through the target. These electrons reach the front surface, with a similar sheath field acting to reflect most of the electrons arriving at the front surface boundary. This process repeats a number of times, depending on the target thickness and laser intensity, and is known as recirculation (or refluxing) [49]. For thinner targets, a single electron will recirculate more times than thicker targets. Due to the diverging electron beam, this results in a sheath field that extends far along the transverse plane of the target. Additionally, some of the electrons on the surfaces travel laterally across the boundaries [50] - further extending the physical extent of the sheath field. It is this sheath field which acts to accelerate ions in the TNSA scheme, discussed in section 2.6.1.

While the current is neutral, on average, some small perturbations are present on a microscopic scale. The growth of electromagnetic fields is seeded due to these local perturbations. Spatial variations of the fast electron current density lead to the generation of an azimuthal magnetic field, which acts to push electrons into regions of a

higher current density. The highest current density exists along the laser propagation axis, which results in an effective pinching of the electron beam. Additionally, spatial gradients in the background plasma resistivity result in the generation of a secondary magnetic field. These spatial gradients are due to the background plasma temperature gradient; an effect resulting from the return current. This drives electrons into regions of higher resistivity, typically in the transverse plane. Depending on the magnitude of these two fields, the beam either pinches or diverges. This magnetic field growth is described according to the equation

$$\frac{\partial \mathbf{B}}{\partial t} = -\nabla \times \mathbf{E} = \nabla \times \eta \mathbf{j}_f - \nabla \times \Big(\frac{\eta}{\mu_0} \nabla \times \mathbf{B} \Big), \tag{2.26}$$

where η is the target electrical resistivity. The second term on the right-hand side describes resistive diffusion of the magnetic field through the target. For the parameters considered in a laser-plasma experiment, this term may be neglected, as the diffusion time is of the order ~ 1 s. The magnetic field growth rate can then be expressed as:

$$\frac{\partial \mathbf{B}}{\partial t} = \eta(\nabla \times \mathbf{j}_f) + \nabla \eta \times \mathbf{j}_f. \tag{2.27}$$

This equation describes the magnetic field generation arising from the variation in the fast electron current density ($\eta(\nabla \times \mathbf{j}_f)$), in addition to the field growth due to variation of the material's resistivity ($\nabla \eta \times \mathbf{j}_f$).

A host of beam instabilities exist, which ultimately lead to a break-up of the electron beam into filaments, resulting in a loss of energy and changes to the spatial profile of the beam. The most prominent in the context of laser-plasma physics is the collisionless Weibel instability [51]. This instability develops due to spatial modulations of the fast electron beam density, seeded by the interaction between the counter-propagating currents. Localised magnetic fields are generated, pinching the beam transversely into filamentary structures. These filaments have a faster growth rate for a higher fast electron beam density and a faster beam velocity. Another instability, similar to the collisionless Weibel instability, is the resistive filamentation instability. The difference concerns what seeds this instability, with each filament related to the material's resistivity.

In the following section, the various mechanisms that result in the acceleration of ions are discussed.

2.6 Laser-driven ion acceleration

Ions are not directly accelerated by the laser field at currently achievable laser intensities, with the required intensity for direct acceleration of protons in excess of 10^{24} Wcm^{-2}. Ions are accelerated via the space-charge effects resulting from electron displacement. Multi-MeV protons can be produced at intensities $> 10^{19}$ Wcm^{-2}, with various mechanisms responsible for this acceleration. This thesis reports on the highest proton energy recorded to date via laser-driven ion acceleration, which is (97 ± 4) MeV (Chapter 4 and Ref. [5]). The dominating mechanism responsible for the acceleration of ions depends on the laser and target parameters used. Hybrid acceleration scenarios may also be invoked, with multiple mechanisms contributing to the net acceleration of ions.

This section serves as a summary of the main, individual mechanisms responsible for ion acceleration with presently achievable laser intensities. Details regarding the various analytical models that exist for each acceleration scheme are also included, with these applied in Chapter 4. Macchi *et al.* [20], Diado *et al.* [52] and the more recent (preprint) article by Macchi [53] provide comprehensive review articles on laser-driven ion acceleration.

2.6.1 Target normal sheath acceleration

The interpretation of early observations of laser-driven ion acceleration from initially solid targets, with $I_L = 5 \times 10^{19}$ Wcm^{-2} and $\ell = 125\,\mu$m, hypothesised that the ions originated from the front of the target [54, 55]. For the laser and target parameters investigated in the work presented in this thesis, a more robust model for ion acceleration was proposed by Snavely *et al.* [15] and Wilks *et al.* [56]. In this scheme, the ions are accelerated from the target rear due to space-charge induced electrostatic fields. This model is known as target normal sheath acceleration (TNSA). To date, TNSA is the most widely investigated laser-driven ion acceleration mechanism, for a wide range of laser pulse durations.

TNSA results from the acceleration of relativistic electrons, detailed in the previous section. The TVm^{-1} electrostatic sheath field that is set up at the target rear acts to ionise the rear-surface hydrocarbon contaminant layer [57], inherently present due to the imperfect vacuum conditions. This Gaussian-like sheath field extends laterally across the target rear, with a typical width (FWHM) between $50 - 100$ µm, depending on the

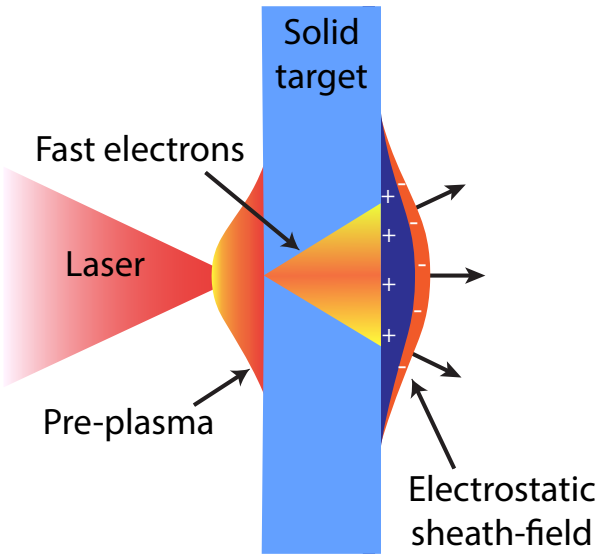

Figure 2.5: Schematic illustrating the acceleration of a population of rear-surface ions via TNSA. The dark blue represents the ion population and the orange represents the electron population. Fast electron dynamics within the target and front surface ion acceleration are not shown.

laser and target parameters used. The first indirect observation, utilising the proton deflectometry technique, of the Gaussian-like sheath field was made by Romagnani *et al.* [58]. A more precise characterisation of this is presented in Chapter 5, using the same diagnostic technique, temporally resolving the build-up of this transient field. A schematic illustrating TNSA in shown in Fig. 2.5.

The hydrocarbon contaminant layer is thin ($\sim$ 10 nm) and, in the case of a metallic target, is the source of the accelerated protons and carbon ions. Ions closest to the solid-vacuum boundary are exposed to the highest field gradients, and act to screen the electric field for ions further from the vacuum-boundary. Protons are most efficiently accelerated, due to their high charge to mass ratio; reaching the highest velocities. Heavier ions will travel at a lower velocity, which results in a layering of the ion species [59]. The accelerating ion beam is centred normal to the target rear surface. Ions are accelerated over a time slightly longer than the laser pulse duration ($\sim 1.3\tau_L$ for the laser and target parameters in Ref. [60]), with the maximum accelerating field occuring shortly after the peak of the laser pulse [60].

TNSA can be modelled using an isothermal plasma expansion model. The most widely recognised and applied model was devised by Mora [61], and is applied in Chapter 4. The Mora model is 1-D, collisionless, assumes that the plasma is quasi-neutral (i.e. $n_e = Zn_i$, where Z is the ionisation state), is at a constant (electron)

temperature, T_e, and there is only a single ion species, uniformly ionised. The ions are initially cold and at rest, with a sharp boundary at the solid-vacuum interface. The electron density follows a Boltzmann distribution,

$$n_e = n_{e0} \exp\Big(- \frac{e\phi}{k_B T_e}\Big), \tag{2.28}$$

where n_{e0} is the electron density of the solid target and ϕ is the electrostatic potential. ϕ satisfies the Poisson equation, and upon integration of this a simple expression for the electric field at the ion front follows as:

$$E_{front} = \sqrt{2/e_N} E_0, \tag{2.29}$$

where $E_0 = \sqrt{n_{e0} k_B T_e/\varepsilon_0}$. A more precise expression for Eq. 2.29, derived in [61] using numerical methods, valid for any time t is

$$E_{front} \simeq \frac{2E_0}{(2e_N + \omega_p^2 t^2)^{1/2}}. \tag{2.30}$$

Through integration of $dv_{front}/dt = ZeE_{front}/m_i$, the ion front velocity v_{front} as a function of time is given by

$$v_{front} \simeq 2c_s \ln(\tau + \sqrt{\tau^2 + 1}), \tag{2.31}$$

where $\tau = \omega_p t/\sqrt{2e}$. The energy spectrum of the ions is given by

$$dN/d\varepsilon = (n_{i0} c_s t/\sqrt{2\varepsilon\varepsilon_t}) \exp(-\sqrt{2\varepsilon/\varepsilon_t}), \tag{2.32}$$

where n_{i0} is the initial solid ion density and $\varepsilon_t = Zk_B T_e$. The cut-off energy ε_{max} (i.e. the maximum proton energy) is

$$\varepsilon_{max} \simeq 2\varepsilon_t (\ln(2\tau))^2. \tag{2.33}$$

A full derivation of these parameters can be found in Mora [61].

Figure 2.6 shows the temporal evolution of the electric field and particle densities, reprinted from Ref. [62], calculated using the Mora model [61]. The electric field (green) peaks at the ion front for all of the times shown, with a trace of this indicated by the

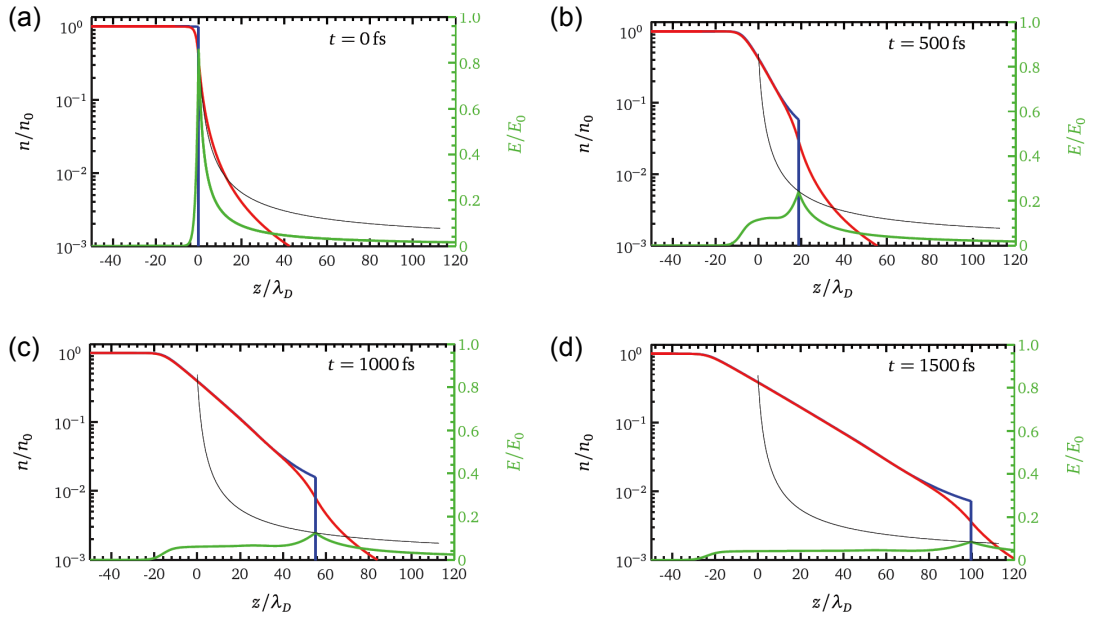

Figure 2.6: Temporal evolution of the electric field (green) and ion (blue) and electron (red) densities, for (a) time $t = 0$ fs; (b) $t = 500$ fs; (c) $t = 1000$ fs and; (d) $t = 1500$ fs. The density and electric field are normalised to the peak density and the expansion length is normalised to the Debye length λ_D. The black curve traces the evolution of the peak electric field. Figure reprinted from Ref. [62].

black curve. Initially, the ion density $n_i = n_{i0}$ for $z \leq 0$ and equal to zero for $z > 0$. This field is strongest at $t = 0$ fs, when the separation between the electrons and ions is greatest. The ions are accelerated towards the electron front as soon as the field forms, with the majority of acceleration experienced at early times when the electric field is highest. At the location of the ion front, for all t, the electric field is a factor of two greater than the average electric field.

As the proton front approaches the electron front, with the electric field subsequently decaying, the eventual result is a quasi-neutral beam of charged particles. This is advantageous, as outlined in Chapter 1, as the beam is far less prone to space-charge spreading effects when compared to a single species charged particle beam as is typical from a conventional accelerator. At later times ($t \geq 500$ fs) the ion population possesses an exponentially decaying energy spectra (note that the number density axis in Fig. 2.6 is on a logarithmic scale), with a sharp cut-off energy at the maximum energy. This type of spectrum is typical of TNSA, as seen from the experimental data shown in Fig. 4.4, Chapter 4, for relatively thick (> 500 nm) plastic targets.

Due to the 1-D nature of the Mora model [61], in addition to the single electron temperature assumed, it is limited in how well it can describe reality. In the work

by Robson *et al.* [63], a model is invoked that accounts for this multi-dimensional expansion in addition to fast electron spreading within the target. This model shows better agreement with their experimental data when compared to the Mora model. This correction is applied in Chapter 4, in addition to a correction accounting for target transparency for thin (< 300 nm) targets.

In a 3-D scenario, the ions are subject to a radial Gaussian-like transverse distribution in the magnitude of the accelerating field, centred on the target normal axis. Ions experiencing the peak of the field are accelerated to the highest velocities, and are accelerated normal to the sheath field, as illustrated by the arrows in Fig. 2.5. This results in the beam of ions having an energy-dependent divergence.

The maximum ion energy achievable is linked to the laser intensity and pulse duration. TNSA proton energies in excess of 85 MeV from ultrathin foils has recently been reported by Wagner *et al.* [64], with similar energies achieved via TNSA in the work detailed in Chapter 4. In both studies CH foils were used, with a thickness in the range 300 nm - 1 µm. Recall that in section 2.5, the target thickness influences the electrostatic sheath field, which is turn influences the ion beam characteristics. Measurements of the maximum proton energy as a function of laser intensity are summarised by Borghesi *et al.* [65]. It is shown that for relatively long pulse duration ($\tau_L = 0.5 - 1$ ps) the TNSA maximum proton energy scales as $\varepsilon_{max} \propto \sqrt{I_L \lambda_L^2}$. This is expected, as the maximum ion energy scales linearly with the peak electric field, which has a square-root dependence on the laser intensity, as seen from Eq. 6.6, Chapter 6.

2.6.2 Radiation pressure acceleration

The incidence of an electromagnetic wave on a solid surface imparts some amount of momentum, resulting in a radiation pressure (for normal incidence):

$$P_{rad} = (1 + R - T)\frac{I_L}{c} = (2R + A)\frac{I_L}{c}, \tag{2.34}$$

where R, T and A are the reflection, transmission and absorption coefficients, respectively, and energy conservation imposes that $R + T + A = 1$. In laser-plasma interactions, the immense pressure exerted by the laser may be enough to overcome the thermal pressure of the heated plasma. This pressure acts to accelerate electrons located within the laser focal spot directly, setting up a space-charge field that accelerates the ions. This type

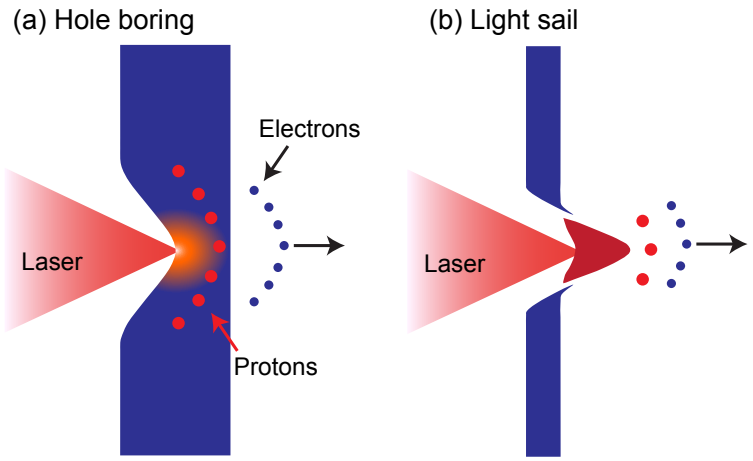

Figure 2.7: Schematic illustrating the two RPA modes of ion acceleration. (a) hole-boring RPA and (b) light sail RPA.

of acceleration is known as radiation pressure acceleration (RPA). For sufficiently high laser intensities, simulations show that RPA begins to dominate over TNSA [66].

Two modes of RPA exist, known as hole boring (HB) and light sail (LS). Both of these modes are illustrated in Fig. 2.7. In HB-RPA, electrons are driven at the critical surface of the target by the radiation pressure, boring a hole in the target and moving at a velocity known as the hole boring velocity v_{HB}. Measurements of v_{HB} are presented in Chapter 4. In LS-RPA, the compressed electron layer reaches the rear of the target while the laser pulse is still present, resulting in acceleration of a whole section of the target. Both of these modes of RPA are summarised, with HB-RPA initially outlined in the following section.

Hole boring

As the laser radiation pressure begins to dominate over the plasma thermal pressure, the front surface target electrons are accelerated forward, creating a sharp spike in the electron density at the critical surface. Due to the charge separation field generated by the moving dense electron population, the ions are accelerated.

HB-RPA is most efficient for low electron temperatures, with the generation of fast electrons reducing its efficiency. Fast electron production is associated with a decrease R, due to an increase in A, and produces a strong thermal pressure due to heating of the target electrons, which counteracts the radiation pressure. Therefore, by using circularly polarised light at normal incidence, fast electron generation can be effectively

quenched, due to the absence of the oscillating $\mathbf{j} \times \mathbf{B}$ heating. Suppressing fast electron generation also leads to a reduction in the X-ray emission [67]. Following Robinson *et al.* [68], the relativistically-corrected hole-boring velocity v_{HB} is given by:

$$\frac{v_{HB}}{c} = \frac{\sqrt{\Xi}}{1+\sqrt{\Xi}}, \qquad \Xi = \frac{I_L}{m_i n_i c^3}, \tag{2.35}$$

where m_i is the ion mass and n_i is the ion density. Note that in this model v_{HB} is related to the instantaneous laser intensity. The maximum ion energy predicted using this model is:

$$\varepsilon_{max} = m_i c^2 \Big(\frac{2\Xi}{1+2\sqrt{\Xi}} \Big). \tag{2.36}$$

HB-RPA continues until either the compressed electron layer has reached the target rear (at which point LS-RPA is invoked), or the laser pulse no longer impinges on the target. The scaling of ε_{max} with density implies that for typical target densities ($n_i > 100 n_c$), tens of MeV may be achieved. The highest energies can be achieved using this scheme if the target density is reduced to a value just above n_c. With upcoming laser facilities ($I_L > 10^{22}$ Wcm^{-2}), proton energies in excess of 100 MeV may be achieved from HB-RPA, as predicted numerically and theoretically [69, 70].

Experimental evidence of HB-RPA was presented by Palmer *et al.* [71], obtained using a CO_2 laser and a gas target, using $\lambda_L = 10\,\mu$m pulses of circularly polarised, $I_L \sim 10^{16}$ Wcm^{-2} light. Spectral peaks at $\varepsilon_p = 1$ MeV were measured.

Light sail mode

If the target is sufficiently thin ($\ell \ll v_{HB}\tau_L$), the compressed electron front reaches the target rear side whilst the laser drive is still present. A typical target thickness of the order of tens of nanometres is required for presently achievable laser intensities. This results in the acceleration of a whole section of the target, resulting in even higher ion energies (GeV/nucleon predicted for $I_L \simeq 1 \times 10^{23}$ Wcm^{-2} [66]) as the ions are no longer screened by the background plasma. This leads to a very efficient acceleration process. This method of ion acceleration can be modelled as a thin mirror that has been boosted by radiation pressure, hence the term 'light sail'.

The interest in LS-RPA was initially stimulated by 3-D PIC simulations of thin planar foil acceleration [66]. These simulations assumed a laser pulse intensity of $\sim 10^{23}$ Wcm^{-2} ($a_0 \simeq 300$) and $\tau_L = 8\lambda_L/c$ (i.e. 8 cycle), with a target thickness of $\ell = \lambda_L$

and $n_e = 49n_c$. These parameters resulted in the coherent acceleration of protons to energies of around 1.5 GeV.

The efficiency of LS-RPA is defined by the ratio between the mechanical energy of the mirror over the electromagnetic energy of the laser pulse, given by

$$\eta = \frac{2\beta}{1+\beta}, \qquad \beta = v/c, \tag{2.37}$$

hence, LS-RPA becomes most efficient as the velocity of the moving mirror approaches unity. For next generation laser facilities, with laser intensities exceeding 10^{24} Wcm^{-2} expected, the LS-RPA scheme is especially appealing.

Following Andreev *et al.* [72], through solving the equation of motion, the maximum proton energy is found by numerically solving

$$\frac{\delta_e \tau_L}{2} = \int_{\zeta}^{\zeta(\gamma_p + \sqrt{\gamma_p^2 - 1})} \frac{dx}{(x^2 + 1 + a_0^2 - \sqrt{(x^2+1-a_0^2)^2 + 4a_0^2})}, \tag{2.38}$$

which determines γ_p, the Lorentz factor of the ions, and therefore ε_{max} as a function of the laser and target parameters. Note that $\delta_e = Zm_e/m_i$ and $\zeta = \omega_p^2 \ell / 2\omega_L c$. The calculation shown in Eq. 2.38 was performed over a series of target thicknesses in Chapter 4, in order to calculate ε_{max} as a function of ℓ for various τ_L. This model also takes into account target transparency. Additionally, the Gaussian nature of the laser pulse can be accounted for by dynamically changing the Lorentz factor of the electrons (which depends on a_0), which is factored into ω_p as seen in Eq. 2.2.

Possible indications of the onset of LS-RPA were reported from an experiment using the Vulcan laser by Kar *et al.* [73], with a narrow-band spectra with peak energies $\simeq 10$ MeV/nucleon measured. Results reported by Henig *et al.* [74] show that, when using linearly and circularly polarised light, the latter case results in a reduction of electron heating and a peak in the C^{6+} energy spectra at around 30 MeV, at an optimum foil thickness $\ell = 5$ nm. More recently, Scullion *et al.* [75] accelerated carbon ions with ~ 30 MeV/nucleon using circularly polarised, $\tau_L = 40$ fs pulses. When using linear polarisation, energies of around ~ 10 MeV/nucleon were accelerated - suggesting RPA is the mechanism of acceleration responsible for $\varepsilon_{max} = 30$ MeV/nucleon in the case of circular polarisation. In all three cases, however, the spectral peaks were accompanied by a relatively low number, broadband spectral signal.

For efficient acceleration, circularly polarised pulses of light should be used, like

with HB-RPA. This is not straightforward, especially for next generation facilities which expect to house even larger beams - requiring large optics to convert the initial linearly polarised light. Additionally, current experimental evidence suggests a relatively broad ion spectrum, likely from transverse inhomogeneity and heating effects. Simulations featuring a circularly polarised laser pulse with a transverse intensity gradient show that the target surface begins to buckle, resulting in the surface no longer appearing normal to the laser pulse and the plasma electrons being heated [76]. This leads to plasma expansion, resulting in TNSA-like behaviour and possibly target transparency.

2.6.3 Relativistic transparency-enhanced acceleration

As discussed in section 2.3.2, if sufficiently thin, the target may undergo relativistic-induced transparency, through a combination of both target expansion and the relativistic increase in the mass of the target electrons. Upon transparency, the effects due to RPA are suppressed, as both modes of RPA require the target to be opaque to the laser pulse. P_{rad} reduces with increasing T in Eq. 2.34. As the laser pulse is transmitted though the target, however, this can act to volumetrically heat the target electrons – leading to an enhancement in the electric field and thereby increase in the accelerated ion energies. The mechanism by which energy is transferred to the sheath-accelerated ions is still under investigation, with the two most prominent discussed here.

Simulation studies investigating energy exchange via streaming plasma instabilities were explored for a transparent target [77, 78], which is invoked in an acceleration scheme known as break-out afterburner (BOA) [79]. Work by Albright *et al.* [79] suggest that this transfer of energy is due to a relativistic two-stream Buneman instability [80].

Two distinct phases are present in BOA: an initial phase of volumetric heating and a secondary, acceleration phase. Initially, BOA is identical to TNSA, with fast electrons generated via the absorption mechanisms described in section 2.4 and a charge separation field resulting from the transport of these electrons, which acts to accelerate ions from the surfaces of the target. For a sufficiently thin target, the laser propagation through the target drives volumetric heating. The target becomes relativistically transparent, with a strong longitudinal electric field resulting via a plasma wave [81]. The relativistic beam of fast electrons and the comparatively slow plasma ions support the growth of a two-stream Buneman instability [80]. The phase velocity of the Buneman instability is resonant with the plasma ions, which acts as a mediator between the electron and ion

energy.

In the BOA scheme, ion acceleration occurs from the point of relativistic transparency ($t = t_1$) until the point of classical transparency ($t = t_2$), i.e. $n^{'} > 1 > n^{'}/\gamma$. Assuming that the target expands in 1-D along the laser axis during the initial phase, t_1 is first derived by balancing the ponderomotive force of the laser light with the charge separation force. As derived in Ref. [82], this results in t_1 being given by:

$$t_1 = \left(\frac{12}{\pi^2}\right)^{1/4} \left(\frac{n_e \tau_L \ell}{n_c a_0 C_s}\right)^{1/2}, \qquad C_s = \left(\frac{Q m_e c^2 a_0}{m_i}\right)^{1/2}, \tag{2.39}$$

where Q is the charge of the main ion species and m_i in the mass of the target ions. At $t = t_2$, acceleration via BOA ceases. Physically, when t_2 is reached, all of the target electrons have been accelerated by the laser, causing strong expansion. The calculation for t_2 employs a 3-D isospheric expansion of the target, and is given by:

$$t_2 = \frac{n_e \ell (\gamma^{1/3} - 1)}{n_c \gamma C_s \sin(\pi t_1 / 2\tau_L)} + t_1 = \Delta t + t_1. \tag{2.40}$$

The final ion energy depends on the electron energy, ε_e, which is given by the time-averaged electron energy due to the ponderomotive force exerted by the laser,

$$\varepsilon_e \simeq \frac{m_e c^2}{t_1 - t_2} \int_{t_1}^{t_2} (\sqrt{a_0^2(t) + 1} - 1) dt. \tag{2.41}$$

Based on the electron relaxing model by Mako and Tajma [83], the non-relativistic response of the ions to the electrostatic field can be derived from the non-relativistic fluid equations [82]. This results in ε_{max} being given by:

$$\varepsilon_{max} \simeq (1 + 2\alpha) Q \varepsilon_e \Big((1 + \omega_p (t_2 - t_1))^{1/(2\alpha+1)} - 1 \Big), \tag{2.42}$$

where α is the coherence parameter in the relaxing model, which describes how efficiently the ions couple to the electrons. α is estimated to be 3, as extrapolated from PIC simulations [82]. The model by Yan *et al.* is used in Chapter 4, to compare with the experimentally obtained proton measurements. In Chapter 4, Eq. 2.42 is solved numerically in order to find ε_{max} as a function of ℓ.

Experiments performed using picosecond laser systems measure an enhancement in ε_{max} for targets expected to be transparent to the laser pulse for some portion of

the laser pulse [84]. 2-D and 3-D PIC simulations indicate that the enhancement is due to a jet-like fast electron structure, forming on the target rear. This jet is confined to the laser axis, due to the azimuthal magnetic field resulting from this current of electrons, which is guided into the expanding ion layer. Electrons trapped within this jet are directly accelerated by the transmitted portion of the laser pulse, resulting in an enhancement of the proton beam. A detailed discussion regarding this effect is described in Chapter 4 and Ref. [5].

Chapter 3

Methods

The investigations presented in this thesis involve a number of complex and challenging methods. In this chapter, the laser systems used, the diagnostics fielded and the numerical simulations performed are discussed.

3.1 Laser systems

Developments over the past few decades has enabled lasers to provide peak powers exceeding 1 PW [85]. The results detailed in this thesis primarily concern the use of short pulse laser systems ($\tau_L \sim 1$ ps), which utilise the chirped pulse amplification technique (CPA) [4] to achieve intensities of the order 10^{20} Wcm^{-2}. CPA involves stretching an ultra-short laser pulse in time, reducing the intensity of the beam such that is passes through the amplifying medium without damaging it. The pulse is chirped, in frequency, using a pair of anti-parallel gratings, resulting in the low frequency components travelling a shorter distance than the high frequency components. This results in temporal stretching of the pulse, with the high frequency components behind the low frequency components. After amplification, the pulse is re-compressed using a second pair of gratings to its original pulse duration.

In CPA systems, the pulse duration is typically limited by the bandwidth of the amplifying medium. To increase the bandwidth, a technique known as optical parametric amplification (OPA) is incorporated to the CPA system; allowing higher laser intensities to be achieved. In OPA amplification is achieved by transferring energy from a pump laser beam to the main (chirped) pulse, as detailed in Ref. [86]. This composite technique is known as OP-CPA.

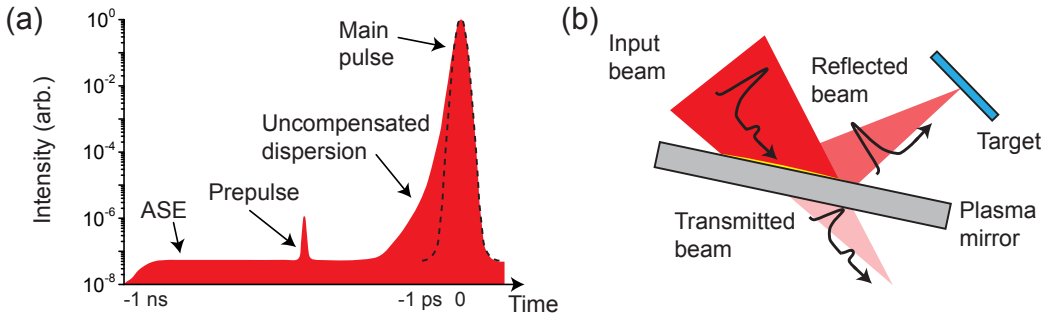

Figure 3.1: (a) Illustration of the temporal profile of a high-intensity laser pulse, propagating from right to left. $t = 0$ corresponds to the arrival of the peak of the pulse and $t = -1$ ns is the time that the Pockels cells will cease gating. The intensity level is typical in a CPA system. (b) Schematic illustrating the principle behind a plasma mirror. A focusing laser pulse is incident on the initially transparent mirror, which acts to transmit the leading edge of the pulse chain. As the intensity of the pulse increases, the plasma mirror surface begins to ionise and become opaque to the light, reflecting the remainder of the pulse.

The now high power, ultra-short pulse is focused onto the target using a parabolic mirror (generally off-axis). An $f/3$ mirror is used for all of the short pulse beam parameters involved in this work, with a spot size of around $\sim$5 µm (FWHM) achieved in all cases. Both the temporal and spatial profile of the focused beam have a Gaussian-like profile, as outlined in Chapter 2.

The amplification process for the short pulse also amplifies the flux of incoherent emission which precedes the peak of the (stimulated) pulse. This, generally unwanted, emission is known as amplified spontaneous emission (ASE), and can be present many nanoseconds prior to the main pulse. The measured intensity contrast (i.e. the ratio between the peak of the pulse and the ASE) of the Vulcan laser is $\sim 10^{7}$ [84]. Often, the intensity of the ASE can be above the threshold for ionisation, and is a particular problem when irradiating ultrathin (tens of nanometer) targets. In the case of such thin targets, the ASE can destroy the target before the peak of the pulse arrives. For thicker (micron) targets, the ASE results in pre-expansion of the target front surface. The ASE can be suppressed up to a nanosecond prior to the main pulse through using a Pockels cell, however still poses problems if a high contrast is required. An additional source of unwanted lasing concerns pre-pulses, which can arise in the laser chain due to internal reflections. These can be limited by implementing wedged optics, such that reflections are not directed down the laser-chain. A schematic illustrating the components of a CPA laser pulse is shown in Fig. 3.1a.

Laser	**TAW**		**TAP**	**Orion**		
Parameters	Beam 1	Beam 2		SP1	SP2	LP
λ_L (µm)	1.053	1.053	1.054	0.527	1.054	1.054
E_L (J)	60	175	210	200	490	50
τ_L (ps)	1	8	1	0.5	0.5	2×10^3
I_L ($\times 10^{20}$ W cm^{-2})	1	0.3	3	6	15	4×10^{-7}

Table 3.1: Parameters of the laser systems used for the investigations presented in this work. SP and LP denote short pulse and long pulse, respectively. Four identical long pulse beams were used (LP1, LP2, LP7 and LP8). The names given to the individual beams are those defined in the chapters detailing the results obtained.

For experiments using ultra-thin targets, the intensity contrast must generally be enhanced. The use of a plasma mirror [87], placed some centimetres away from the focal position, may enhance the contrast by a factor of 10^2, allowing the physics concerning ultra-thin targets to be explored. To a low intensity beam, the plasma mirror appears transparent – with the majority of the light passing through it. By coating the optic with an anti-reflection coating, the maximum enhancement (10^2 for an incident laser intensity of $\sim 10^{15}$ Wcm^{-2}) is achievable. As the rising edge of the main pulse approaches, and the intensity exceeds the ionisation threshold ($\sim 10^{14}$ W cm^{-2}), the optic ionises, forming a thin overdense plasma layer on the surface of the substrate. This reflects the remainder of the pulse. A schematic illustrating the proof-of-principle of a plasma mirror is shown in Fig. 3.1b.

Two laser systems were used in the experimental investigations presented in this work: the Vulcan laser [85], located at the Central Laser Facility (CLF) at the Rutherford Appleton Laboratory (RAL), UK, and the Orion laser system at AWE plc, UK. Table 3.1 summarises the key laser pulse parameters used on the experiments. In the following section, the Vulcan laser is outlined.

Vulcan laser

The Vulcan laser delivers pulses into two target areas: Target Area West (TAW) [89] and Target Area Petawatt (TAP) [85]. A schematic of the laser system is shown in Fig. 3.2. These two areas operate using different laser-drive parameters, as shown in Table 3.1. TAW was used to perform the experiment that is discussed in Chapters 5 and 6, utilising its dual-beam capability to investigate the dynamics of the electrodynamic sheath field and target expansion, respectively. TAP was used for the experiment outlined in Chapter 4, with the high laser intensities achievable on the system enabling the

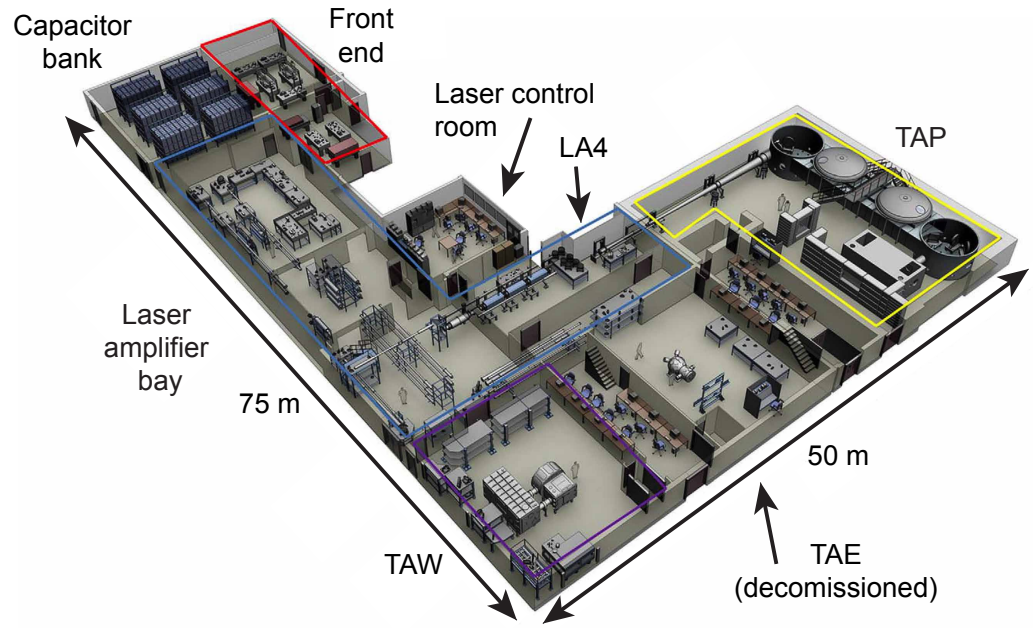

Figure 3.2: Layout of the Vulcan laser system. The key elements are highlighted, including the two target areas where the experiments are set-up and performed. Figure reprinted from [88].

efficient acceleration of protons with energies in excess of 94 MeV to be accelerated [5]. The use of a plasma mirror was key to this result, as the targets used (which produced the highest proton energies) were around 100 nm in thickness. The specific laser requirements are outlined in the individual chapters.

Orion laser

Orion [90] is a relatively new laser system, first beginning operations in 2010. The facility houses a unique capability, comprising two short pulse beams and ten long pulse beams. A schematic of Orion, along with photographs of the facility and target chamber, are shown in Fig. 3.3. Orion was used to perform the experiment discussed in Chapter 7, with its unique capability utilised to address the physics underpinning high-current proton acceleration and focusing using novel conical targets. The specific laser parameters used on the experiment are fully summarised in Chapter 7.

3.2 Ion beam diagnostics

This section details the typical diagnostics used on a laser-plasma experiment; specifically, those used to characterise the ions accelerated during the interaction. Other forms of

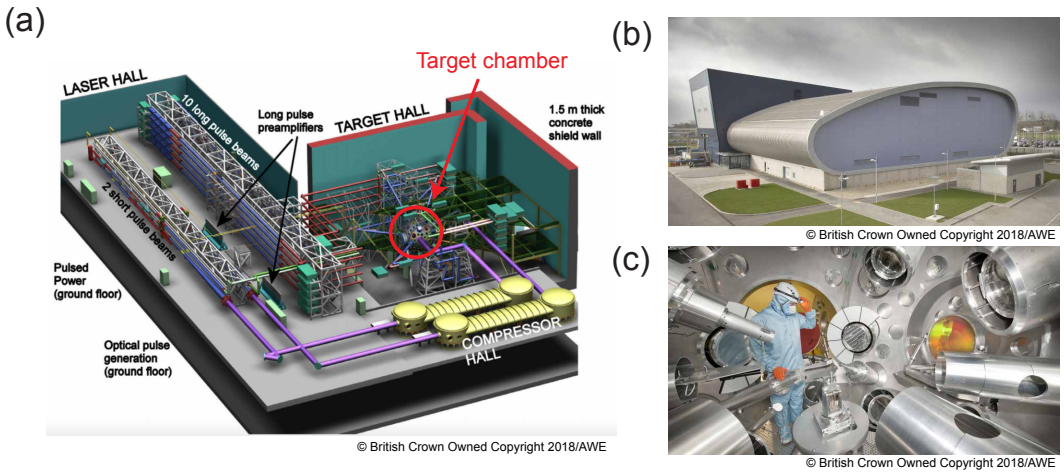

Figure 3.3: (a) Schematic of the Orion laser system, with several key elements labelled. Figure reprinted from [90]. (b - c) Photographs of the building housing the Orion laser and inside the spherical Orion target chamber, respectively. Photographs reprinted from [91].

radiation are also measured, such as X-ray emission in Chapter 7 and the degree of transmitted light in Chapter 4. However, as these diagnostics were only fielded for one particular experiment, it is more relevant to describe them within context in those chapters. Therefore, this section solely details the diagnostics used to characterise a beam of accelerated protons, along with some discussion of other possible techniques. A comprehensive review of the various diagnostics typically fielded on an experiment investigating the physics of laser-solid interactions can be found in Ref. [92].

Radiochromic film (RCF) features in all of the chapters detailing the experimental results, and is one of the most commonly used proton beam diagnostics featured in a laser-driven ion acceleration experiment. It is a self-developing dosimetry film, sensitive to ionising radiation, and provides a simple and robust means of diagnosing the spatial-intensity profile of laser-generated ion beams. Multiple types of RCF exist, each exhibiting a different response to ionising radiation, with the types used in this thesis shown in Fig. 3.4. The main difference between the various types of film is the level of sensitivity, with the type chosen depending on the proton flux expected. HD is the least sensitive type, followed by MD and then EBT ($\sim 10^2$ more sensitive than HD).

3.2.1 Radiochromic film

The active layer of all RCFs consists of a colourless monomer which, when exposed to ionising radiation, reacts to form an optically dense polymer. Further details of the

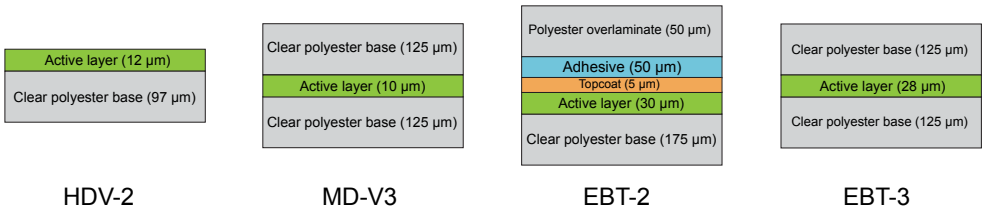

Figure 3.4: Composition of the various type of dosimetry film (RCF) used in the experiments presented in this thesis.

reaction process can be found in Ref. [93] (and references therein). The higher the flux of radiation, the darker the film appears. The optical density (OD) is related to the fraction of transmitted light through the film:

$$OD = \log_{10}\left(\frac{I_0}{I_t}\right), \tag{3.1}$$

where I_0 is the incident light and I_t is the amount of light transmitted through the film. The OD of the film can be absolutely calibrated by exposing the RCF to a known dose of proton flux. This is typically achieved using a monoenergetic ion source. The source used for all of the calibrations in this thesis was the Birmingham University cyclotron. The primary interest towards calibration efforts concerns the relationship between the OD (specifically, the RGB values) and the deposited energy in the film. By knowing this relationship, it's possible to calculate how much energy is contained in the proton beam solely from the RCF measurements. After irradiation, the RCF is digitised (generally using a flatbed scanner), such that the proton data can be computationally analysed. Depending on the flux of protons present, only one colour channel is analysed. The optically dense polymer most readily absorbs red light, resulting in the red channel reaching the maximum OD measurable (i.e. saturation) before the other two channels. The red channel is therefore used for low dose signals, while for higher doses either the green or blue channel is chosen. While complicating the analysis, separating the colour channels extends the overall dynamic range of the diagnostic. This is particularly useful as the particle spectrum can vary strongly over a single beam measurement.

By using multiple pieces of RCF in a stack configuration, interspersed with filter materials (e.g. mylar, Fe and Cu), spectral resolution can be achieved. Cu may also act as a diagnostic in itself, detailed in section 3.2.2. A typical stack configuration is illustrated in Fig. 3.5. The capability of an RCF stack to spectrally resolve the proton

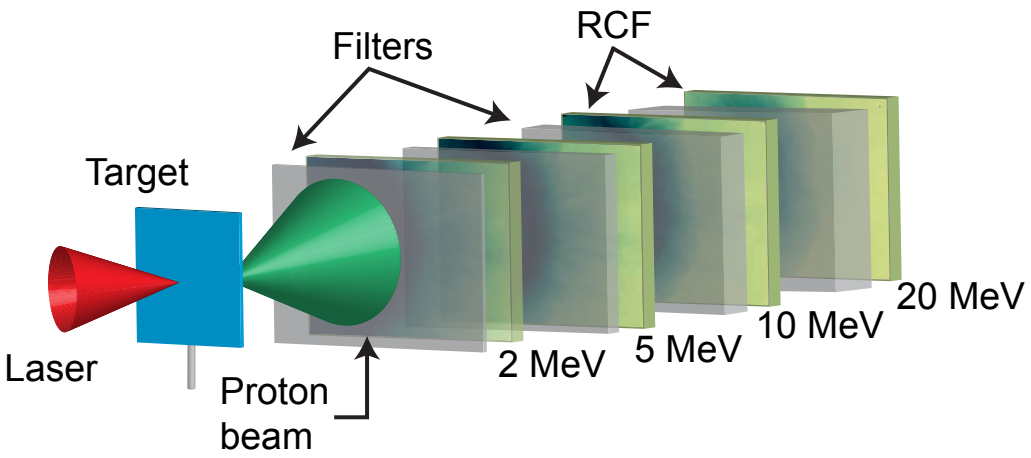

Figure 3.5: Typical dosimetry film (RCF) stack configuration, interspersed with filter material, with typical raw data for several ion energies shown.

beam is a result of the characteristic Bragg peak energy deposition profile of ions, in which ions deposit most of their energy over a small region as they near the end of their propagation distance. This maximum distance of propagation is dependent on the initial ion energy, the charge-to-mass ratio of the ion and the material the particle is traversing. Figure 3.6 displays the stopping power and energy of several energies of protons as a function of distance within the target (Al, in this instance). The results shown in Fig. 3.6 were modelled using the approach outlined in Appendix B for cold stopping. However, similar results may be obtained from the Monte Carlo algorithm SRIM [94].

In comparison to standard particle spectrometers, a 3-D (x, y, ε_p) proton distribution can be obtained by using an RCF stack. Caution should be exerted when diagnosing protons with an RCF stack, however, as the film is also sensitive to X-rays, electrons and heavy ions. From Eq.B.1, Appendix B, materials exhibit an increased stopping power for a higher-mass ion. By introducing a thin Al layer to the front of the stack, the contribution of heavy ions can be effectively removed. Generally speaking, it is quite straightforward to distinguish protons from the other two forms of radiation, by: (i) how quickly the signal decays and; (ii) the spatial distribution of the signal. As described in Chapter 2, a TNSA proton beam has a Maxwellian-like spectral profile. Therefore, the signal on the RCF should fall quite suddenly as the end of the spectrum is approached. For the other forms of radiation, this drop in signal through the RCF layers is more gradual. Figure 3.7 displays a typical TNSA proton beam, together with an X-ray/electron background signal. In terms of both the spatial structure and

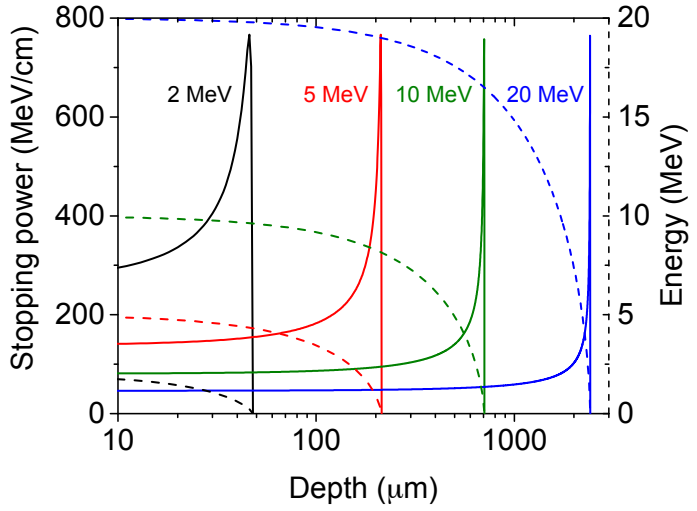

Figure 3.6: (Solid axis) proton energy deposition curves in aluminium as a function of target thickness, for protons with several different initial energies. (Dashed axis) proton energy as a function of propagation distance.

change in spectral profile, protons can clearly be distinguished from other forms of radiation. Nevertheless, to increase confidence that a signal corresponding to proton energy deposition has been recorded, nuclear activation measurements may be used in conjunction with RCF to confirm the presence of protons on a particular RCF layer. These types of measurements are detailed in section 3.2.2.

A laser-generated proton beam, due to its broadband nature and short temporal duration, is an excellent candidate for the purposes of probing transient electromagnetic fields. This is known as deflectometry, and is detailed in the following section.

Proton probing technique

The use of ion beams for the purposes of radiography was first proposed in the 1960s [95], where Koehler used a scattered proton beam, initially accelerated from a cyclotron, to radiograph an aluminium sample. Later, in 1975, Mendel and Olsen [96] used He^+ ions to measure the electric fields of a laser-irradiated target via the detection of the deflected ions. The cost involved with coupling external particle accelerators, in addition to the relatively long bunch-duration of the ion pulses, limits the applicability of conventional accelerators as such a diagnostic.

All-optical approaches [97], such as polarimetry, are difficult to set up. Additionally, the difficulty involved with temporally resolving events over picosecond time-scales

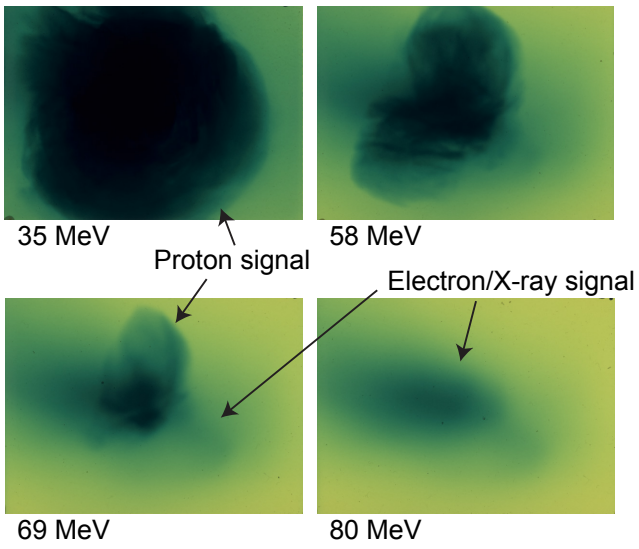

Figure 3.7: Raw dosimetry film (RCF) measurement of a typical proton beam. The target used was plastic (CH) with a thickness $\ell = 90$ nm. The signal due to protons and other forms of radiation are indicated. The indicated energy is the spectral slice of the proton beam diagnosed by the piece of film shown.

through optical means limits the number of time-frames to ~ 4 (i.e. s- and p-polarised, 1ω and 2ω). Incidentally, a laser-accelerated proton beam is by far the most suitable diagnostic to fulfil these criteria. Unlike those accelerated from a conventional accelerator, a broadband energy spectrum is a key feature of a TNSA beam [15]. Additionally, the bunch length is orders of magnitude shorter, provided the diagnosed target is relatively close. When detected using an RCF stack, multiple temporal frames are produced due to the difference in time-of-flight (t_f) travelling between protons of different energies:

$$t_f = \sqrt{\frac{m_p d_1^2}{2\varepsilon_p}}, \tag{3.2}$$

where m_p is the proton mass, d_1 is the distance between the proton source and target and ε_p is the proton energy. A schematic demonstrating a typical proton probing set-up is shown in Fig. 5.1a, Chapter 5. The spatial resolution is set by the virtual source size of the proton beam (i.e. the apparent size of the proton source) and the width of the point spread function of the detector (i.e. lateral spread due to scattering inside the detector), which typically leads to a resolution of the order of several micrometers [98, 99] at the interaction plane. The temporal resolution depends on the geometrical distances involved, as well as the beam energy spectrum. A typical resolution from sub-picosecond to tens of picoseconds is routinely achieved. A review of the various uses

of this diagnostic technique can be found in Chapter 5.

Protons probing electromagnetic fields are subject to deflections, with the force ($\mathbf{F}$) experienced by these particles calculated from the Lorentz force equation (Eq. 2.10, Chapter 2). The deflections recorded on the diagnostic plane are therefore a measure of the fields experienced by the probe protons at the interaction region. If the position at which the protons originally encounter the field is known, the average electric field experienced by the protons can be calculated from [58]:

$$E_{x,ave} \simeq \frac{2\varepsilon_p dx}{ed_2 b}, \tag{3.3}$$

where dx is the distance on the diagnostic plane that the protons have been deflected, d_2 is the distance from the interaction plane to the detector, e is the electronic charge and b is the length of the path travelled by the protons through the field. A mesh imaging technique can be used to estimate where the protons originated from, as detailed in Ref. [100]. Alternatively, in the case of Chapter 5, some of the deflections are due to the rear-surface sheath field, therefore the deflected protons originally encounter the deflecting field near the target rear.

Deflectometry is imperative to the results presented in Chapter 5, and important in Chapter 7 in order to confirm the presence of electromagnetic fields surrounding the conical target used and diagnose their field structure. The calculations outlined here are used to estimate the fields experienced by the protons in both cases, and prove to be in good agreement with the simulations performed.

3.2.2 Other ion beam diagnostics

Another commonly used ion beam diagnostic is the Thomson parabola ion spectrometer (TPS), which can be used to detect and discriminate between ion species of different charge-to-mass ratios and measure their energy spectra. The working principle behind a TPS is based on a magnetic and electric field orientated perpendicular to the ion beam propagation direction [101]. Within the TPS ions are deflected, via the Lorentz force, parallel to the electric field and perpendicular to the magnetic field. This results in a series of parabolic tracks on the detector, with each parabola produced by an ion with a different charge-to-mass ratio. The ion density along the parabola represents the beam spectral profile. A schematic illustrating the working principle of a TPS is shown in

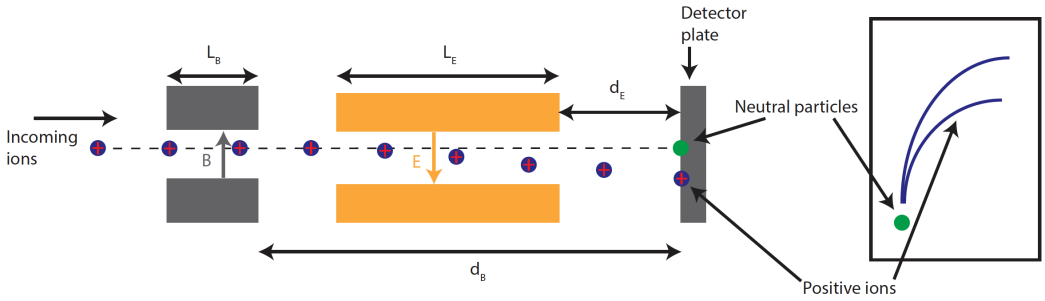

Figure 3.8: Working principle of a Thomson parabola spectrometer, showing a top-down view of the diagnostic. Figure reprinted from [103].

Fig. 3.8. Further information on this diagnostic can be found in Ref. [102].

One of the detectors typically used in a TPS is image plate (IP) [104]. IP is a reusable film that is sensitive to ionising radiation, and is widely used both in the laboratory and for medical purposes. When radiation is absorbed in the active layer (Eu) of the detector, electrons are excited to a metastable state (Eu^{2+}). By illuminating the IP with a laser, the trapped electron is released; emitting a photon ($\lambda \sim 400$ nm) by photo-stimulated luminescence. By imaging the IP as it is irradiated by the laser, information regarding the spatial and intensity profile of the radiation can be obtained. IP is commonly used alongside RCF for beam measurements. Microchannel plate detectors (MCPs) may also be used, however due to the electromagnetic pulse (EMP) produced during the interaction failure of these devices is common.

Nuclear activation measurements are another commonly used technique to characterise the laser-driven ion source, and was used in conjunction with RCF in Chapter 4 to confirm the high proton energies measured. Cu is a commonly used material for these measurements, undergoing the reaction: ^{63}Cu(p,n)^{63}Zn. This positron-emitting ^{63}Zn radioisotope has a half-life of 38.5 minutes. When the positron is emitted, it annihilates with an electron in the activated material, resulting in the production of two counter-propagating 511 keV photons (i.e. the electron and positron rest mass energy). These can be detected using a pair of NaI detectors angled at 180° with respect to each other, with one count obtained when both detect a 511 keV photon in coincidence [105]. A schematic of the set-up used on the experiment is shown in Fig. 4.2, Chapter 4. Unlike RCF, which is sensitive to all radiation, the ^{63}Zn half-life is characteristic of proton-induced activation when produced by a ^{63}Cu(p,n)^{63}Zn reaction. Therefore, a measure of a decay with this half-life in a Cu sample means the material was activated

by proton irradiation. By interleaving Cu filters with the dosimetry film in a stack configuration, the radiation species encountering each filter can be confirmed as protons.

Solid state nuclear track detectors (e.g. CR-39) [106] are also commonly implemented, which have the advantage of identifying every particle that is incident on the detector. Extracting the data, however, requires etching the CR-39. This is time-consuming, taking up to 90 minutes to extract the data per piece of CR-39.

3.3 Numerical modelling

Experimental measurements provide important insight into laser-plasma physics. However, there are a number of parameters that cannot be easily measured in an experimental campaign, and many of the most important measurements are time-integrated (i.e. RCF). Numerical simulations in conjunction with experimental data and analytical methods are used to provide a fuller picture.

There are two commonly used simulation techniques in the context of laser-plasma physics: kinetic and hydrodynamic. Hybrid methods also exist, utilising aspects of both approaches, where bulk quantities such as the cold target are considered fluid, while the accelerated ions and electrons are considered as kinetic macroparticles. The specific numerical tools used to develop an understanding of the physics addressed in this thesis are detailed in this section. A comprehensive review of the plethora of numerical tools available in laser-plasma physics can be found in Refs [33, 107].

Particle-in-cell simulations

Particle-in-cell (PIC) simulations [108] kinetically describe a plasma, with the plasma defined as a collection of macro-particles that occupy some volume in phase space. These particles can interact with an external radiation source, such as a laser beam; offering key insights into the interaction dynamics. While approximating a cloud of particles as a macroparticle may lead to unphysical behaviour, at present it is infeasible to fully simulate the process using the Vlasov equation to model the plasma. Therefore, PIC simulations provide the most accurate depiction of the key physical processes present in laser-plasma physics.

Fig. 3.9 displays the central PIC algorithm. For the end user, the parameters simulated are defined by the user in a file known as an input deck. Initial conditions

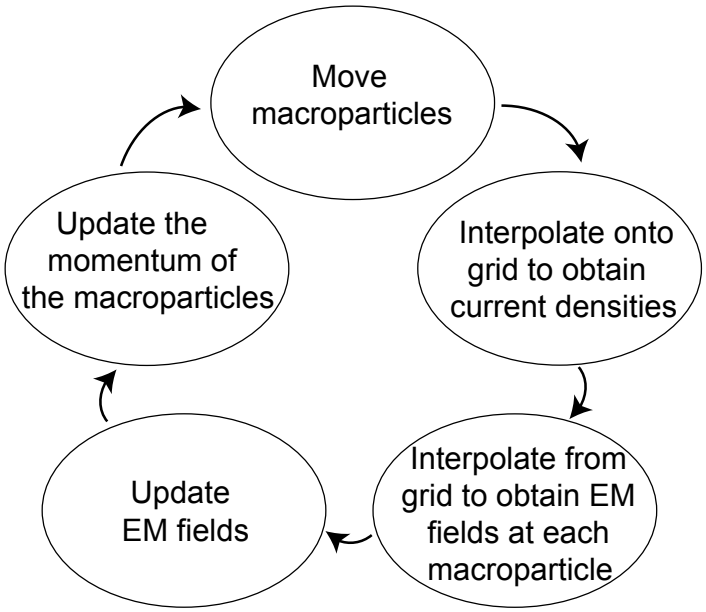

Figure 3.9: Flowchart illustrating the central PIC algorithm.

such as the laser parameters, target properties and resolution are defined here. For the simulations presented in this thesis, these conditions are typically based on the parameters of the experiment. Additionally, how certain physical processes are interpreted in the code may be indicated here, such as defining which particles should behave collisionally.

The PIC code used to investigate the physics addressed in this thesis is EPOCH [109]. The code is fully relativistic, and can operate in one to three dimensions. It is an open source code, allowing users to make modifications to the source code. Throughout this thesis any results produced by the code utilise the 2-D version.

Hydrodynamic simulations

In contrast to the kinetic approach, where the particles are treated as a collection of macroparticles, the hydrodynamic approach treats the plasma as a fluid. This eliminates the notion of microscopic behaviour of the constituent particles, and considers only the mass. This results in the fluid being described by the variables of density, velocity and pressure. An appropriate equation of state (EOS) is calculated for the material, which is generally based on experimental measurements in conjunction with analytical modelling.

The hydrodynamic code used to develop an understanding of some of the physical pro-

cesses investigated in this thesis is the 1-D Lagrangian radiation-magnetohydrodynamics code HELIOS-CR [110]. In this code, solid targets can be defined that comprise of layers of multiple species. For the parameters studied, the material EOS properties are based on PROPACEOS tables (details of which can be found in Appendix A, Ref. [110]). The evolution of the materials properties are described by the EOS and opacity databases.

For the results detailed in Chapter 6, a proton beam was used in HELIOS to heat various target materials. Proton energy deposition is modelled using a Monte-Carlo algorithm for determining the ion trajectories in the target, enabling the temperature and density profiles of the proton-heated targets to be simulated. In Chapter 7, a laser source irradiates a target material. The laser energy deposition is calculated using an inverse Bremsstrahlung model, which acts as a heating source. This allows the shock-transit and plasma profile to be characterised; key to determining the long pulse laser parameters that should be used on the experiment.

Chapter 4

Ion acceleration via a laser-driven transparency-enhanced hybrid acceleration scheme

This chapter reports on an experimental and numerical investigation of proton acceleration from ultrathin foils irradiated by relatively long (picosecond) linearly-polarised laser pulses. The experiment was performed in 2016, using the Vulcan laser system, in Target Area Petawatt (TAP). Ref. [5] directly results from the work presented in this chapter. Efficient acceleration to energies exceeding 94 MeV is demonstrated, and PIC simulations suggest that this is driven by a dual-peaked electrostatic field, producing a hybrid acceleration scenario, and that for optimum target thicknesses it is enhanced by the onset of relativistic-induced transparency (RIT). The experimental results, analytical modelling and 2-D PIC simulations are presented. An additional discussion related to the implications of this work on future, higher intensity laser systems is also presented.

4.1 Introduction

The potential of laser-plasma based accelerators to produce compact sources of energetic ions with unique beam properties, including short temporal durations, motivates intense international research activity in high power laser-driven ion acceleration [20, 52]. Such a radiation source has been applied for radiographic density diagnosis with micron-scale resolution [111], for probing highly transient electric and magnetic fields in plasmas with picosecond resolution [100], for the isochoric heating of matter [17] and

for probing radiation-induced processes in matter [112]. Several of these applications are demonstrated in the following chapters. Other applications, such as in biomedicine (e.g. hadron therapy [113]) and fusion energy (e.g. fast ignition of fusion targets [16]), have also been proposed. Some of the applications require higher ion energies than presently achieved, and many require high laser-to-ion energy conversion efficiency, as well as spectral and spatial control.

Efforts have been made to increase the maximum ion energy, largely focusing on the development of novel acceleration mechanisms involving ultrathin (tens-to-hundreds of nanometres) foil targets. To date, the most widely investigated ion acceleration mechanism is TNSA [56] scheme. TNSA proton energies in excess of 85 MeV from ultrathin foils have recently been reported [64]. A different approach, based on using the radiation pressure of the laser light has also been explored, which has been shown to result in peaked ion energy spectra [73]. RPA benefits from the use of circularly polarised light due to the absence of the oscillating $\mathbf{j}\times\mathbf{B}$ heating [114] and this has recently been demonstrated experimentally [75]. The polarisation dependence of RPA has also been used to attribute this mechanism to measurements of high energy protons with a broad energy spectrum [115]. By contrast, the use of linearly polarised light is predicted to result in the formation of a dual-peaked electrostatic field, due to RPA at the target front and TNSA at the rear [28], and hybrid scenarios in which ions from both mechanisms combine [116]. These acceleration mechanisms are discussed in more detail in Chapter 2.6.

While ion acceleration is particularly effective in ultrathin foils, such targets undergo RIT [37] (detailed in Chapter 2) resulting in some of the laser pulse being transmitted through the target. This results in several phenomena that can strongly affect ion acceleration. In the case of short, high contrast pulses, RIT produces a relativistic plasma aperture in the foil, resulting in diffraction of the transmitted laser light [117]. This diffraction modulates the electrostatic acceleration field and thus the spatial distribution of the resulting proton beam [118]. Volumetric heating by the transmitted laser light has been shown to enhance the energy of TNSA-ions [81]. Energy exchange via streaming plasma instabilities has also been numerically explored under these conditions [79, 119] and is invoked in the BOA scheme [77]. In the same ultrathin-foil-RIT regime, driven by relatively long (hundreds of femtoseconds) and linearly polarised laser pulses, Powell *et al.* [84] reports that a relativistic plasma jet is produced, which locally enhances the

maximum proton energy. Similar jet structures are reported in Palaniyappan *et al.* [39] to explain measured energy enhancements and narrow energy spread features in Al and C ions.

Given the importance of ultrathin foils as ion acceleration targets, it is important that our understanding of the coupling between acceleration mechanisms and the collective particle and field dynamics driven by transparency in this complex interaction regime is improved upon. No one ion acceleration model can explain the physics in this regime, as shown by the analytical modelling presented in section 4.4. It is also particularly important for future investigations of ion acceleration using next-generation, multi-petawatt laser facilities presently under development, such as the Extreme Light Infrastructure [26, 27], Apollon [120] and XCELS [29]. Difficulties in converting the inherent linearly polarised light to circular polarisation (due to the large diameter of the unfocused beam) means that linearly-polarised-driven hybrid acceleration scenarios are highly likely to prevail. In addition, these facilities are expected to produce focussed intensities up to 10^{23} Wcm^{-2}, which would render near-solid density foils relativistically transparent, increasing the role of RIT-enhanced processes.

4.2 Experiment set-up

As mentioned previously, the experiment was performed using the Vulcan laser in TAP at the Rutherford Appleton Laboratory, UK. The pulses were p-polarised, with a wavelength $\lambda_L = 1.053\,\mu$m. An $f/3$ off-axis parabolic mirror was used to focus the beam down to a spot size $\phi_L = 5\,\mu$m, with a plasma mirror incorporated for contrast enhancement. Details of how a plasma mirror operates can be found in Chapter 3. Figure 4.1a displays a schematic of the set-up. The measured intensity contrast, and enhancement due to the use of a plasma mirror is shown in Fig. 4.1b. The pulse duration was $\tau_{\mathrm{L}} = (0.9 \pm 0.1)$ ps (FWHM) and the energy after the plasma mirror was (210 ± 40) J, with an average of 30% contained within the focal spot. The peak intensity was $I_{\mathrm{L}} = (3 \pm 2) \times 10^{20}$ Wcm^{-2}. The uncertainty in the intensity measurement is mainly due to the position of the focal spot relative to the alignment focus position (known as the 'defocus'), however fluctuations in the laser energy and focal spot size at best focus were also a factor. Previous experiments did not quantify this defocus, however on this experimental campaign the on-shot aberrations were measured. The most prominent

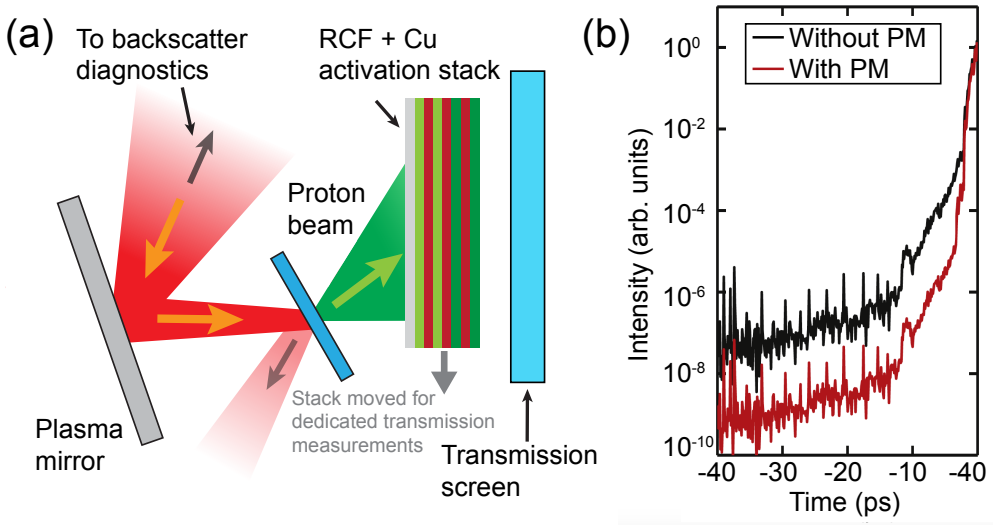

Figure 4.1: (a) Schematic of the experiment set-up. A pulse from the Vulcan laser is focused by an $f/3$ off-axis parabola and reflected from a planar plasma mirror onto a target foil. The spatial-intensity profile of the beam of accelerated protons is measured using stacked dosimetry film (RCF), interwoven with Cu foils for nuclear activation measurements. The transmitted laser energy is characterised on a transmission screen (with the stack retracted). The backscattered light it measured with a spectrometer, to determine the velocity of the critical surface. (b) Measured intensity contrast with and without a plasma mirror (PM) on the same laser system. (b) reprinted from [84].

aberration was a small amount of defocus in the beam, at a position in the laser chain where the beam should be collimated. The defocus fluctuated, with the beam either converging or diverging. By quantifying the defocus, measures were made in an attempt to limit its effect. This is detailed thoroughly in Appendix A.

The targets were thin planar plastic foils, with a quoted manufacture thickness ℓ, in the range 10 nm-1.5 µm. The hydrocarbon contaminant layer is around several nanometers in thickness, which may make the thinnest targets comparatively thicker. Al targets of comparative thicknesses to the plastic targets were also used. The targets were irradiated at 30° with respect to the target normal axis (TN), to enable the proton beam components directed along the laser and TN axes to be distinguishable on the detector, as discussed in Ref. [84]. The proton beam spatial-intensity distribution was measured using stacked dosimetry (RCF) film, which was positioned 5 cm downstream from the target. The dosimetry film was interleaved with Cu filters for activation measurements, with the number of events measured using a pair of NaI detectors operating in coincidence, using the set-up shown in Fig. 4.2a. Both of these proton beam diagnostics are detailed in Chapter 3. In our diagnostic set-up, a large fraction of the

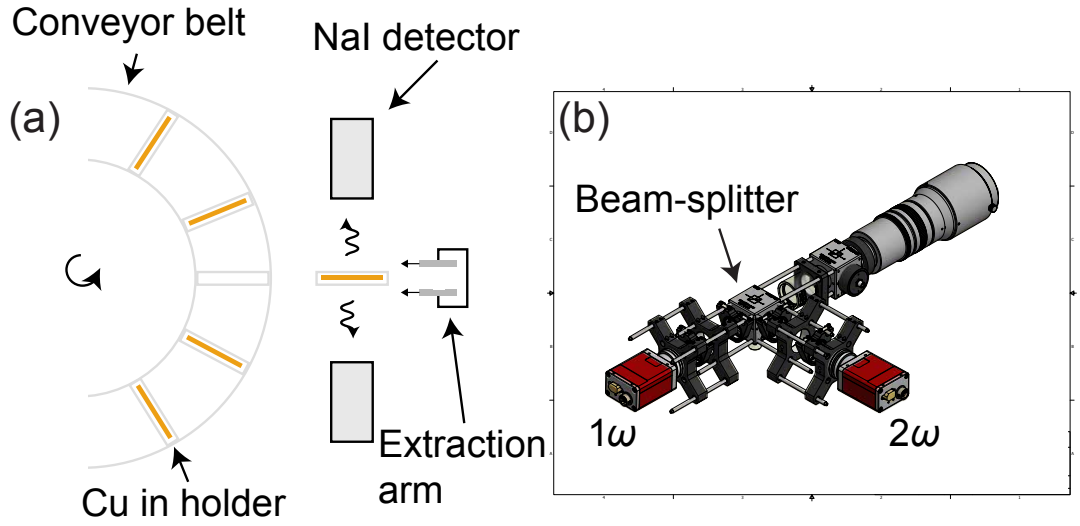

Figure 4.2: (a) Schematic illustrating the set-up used to measure the coincidence counts of the activated Cu samples interleaving the dosimetry film in the proton diagnostic packs. (b) Multi-wavelength imager for imaging the 1ω and 2ω light on the transmission screen.

counter-propagating 511 keV photons are intercepted by a pair of NaI detectors angled at 180° with respect to each other, with one count obtained when both detect a 511 keV photon in coincidence [105]. A fully-automated conveyor-based system was implemented on the experiment. The samples were loaded into holders on the conveyor belt, with the extraction arm selecting one piece at a time and placing it between the detectors for 3 mins. With the counts recorded, the arm replaced the Cu sample, the conveyor belt rotated to the second sample and the process repeated. Each piece was analysed ~ 10 times. Due to the low signal on the final Cu layers in the stack configuration, it is imperitive the samples are loaded within one half-life of the laser-shot (~ 40 min). Additionally, no more than five samples should be loaded to confirm proton signal on the later layers. This is both to provide a reasonable number of scans such that a half-life fit can be made to each sample, in addition to a reasonable amount of time allowed for each scan.

Several other diagnostics were fielded on the experiment, as indicated in Fig. 4.1. The degree of transmitted light was measured by imaging the light on a uniformly scattering material (Spectralon screen), place 70 cm downstream from the target. Both the 1ω and 2ω light was imaged, with a model of the imaging system shown in Fig. 4.2b. The RCF stack was removed for these measurements. The screen was absolutely calibrated by performing a dedicated control shot with no target in place. On the control shot

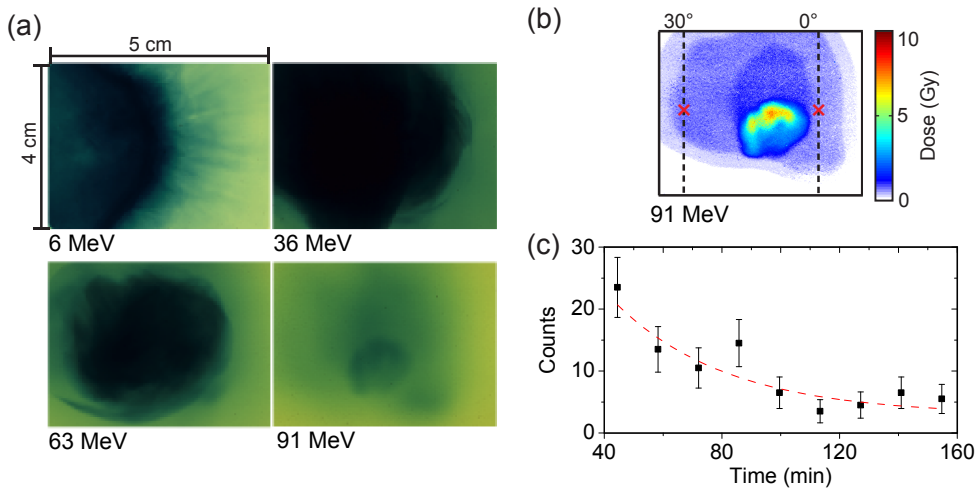

Figure 4.3: (a) Raw dosimetry film (RCF) measurements for an $\ell = 75$ nm CH target, at several energies. (b) The 91 MeV layer shown in (a) converted into dose. The red markers correspond to the laser axis (0°) and target normal axis (30°). (c) Example measurements of the positron-emission decay of the ^{63}Zn radioisotope for protons with ε_p >92 MeV. The time is measured from the time of the laser-plasma interaction and the error bars are determined from the statistical uncertainties in the measured counts. The dashed curve is a fit corresponding to the 38.5 minute half-life of ^{63}Zn, confirming proton induced activation in the high energy region of the filter stack.

the laser energy was lower than on a full-power shot, due to the fluence-limit of the coated scatter-screen. The velocity of the critical density (n_{crit}) surface was calculated by measuring the Doppler shift of the backscattered 2ω light (which is generated at the critical surface) produced near the peak of the laser intensity. This wavelength shift was measured using an Avantes optical spectrometer.

4.3 Experimental results

Figure 4.3 displays example proton measurements for an $\ell = 75$ nm CH target. Multiple spectral slices of the raw RCF data are shown in Fig. 4.3a, with two types of film shown: HDV-2 (first slice) and EBT-2. The latter film type is approximately 100 times more sensitive than the former, with both described in detail in Chapter 3. Figure 4.3c displays a background-corrected dose-map of the 91 MeV layer (red colour channel) shown in Fig. 4.3a. The high proton energies measured with the RCF were confirmed using the activation measurements outlined in the previous section, with an example measurement corresponding to ε_p >92 MeV shown in Fig. 4.3b. The highest proton energy detected on the experimental campaign was between 94 and 101 MeV - strong

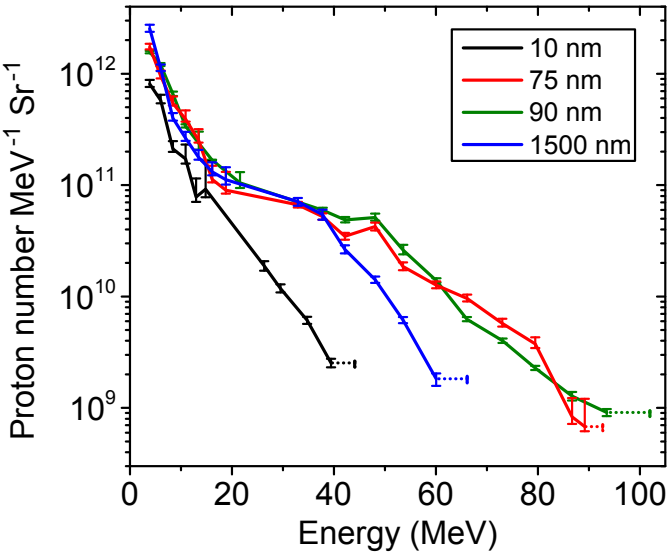

Figure 4.4: Example proton energy spectra, as deconvolved from the RCF measurements, for given foil thickness, ℓ. The error bars are explained in the main text.

signal was measured on the 94 MeV RCF layer, but not on the next, 101 MeV, layer. This was achieved for a plastic target foil, with thickness, ℓ, equal to 90 nm.

Representative spectra (sampled over the whole proton beam) for four target thicknesses is shown in Fig. 4.4. The data is deconvolved from the RCF measurements, with the vertical error bars defined by the level of uncertainty in the calibration of the RCF. The horizontal error bars at the maximum proton energy, ε_{max}, are defined by the energy corresponding to the final RCF layer for which proton signal is measured (lower limit) and the energy of the next RCF layer (upper limit). The red (75 nm) series contains data derived from the RCF film shown in Fig. 4.3.

An example of the proton beam direction (beam centre) as a function of energy is shown in Fig. 4.5. Figure 4.5a displays a matrix of dose-maps of the high energy spectral components for an $\ell = 75$ nm CH target (same as shown in in Fig. 4.3). For increasing proton energies the beam centre is enhanced at a position closer to the laser axis (LA, 0°). Different colour channels were analysed depending on the dose deposited on the individual RCF slice. Figure 4.5b quantifies this change in the beam centre, showing the position of the beam centre as a function of energy for the $\ell = 75$ nm target alongside an $\ell = 1.5$ µm target. The high energy component is increasingly enhanced at a position approaching the laser axis in the case of targets undergoing RIT, while in the thicker target case the beam is centred on the TN axis for the full spectral profile (typical of TNSA). The error bars in Fig. 4.5b are defined by the uncertainty in determining the

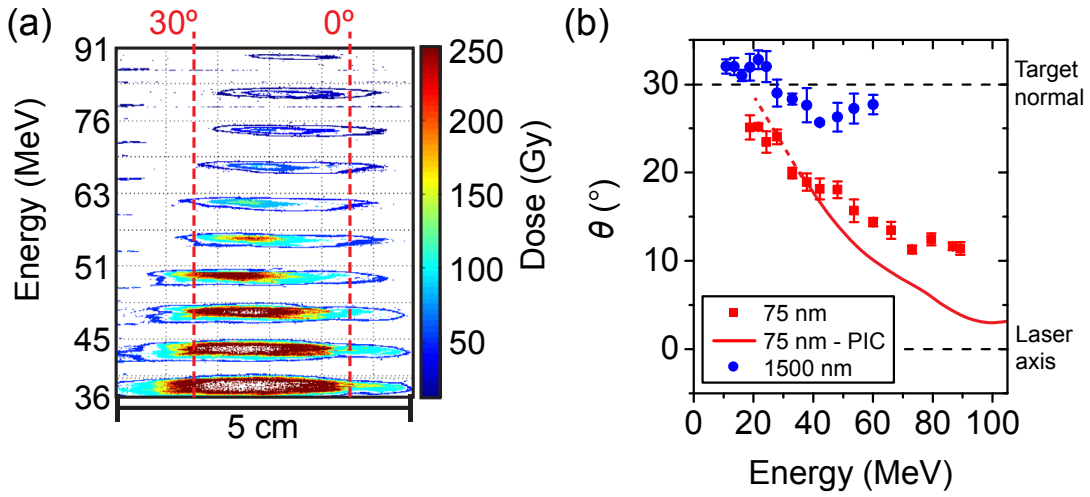

Figure 4.5: (a) Contour plot of the dose-maps from the high energy spectral components of a proton beam from an $\ell = 75$ nm CH target. The laser axis (LA, 0°) and target normal axis (TN, 30°) are indicated. (b) Measured angle of the centre of the proton beam, θ, with respect to the LA as a function of energy, for $\ell = 75$ nm (red) and 1.5 µm (blue). The error bars are explained in the main text. An example PIC simulation result for $\ell = 75$ nm (red curve) is included for comparison. The dashed lines mark the TN and LA.

angle of the centre of the proton beam from application of a beam fitting routine. An example 2-D PIC simulation result for an $\ell = 75$ nm is shown, with good agreement found with the experimental result for the same thickness.

The measured maximum proton energy, $\varepsilon_{\max}$, and laser-to-proton energy conversion efficiency, η, are plotted as a function of ℓ in Figs. 4.6a and 4.6b, respectively, alongside results from 2D PIC simulations (discussed in section 4.5). In the range $\ell >$170 nm, the results agree with the measurements reported in Wagner *et al.* [64], with similar plastic targets and 0.5-0.8 ps-duration, (0.7-2.6)$\times 10^{20}$ Wcm^{-2} laser pulses. In the results presented here, $\varepsilon_{\max}$ and η are maximised at an optimum thickness range, $\ell_{\text{opt}} \sim$70-100 nm. It is in this range that the target undergoes RIT near the peak of the laser intensity. The error bars in the maximum energy (Figs. 4.6a) are defined by the energy corresponding to the last RCF layer for which protons signal is measured (lower limit) and the energy of the next RCF layer (upper limit). The error bars in the conversion efficiency (Figs. 4.6b) are determined from the uncertainties in the measured proton energy spectra.

Figure 4.7a shows the measured degree of laser light transmission (1ω) as a function of target areal density, ρ_{a} (to facilitate comparison of Al and plastic foils), which

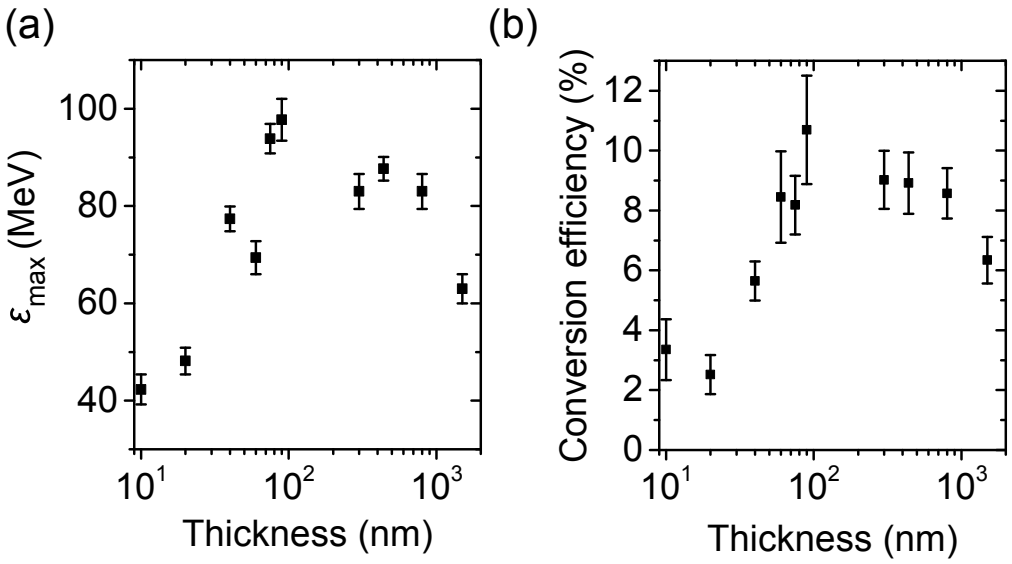

Figure 4.6: (a) Maximum proton energy ($\varepsilon_{\max}$) and; (b) laser-to-proton energy conversion efficiency (η), as a function of foil thickness (red). Both parameters are maximised at an optimum target thickness range of 70-100 nm. The error bars are explained in the main text.

increases with decreasing ℓ. Results from 2-D PIC simulations are also shown for Al, with good agreement found with the experimental results. The error bars are determined from the uncertainties in the calibration of the light level on the transmission screen and the area of the transmitted beam sampled. From Figs 4.6 and 4.7a, for $\ell < 100$ nm, the magnitude of both $\varepsilon_{\max}$ and η decrease with increasing transmission. As shown in Fig. 4.7b, the recession velocity of the plasma critical density, driven by radiation pressure, decreases with increasing transmission. This is expected. The results suggest that the measured enhancement in proton acceleration is expected with some degree of transparency occurring, however significant transmission of the laser energy (due to the onset of RIT too early in the interaction) negatively impacts proton acceleration. In Fig. 4.7b, the lower and upper limits of the error bars are determined from the maximum red-shifted wavelength where the signal is resolvable above the noise-level and by application of a fitting routine, respectively.

In the following section, established ion acceleration models are are applied in order to attempt to explain the experimental data.

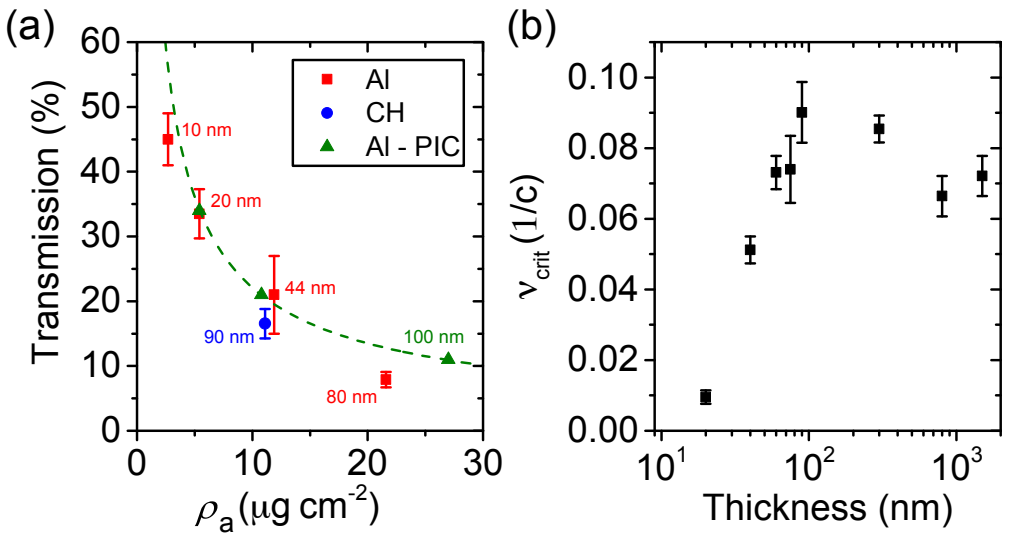

Figure 4.7: (a) Percentage of laser light transmitted as a function of target areal density (ρ_a) for stated thicknesses (ℓ), for plastic (blue; CH) and Al (red) foils. Results from the 2D PIC simulations with Al foils (green; Al-PIC) are included. (b) Recession velocity of the critical density surface (v_{crit}) as a function of ℓ for plastic targets, as determined from measurements of the spectral shift in second harmonic light produced at the critical density surface. The error bars are explained in the main text.

4.4 Analytical modelling

Figure 4.8 illustrates calculations performed using established models, applied using the parameters of this study and plotted alongside the measured ε_{max} as a function of ℓ. The experimental data is shown for comparison. The plasma expansion model introduced by Mora [61] is used for TNSA, with corrections for the multi-dimensional expansion and fast electron spreading within the foil (assuming 30° half-angle of divergence), as applied in Ref. [63]. Although HB models (e.g. [114]) can be applied, we note that v_{HB} is strongly dependent on the extent of target decompression and therefore we use the values determined experimentally to calculate the HB proton energy. The BOA model introduced by Yan *et al.* [82] is applied over the temporal range between the target becoming relativistically and classically transparent, as described in that reference. Although the LS mode of RPA is expected to occur in ultrathin foils, it is not observed in the simulations (as seen in the following section) due to the degree of target decompression induced by the linear polarisation. For completeness, the LS model by Macchi *et al.* [121] is applied (adapted by Andreev *et al.* [72]), for three example acceleration times, to illustrate the strong dependency of ε_{max} on this parameter. For our laser and target parameters, if LS acceleration were to occur it would be over a small

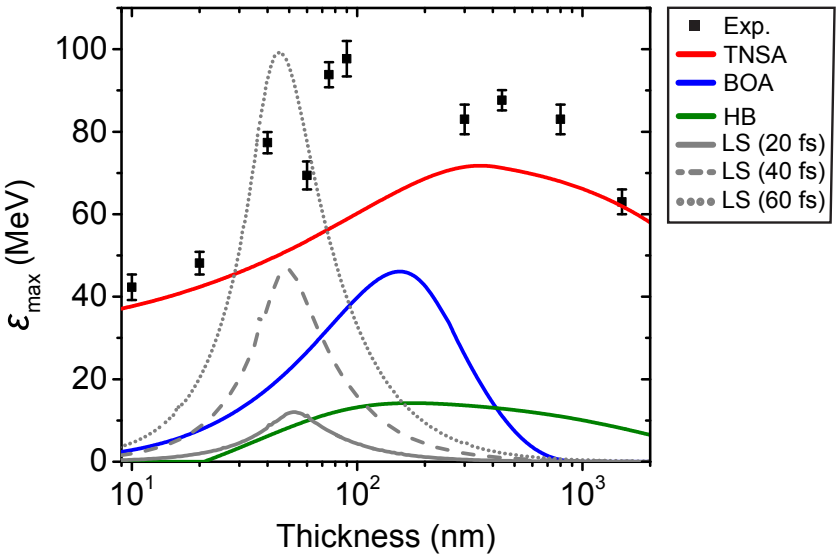

Figure 4.8: (a) Calculated maximum proton energy (ε_{max}) as a function of target thickness, ℓ, using several established models for the stated acceleration mechanisms, applied as described in the main text. The experimental data are included for comparison.

portion of the laser pulse. It peaks for ℓ = 40-50 nm. The TNSA, HB and LS models are all applied up until target transparency occurs. For TNSA and HB, this time is calculated from the BOA model (where the target becomes relativistically transparent). The LS model used incorporates target transparency, and is ran for the times stated in the figure key. All of the models are explained in detail in Chapter 2.6.

Clearly, none of the models describe the full behaviour observed experimentally. TNSA accounts for ε_{max} at the thinnest and thickest values of ℓ, but not for the thicknesses in between. In the following section, simulations indicate an intra-pulse transition occurs between some of the mechanisms discussed here. From the simulations, TNSA occurs early on in the interaction, followed by a brief phase of HB-RPA. For targets at an optimum thickness for ion acceleration, the maximum proton energies driven by this dual-peaked structure are enhanced by the onset of RIT.

4.5 Simulations

The simulations were performed using the fully relativistic, 2-D EPOCH PIC code [109]. The targets were initialised as a uniform mixture of C^{6+} and H^+ ions, both at $60n_{\text{crit}}$, neutralized by an appropriate density of electrons with initial temperature equal to 10 keV. The initial target thickness was varied over the range 20 nm to 1 µm. The boundaries of the simulation box were all defined as free-space. For the main set of

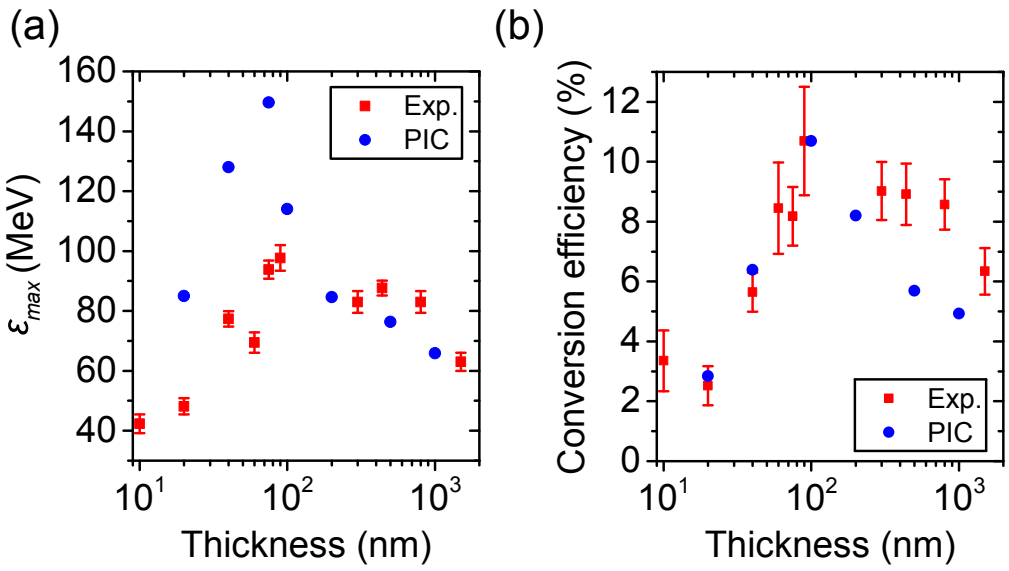

Figure 4.9: (a) Maximum proton energy ($\varepsilon_{\max}$) and; (b) laser-to-proton energy conversion efficiency (η), as a function of foil thickness (red), together with results from 2D PIC simulations (blue). η from the simulations are scaled by a fixed value, such that the maximum value is normalised to the measured maximum efficiency. The maximum energies from the simulations are unscaled. Both proton beam parameters are maximised at an optimum target thickness range of 70-100 nm. The error bars are explained in the main text.

simulations, reported in Figs 4.9–4.13, the simulation box was 160 µm × 70 µm with mesh cell size equal to 5 nm × 12 nm. The incoming laser pulse temporal and spatial profiles were both Gaussian, with FWHM equal to 0.4 ps and 5 µm, respectively, and the peak intensity was equal to 2×10^{20} Wcm^{-2}. The shorter pulse duration, compared with the experiment, is necessary due to the computational power required for long pulses and is justified because the ion energies tend to be exaggerated in 2-D simulations, particularly in the RIT regime, due to the reduced degrees of freedom. This results in excessive ion expansion and impacts the interaction dynamics. By reducing the pulse duration, it is ensured that the peak of the laser field can interact with a more realistically expanded plasma.

Figure. 4.9 displays the experimental data (shown in Fig. 4.6) alongside the simulation data points for multiple plastic target thicknesses. Both sets of results are very similar in terms of overall trend, including the optimum target thickness ℓ for maximising $\varepsilon_{\rm p}$ and η. The absolute values are higher in the case of the simulations due to the 2-D dimensionality. To provide an overview of the overall behaviour, Fig. 4.10 shows example electron, proton and C^{6+} ion density distributions at three snap-shots in time,

for an optimum target thickness case, $\ell = 75$ nm. At early times (Fig. 4.10a and c) the target expands due to the TNSA mechanism. Ions with the highest charge-to-mass ratio gain most energy in the sheath field, resulting in the ion species becoming layered, with the protons at the front [84], and a buffering effect between the carbon and proton ions, similar to that reported in Ref. [59]. As there is minimal overlap between the protons and carbon ions, there is negligible electron-screened Coulomb repulsion effects, such as reported in Liu *et al.* [122] for the case of circularly polarised laser pulses. As the laser intensity increases, the radiation pressure induces an electric field component that accelerates a population of both the protons and carbon ions forward. At time t = -0.15 ps (where $t = 0$ ps corresponds to the peak of the pulse interacting with the target), the electron density along the laser propagation axis decreases below the relativistically corrected critical density and the target becomes relativistically transparent. As the laser propagates through the remainder of the target volume, it can directly accelerate electrons, forming a high energy electron jet, as introduced and investigated by our group in Ref. [84]. The jet extends through the TNSA ion front. The highest energy proton bunch is observed in the vicinity of the electron jet, concurrent with the high energy component in the experiment for a target at ℓ_{opt} (shown in Fig. 4.5). There may also be some additional energy transfer to the carbon ions, but they do not achieve sufficient energy to influence the highest energy protons. This layering effect of the ion species is also observed in simulations of a proton heated target, as seen in Chapter 6.

The evolution of the electrostatic fields and the proton density is investigated, in order to understand the process by which ε_{p} is enhanced (again for an optimum case of $\ell = 75$ nm). The results are shown in Figs. 4.11 and 4.12. First considered are the main acceleration mechanisms occurring. Figure 4.11a shows the proton density and corresponding longitudinal electrostatic field, along the laser axis, as a function of time. The acceleration is dominated by a dynamic dual-peaked electrostatic field, similar to that investigated numerically in Ref. [28]. The peak labelled S is the TNSA sheath field, generated at the target rear early in the interaction. Peak R is produced slightly later by the laser radiation pressure at the front (resulting in HB-RPA). Line-outs at three example times, corresponding to the dashed lines in Fig. 4.11a, are presented in Fig. 4.11b-d. Protons accelerated by peak R catch-up with those accelerated by S, producing a single bunch between the peaks, which is accelerated by the hybrid RPA-TNSA scheme, as introduced by Qiao *et al.* [116]. The peak eventually broadens

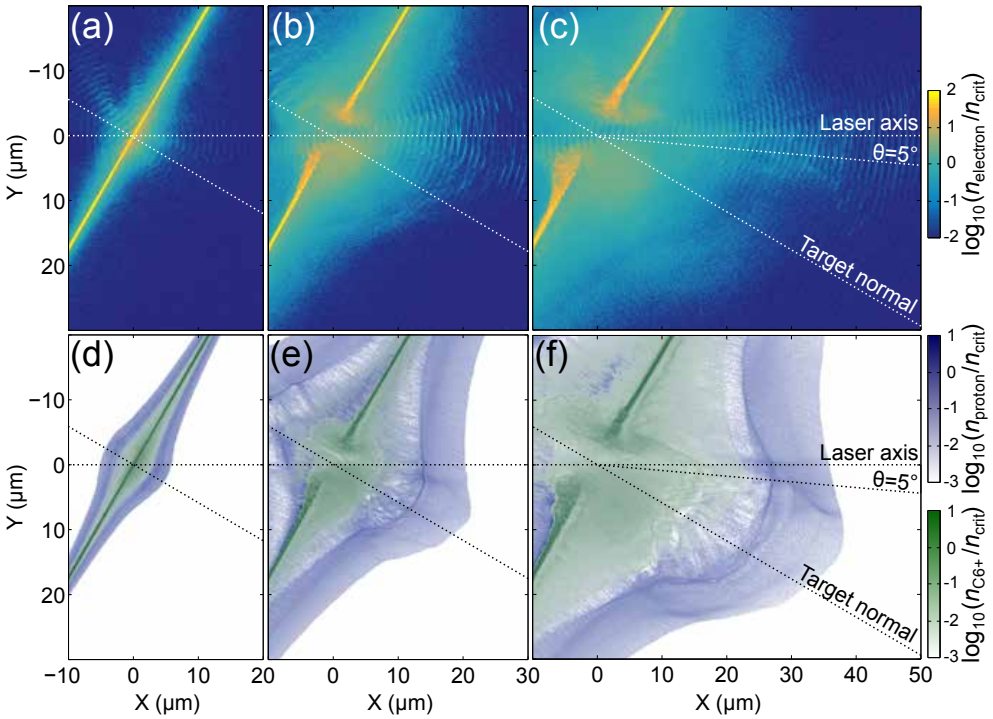

Figure 4.10: Simulation results showing the electron and ion density spatial profiles. (a-c) Electron density at: (a) $t = -0.2$ ps; (b) $t = 0.1$ ps; (c) $t = 0.3$ ps (time $t = 0$ corresponds to the peak of the pulse arriving at the target). (d-f) Corresponding plots showing the proton (blue) and C^{6+} (green) ion density profiles.

out at late times when the dual field structure decays.

The increased heating of the plasma electrons by the portion of the laser pulse which propagates through the expanding foil, due to RIT, enhances the magnitude of both peaks in the longitudinal electrostatic field. This occurs in a transient way, in that peak R is enhanced first (by almost a factor of 2), which temporarily results in a merging of the field structures, as shown in Fig. 4.11c. As the laser pulse propagates forward, peak S then increases in magnitude and the space charge of the proton bunch suppresses the field between the peaks as the interaction evolves (Fig. 4.11d). The dual peak structure with bunched proton population continues until the overall field decays.

The highest energy protons are observed at $\theta \sim 5°$, where θ is the angle with respect to the laser propagation axis. Figure 4.12a shows the proton density-time plot at this angle. When compared to the example results in Fig. 4.11a, it is clear that part of the proton bunch is accelerated to higher energies. This is also clearly observed in the ε_p-θ plots shown at three example times in Fig. 4.12b-d. Early in the interaction, the proton beam is centred on the target normal axis ($\theta = 30°$). As the simulation evolves, a ring-like density distribution emerges at relatively low proton energies, similar to that

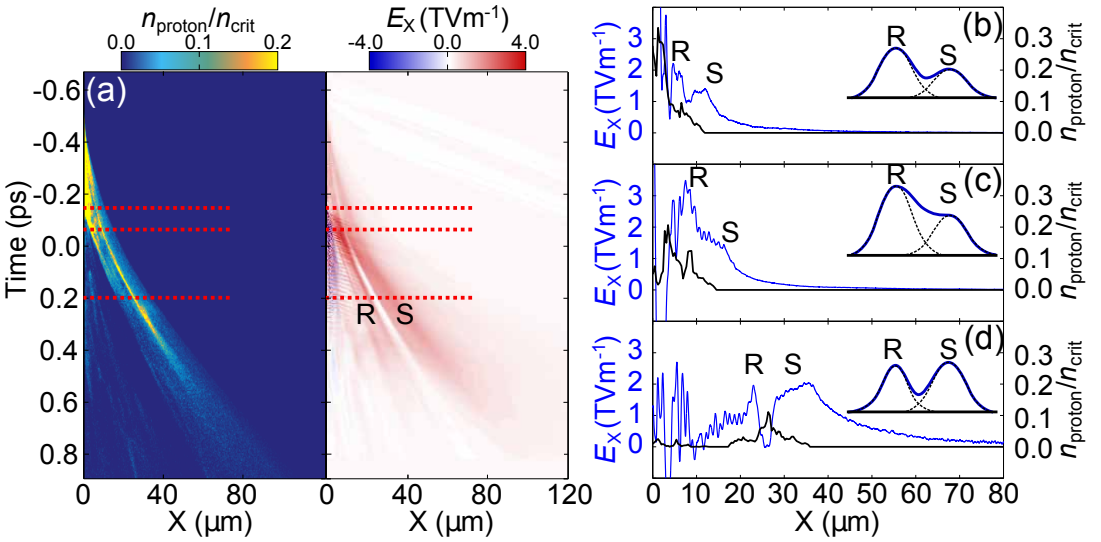

Figure 4.11: Simulation results illustrating the hybrid acceleration scheme. (a) Proton density (n_{proton}) and longitudinal electrostatic field (E_{X}; along the laser axis) as a function of X and time (where time $t = 0$ corresponds to the peak of the pulse arriving at the target) for the interaction of a 0.4 ps, $2{\times}10^{20}$ Wcm^{-2} laser pulse with a $\ell =$ 75 nm plastic foil. The three dotted lines correspond to the example times considered in (b-d), from top to bottom, respectively. (b-d) Longitudinal electric field (blue) and proton density (black) at: (b) $t = -0.15$ ps; (c) $t = -0.05$ ps and; (d) $t = 0.2$ ps. Peaks R and S are the RPA and TNSA fields, respectively. The insets in (b-d) schematically illustrate the evolution of the dual-peaked structure.

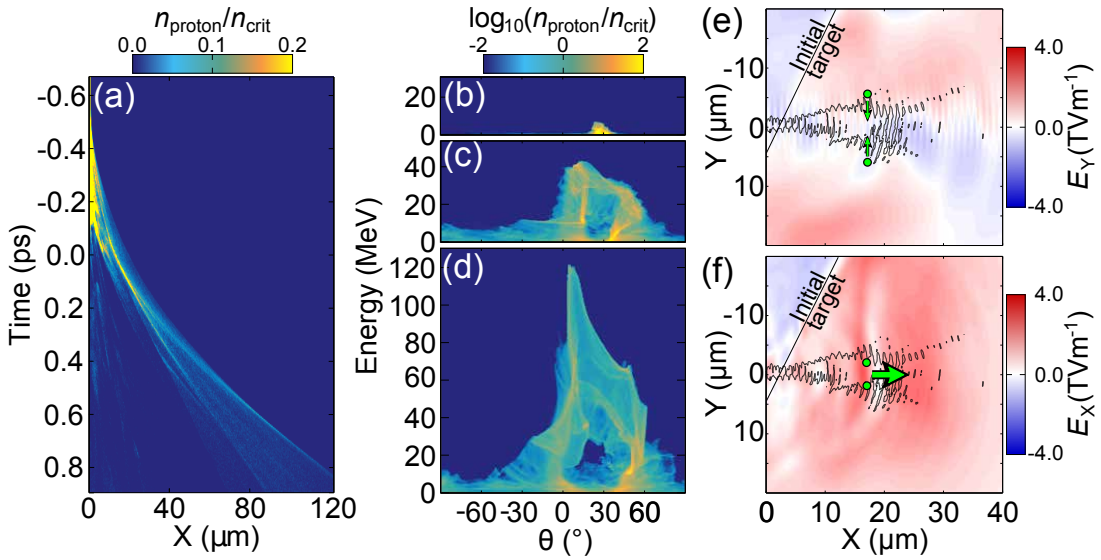

Figure 4.12: Simulation results illustrating the influence of the electron jet on the proton beam. (a) Evolution of the proton density (n_{proton}) at angle θ=5° (Same simulation as in Fig. 4.11). (b-d) Proton density and energy as a function of angle θ (with respect to the laser axis) at: (b) $t =$ -0.3 ps; (c) $t = 0.1$ ps; (d) $t = 0.5$ ps. (e) Transverse electric field (E_{Y}) with super-thermal electron jet, as shown by contours for electrons with energy >10 MeV at $0.1n_{\text{crit}}$. The arrows show the direction of the resultant force on protons, as represented by the green dots. (f) Same for the longitudinal electrostatic field (E_{X}).

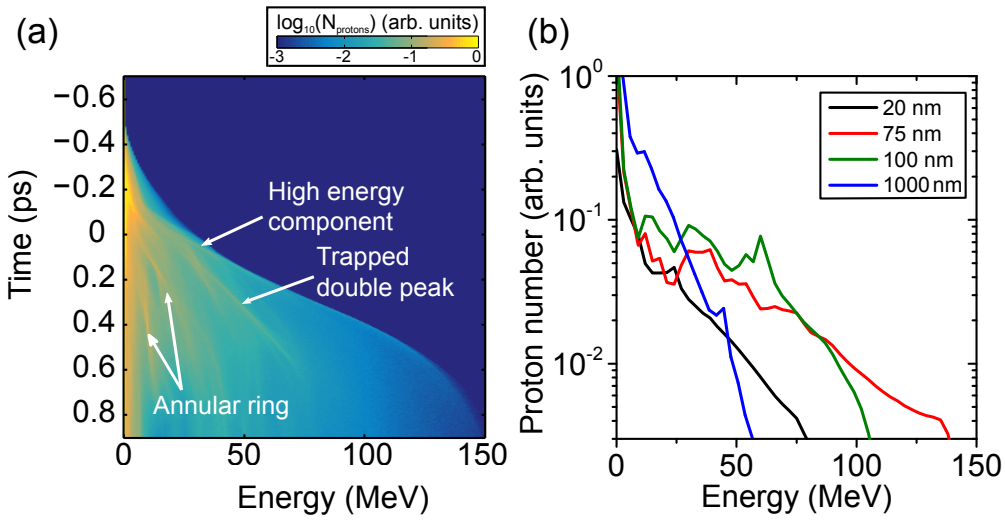

Figure 4.13: Energy spectra from the simulation results. (a) Temporal evolution of the proton energy spectrum for a $\ell = 75$ nm target, sampled within an angular cone of $\pm 60°$ of the laser axis. Distinct proton energy components are labelled. (b) Proton energy spectrum at $t = 0.8$ ps for given foil thicknesses, ℓ.

discussed in Refs [59, 123]. After the onset of RIT occurs, part of the proton population (in the angular range $\theta = 5°$-$15°$), gains energy much faster than the rest. This localised enhancement in the acceleration is driven by the jet of super-thermal electrons produced by the propagating portion of the laser pulse and collimated by a self-induced azimuthal magnetic field [39, 84]. Figures 4.12e and 4.12f show the transverse and longitudinal electrostatic fields, respectively, in the region of the jet, which is shown as a contour plot, at an example time of $t = 0.1$ ps. The very high electron current density within the jet produces a transverse electrostatic field, which attracts protons towards the laser axis, as shown schematically in Fig. 4.12e. Figure 4.12f shows that the magnitude of the dual-peaked longitudinal electrostatic field is maximum in the vicinity of the jet. As the interaction evolves, the sheath-accelerated protons are gradually pulled towards the jet and into the enhanced field region. Protons pulled into the RPA (or temporarily merged) field can gain enough energy to traverse the depression in the field structure and into the boosted sheath field region, allowing continued acceleration. As such, with increasing proton energy the centre of the beam changes from target normal to an angle closer to the laser axis, as shown in Fig. 4.12d. The energy dependence of this effect is shown in Fig. 4.5b (same simulation). Importantly, this figure shows that a similar energy dependent change in the beam centre is measured experimentally (albeit to a lesser extent than in the 2D simulation) and only for targets which undergo RIT.

Signatures of the various features described above are observed in the evolution of the proton energy spectra, as shown in Fig. 4.13a. Prior to RIT, the spectrum, sampled over a wide solid angle to enable comparison with experiment, is dominated by TNSA. As RPA begins just after t = -0.2 ps, a peak corresponding to the proton bunch trapped by the dual-field structure can be observed forming, part of which is further accelerated to energies higher than the sheath-accelerated protons. The remainder of the trapped bunch continues to gain energy before dissipating into a thermal spectrum late in the interaction ($t \sim 0.6$ ps). Similarly, spectral features resulting from the ring structure are also observed at low energy, but also degrade late in the interaction. The end result is an overall broad thermal spectrum with little evidence of distinct spectral features, similar to that measured experimentally, as shown in Fig. 4.4. Figure 4.13b shows the proton spectra from the simulations at $t = 0.8$ ps for several target thicknesses. Similar to the experimental results in Fig. 4.4, a thermal spectrum is observed, with a higher energy component emerging for thicknesses of the order of ℓ_{opt}. Note that the absolute energies in the simulations are higher than experiment because they are performed in 2D. The overall spectral shapes are very similar and are directly compared in Fig. 4.14. Three example cases are shown, corresponding to targets at $\ell \ll \ell_{opt}$, ℓ_{opt} and $\ell \gg \ell_{opt}$ (Figs. 4.14a, b and c, respectively). The spectra are shown as a function of ε_{max} for each case and normalised to the proton flux. The spectra are obtained at the end of the simulation ($t = 0.8$ ps), after any significant peaks and other features have degraded. The overall shape of the spectra are in good agreement.

In the following section, the broader relevance of RIT-enhanced hybrid TNSA acceleration and its potential to be applied at multi-petawatt laser facilities under development is explored.

4.6 Implications for multi-petawatt lasers

Figure 4.15a shows the ℓ parameter ranges over which the TNSA-dominant and RPA-dominant (shaded region) hybrid regimes occur as a function of laser intensity, I_{L}, as calculated using the model in Qiao *et al.* [116], for plastic density. In addition to the relatively long pulses explored experimentally in this work, short pulses typically achieved with Ti:sapphire lasers are also considered. Specifically, $\tau_L = 40$ fs as an example pulse duration is chosen, which is routinely achieved with a Ti:sapphire system

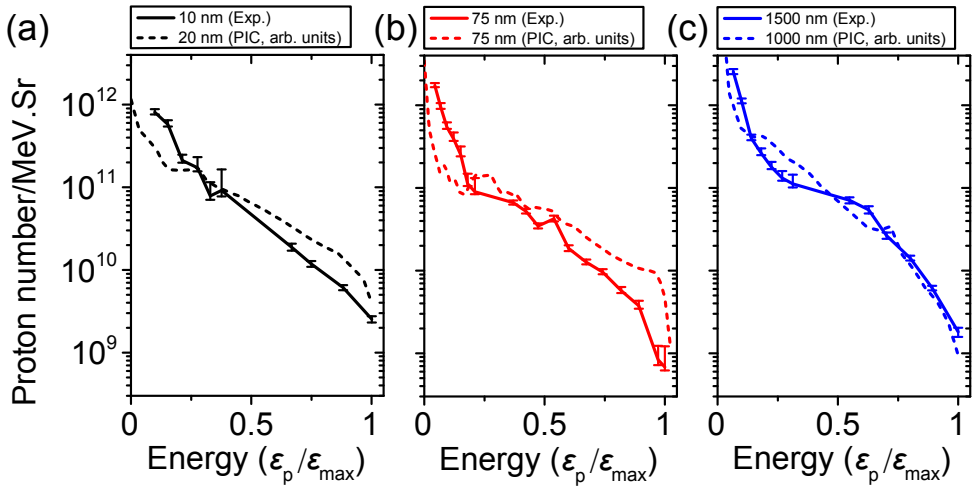

Figure 4.14: Measured proton energy spectrum and normalised spectrum from the PIC simulations, for: (a) $\ell \ll \ell_{opt}$; (b) $\ell \sim \ell_{opt}$; and (c) $\ell \gg \ell_{opt}$. The error bars are defined by the level of uncertainty in the calibration of the RCF.

and is within the range expected to be delivered at a number of multi-petawatt laser facilities.

The thickest target for which RIT occurs within the temporal window defined by $\pm\tau_{\mathrm{L}}$ (centred on the peak) is plotted as a function of intensity for $\tau_{\mathrm{L}} = 900$ fs and $\tau_{\mathrm{L}} = 40$ fs as dotted red and blue lines, respectively. This upper ℓ limit for the onset of RIT can be determined using the analytical model in Ref. [82], although we find that the strict application of this model overestimates the degree of transparency when compared to experimental measurements (RIT occurs too early in the model). We compensated for this by using the maximum value of ℓ for which transmitted light is detected experimentally (for $I_{\mathrm{L}} = 3{\times}10^{20}$ Wcm^{-2}) to adjust the onset time of RIT in the model and used that in the calculations of ℓ as a function of I_{L}. A similar correction was applied for the $\tau_{\mathrm{L}} = 40$ fs case, based on the largest ℓ for which transmitted light is measured at that pulse duration, as reported in reference [124]. In both cases, the differences in target areal density are included in the calculations.

For the $\tau_{\mathrm{L}} = 900$ fs case, the optimum thickness for enhancing hybrid acceleration in the experiment ($\ell_{\mathrm{opt}} \sim 90$ nm; the red point in Fig. 4.15a) corresponds to RIT occurring close to the peak of the pulse. The corresponding scaling of ℓ_{opt} with intensity for $\tau_{\mathrm{L}} = 900$ fs and $\tau_{\mathrm{L}} = 40$ fs is plotted as the dashed red and blue lines, respectively. For the relatively long pulse case, this optimum condition coincides with the interface between the two hybrid regimes, at which the maximum ion velocities due to RPA and TNSA

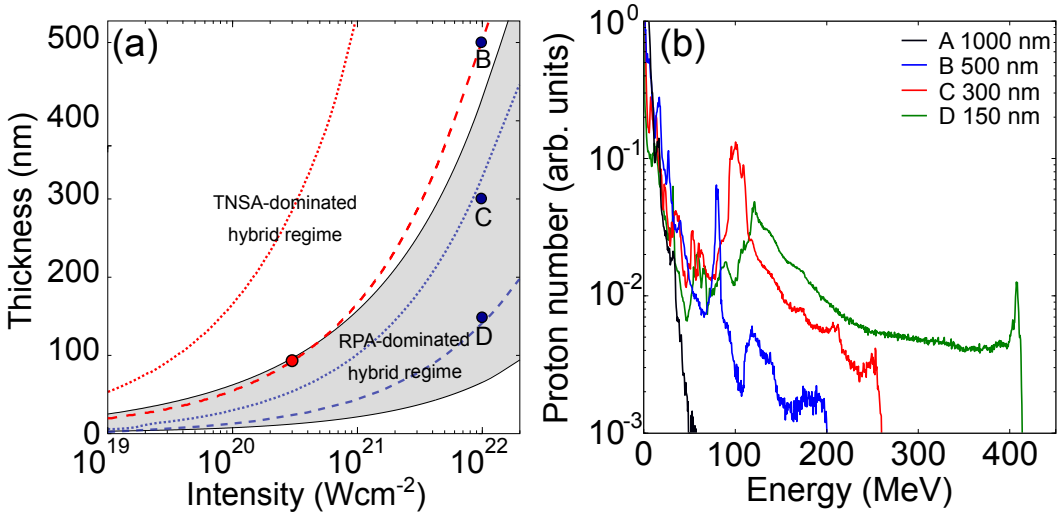

Figure 4.15: (a) $\ell - I_{\mathrm{L}}$ parameter space for the TNSA- and RPA-dominant hybrid regimes, for plastic [116]. Scaling of the maximum ℓ for which RIT occurs (dotted) and optimum ℓ for which RIT occurs near the peak of the pulse (dashed) with I_{L}, for pulse durations $\tau_{\mathrm{L}} = 900$ fs (red) and $\tau_{\mathrm{L}} = 40$ fs (blue). The red point corresponds to ℓ_{opt} in the experiment. The blue points labelled B, C and D correspond to example cases discussed in the main text. (b) Proton energy spectra for four example target thicknesses, from 2D PIC simulations for 40 fs and 10^{22} Wcm^{-2} laser pulses.

are approximately equal, over much of the intensity range. Thus RIT-driven processes strongly influence the acceleration dynamics in the case of relatively long laser pulses, with the highest proton energies achieved via enhancement of the dual RPA-TNSA field structure. By contrast, for the $\tau_{\mathrm{L}} = 40$ fs case the thickness range for which RIT occurs at a given intensity is smaller, enabling RPA-dominant hybrid regimes with and without RIT enhancement to be accessible (below and above the dotted blue line in Fig. 4.15a, respectively). As discussed by Qiao *et al.* [116], RPA-dominant hybrid acceleration may be advantageous in terms of producing ions beams with desirable RPA features, such as reduced energy spread.

To explore this further, we performed a series of simulations for laser pulses with τ_{L} = 40 fs and $I_{\mathrm{L}} = 10^{22}$ Wcm^{-2}; parameters achievable at next generation, multi-petawatt laser facilities. These facilities are expected to deliver even shorter pulses and higher focused intensities when fully operational, but we choose conservative values which could be achieved in the early stages of operation. By doing so we also avoid high field processes, such as radiation reaction, which are expected to influence ion acceleration (via the action of this force on the plasma electrons) at laser intensities of the order of 10^{23} Wcm^{-2} [125–127]. Simulations were performed as a function of ℓ in the range 50

nm to 1000 nm.

Representative proton spectra are shown in Fig. 4.15b for four example thicknesses. Case A, $\ell = 1\,\mu\text{m}$, is in the TNSA-dominated thickness regime and the resultant spectrum is a thermal distribution with a relatively low maximum energy. As ℓ is decreased to 500 nm (case B), which is within the hybrid acceleration regime, but is too thick for transparency (see Fig. 4.15a), the maximum proton energy increases and a narrow energy peak produced by RPA emerges (at $\sim$ 80 MeV). For case C, corresponding to $\ell = 300$ nm, a clear RPA-driven proton energy peak is observed, which together with the overall proton spectrum is boosted in energy by the onset of RIT. As ℓ is decreased down to 150 nm (case D), for which transparency occurs near the peak of the pulse, both the RPA and TNSA components are boosted to their highest observed energies, although the width of the RPA peak has increased significantly. For thinner targets, the proton energies decrease again, and below the lower bound ℓ of the hybrid regime low numbers of protons are accelerated by the rapid expulsion of the target electrons inducing Coulomb explosion of the foil. We note that, as with the longer pulse and lower intensity case explored in the modelling discussed above, the 2D nature of the PIC simulations are likely to overestimate the achievable ion energies. Nevertheless, the overall trend of moving from a TNSA-dominated to a hybrid regime in which both RPA and TNSA occur, and finally to a regime in which this hybrid process is enhanced by relativistic transparency, is clearly observed as ℓ is decreased.

The corresponding total laser-to-proton energy conversion efficiency is plotted as a function of ℓ in Fig. 4.16a and shows an optimum thickness at 200 nm. The fractional conversion efficiency to four stated energy bands across the spectral range is also presented. There is a general decrease in the conversion to the lowest energy band and increase in the upper energy band as ℓ is decreased to 150 nm. Below this value, there is a decrease in the conversion to all parts of the spectrum. The conversion efficiency to the second band, which contains the RPA peak, is maximised for $\ell \sim 300$ nm. This is the thickness region at which the onset of relativistic transparency occurs late in the interaction (just below the upper bound ℓ limit for RIT in Fig. 4.15a), for these laser pulse and target density parameters. It is therefore in this thickness range that RPA is most effective (the RPA acceleration time is longest).

Finally, the influence of the laser intensity contrast on the acceleration dynamics is explored. Suppression of the laser ASE levels to achieve ultrahigh laser intensity

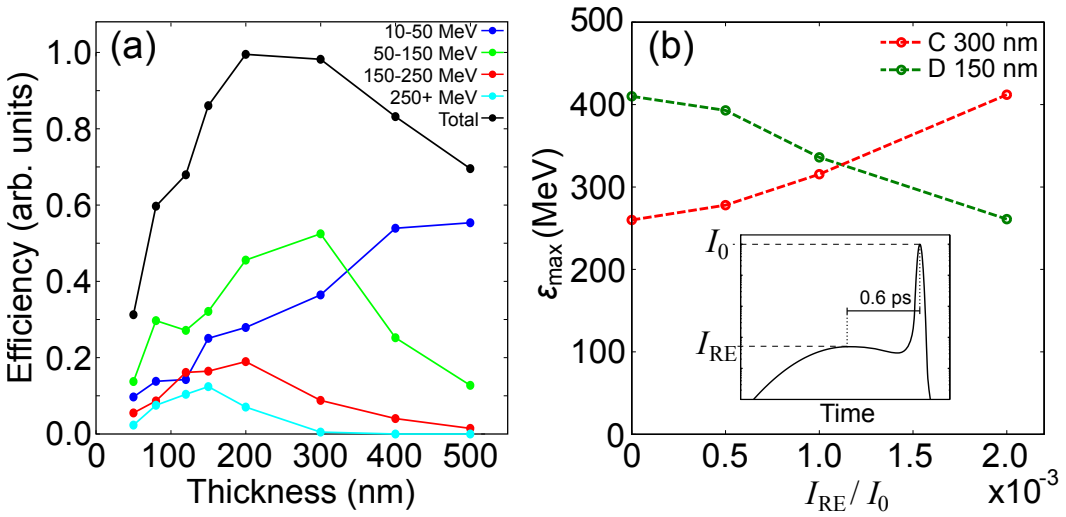

Figure 4.16: (a) Laser-to-proton energy conversion efficiency as a function of ℓ (for the same laser pulse parameters). The total efficiency is shown (black), as well as the fraction in each of the four energy bands: 10-50 MeV (blue); 50-150 MeV (green); 150-250 MeV (red); and, >250 MeV (cyan). (b) Maximum proton energy as a function of the ratio of the intensity on the pulse rising edge, $I_{\rm RE}$, at an example time of 0.6 ps, to the peak laser intensity, I_0. This is simulated by the addition of a wide, low intensity, prepulse, as illustrated in the inset, for the two example foil thickness cases C and D.

contrast on the timescale of tens-to-hundreds of picoseconds prior to the peak intensity is a necessary first step to use foils of the thickness range considered here. However, this does not in itself enable control of the acceleration physics because, as discussed in Powell *et al.* [84], the expansion dynamics of ultrathin foils are highly sensitive to the intensity of the picosecond rising edge of the laser pulse. This in effect changes the time during the interaction at which transparency occurs. Thus, $\ell_{\rm opt}$ depends on the intensity profile on the rising edge of the laser pulse. To illustrate this, the intensity level within a picosecond of the peak intensity was varied by the addition of a broad, low intensity pulse; the rising edge intensity at an example time of t = -0.6 ps is denoted $I_{\rm RE}$. The pulse duration of this pre-pulse was 0.4 ps (FWHM), with a peak intensity varied in the range (0.5-2.0)$\times 10^{19}$ Wcm^{-2}, 0.6 ps before the main (40 fs; 1×10^{22} Wcm^{-2}) pulse.

The effect of varying $I_{\rm RE}$ on the maximum proton energy is considered for cases C and D in Fig. 4.16b. The maximum energy achieved in case D, which corresponds to $\ell_{\rm opt}$ for an ideal pulse, decreases because RIT occurs earlier in the interaction, thus decreasing the time over which RPA occurs. By contrast, the maximum proton energy increases for the ℓ = 300 nm case C target. This target is close to the threshold for RIT to occur (near the end of the interaction) for the ideal pulse (just below the dotted

blue line in Fig. 4.15a) and therefore far from optimal for the transparency-enhanced hybrid acceleration scheme. With increasing I_{RE}, the target expands faster, bringing the RIT time closer to the peak of the laser pulse interaction and thereby increasing the maximum proton energy. We note that the overall acceleration mechanism is the same, but the target thickness at which the maximum proton energy is achieved changes.

4.7 Conclusion

Experimental and simulation results for proton acceleration in the interaction of ultraintense, linearly polarised laser pulses with ultrathin foils are reported. Efficient acceleration of protons to energies exceeding 94 MeV is demonstrated. Established models were applied, with no single acceleration mechanism explaining the experimental results obtained. The experimental results indicate that, provided the target is thin enough, it undergoes RIT. Additionally, the measured critical surface velocity indicates that all of the targets undergo some degree of RPA. Simulations were performed, showing that the acceleration occurs via a dual-peaked electrostatic field, produced by a combination of the RPA and TNSA mechanisms, and that protons are efficiently accelerated in this hybrid RPA-TNSA scenario. RIT enhances the fields and produces a magnetically-confined and directional jet of super-thermal electrons that drives higher proton energies over a relatively narrow angular range. The results demonstrate that by controlling the onset of RIT it is possible not only to enhance the maximum proton energy in the RPA-TNSA hybrid acceleration regime, but also to manipulate the directional properties of the final proton beam.

Extrapolating the results via analytical and PIC modelling, RIT is expected to be important for relatively long pulses over a wide range of intensities achievable with present high power lasers. In the case of short pulses and ultrahigh intensities planned for multi-petawatt laser facilities, several different regimes of hybrid acceleration occur. By tuning the target thickness, and potentially the pulse rising edge intensity profile, it is possible to transition between TNSA- and RPA-dominated hybrid schemes, and between regimes with and without RIT-driven enhancement (either side of the dotted blue line in Fig. 4.15a). As shown in Fig. 4.15b, with fixed laser pulse parameters, the resulting proton spectrum can thus be tailored to produce a RPA-driven spectral peak at mid-range energies (FWHM energy spread equal to 6%, 18% and 34% for cases B,

C and D, respectively), or to enhance the maximum and peak proton energies at the expense of the energy-width of the peak.

These results illustrate the potential to use hybrid acceleration schemes to tune the spectral and spatial properties of the resulting proton beams, even in the absence of an ability to change the polarisation of the drive laser pulse, in the early stages of operation of next generation, multi-petawatt laser facilities.

Chapter 5

Investigation of the electrodynamic sheath field driving proton acceleration

While the previous chapter was on the optimisation of laser and target parameters for ion acceleration, this chapter details the use of a laser-driven ion beam as a charged particle probe. A beam of accelerated protons is used to probe the electrodynamic sheath field, generated on the rear of a target following the interaction of an ultra-intense laser pulse with the front surface. The onset and evolution of this field, which is responsible for driving proton acceleration in the TNSA regime [56], is investigated.

5.1 Introduction

Laser-driven proton beams have several radiographic applications, with deflectrometry being the technique used in this chapter. This is discussed in detail in Chapters 1 and 3. Aside from acting as a diagnostic, this technique may be used to measure the relative timing between two laser pulses [128, 129]. This was the initial purpose of the measurements presented here. The detailed images, however, provided far more information of the laser-solid interaction than simply the relative timing of the two laser pulses.

In this chapter, the phenomenon diagnosed is the electrodynamic sheath field. The term 'electrodynamic' is used here as opposed to the more conventional 'electrostatic' adjective used to describe the sheath field, as the sheath field dynamically changes over

the temporal range of the probe. A thorough theoretical description of the sheath field is detailed in Chapter 2. Due to its highly-transient nature, experimental diagnosis of the field is challenging. The diagnostic used to measure the probe proton beam was radiochromic film (RCF) in a stack configuration, providing both spectral and spatial information of the diagnosed proton beam. Details of this diagnostic can be found in Chapter 3. By using an auxiliary laser-accelerated proton beam to transversely probe a laser-irradiated wire target, the field evolution is characterised. Previously, the most sensitive (in terms of spatial and temporal resolution) detection of the expanding sheath field [58] (which also provided the first direct evidence of the generation of an initial intense sheath field) was limited in terms of spatial and temporal resolution. The temporal resolution of this previous study was ~ 4 ps, with a magnification of 30. As the duration of the laser pulse interaction was equal to 1.5 ps, this resulted in a coarse measurement of the sheath field evolution, which evolves over a time-scale comparable to the pulse duration.

The results presented in this study has an order of magnitude increase in temporal resolution (~ 0.2 ps) and a factor of two increase in spatial resolution on the work reported in Ref. [58]; providing more information regarding the early-onset of the electrodynamic sheath field. This increase in resolution is due to the higher energy resolution of our stack detector (~ 0.5 MeV) and the relatively high energy of the spectral components diagnosing the fields (which results in a low temporal dispersion), in addition to the high-magnification of the images achieved. Scaled 2-D PIC simulations were performed, with a detailed comparison made between the experimental measurements and results from a charged particle-tracker simulating the propagation of a proton beam through the field structures calculated in the simulations.

5.2 Experiment set-up

Two pulsed laser beams were used (Beam 1 and Beam 2), which were separately compressed to temporal durations, τ_L, of 1 ps and 8 ps, respectively. Both pulses were p-polarised, with wavelength $\lambda_L = 1.053\,\mu$m and focused using two separate $f/3$ off-axis parabolic mirrors to spot sizes of $\omega_L = 5\,\mu$m (FWHM), containing approximately 30% of the incident laser energy. Beam 1 had a measured throughput of 63%, with a calculated on-target energy, $E_L = (63 \pm 5)$ J. This corresponds to a peak intensity, $I_L \sim 1.0 \times$

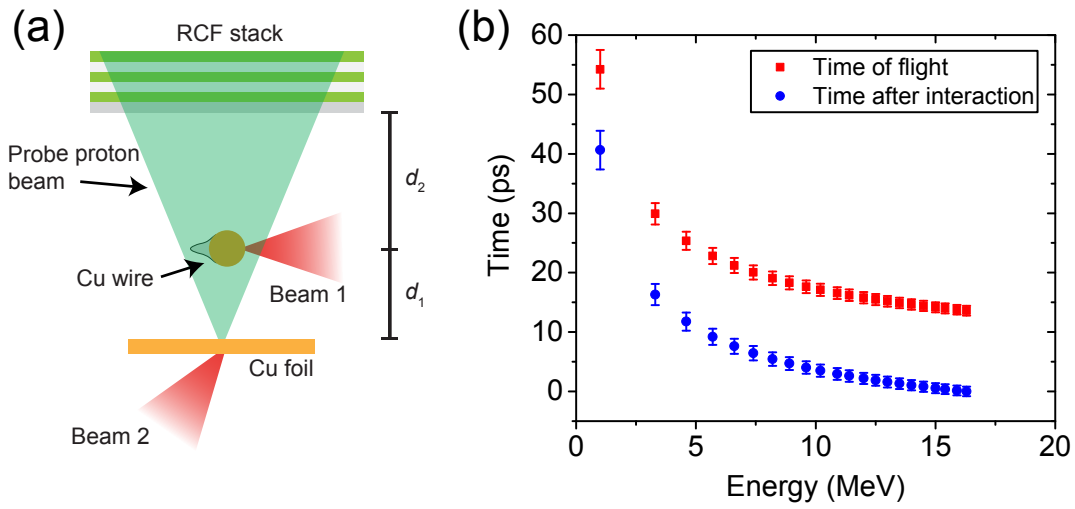

Figure 5.1: (a) Schematic showing the experiment set-up for the diagnosis of the sheath field. (b) Time of flight calculations for the proton energies diagnosed with the RFC stack (red) and the time relative to the leading edge of the pulse (blue). The two series are discussed in the main text.

10^{20} Wcm^{-2}. Beam 2 had a measured throughput of 87%, with a calculated $E_L = (175 \pm 15)$ J, corresponding to $I_L \sim 3.0 \times 10^{19}$ Wcm^{-2}. Beam 1 was used to irradiate the wire target and Beam 2 the proton probe driver target, with a schematic of the set-up shown in Fig. 5.1a. All of the probe protons used to probe the time of interest have a proton energy comparable to the maximum proton energy. These are expected to be accelerated over a very narrow time window, relative to the duration of the pulse. From the radiographs shown in the following section (shown in Fig. 5.2), the very clear features diagnosed indicate that, at early times ($t < 2$ ps), the protons pertaining to the indicated energy bins must have been accelerated over a narrow time window. The thickness of the expanding bell-shaped distribution (explained in the following section) does not seem to change over the first 2 ps, indicating that each spectral component is accelerated over a comparable time. For values of $t > 2$ ps the radiographs become unclear, which may indicate the features are changing over the duration of the proton pulse with the indicated proton energy.

The relative timing of the two beams was initially characterised using a high dynamic-range optical streak camera (Hammamatsu C7700), which measured the temporal separation to within an uncertainty of ± 7 ps; limited by electrical jitter of the trigger signal. Both beams are triggered by the same RF source, however the inherent jitter, in addition to the jitter accumulated from distribution hubs and delay boxes, results in the

minimum sweep window useable by the streak camera to be equal to 1 ns. With this window, the resolution is ± 7 ps. Space-charge issues are minimised by injecting only a small amount of light into the streak camera, with a high MCP gain. The timing was improved upon using the results presented in this chapter, by inferring the interaction time from the obtained radiographs.

A beam of laser-accelerated protons possess a high degree of laminarity, and are equivalent to a virtual point source [98, 99]. This is a result of sheath-acceleration, where protons are accelerated normal to the Gaussian-like sheath field (as seen in Fig. 2.5, Chapter 2). This eliminates the issue that would have arisen due to the physical extent of the proton source. In the case of relatively thin targets, where collisional stopping/scattering of the protons is negligible, this technique provides the capability of detecting the onset and decay of highly transient electromagnetic fields, due to the broadband nature of the proton source and the space charge spreading of the proton beam. When timed correctly, the field evolution from time zero can be temporally resolved. A deeper discussion regarding the proton probing technique is given in the Chapter 3.

As mentioned previously, the proton beam was measured using an RCF stack; providing both spectral and spatial information. The angular divergence half-aperture, $\theta_{1/2}$, of the proton beam ranged from 5° – 30° (from the high to low energy components, respectively), with a cut-off energy equal to $\sim$16.5 MeV. As the detector spectrally selects small energy bins each layer contains information pertaining to a short temporal delay range. The temporal range was between 0 (i.e. arrival of the leading edge of the pulse) and 40 ps, as shown in Fig. 5.1b, which is set by the finite transit time, t_f, between the two targets:

$$t_f = \sqrt{\frac{m_p d_1^2}{2\varepsilon_p}}, \tag{5.1}$$

where m_p is the proton mass, d_1 is the distance between the proton source and wire and ε_p is the proton energy. Each data point in Fig. 5.1b represents an individual RCF layer at the corresponding ε_p, illustrating the high temporal resolution of the diagnostic configuration used - particularly at early times. The blue series displays the time relative to the interaction, with time zero inferred from the deflected protons due to the charging-up target. As mentioned previously, time zero is taken as the arrival of the leading edge of the pulse (i.e. the time when the rear-surface field strength is high

enough to deflect the probe protons). The spatial resolution is of the order of several micrometers, as explained in Chapter 3. The magnification of the interaction plane is set by the geometrical distances involved, and is given by $M \simeq d_1/d_2$, where d_2 is the distance between the wire and imaging plane (the RCF stack). $d_1 = 0.75\,\text{mm}$ and $d_2 = 40\,\text{mm}$, resulting in a magnification of $M = 53$. Note that the concept of magnification only applies to direct imaging and not deflection of the probe protons, and is included here to illustrate the high spatial resolution achieved due to the high value of M.

In this experimental arrangement, Beam 2 ($\tau_L = 8$ ps) irradiates a planar Cu target of thickness $\ell = 20\,\mu\text{m}$ at an angle of 40°, with the accelerated protons directed transverse to the 100 µm-diameter Cu wire. A wire target is an ideal specimen for imaging the electrodynamic fields produced in an intense laser-solid interaction, as the curvature of the wire minimises the deflections due to global target charge-up [128] at the edges of the target. Additionally, the use of a wire eliminates any issue arising due to non-uniformity in the transverse profile of the target (a planar foil target generally has modulations in its transverse profile). During/after the Beam 2 interaction, Beam 1 ($\tau_L = 1$ ps) irradiates the wire perpendicular to the target normal (TN) axis of the planar foil. This results in a generated sheath field that is also perpendicular to the TN axis of the Cu foil, and therefore perpendicular to the average angle subtended by the probe proton beam. The timing was configured by inferring time zero of the laser-wire interaction, by assuming a linear decrease in deflection to the point where the field began to build up on the target rear.

5.3 Experimental results

The analysis and experimental data presented in this chapter focuses on data obtained from a single event, where the high temporal and spatial resolution enabled a vast amount of information to be obtained from one event. Figure 5.2 displays the proton imaging data, with the times, t, relative to the arrival of the pulse leading edge. From these images, the proton beam cross section is clearly modified. Since the protons will not be stopped/scattering in the wire or rear-surface plasma, due to their relatively low areal density, the modification must be due to the electromagnetic fields produced by the interaction. Note that all of the scales featured in this chapter refer to the diagnostic plane, as it is not correct to assume the scale at the interaction plane is $1/M$ times

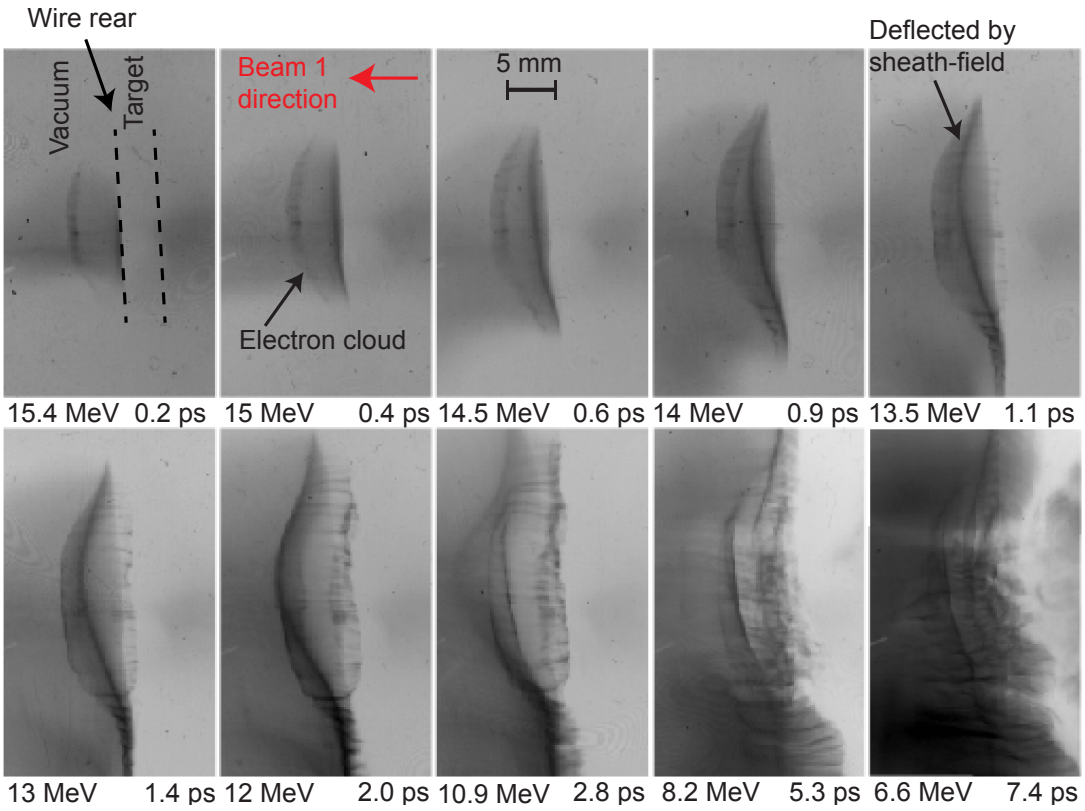

Figure 5.2: RCF slices showing the temporal evolution of the sheath field at the wire rear. The magnification, M, was 53. The scale on the third image refers to the detector plane (scale on the interaction plane is $1/M$ times the given scale in the figure) and is the same spatial scale for all of the images. The contrast of the images have been scaled independently for clarity and are not representative of relative dose. The peak of the pulse arrives at $t = 2.0$ ps, where 0 ps is the approximate arrival time of the pulse leading edge.

the size measured on the RCF. This is due to the nature of the measurement, as it is deflection of the protons and not imaging of the sheath that is being measured.

In the images, darker regions correspond to areas with a higher proton density. An outline of the wire can be seen at early times, due to the wire charging up some picoseconds ahead of the peak of the pulse driven by the interaction with the leading edge of the pulse. The intensity on-target due to the rising edge profile is estimated to be of the order 10^{17} W cm^{-2} at $t = 0$ ps (i.e. ~ 2 ps ahead of the peak), which is high enough to ionise the front surface and accelerate electrons through the target, leaving it positively charged. This intensity estimate is based on third-order autocorrelator measurements of the rising edge profile on Target Area Petawatt (TAP) [84]. Note the measurements are made by bypassing the amplifier chain. Beam 1 follows the majority of the laser-chain used for the beam in TAP, excluding an additional amplifier,

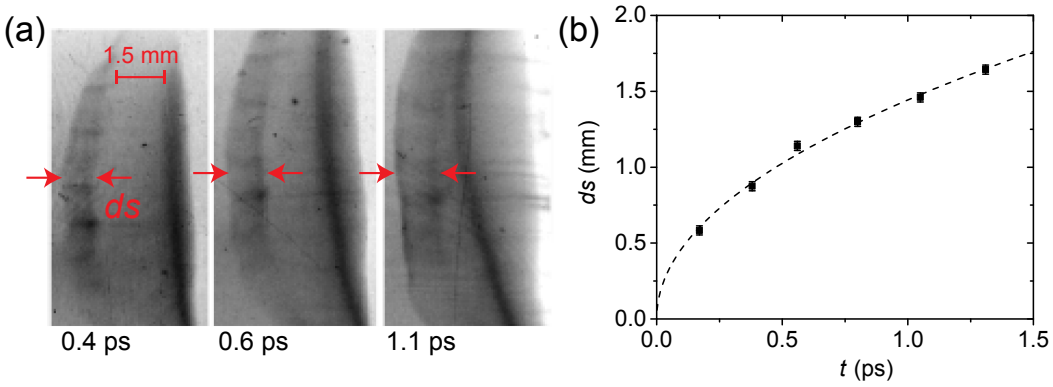

Figure 5.3: (a) Enlarged regions of the deflected protons, displaying the width of the denser band that increases with time (indicated by ds). (b) ds as a function of time.

therefore providing a good estimate of the rising edge profile as a fraction of the peak laser intensity.

Aside from the wire outline, two qualitatively distinct structures can be seen to develop in time. One appears at early times ($t = 0.2\,\text{ps}$), which distinctly perturbs the probe protons into a diffuse cloud. Over the duration of the Beam 1 laser pulse (i.e. until $t \simeq 2.8$ ps) the deflection causing this diffuse structure remains mostly static in the longitudinal direction (i.e. Beam 1 laser direction), before disappearing shortly after this time. The cloud appears to grow laterally, and becomes more turbulent at later times. Some longitudinal movement of the cloud of protons is observed, with the displacement from the wire rear at the imaging plane equal to (2.9 ± 0.3) mm. Figure 5.3a displays several snapshots of the cloud structure. From this, it is clear that at the edge of this cloud exists a slightly denser band of protons, with the width of the denser band increasing with time. In Fig. 5.3b, the width at the imaging plane, ds, of the the denser band as a function of time with respect to arrival of the pulse leading edge is characterised. The displacement scales as $ds \propto t^{0.49}$. The error bars are a consequence of the measurement accuracy. This feature was not reported previously [58].

The second distinctive feature, appearing as a pronounced deflection of the protons into a bell-shaped distribution, starts to become most apparent at $t = 0.4\,\text{ps}$. This expands from the rear of the target and extends transversely across the target. Behind this region (i.e. closer to the target) the proton density drops below that of the background signal, indicating the protons have been deflected from this region and pile-up into the bell-shaped feature. This is especially prominent in the $t = 2$ ps slice. Beyond 2 ps the front becomes less distinctive, and appears to break-up into several

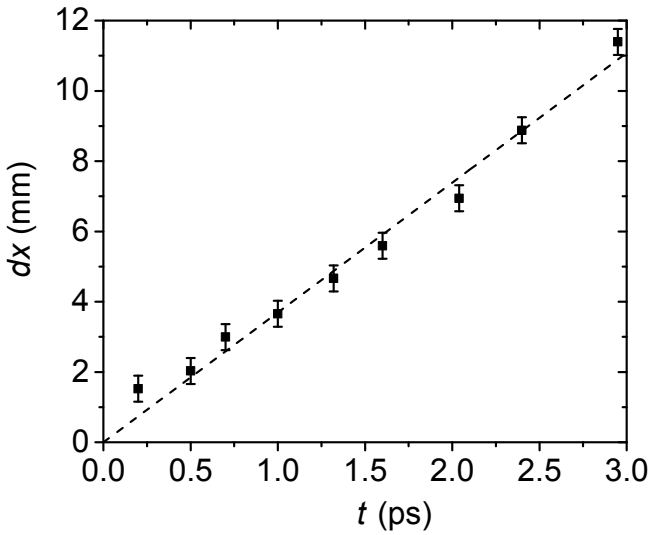

Figure 5.4: Displacement (dx) of the protons at the detector, appearing as a front, from the rear of the wire as a function of time. The black dashed line is a straight-line fit, with origin at $dx = 0$ mm. As before, the peak of the pulse arrives at ~ 2 ps.

other bands at various longitudinal positions, before mostly disappearing at late times. The measured displacement of the ion front with respect to the rear of the target, dx, is shown in Fig. 5.4 as a function of time. Time zero is defined from a straight-line fit to the data which is set to intersect at zero. This definition of time zero is used both in this chapter and in the following.

Both of these features can be interpreted within the framework of the TNSA model [56]. During the interaction, a population of relativistic electrons are generated at the interaction region; with a Boltzmann-like energy distribution and temperature dependent on the laser intensity. These electrons are accelerated through the target, with a small fraction of them having a sufficiently high velocity to escape the target. This leaves the target positively charged, which acts to deflect the probe protons away from the target. This is why the wire appears as an outline in all of the images. Electrons which arrive later will escape into vacuum, with their velocity continually decreasing until they stop and are pulled back to the target. This is a consequence of three effects: the net-positive charge of the target, the lack of background electrons available to draw a return current and the negative electron population beyond the target rear reflecting subsequent electrons. This separation between the positively-charged target and negatively-charged electron sheath leads to an electric potential. From this interpretation of the radiographs, the initial deflection is attributed to the strong

electric field that is associated with the dense electron sheath field at the target rear. The electrons reach a maximum distance longitudinally, dependent on the laser-drive parameters and background plasma characteristics. The transverse size of the cloud appears to increase with time, which is expected and is due to lateral electron transport [50]. This apparent increase may also partially be due to the increased beam size of the lower energy portion of the probe proton beam.

From Fig. 5.3a, the width of the denser band of protons increases, with only the boundary closest to the target moving (closer to the target). This suggests that some of the electrons causing this deflection are moving towards the target. In the TNSA model, protons from the rear-surface contaminant layer are accelerated by this strong electric field [130]. As the protons begin to approach the boundary of the electron cloud, electrons will be attracted towards them, creating an electron front which moves back towards the target. The inward-moving electrons (i.e. those moving towards the target) appear to uniformly decelerate, with their return-transit possibly being inhibited by the additional electrons arriving as the laser intensity increases. The deceleration has a square-root dependence, with a extremely high coefficient of determination, suggesting a steady increase in electrons being supplied to the electron sheath field. An additional observation is the appearance of lines that connect the dark boundaries of the cloud, possibly due to hydrodynamic or electrostatic instabilities. A consequence of the Alfvén current limit, provided the self-magnetic field is sufficient, is that the electron beam reverses its direction of travel and begins to filament; possibly describing this behaviour.

The second, dense thin region is a result of the growing sheath field. As the electric potential increases, due to the increasing (with the laser intensity) population of plasma electrons on the rear of the target, the transverse proton beam becomes increasingly deflected by this field. This follows a linear trend as a function of time, as seen in Fig. 5.4. Behind this apparent front is a void of protons. This is due to the probe protons that originated in this area being deflected, and piling up in this dense layer that moves with time. The front becomes less prominent at later times ($t > 2\,\mathrm{ps}$) and appears to break up into several components, consistent with the expected decrease in field strength after the duration of the laser pulse. The maximum deflection is experienced by protons probing at $t \sim 2$ ps, which suggests the peak of the pulse arrives approximately at this time.

In principle, it's not possible to unambiguously attribute the measured deflections to

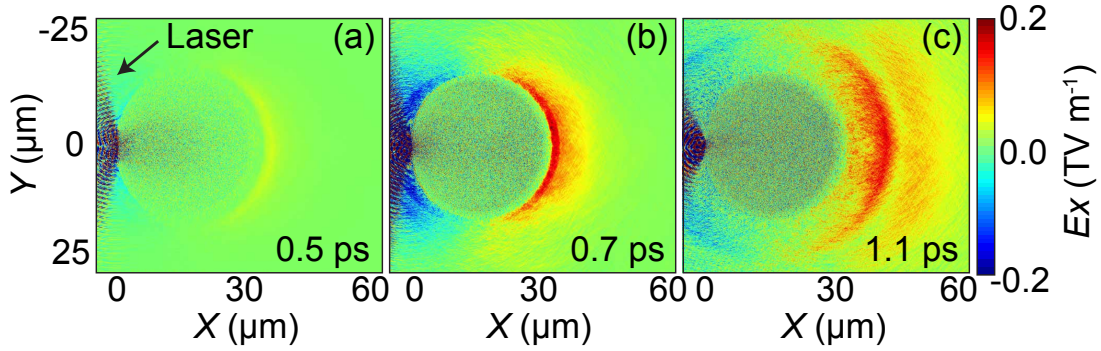

Figure 5.5: Simulation results illustrating the evolution of the longitudinal electric field (E_x) induced by a $I_L = 1 \times 10^{20}$ Wcm^{-2}, $\tau_L = 500$ fs laser pulse irradiating the wire target. Note the peak of the pulse arrives at ~ 0.7 ps.

solely either electric or magnetic fields. In order to gain further insight, particle-tracing in conjunction with 2-D EPOCH simulations was employed.

5.4 Simulations

The magnitude, spatial extent and temporal dependence of the fields induced by Beam 1 were investigated using the fully relativistic, 2-D EPOCH PIC code [109] (detailed in Chapter 3). The target was initialised as a 30 µm-diameter Al^{+11} cylindrical wire, with an electron density of $100n_c$, neutralised with an appropriate number of ions. The initial electron temperature was equal to 10 keV. The wire was scaled down in size due to computational constraints. The simulation box was 130 µm × 60 µm, with a mesh cell size equal to 5 nm × 10 nm. All simulation boundaries were defined as free-space. The laser was incident normal to the target, with Gaussian temporal and spatial profiles. For the intensity scan data sets, the temporal FWHM was equal to 500 fs, with $I_L = (1 - 3) \times 10^{20}$ Wcm^{-2}. The simulations were conducted for 1.2 ps, with field data output every 0.1 ps. The evolution of the longitudinal electric field, E_x, for $I_L = 1 \times 10^{20}$ Wcm^{-2} is shown in Fig. 5.5. Note that the peak of the pulse arrives at 0.7 ps, with 0 ps the time of arrival of the pulse leading edge (the same definition used in the experimental discussion).

A particle-tracing algorithm was implemented to investigate the effects that the calculated electromagnetic fields would have on a proton test particle. The routine works by computing the particle trajectories in the presence of the calculated electromagnetic fields in the simulations. The E_x, E_y and B_z fields are the only fields considered as

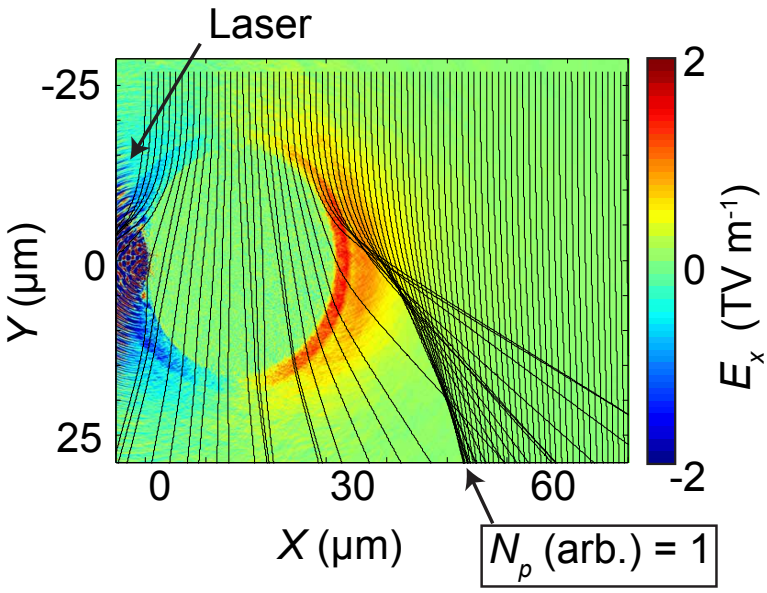

Figure 5.6: Path taken by 10^2 evenly distributed protons due to the longitudinal electric field map, E_x, shown. The region where the proton density is highest, $N_p = 1$, is indicated. Same simulation as Fig. 5.5.

the others are small in comparison. The field-maps are initially loaded, with each test particle projected through the fields. For each time-step and particle, the tracing algorithm solves the equations of motion, and moves it to the new position. The force acting on the particle at this new location is calculated, as a function of position and time, through the Lorentz force (Eq. 2.10, Chapter 2). In the particle tracker, 10^6 protons each with an energy equal to 15 MeV were randomly distributed along the entire of the X dimension encompassed by the simulation at $Y = -30\,\mu\text{m}$ (i.e. the simulation boundary) and propagated over the extent of the simulation box, plus an additional 520 µm (for a total distance equal to 650 µm). The additional distance was incorporated to allow the particles to travel a reasonable distance ballistically such that they are sufficiently resolvable. The particles were moved in 1 fs time-steps. The field-map was not temporally evolving for any one test particle, due to computational constraints. Therefore, a dynamically evolving field over the duration of the particle transport is not incorporated, with the field appearing static to the protons over the whole distance of propagation. This is justifiable as the simulations were ran in order to observe the effects that an increasing field strength had on the trajectory of the proton beam, and not the effect that an evolving field would have on any one test particle.

Figure 5.6 displays the path taken by 10^2 protons, evenly distributed along the

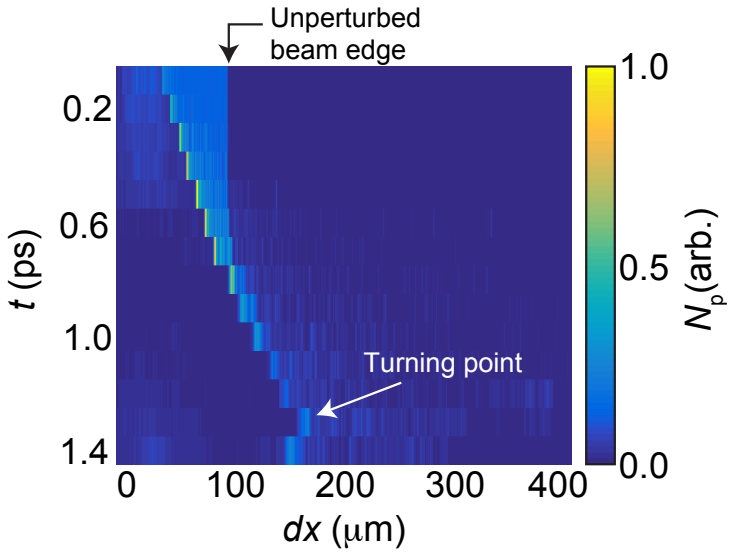

Figure 5.7: Particle-tracing results displaying a histogram of the proton beam population, as a function of time and displacement (dx). The field maps used correspond to those obtained in the simulations with $I_L = 1 \times 10^{20}$ Wcm^{-2}, $\tau_L = 500$ fs (same simulation as in Fig. 5.5). Note the peak of the pulse arrives at ~ 0.7 ps. Key features are indicated and explained in the main text.

X dimension, overlaid with the E_x field from a $I_L = 1 \times 10^{20}$ Wcm^{-2} simulation. The path of each proton is represented by a black line. The protons are very clearly deflected by the strong E_x field, with some deflected by an angle close to 45°. As observed experimentally, a region can be seen that contains a far higher number density of protons than the input beam. This is due to a superposition of the electric field gradient just beyond the peak of the field, resulting in the eventual path of some protons overlapping.

A temporally resolved histogram of the same simulation is shown in Fig. 5.7 for 10^6 protons, along the detector plane. This more clearly illustrates several key similarities between the experimental results and those obtained from the particle tracker. Firstly, the amount of deflection experienced by the protons increases with the laser intensity in a linear fashion, and initiates long before the peak of the pulse ($t = 0.7$ ps). Many of the protons begin to pile up into one particular area, and the resulting dense feature moves as a function of time. Behind this peak (i.e. closer to the target) a void in proton density is apparent, as many have been deflected to the region of $N_p = 1$ or beyond. This is seen more clearly in Fig. 5.6. Shortly after the peak of the pulse has arrived, the deflection becomes more sporadic; with the prominent peak in proton density disappearing. The beam breaks up into several components at this time, with

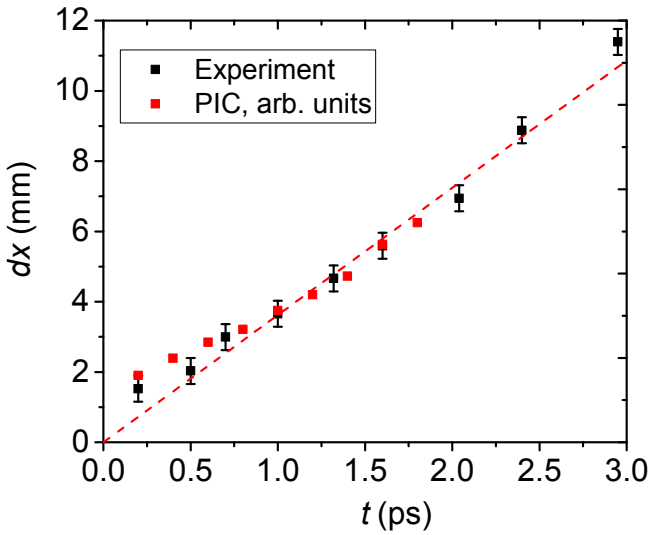

Figure 5.8: Displacement (dx) of the protons from the rear of the wire as a function of time, for both the experimental measurements and from simulations. The red dashed line is a straight-line fit to the PIC data, with origin at $dx = 0$ mm. The simulation data points are normalised to the experimental data points, as explained in the main text.

some appearing to move closer to the target. This is observed experimentally at $t = 2.8$ ps in Fig 5.2. At later times in simulations the field is far more extensive (such as in Fig. 5.5c). This broadened field results in a more uniform deflection. Note that at early times the unperturbed beam edge is visible.

Figure 5.8 shows the experimental data (Fig. 5.4) alongside the position from the particle-tracker where the highest proton number, $N_p(\text{arb.}) = 1$, is located. A straight-line fit to the latter originating at $dx = 0$ mm is also shown. The times determined from the simulations are scaled by a factor of two because of the factor of two difference in the pulse durations. Additionally, the simulation displacement dx has been normalised to the experimental dx. As the technique used is deflectometry, as opposed to imaging, only the relative change in dx is important. For the duration of the laser pulse, the displacement of the high-density proton front measured experimentally agrees extremely well with the simulation data. This further supports the hypothesis that this deflection is caused by the strong sheath field at the target rear.

By quantifying the deflection due to the electric field, dx, it is possible to estimate the peak electric field strength, averaged over the path of propagation, of the sheath field that these protons experience. Following [58], Eq. 3.3 in Chapter 3 calculated

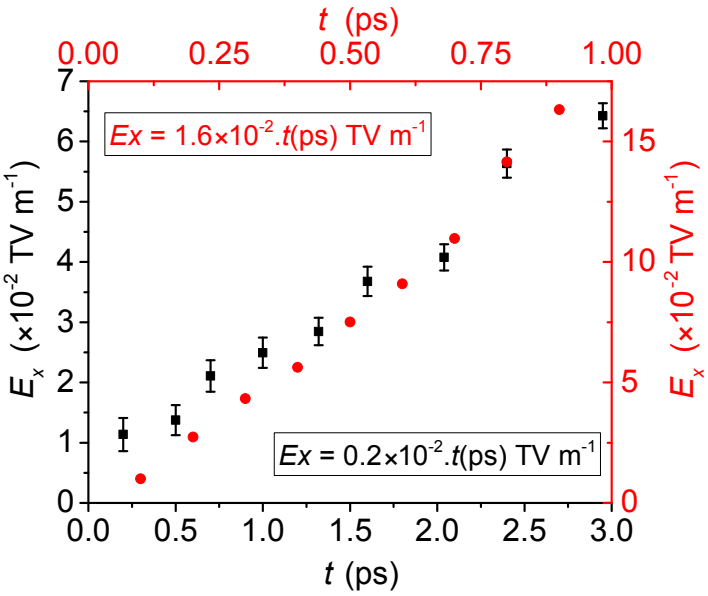

Figure 5.9: Electric field strength, E_x, calculated from Eq. 3.3 as a function of time, t, relative to arrival of the pulse leading edge (same definition as before). The experimental data is in black and the simulation data is in red. The gradients of the respective straight-line fits are shown.

the average electric field experienced by the protons. b is estimated to be equal to the diameter of the wire. Note that by using the measured value of dx in Eq. 3.3, the protons located in the ion front are assumed to originate at the target rear. Figure 5.9 shows how this field strength, as calculated from Eq. 3.3, varies as a function of time for both the experimental data and the simulations. Note that the two series are plotted on separate axes.

From the experimental calculations, the field strength at the peak of the pulse is ~ 0.06 TV m^{-1}. This value is spatially and temporally averaged, and therefore is much lower than the peak field strength predicted from the simulations and experimentally. In the simulations, the gradient is a factor of ~ 8 higher. This is a consequence of the pulse length being a factor of two lower and the wire diameter a factor of ~ 3.5 lower. This leads to a far higher average field around the wire in the simulations. However, this serves to illustrate how much lower the average field is compared to the peak (~ 2 TV m^{-1} at 0.7 ps in the simulations). Figure 5.10 displays the longitudinal electric field averaged over the full Y-dimension from the simulations, for several times, as a function of longitudinal position X. The difference between the peak electric field and $E_{x,ave}$ is a factor of ~ 15. By applying the same scaling to the experimental measurements at the point of furthest deflection, a peak field strength of the order ~ 1 TV m^{-1} is expected. It

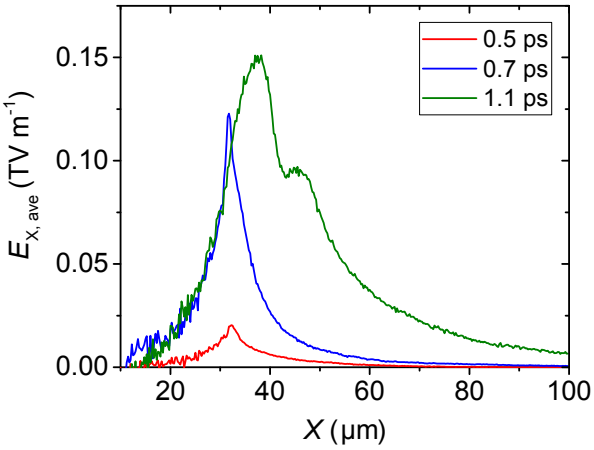

Figure 5.10: Average electric field, $E_{x,ave}$, as a function of longitudinal position, X, for three times. Averaged over the entire Y dimension.

should be noted that this comparison assumes the protons are experiencing the average field depending on their input position. In reality, the position of the proton moves longitudinally, so at early times (when the field gradient is highest), the average field will inadequately describe the particle motion at any one point in the high-field region.

Higher laser intensities were simulated, in order to measure the dependence of the displacement dx on I_L. Figure 5.11 displays results from the particle tracing algorithm for the fields calculated for three values of I_L. In Fig. 5.11a, the position, as a function of time, where the largest population of protons is located for the three values of I_L is shown. Figures 5.11(b - d) display the histograms for the three intensities, at the peak of the pulse.

It is clear from these results that an increasing I_L results in a greater degree of deflection of the probing protons. From Eq. 2.10, the force acting on the protons scales linearly with the electric field. The electric field scales with the square root of the laser intensity [61], so therefore $dx \propto I_L^{0.5}$. Figure 5.12 displays dx for the final time-step shown in Fig. 5.11 for the three values of I_L. A power fit was made to the data, with a scaling of $dx \propto I_L^{0.49}$. This further confirms this is an effect of the laser-generated electric field, and demonstrates the use of a laser-accelerated proton beam to time-resolve the electric field evolution of a laser-irradiated target.

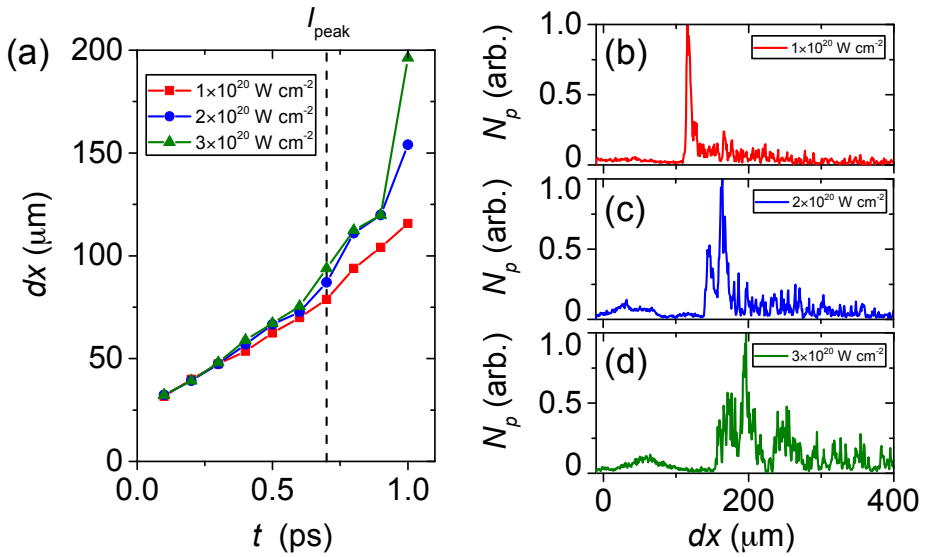

Figure 5.11: Results from the modelling for laser intensities $I_L = (1, 2 \text{ and } 3) \times 10^{20}$ Wcm^{-2} in the simulations. (a) The longitudinal position of the highest proton density as a function of time. (b - d) Histogram at $t = 0.7$ ps (i.e. at the peak of the pulse, I_{peak}) for the three laser intensities.

5.5 Conclusion

An auxiliary laser-driven proton beam was used to diagnose the evolution of the electrodynamic sheath field. The single-shot measurement presented in this chapter is the most detailed of its kind, where the dynamics responsible for laser-driven ion acceleration via TNSA are directly observed. Two key features were diagnosed. From our interpretation, these include the rear-surface electron plasma, with detailed spatial information obtained and dynamics discussed, including the near-static longitudinal extend of the cloud and how it evolves transversely.

Deflections due to the magnitude of the sheath field were also measured, with the average field strength quantified and peak field strength estimated. These were, respectively, ~ 0.06 TVm^{-1} and ~ 1 TVm^{-1}. A detailed comparison was made between these experimental measurements and the electric fields modelled in 2-D PIC simulations. A charged particle-tracker simulated the propagation of a probe proton beam through the field structures obtained, showing excellent agreement.

Using ion beams for the detection of transient electromagnetic fields is one of their most promising applications, due to their short temporal duration and spatial quality. They have opened up a new area of application-based studies, with possible applications outwith laser-plasma physics. Scaled-up simulations were also performed, to gauge the

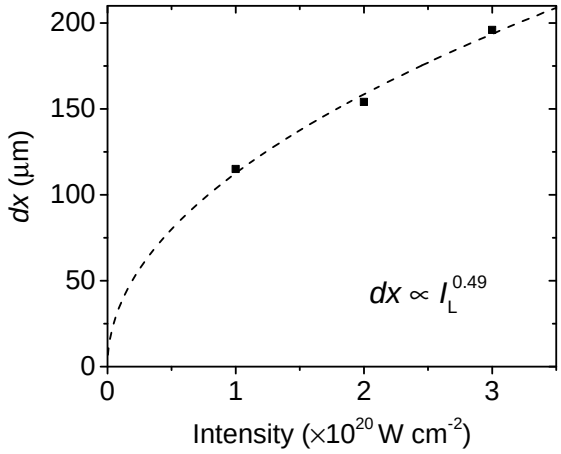

Figure 5.12: Scaling of the displacement of the ion front, dx, as a function of laser intensity (I_L) at $t = 1$ ps in the simulations. The dashed black line is a power fit to the data, with the indicated scaling.

diagnostic's response to higher laser intensities. The magnitude of deflection scaled as expected, demonstrating that proton deflectrometry works for a wide variety of parameters.

Chapter 6

Investigating target expansion dynamics via ion acceleration

In this chapter, the dynamics of target expansion are investigated by measuring the effects that an increasingly expanded target rear-surface has on proton acceleration. A low energy laser-driven proton source, accelerated from the front surface of a laser-irradiated target, is used to heat a secondary foil target. This leads to expansion of the secondary foil. A second laser beam irradiates the expanding target, with the rear-surface accelerated beam of protons spectrally and spatially characterised.

It is observed that for an increasingly expanded rear-surface, the parameters of the accelerated proton beam consistently change. This change includes a reduction of the maximum proton energy, absolute flux and beam divergence. A detailed flux (of the heating proton beam by varying the separation between the two targets) and temporal parameter scan were performed, with the plasma length determined from a simple analytical model. The results are found to be in good agreement with 1-D radiation-hydrodynamic simulations. Upon comparisons with the simulation results the temperature of the targets can be inferred, presenting a new, novel use of sheath-accelerated ions to diagnose target temperature. Prospective ion-driven fast ignition schemes will use multi-kilojoule petawatt laser pulses, where a relatively high degree of rear-surface expansion will be induced by the large electron current generated by the leading edge of the extremely energetic pulse. Estimates based on the results here indicate the degree of expansion expected may change the ion beam parameters significantly, in contrast with previous results [131] using a laser source to induce target expansion.

This chapter is presented as follows: section 6.1 outlines the previous work studying similar dynamics, and puts the work presented here into context. Section 6.2 details the experiment set-up. In section 6.3, the heating proton beam is spatially and spectrally characterised. The experimental results are then shown in section 6.4, illustrating the changes in spatial and spectral behaviour of the beam as a function of proton flux and heating time. This is followed by a discussion of the experimental data in section 6.4.1, with an explanation of the analytical model presented and how the experimental data is interpreted within its framework. Additional discussion further explaining some of the spatial structures observed in the RCF images that are not encompassed by the model is presented. Next, 1-D radiation-hydrodynamic simulations with the HELIOS code [110], using an energy input derived from the measured front-surface proton spectrum, are presented in section 6.5. These were used to characterise the temperature profile and target expansion of the heated Al target. This is followed by section 6.6, where the expected hydrodynamic expansion, calculated from the energy loss of the heating proton beam, is shown. Comparisons are made between these results and those calculated from the simulations, with good agreement found. A detailed discussion regarding the implications this work may have on proton fast ignition (PFI) and proton focusing is shown in sections 6.7.2 and 6.7.3 respectively. Further developments regarding the experimental methodology and simulations are then outlined in section 6.7.1.

6.1 Introduction

Initially, the aim of this chapter was to investigate the effects that warm dense matter (WDM) [21] had on a laser-driven proton beam. In this scenario, one target was irradiated with a short pulsed laser, resulting in heating of the material. A secondary foil was then irradiated with a second short pulsed beam, with the accelerated protons directed through the transient state of WDM (induced by the initial laser beam) and detected downstream. While some proton energy loss is expected in a heated compared to cold target, our observations vastly exceeded what the analytical modelling predicated [132–134], experimental results measured [135] and simulations modelled [136]. Additionally, we observe an increase in beam collimation, which is contrary to what additional stopping would entail due to the higher degree of scattering expected. Under our experimental conditions (relatively high proton energies; relatively thin

targets) the effects due to electronic stopping of the protons is near-negligible. A detailed discussion of proton stopping in heated matter can be found in Appendix B. An additional discussion, with the aid of 2-D PIC simulations, is found in the same appendix, detailing the effects on the proton beam due to the electrical charging of the target. The effects that these fields would have on the proton beam, for the time-scales studied, is also negligible.

Further analysis of the key factors that could be attributing to the surprisingly high energy loss resulted in the discovery of a far more prominent effect than the two mentioned previously. This effect concerns the heating of the probe target (Target 2) by the front surface-accelerated proton beam from the laser-irradiated target that was, initially, the subject of the investigation (Target 1). The proton heating of matter results in the creation of a transient state of WDM, that stays near solid density for up to ~ 100 ps, due to the ion pulse causing significant heating before hydrodynamic expansion occurs. The first demonstration of laser-driven proton heating was made by Patel *et al.* in 2003 [17].

In the work presented here, simulations coupled with analysis of the experimental data indicate that the energy loss is, instead, a consequence of the expansion of the rear-surface layer, due to the heating of the target. The energy loss of the protons scales according to both the flux of the irradiating protons and the time after the laser is incident with respect to the proton arrival time. This type of effect was reported previously [137], where a very long ($\sim 100\,\mu$m) plasma scale-length on the target rear side almost quenched proton acceleration entirely. A more systematic study of rear-surface expansion, where the changes were measured as a function of expansion length, reported similar observations [131]. Fuchs *et al.* measured a gradual decrease in the maximum proton energy, and overall proton number, as a function of plasma scale length. Both of these studies on rear-surface expansion used a laser to irradiate a small fraction of the target rear in order to induce expansion. Neither of these studies reported the clear divergence changes observed in our results, with only spectral changes reported. Another study by McKenna *et al.* [138] found that a small scale-length on the front surface enhanced the maximum proton energy, due to self-focusing of the laser pulse. However, for very long pre-plasma expansion, they found a reduction in energy due to filamentation of the laser pulse.

The study shown here presents a novel use for laser-driven proton beams - by using

them to diagnose the expansion dynamics of the target they are being accelerated from. Consistent measurements are made across the breadth of the parameters varied: flux of protons used to heat the materials, the target species used to generate the heating beam and the amount of heating experienced by the target. Radiation-hydrodynamic simulations are performed, with input beam parameters derived from those measured, to investigate the temperature and expansion of the Al target, with good agreement found over the time-scales studied.

The work is of relevance to PFI [16], which requires a beam energy of 10 - 30 kJ and proton energies in the range 3 - 20 MeV (assuming a Maxwellian spectral slope between 3-4 MeV) [139]. This spectra is typical for laser intensities $> 10^{19}$ W cm^{-2}. With typical laser-to-proton conversion efficiencies ($< 10\%$), the laser energy required would be in excess of 100 kJ, delivered in a few picoseconds, with a spot size of $> 200\,\mu$m [16, 18]. For these parameters, the hot electrons injected into the target by the leading edge of the pulse induces rear-surface expansion of the target [131], before the maximum proton accelerating field occurs just after the peak of the pulse [60]. This would negatively impact on the acceleration of ions. The expansion would peak in the central position of the sheath field and extend laterally, with expansion along the whole target rear expected.

In our experiment configuration, the diameter of the proton beam is roughly the same transverse size as the target; more accurately replicating a PFI scenario. A schematic of the set-up is shown in the following section (Fig. 6.1). This is advantageous when compared to the previous studies [131, 137], where (in the latter experiment) only a $50\,\mu$m spot was irradiated. This is an issue, as the size of the field is of the order of $60\,\mu$m [62] (FWHM) and the precise position the sheath field is generated cannot be accurately determined. The former issue results in the wings of the sheath field being unaffected, where most of the low energy protons are accelerated from (i.e. those relevant for PFI). It also results in most of the spatial characteristics remaining unchanged. It also relies on the laser spot precisely irradiating the position where the sheath field is generated, which is unlikely due to the difficulty in positioning both relative to one another. In our case, as the whole of the target rear is heated, more flexibility in the position of the heating proton beam relative to the sheath field is granted.

Plasma expansion [61] is difficult to observe directly, primarily due to geometric constraints. For single-image, long time-scales and high densities, optical techniques such

as shadowgraphy [140] and interferometry can provide length and density information. To gain insight into the expansion dynamics however, a time-resolved approach is required. The first direct observation of this expansion (using WDM gold and diamond), by heating using a quasi-monoenergetic aluminium ion source, was made by Bang *et al.* in 2015 [141]. In this study they visualised the expansion using an optical-streak camera, achieving a spatial resolution of $\sim$3 µm. The time-window in their study was on the order of nanoseconds, where they observe a near-linear expansion as a function of time. The dynamics relevant to ion acceleration are more sensitive, with a small plasma gradient causing evident changes in the beam of accelerated protons, allowing an accurate quantification of the degree of expansion to be obtained. This relies on absolute certainty of the ion source, which can be characterised by incorporating the suggestions outlined in section 6.7.1. By incorporating these changes, a higher spatial resolution can be achieved than in the previous study [141]. Additionally, we operate in an entirely different time-window (10 - 150 ps). At these times, the expansion dynamics change significantly. This dynamic process is the product of two things. Firstly, a non-linear scaling of the temperature as a function of time is expected. This is due to the additional energy deposited by the subsequently lower energy protons, by the broadband TNSA beam, as time progresses. Secondly, a non-uniform longitudinal (i.e. through the target) heating gradient induced by the high flux of low energy protons is expected.

Aside from acting as a diagnostic, rear-surface proton irradiation presents a new technique for the manipulation of not just the spectral make-up of the secondary accelerated proton beam, but also the angular distribution and spatial characteristics. Other studies have achieved this via complicated target geometries [17] for proton focusing, experimenting with different target compositions [142], changes to the laser beam profile [143] or using two pulses to create an elliptical proton beam [67]. Other studies introduced a controlled shock at the target front surface using the ASE preceding the main pulse, some time before the main pulse arrives [144]. This creates a curved density gradient on the rear surface, which is used to manipulate the spatial profile and directionality of the beam. In our arrangement, by inducing a long, even scale-length plasma on the target rear, the flux of the entire proton beam is evenly reduced. We also observe an increase in beam collimation, with the resulting beam being of much higher spatial quality, in addition to what appears to be a focused component in the

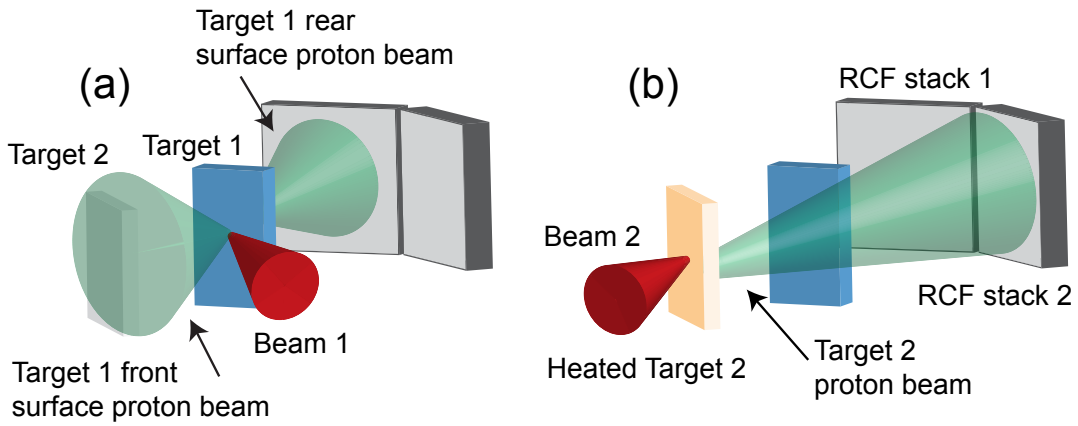

Figure 6.1: Schematic of the experiment set-up at two times. Target 1 is the proton driver used to heat Target 2. The spatial-intensity profiles of both rear-surface beams of accelerated protons are diagnosed using stacked dosimetry film (RCF) placed downstream from the two targets. At time (a) Beam 1 irradiates Target 1, and the accelerated front surface protons heat Target 2. At time (b), Beam 2 irradiates the now-heated Target 2, with the accelerated protons passing through the laser-heated Target 1 and measured downstream with RCF stack 2.

proton beam at low energies for certain expansion parameters.

6.2 Experiment set-up

The experiment was performed during the same campaign as the previous chapter, with the exact same laser parameters used. The experiment set-up used is shown in Fig. 6.1. For reference, Target 1 refers to the proton-driver target and Target 2 refers to the proton-heated target (the latter is the subject of this investigation). Two temporal phases are shown in Fig. 6.1, due to the complicated nature of the set-up. The targets were angled 45° to one another, with two RCF stacks used to characterise the rear-surface accelerated proton beams of both targets. Both diagnostic packs were placed 40 mm away from the two targets and angled perpendicular to their respective TN axes. At time (a), Beam 1 irradiates Target 1, incident at an angle of 20°. The accelerated front surface protons of Target 1 (which was characterised using a separate set-up) heats Target 2, over the duration of the proton bunch. The rear-surface proton beam of this initial interaction is measured downstream, to verify that a consistent beam of protons is produced shot-to-shot. This is used to determine that the front surface proton beam remains consistent. The maximum energy fluctuation of the rear-surface proton beam from Target 1 is minimal (ε_{max} = 10.6 – 12.7 MeV), as is the proton flux. As such,

it is inferred that the front surface proton beam profile does not significantly change shot-to-shot. At time (b), Beam 2 irradiates the now-heated Target 2, at an incidence angle of 40°. The accelerated protons travel through Target 1, and are measured with RCF stack 2.

Target 2 was a planar $\ell = 20\,\mu m$ Al foil. The species and thickness of Target 1 was varied for a separate scientific objective concerning proton stopping in WDM (detailed in section 6.1, with the modelling results shown in Appendix B). Two thickness' of Al were used for Target 1: $\ell = 10\,\mu m$ and $200\,\mu m$; and three thickness's of Si: $\ell = 2\,\mu m$, $30\,\mu m$ and $225\,\mu m$. Effects due to Target 1 are near-negligible, with detailed analytical modelling and 2-D PIC simulations performed to address this concern, detailed in section B. Any effects resulting from interactions of the protons with the Target 1 material are accounted for using dedicated reference shots, where Target 1 is present (for all species) with no Beam 1. Further information can be found in Appendix B detailing these effects in addition to any effects expected due to the Beam 1-Target 1 interaction.

The beam timing was characterised in the previous chapter using the inferred time-zero from Fig. 5.4. The time delay between Beam 1 and Beam 2, and therefore the degree of proton heating and target expansion time, could be optically adjusted with picosecond precision. The temporal separation was varied, by either increasing or decreasing the path length of Beam 2 by careful control of a translation stage, monitored using a Magnescale digital gauge with micrometer accuracy. The timing between the front-surface proton beam irradiating Target 2 and Beam 2 irradiating Target 2 was varied between 10 ps and 150 ps (known as the heating time, t_{heat}). A larger value of t_{heat} corresponds to a higher degree of target expansion, due to the higher number of incident protons (as a result of the time-of-flight spreading of the spectral components of the heating beam) in addition to the longer time the target is left to expand before laser-irradiation.

The separation between the two targets, L, was also varied, in order to investigate the effects of proton flux on target expansion. All values of L fell into two broad categories. In the 'small' L case, where the proton flux reaching Target 2 before it is irradiated by Beam 2 was highest, $L = (0.7 \pm 0.1)$ mm. In the 'large' L case, $L = (1.2 \pm 0.2)$ mm, corresponding to a lower proton flux and thus slower expansion speed.

In the following section, the front-surface proton heating beam is spectrally and spatially characterised.

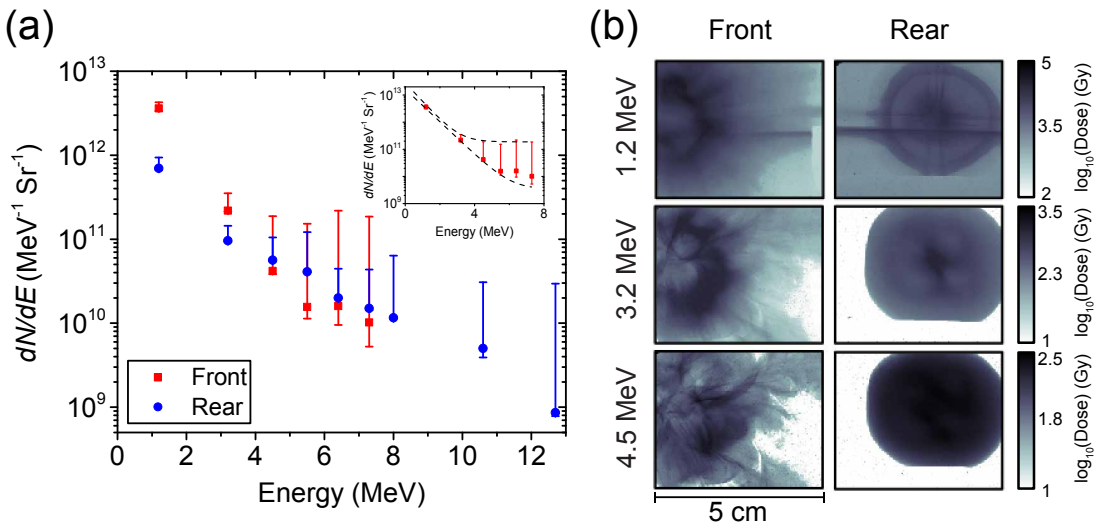

Figure 6.2: Characteristics of the heating proton beam. (a) Proton energy spectra of the front and rear surface proton beams accelerated from a 225 µm target (Target 2). Inset shows the exponential fit made to the error bars, which is where the energy inputs are derived from in the simulations. (b) Example RCF slices of the front surface beam (left column) and rear surface beam (right column), plotted in terms of dose. The same dose colour map applies to both RCF slices at the same proton energy.

6.3 Heating beam characterisation

A sheath-accelerated proton beam, used for the purposes of heating matter, has the favourable property of uniformly heating a target material over the course of tens of picoseconds. This is due to the broadband spectral nature of laser-driven ion beams coupled with the energy deposition profile of ions, resulting in a uniform energy deposition profile throughout the target when considering the mid-to-high energy spectral components (provided the target is thin enough such that the Bragg peak stopping regime is not encountered). In our experiment, all of the spectral components are considered. The target rear-side is heated with a low cut-off energy, high-flux proton beam, which results in a high temperature gradient (due to Bragg peak energy deposition) peaking near the target rear after the low energy protons have arrived. This induces a measurable change in the accelerated ion beam from the heated target.

In order to determine the heating profile induced in the Target 2 Al foil, the front surface proton beam used to heat the foil was characterised and the time-of-flight of each spectral component calculated. Figure 6.2a displays the spectra (sampled over the whole proton beam measured) of both the rear and front surface beam of protons accelerated from an $\ell = 225\,\mu$m Si Target 1, as a function of proton energy. The error

bars are defined by the level of uncertainty in the calibration of the RCF. These are large at higher proton energies as a low sensitivity RCF type (HDV2) was used throughout the entire stack, when normally a more sensitive type would be used for the low flux (high energy) spectral components. Figure 6.2b displays some example RCF layers of both proton beams, plotted in terms of dose on a logarithmic axis. Note that the RCF stack was positioned 6 cm downstream for the front surface beam and 4 cm downstream for the rear surface beam. The parameters of the front surface beam were used as inputs for the HELIOS simulations, with the results detailed in section 6.5. From previous measurements [145] on the same laser system, the energy spectra follows an exponential trend, down to a minimum energy $\varepsilon_{min} = 0.5$ MeV. This is typical of a TNSA proton beam. In order to replicate the experimental parameters, simulations were performed with ε_{min} set to this value in addition to the lowest measured cut-off energy $\varepsilon_{min} = 1$ MeV. Protons with $\varepsilon_p < 0.5$ MeV are far less numerous in the previous measurement made, and do not follow the exponential fit, so are not included in the calculations. Additionally, for most of the temporal scan, they do not play a role due to their late time of arrival at Target 2. Note that the spatial profile of the beam is not uniform, and instead appears annular at lower energies. The diameter the high-density ring would have on-target is ∼300 µm (assuming a separation between the two targets equal to 1 mm).

The time of arrival, t, of each spectral component, relative to the time of arrival of the maximum energy component, is shown in Fig. 6.3. The black vertical axis displays t, for each spectral component, as a function of proton energy for both values of L. Time t is equivalent to the heating time, t_{heat} (i.e. the amount of time the target has been left to expand, relative to the arrival of the first, high energy, protons).

The spectral cut-off (ε_{max}) of the rear-surface beam is roughly twice as high as the front surface beam; however, crucially, the number of protons with $\varepsilon_p < 4$ MeV is much higher in the front-surface proton beam. A high flux of low energy protons is useful for proton heating a thin foil target, which is apparent with reference to the red vertical axis of Fig. 6.3, which displays the fraction of energy remaining for each spectral component as it exits Target 2. This was calculated from the Bethe-Bloch cold stopping formula [133, 134] (see Appendix B for similar calculations). A $\ell = 28$ µm Al target was modelled in the stopping calculations, with the additional 8 µm due to the 45° angle between the two targets. From Fig. 6.3, it is clear why a high-flux low

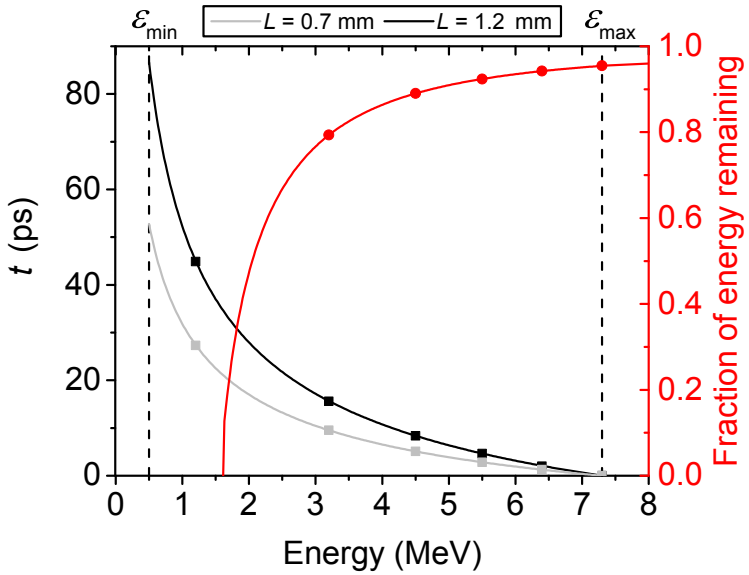

Figure 6.3: Time of arrival, t, as a function of proton energy of Target 1's front surface proton beam, relative to the spectral cut-off (ε_{max}), for both propagation distances, L. $\varepsilon_{min} = 0.5$ MeV is shown, which is the lowest energy component used in the simulations. The red vertical axis plots the fractional energy remaining in the beam of each spectral component after passing through Target 2. Zero indicates the proton stops in the material. The data points correspond to the spectral components measured experimentally.

cut-off proton beam would be useful for heating thin target foils to high temperatures. By way of example, protons with $\varepsilon_p = 2$ MeV will lose roughly half of their energy in Target 2. Protons of this energy will contribute to target heating far more than protons with, say, $\varepsilon_p = 5$ MeV, losing $< 10\%$ of their energy. With the additional consideration that there are $\sim 10^2$ more 2 MeV protons compared to 5 MeV protons, the amount of energy contributing to target heating by the lower energy protons is especially prominent. When comparing the front and rear surface spectra from Fig. 6.2, the higher flux of $\varepsilon_p < 4$ MeV (factor of three at 3.5 MeV; factor of ten at 1.2 MeV) results in the front surface beam having more desirable properties for proton heating of a $\ell = 28\,\mu$m Al target.

In the following section, the key experimental results are shown from the heating of Target 2 by the front surface proton beam characterised here.

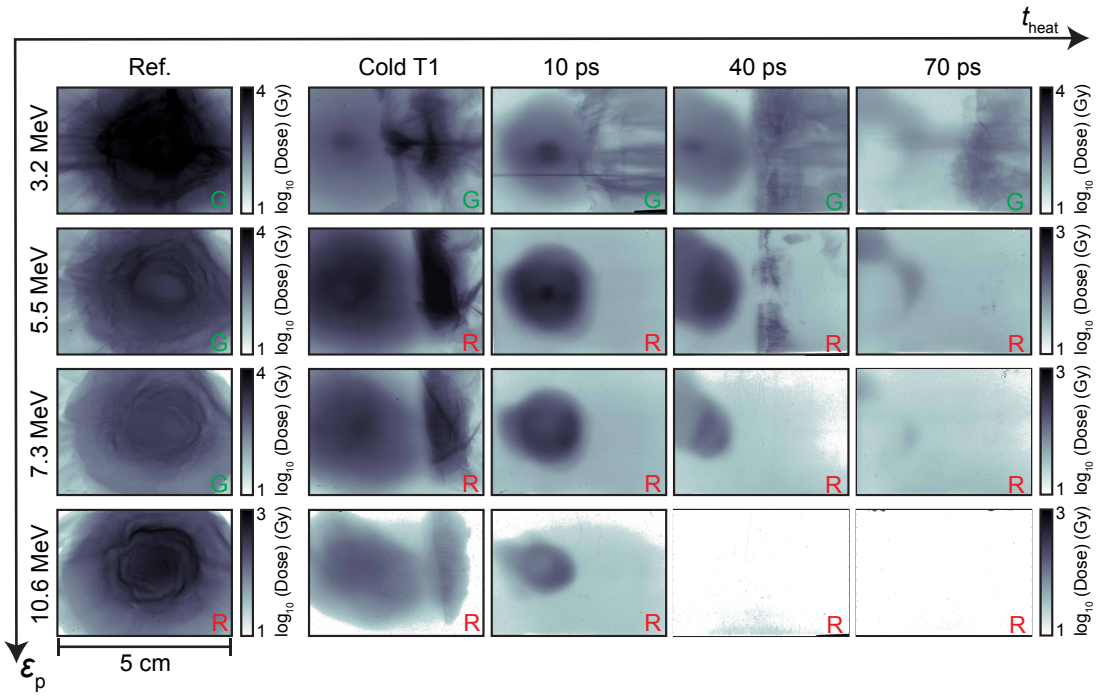

Figure 6.4: Dosimetry film matrix from several laser-shots showing the effects that an increased amount of target heating (t_{heat} increasing from left to right) has on the resulting proton beam. Three example times, along with a beam reference and cold target example, are shown, each with several spectral components (increasing proton energy, ε_p, from top to bottom). The colour channel analysed is indicated on the bottom right of each image (R = red; G = green).

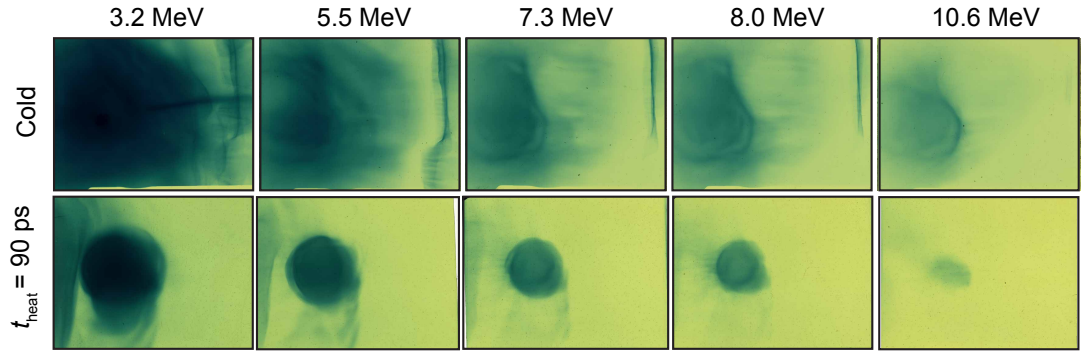

Figure 6.5: Raw dosimetry film (RCF) measurements of the proton beam for a cold (top row) and a heated (t_{heat} = 90 ps, target separation = 1.3 mm) Target 2.

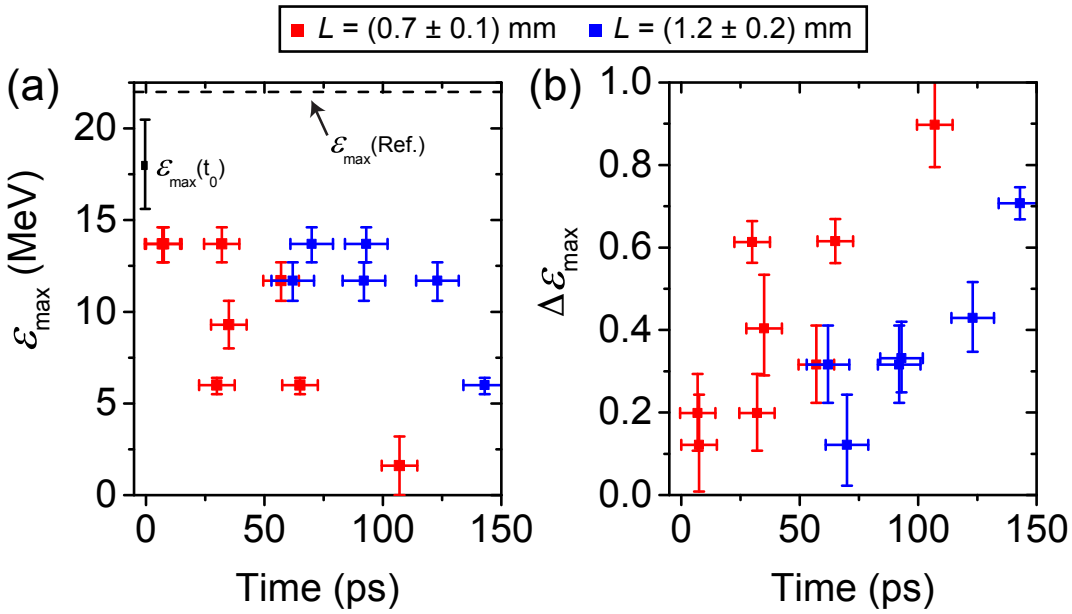

Figure 6.6: (a) Variation of the maximum proton energy, ε_{max}, as a function of heating time, t_{heat}, for both values of target separation L. The dashed black line refers to the ε_{max} of the reference beam, while $\varepsilon_{max}(\mathrm{t_0})$ represents the maximum proton energies recorded in the cold Target 1 cases. (b) Energy lost, as a fraction of initial energy with reference to each $\varepsilon_{max}(\mathrm{t_0})$. A value of one corresponds to no proton signal.

6.4 Experimental results

Several example proton beam profiles are shown in Fig. 6.4, for the high-flux configuration $L = (0.7 \pm 0.1)$ mm. Multiple t_{heat} are shown, along with measurements of the reference beam (i.e. no Target 1) and cold Target 1 (i.e. Target 1 in place; without Beam 1). The four example measurements with Target 1 in place are for the same Target 1: Si, $\ell = 225\,\mu$m. The individual RCF images are presented in terms of dose, with a darker colour corresponding to a higher flux of protons. Note that the colour scale is on a logarithmic axis. Depending on the level of signal measured on the individual RCF slices, either the red or green colour channel is analysed (a high proton signal will saturate the red channel, but not necessarily the green channel). Most of the reference slices are plotted on a different scale than the other measurements (as indicated) due to the relatively high proton flux measured. Each of the separate energy bins, excluding the reference images, are shown with the same scale.

Several clear effects are observed for an increased t_{heat}: (i) the maximum proton energy, ε_{max}, decreases; (ii) the overall proton number decreases, and; (iii) the angular divergence, $\theta_{1/2}$, decreases. An additional RCF example is shown in Fig. 6.5, for an ℓ

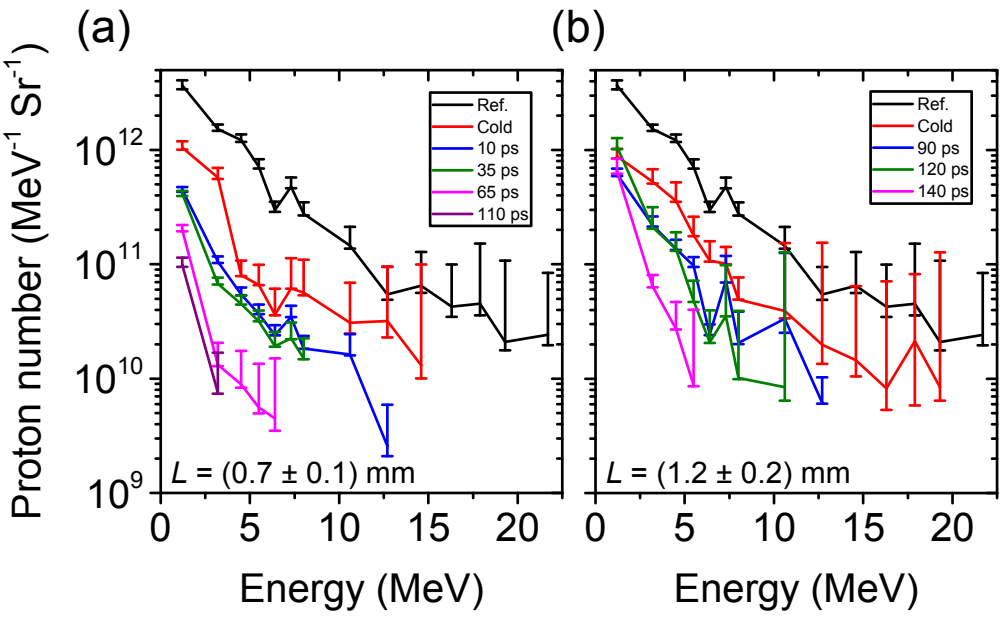

Figure 6.7: Example proton energy spectra, as deconvolved from the RCF measurements, for several heating times along with the reference and cold data. The target separation is equal to: (a) $L = (0.7 \pm 0.1)$ mm and (b) $L = (1.2 \pm 0.2)$ mm.

= 10 nm Al Target 1 and $L \sim 1.3$ mm, which exhibits all of these effects; in particular the increased beam collimation.

Figure 6.6a displays ε_{max} as a function of t_{heat}, for both values of L. The error bars in the energy measurement are a result of the spectral resolution of the detector; the lower error bars correspond to the layer where a strong proton signal is measured, while the upper error is the next layer in the stack configuration, where no proton signal was measured. The boundaries for the cold reference data point (black square) are the maximum and minimum measured ε_{max} for all of the target species. There is variation in this, due to additional stopping in a thick target compared to a thin one. This is examined in depth in Appendix B. Figure 6.6b, shows the amount of energy lost relative to the cold reference of each target species ($\Delta\varepsilon_{max}$), as a function of t_{heat}. This allows each data point to be readily compared. From Fig. 6.6 it is clear there is a strong dependence on both t_{heat} and the flux of protons heating the target, with an increasing amount of target heating and flux of protons resulting in a reduced maximum proton energy.

Representative proton energy spectra for both values of L, sampled over the entire proton beam measured, are shown in Fig. 6.7 for multiple heating times. A Si Target 1 was used for all of the data shown. $\ell = 225\,\mu$m for $L = (0.7 \pm 0.1)$ mm, and $\ell = 30\,\mu$m

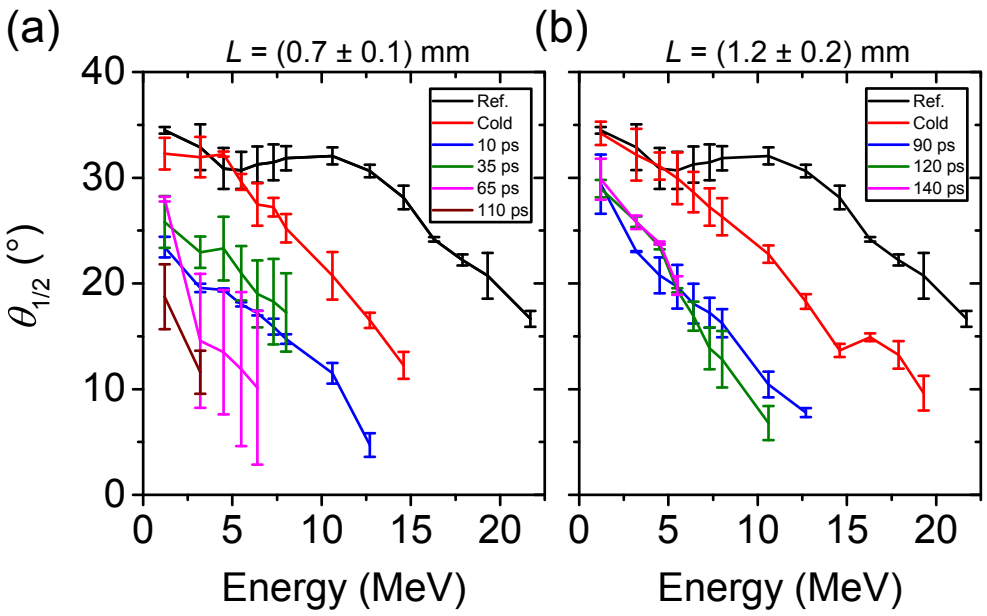

Figure 6.8: Measured divergence half-angle, $\theta_{1/2}$, as a function of proton energy, for several heating times along with the reference and cold data. The target separation is (a) $L = (0.7 \pm 0.1)$ mm and (b) $L = (1.2 \pm 0.2)$ mm.

for $L = (1.2 \pm 0.2)$ mm. The vertical error bars are defined by the level of uncertainty in the calibration of the RCF, described in detail in Chapter 3. A clear reduction in the overall proton number is observed for a higher degree of target expansion, and not simply a reduction in ε_{max} alone. It should be noted that while the difference in energy loss due to the proton stopping in the thicker material is low for most of the spectral components, $\varepsilon_p < 4$ MeV will be affected. As such, the laser-to-proton conversion efficiency is not shown, as a high percentage of the laser energy is eventually coupled to this energy band. This stopping is described in more detail in Appendix B.

Measurements of the divergence half-angle, $\theta_{1/2}$, as calculated from the RCF are shown in Fig. 6.8 as a function of t_{heat}, for both values of L. The Target 2 species used in (a) was $\ell = 225\,\mu$m Si and in (b) $\ell = 30\,\mu$m Si (corresponding spectral information shown in Fig. 6.7). The error bars in the $\theta_{1/2}$ measurement arise due to the proton beam having some degree of ellipticity. The lower and upper error bars correspond to the radius of the minor and major axes of the ellipse, respectively. For a greater t_{heat}, in general the beam becomes more elliptical. This may be due to the lateral temperature gradient, discussed in section 6.7.1. Again, from the data shown, a clear reduction is observed.

In order to experimentally verify that the general decrease in heating changes

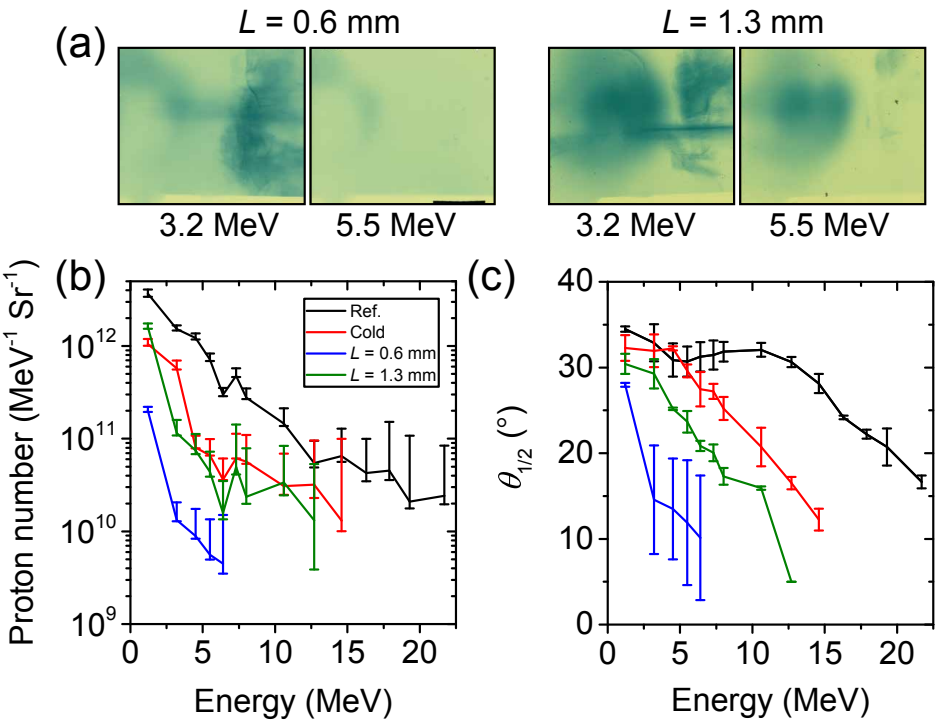

Figure 6.9: Comparing the same parameters for two target separations, L. The heating time for both sets of measurements is 70 ps and the Target 1 species is 225 µm-thick Si. (a) Example raw dosimetry film layers. (b) Proton energy spectra and (c) divergence half-angle, $\theta_{1/2}$ for the reference, cold, $L = 0.6$ mm and $L = 1.3$ mm proton beams. The key is the same in (b) and (c).

depending on the value of L, excluding stopping/scattering effects in Target 1, a comparison is made for two different values of L for the same $t_{heat} = (70 \pm 5$ ps) and Target 1 (Si, $\ell = 225\,\mu$m). This is shown in Fig. 6.9, where (a) displays the raw RCF data; (b) proton energy spectra and (c) $\theta_{1/2}$, as a function of ε_p. There is clearly a decrease in signal and divergence in both L cases compared to the cold reference, with the effects appearing to progress far slower in the $L = 1.3$ mm case. This implies that the target is expanding at a slower rate in the latter case, verifying that it is a flux effect.

For some of the $L = 0.7$ mm, $t_{heat} < 40$ ps data-set, a high-density spot appears at low energies. Figure 6.10 shows raw RCF images of this spot for two values of t_{heat}. For large target separations or long heating times the spot disappears. The possible cause of this is discussed in the following section.

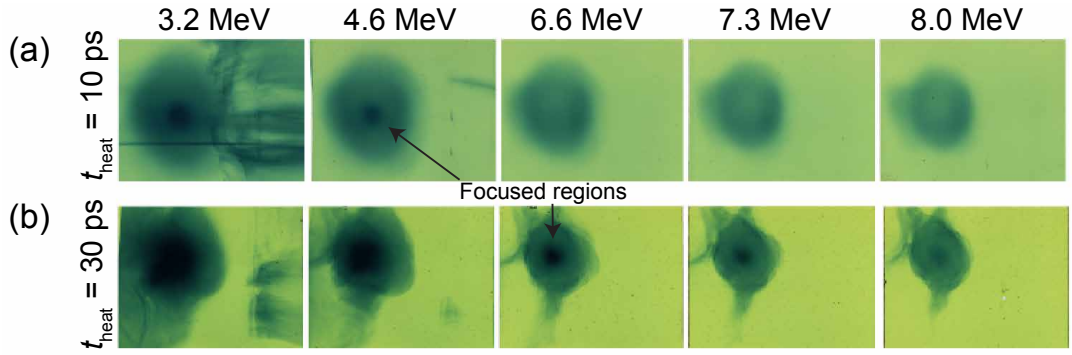

Figure 6.10: Raw dosimetry film measurements of the proton beam for two heating times (t_{heat}) equal to (a) 10 ps and (b) 30 ps. For both, the target separation $L \sim 0.7$ mm. The Target 1 (i.e. proton driver) targets are, respectively, $\ell = 200\,\mu$m and $\ell = 2\,\mu$m Si.

6.4.1 Experimental discussion

Efficient ion acceleration depends on a high hot electron temperature and, initially, a short ion density scale length at the back of the target [56]. To a first order, the measured spectral changes are expected for an increasing t_{heat}, due to the increase in plasma scale-length. As the heating protons deposit energy, the electrons are first heated. These heated electrons transfer energy to the lattice ions (via electron-phonon interactions) while the target remains at solid density [146]. This results in hydrodynamic expansion. Figure 6.11 schematically illustrates the framework of the model where an expanded target would result in a lower energy, more collimated proton beam. As the target expands, the hydrocarbon contaminant layer is brought closer to the maximum extent of the electrostatic sheath field, X_{max}. X_{max} is the maximum extent of the fast electron separation from the target and therefore the maximum longitudinal extent of the field. The hydrocarbon contaminant layer for the heated cases is represented by the dashed horizontal lines. It is assumed the point of X_{max} (derived and calculated in section 6.6) remains fixed relative to the target, with this position based on the laser drive parameters and target absorption, which are assumed to be constant over the heating times investigated. Significant hydrodynamic expansion of the front surface (relative to Beam 2) of Target 2 is not expected, due to the heating predominantly occurring on the target rear-side. A temperature map calculated from the simulations in the following section, shown in Fig. 6.13, illustrates this.

When considering the maximum proton energy, the position that the fast electrons reach at the centre of the sheath field, relative to the solid target, is assumed fixed (at

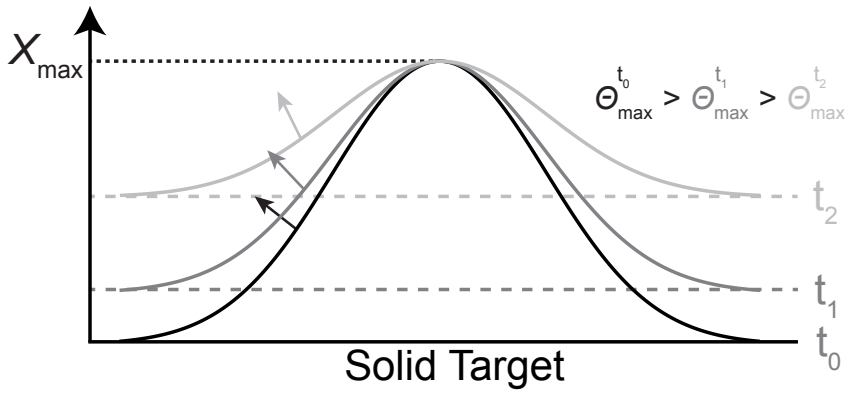

Figure 6.11: Schematic of a simple model showing the expansion of the electrostatic sheath field into vacuum, illustrating how an expanded target results in a reduction in the amount of energy in the proton beam, and also produces a more collimated beam. Arrows indicate the maximum divergence, θ_{max}, of the proton beam for each scenario. Three scenarios are shown: cold (i.e. no expansion, t_0), heated; early in time (t_1) and heated; later in time (t_2). The black/grey lines indicate the extent of the plasma

the point X_{max}). In reality, this is not the case, with the electrons reaching a further distance due to the plasma density allowing a return current to be drawn, up to a density approximately equal to the critical density. This assumption is made here to simplify the modelling and calculations regarding the maximum proton energy.

The protons accelerated from a more heated target therefore traverse a smaller region of the electrostatic field, resulting in a proton beam with a lower spectral cut-off energy. Additionally, the total energy contained within the beam will be less, due to the decreased length over which the protons are accelerated.

Under the assumptions of this model, a more collimated beam would result from an increasingly heated target, due to the lower gradient in the electric field (indicated by the arrows in Fig. 6.11). This is observed experimentally, and is the first experimental observation of an increase in beam collimation due to rear-surface expansion - likely resulting from the larger heating area than used in previous studies [131, 137].

It should be noted that in reality, the temperature gradient will not be symmetrical. This would lead to a non-symmetrical sheath field along the longitudinal (target-normal) axis, which would manifest in a non-symmetrical/elliptical proton beam. A beam profile of this description can be seen for later times, as shown in Fig. 6.4. The modelling of this heating gradient, based on both the target angle and non-uniformity in the heating proton beam, and it's implications on the experimental results, is discussed in section

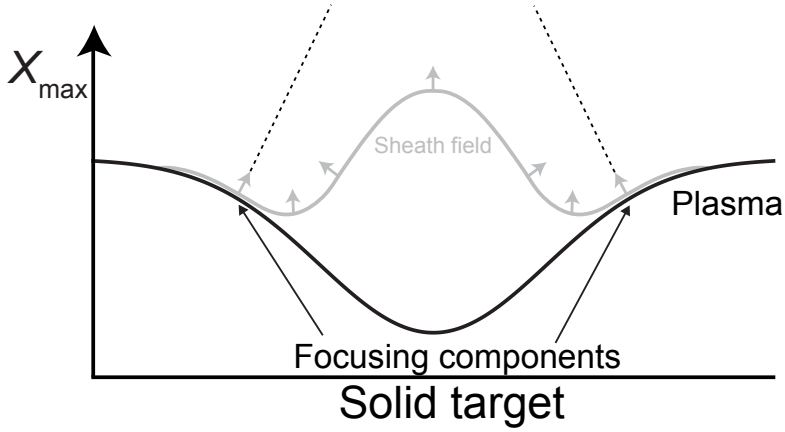

Figure 6.12: Schematic showing the expansion of the electrostatic sheath field into vacuum, with expansion induced by an annular proton beam. The edges of the target, relative to the peak sheath field position, are heated to a greater degree than the centre. This results in the generation of a sheath field with focusing components. The positions marked 'focusing components' are the positions of the sheath field where the protons that appear focused on the diagnostic plane are accelerated from. The black line indicates the extend of the expanded plasma and the grey line the position of the sheath field.

6.7.1.

As commented on in the previous section, the front surface heating beam has an annular density distribution. At early times, this would result in a greater degree of heating and thus expansion off-axis from the central point of the sheath field. Figure 6.12 displays a schematic of how the plasma spatial profile may evolve due to an annular proton beam. As a result of the transverse density gradient, reaching a minimum in the centre relative to the position of X_{max}, the wings of the sheath field act to focus some of the low-energy protons. This may explain the prominent dot that appears in the RCF shown in Fig. 6.10. The apparent focused component only appears for targets with $L \sim 0.7$ mm, suggesting that for a larger target separation such a gradient over the transverse extent of the sheath field does not exist. This may be due to the fact that the ring would be larger on the surface of the targets in the large L cases. Additionally, for long heating times, the focused component disappears. Given more time to expand, the plasma gradient is expected to become more uniform due to lateral diffusion, resulting in a smooth plasma gradient. This would lead to a lower divergence, smoother proton beam, as seen in Fig. 6.5.

The effects due to the Target 2 radiation affecting Target 1 are not discussed in the analytical model (before the transit of the protons from Target 1 through Target

2). From Fig. 6.4, a structure in the beam profile is observed in the cold case that is likely due to the charging of Target 1, up to ε_{max}. This is also present for heated targets, albeit to a lesser extent. As the field structure is observed in the highest energy components of the generated beam from Target 2, it is likely this effect involves the fast electrons that precede these protons. They may act to charge Target 1, and deflect some of the protons from Target 2 such that they appear on one side of the RCF stack. This effect was clear in the previous chapter, where a wire outline is observed due to the probe proton beam being deflected by the charged wire. The effect is more prominent at low energies, which may be a combination of both the slower protons being more susceptible to the electric fields, in addition to the further charging experienced by Target 1, by the preceding protons and accompanying electrons. The effect is far less noticeable in the heated cases, in particular for a large value of t_{heat}, where it entirely disappears (such as in the heated case of Fig. 6.5). Two effects may be responsible for this. Either the fast electrons from Target 2 are deflected away from Target 1, due to the (small) charging effect induced by the laser, or Target 1 does not hold charge as effectively in the heated case. The target resistivity decreases as it is heated [147], however this would act to leave the target more susceptible to charging, so would not cause this effect.

It is not just the proton structure that is modified. The value of $\Delta\varepsilon_{max}$ is greater than predicted from both SRIM modelling [94] and using the Bethe-Bloch approach outlined in Appendix B. The discrepancy is around several MeV. Due to the stability of the rear-surface measurements of Target 1, it is unlikely this is due to fluctuations in the laser-drive parameters. This further suggests that the Target 2 interaction affects Target 1, before the Target 2 protons arrive. This is accounted for by using the cold measurements (i.e. no Beam 1) as the reference, as opposed to the 'Ref.' measurements in Fig. 6.4 for which Target 1 is not present. The reason for this reduction in energy may be related to the electrical charging of Target 1 acting to reduce the impinging proton velocity.

In the following section, simulations were performed in order to characterise the heating profile expected from the measured front-surface accelerated proton beam (detailed in section 6.3), to provide insight into the underpinning physics.

6.5 Simulations

The 1-D Lagrandian radiation-hydrodynamic simulation code HELIOS-CR [110] was used to investigate the expansion dynamics of a heated target due to proton beam energy deposition within the material, with parameters derived from the characterised beam shown in section 6.3. Details of the code can be found in Chapter 3.

The intensity of the input proton beam was derived from the measured dose, shown in Fig. 6.2a. The intensity calculation takes into account the divergence of the beam, target separation, bunch duration and energy within the beam. HELIOS performs a linear interpolation between the tabulated data points, to increase the accuracy of the simulated beam. Two exponential fits were made to the data, corresponding to the upper and lower error bars in the dose measurement, with multiple tabulated values entered based on the calculated exponential fits. These are shown as dashed lines in the inset of Fig. 6.2a. For each parameter scan two sets of simulations were ran, corresponding to the upper and lower error bars of the measured dose. The obtained values delimit the expected target temperature. The numerical calculations include the time-of-flight spreading of the proton beam between the two targets, as shown in Fig. 6.3, for both values of L. Additionally, two values of ε_{min} were used: 0.5 MeV and 1 MeV, the latter is the lowest energy measured and the former is the lowest energy expected to contribute to target heating.

Three target types were simulated. The first target type was initialised as a 1-D slab of Al (at solid density and $\ell = 28\,\mu\text{m}$). The second was the same but with two $\ell = 10$ nm H layers on either side of the Al, in order to replicate the hydrocarbon contaminant layer expected under experimental conditions. Note that 100 nm H layers were also simulated, with little difference in expansion observed when compared to 10 nm layers. Also simulated was a $\ell = 28\,\mu\text{m}$ pure H target at solid density, to investigate any differences in the acceleration of hydrogen between pure H and the layered target. The resolution of the 28 µm targets was 2.8 µm, and for the 10 nm contaminant layers it was 2 nm. All targets were initialised with a starting temperature of 0.025 eV (i.e. room temperature), and the simulations were performed in 10 fs time-steps.

Figure 6.13 displays the temperature profile of layered Al targets (the main subject of this investigation), showing several values of t_{heat} for both values of L and the two values of ε_{min}. In each graph the final time is shown, where no additional heating is

induced. Note that on the time-scales studied cooling of the target is negligible, with little change observed in the temperature profile for any time after the lowest energy protons have arrived. The lines delimiting the shaded region are determined from the uncertainties in the measured proton energy spectra, as stated previously. As discussed in section 6.4.1, when radiation deposits energy in a material, the material's electrons are first heated, and transfer energy to the lattice ions mediated by electron-phonon interactions. Considering the $L = 1.2$ mm cases, at early times ($t_{heat} = 20$ ps), protons with $\varepsilon_p > 3$ MeV have began to heat the material. Due to the relatively high energy of these protons, they deposit their energy quasi-uniformly throughout the target, losing < 30 % of their energy (as seen in Fig. 6.3). At $t_{heat} = 40$ ps, protons with energy down to 1.5 MeV have arrived, which quasi-uniformly heat the first 20 µm of the target (relative to the incoming proton beam) before losing a slightly higher fraction of their energy (per µm) at the target rear. This is because they are approaching the Bragg-peak regime of energy loss. For $t_{heat} = 80$ ps, all of the protons have arrived, which drives a sharp temperature gradient near the front of the target. For reference, protons with energy $\varepsilon_p = 0.5$ MeV will fully stop at ~ 7 µm.

Comparing the simulation results for both values of L, a vastly different temperature profile is observed, with a factor of ~ 2 higher for the smaller L case. This is a result of the higher flux of protons leading to a higher degree of target heating. Comparing the two values of ε_{min}, again a factor of ~ 2 difference is observed between the two cases. A value of $\varepsilon_{min} = 0.5$ MeV is believed to be more realistic in the experiment because, as stated previously, previous measurements on the same laser system [145] measured a high number of protons at a minimum energy of around $\varepsilon_p = 0.5$ MeV. In all cases, far more expansion is observed at the target rear (where the protons are first incident) compared to the target front, relative to the Beam 2 interaction, particularly when considering protons with energies down to $\varepsilon_{min} = 0.5$ MeV.

In the experiment, heating from the laser-irradiated side would result in a low temperature on the rear-surface (where the sheath field is generated), which in the scope of the experimental errors may result in little-to-no observable change in the proton beam. Additionally, heating from the front surface would heat the front of the target far more, potentially changing target absorption when the interaction pulse is incident [148]. Therefore, in our configuration, rear-side heating is advantageous.

In order to verify that reliable expansion velocities were calculated in HELIOS, the

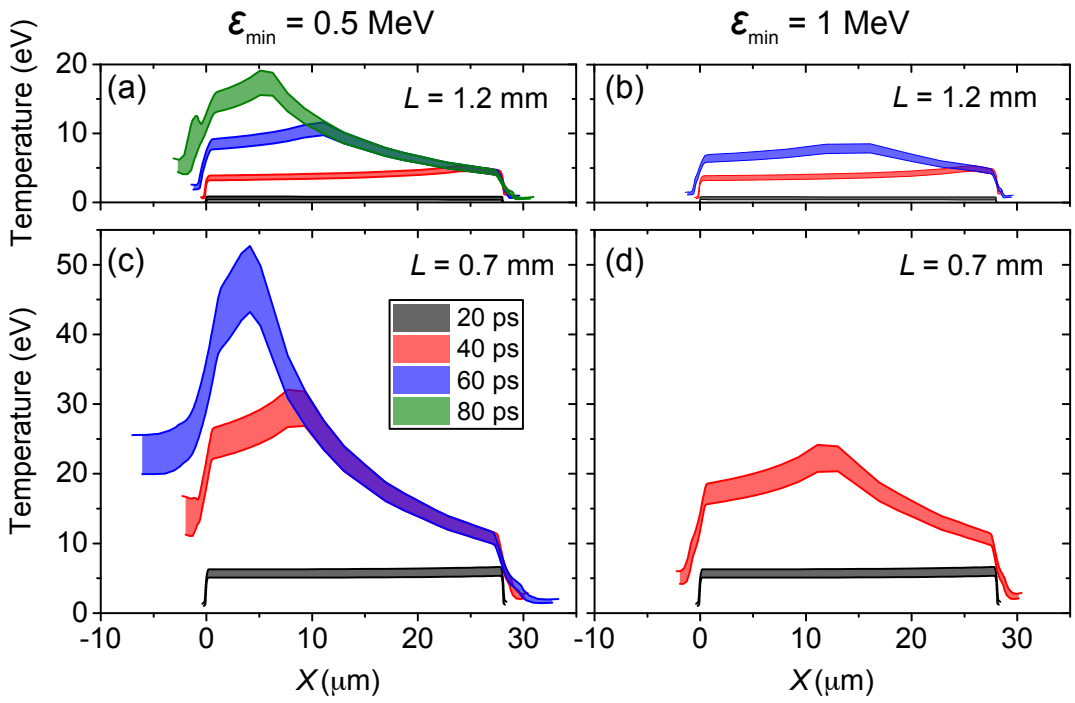

Figure 6.13: Temperature profiles simulated using HELIOS, using the parameters of the measured front surface proton beam used to heat Target 2. The two separate configurations corresponding to target separations $L = 1.2$ mm (a-b) and $L = 0.7$ mm (c-d) are shown, for several stated heating times. Results from the two values of the lower energy bound, ε_{min}, are given for both values of L. The boundaries of the shaded regions correspond to the upper and lower error bars in the proton energy spectra. $X = 0$ indicates the rear surface of the target, with the proton beam initially incident at this point.

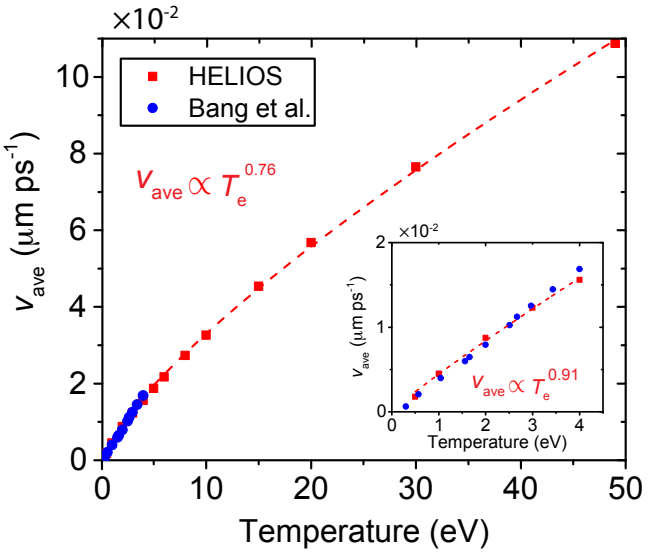

Figure 6.14: Benchmarking expansion velocity of a hot plasma in HELIOS as a function of initial carbon plasma temperature with results detailed in [141] using the 2-D RAGE code. The inset displays the region Bang *et al.* simulate. The HELIOS results are averaged over the first 0.5 ns, and show excellent agreement with the results from Bang *et al.*

results were compared to those found in Bang *et al.* [141], which were obtained using the 2-D radiation-hydrodynamics code RAGE [149]. The results of this comparison are shown in Fig. 6.14, where the average expansion velocity, v_{ave}, is shown as a function of initial plasma temperature. In both cases, the targets were initialised as a uniform slab of C with various starting electron temperatures. For the HELIOS simulations, the targets were left to expand for 0.5 ns before an average velocity was calculated at this time. The inset shows the temperature region Bang *et al.* investigate, with excellent agreement found. Additional higher temperatures were ran in HELIOS, up to the values expected experimentally. The dependence of the average velocity changes as a function of the initial plasma temperature, and takes the form:

$$v_{ave} \propto \begin{cases} T_e^{0.92} & T_e < 5 \text{ eV} \\ T_e^{0.76} & 5 \text{ eV} \leq T_e < 50 \text{ eV}. \end{cases} \tag{6.1}$$

This is contrary to the statement in Bang *et al.* [150], where they state that the average expansion speed increases almost linearly with temperature. They also state that the common belief of it being proportional to $\sqrt{T_e}$ is incorrect. In the temperature range they studied this is true, however we find that as the temperature increases above

5 eV the scaling changes, and will approach $\sqrt{T_e}$ for much higher temperatures. This is expected for a plasma in equilibrium, as the thermal velocity in 1-D (i.e. in any single direction) is related to the electron temperature through: $v_{th} = \sqrt{k_B T_e / m_e}$

Figure 6.15a displays an example velocity-time plot from the Al/layered-Al simulations, showing the maximum velocity (v_{max}) as a function of t_{heat} for $L = 1.2$ mm and $\varepsilon_{min} = 0.5$ MeV. These are the parameters most likely to represent the low-flux configuration well. The input beam energy is taken as the upper boundary delimiting the dose, shown in Fig. 6.2a. v_{max} corresponds to the velocity of the plasma at the furthest position away from the initial target rear ($X = 0$), which is taken as the point where the protons are accelerated from in the simple analytical model outlined in the previous section. The dashed lines correspond to the times in Figure 6.15b. The average expansion velocity, v_{ave}, is shown as a function of t_{heat} in the figure inset. Note that v_{ave} for the H target is higher than for the H-layered Al target, however v_{max} is slightly higher in the layered target case. The former difference is due to the Al atoms reaching a higher temperature than the H (likely due to the larger collisional-cross section of the nuclei), by a factor of ~ 2 in the simulations. The latter difference is due to the Al constituents coupling additional energy to the H atoms, before they separate from the Al. This acts to accelerate them to higher ($\sim 15\%$) velocities than in the pure H case. In all cases the Al has a lower velocity, which is due to their lower charge to mass ratio. This poses an interesting question regarding the possibility of heating matter to higher temperatures, using radiation, by layering targets such that the heavier species is behind the lighter (relative to the proton beam). The more readily heated heavy material would transfer additional energy to the lighter species, which would reach temperatures and expansion velocities in excess of those experienced by a pure target consisting only of the lighter material.

The electron density as a function of distance from the target is shown in Fig 6.15b, for the same simulation as shown in the layered case of Fig. 6.15a. The maximum distance that the plasma extends to is taken as the final expansion distance.

In the following section, the reduction in maximum proton energy measured experimentally is used to calculate the plasma expansion distance, and is compared to that determined from the simulations for the measured heating beam parameters.

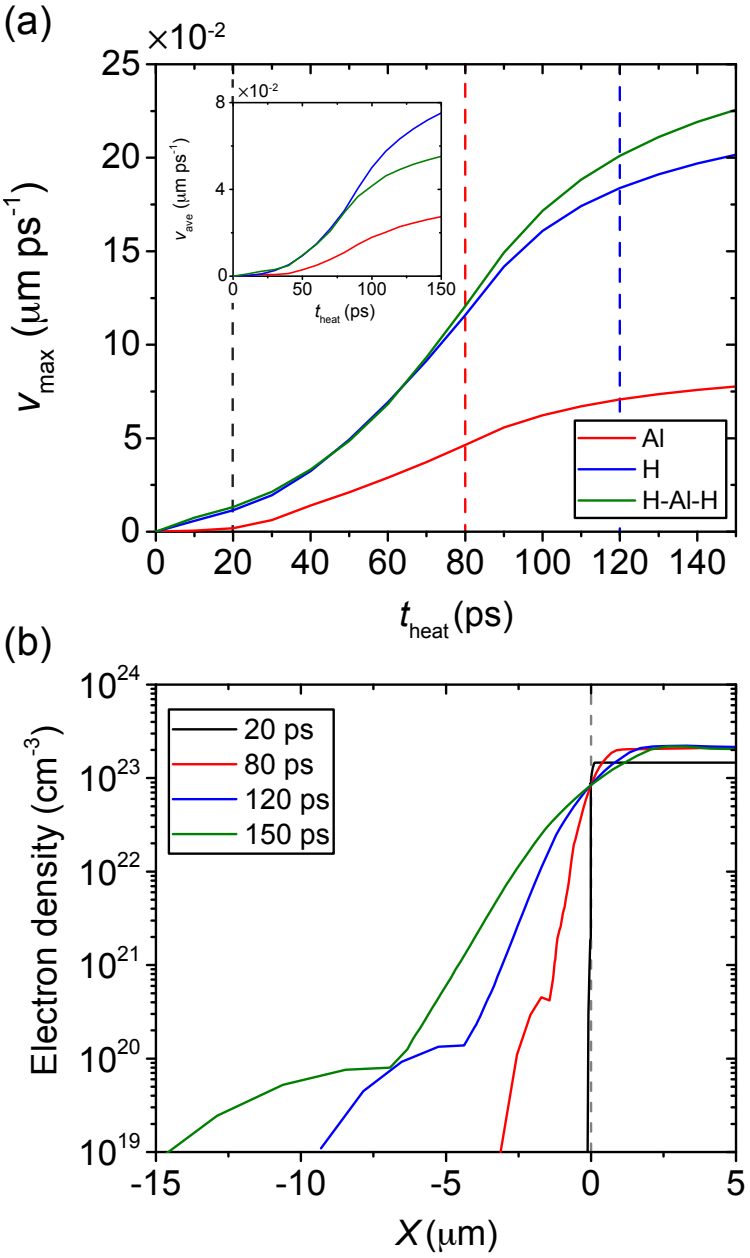

Figure 6.15: (a) Maximum velocity, v_{max}, as a function of heating time (t_{heat}) for an Al target of thickness $\ell = 28$ µm (red), $\ell = 28$ µm H target (blue) and an $\ell = 28$ µm Al target with 10 nm H layers on either side (green). Inset displays the average velocity, v_{ave}, as a function of t_{heat}. The dashed lines correspond to the times shown in: (b) Electron density at several t_{heat} for the mixed target as a function of distance from the target rear (dashed grey line is the position of the target rear, $X = 0$). The incident proton beam comes from LHS of the figure. For both graphs, the results are from the simulations with a target separation of 1.2 mm and a minimum incident proton energy of 0.5 MeV.

6.6 Comparisons between experiment and simulations

In the framework of the analytical model used to describe the decrease in maximum proton energy, described previously in section 6.4.1, the field strength is assumed constant over the acceleration length. The peak rear-surface electric field, due to the laser-drive parameters, is first calculated. Following Mora [61], a simple expression for the electric field is given by [151]

$$E_{max} = E_0\sqrt{2/e_N}, \tag{6.2}$$

where e_N is Euler's number and E_0 is

$$E_0 = \sqrt{\frac{n_{e0}k_BT_e}{\epsilon_0}}, \tag{6.3}$$

where k_B is Boltzmann's constant, ϵ_0 is the permittivity of free space, T_e is the electron temperature and n_{e0} is the initial fast electron number density, which can be approximated as:

$$n_{e0} = \frac{N_f}{Ac\tau_L}. \tag{6.4}$$

N_f is the number of fast electrons, A is the area of the sheath field, c is the speed of light (and thus assumed velocity of the relativistic fast electrons) and τ_L is the measured pulse duration (8 ps). A can be determined by assuming a laser spot size $\omega_L = 5\,\mu m$ and a divergence half-angle $\theta_{1/2} = 30°$ within the $\ell = 20\,\mu m$ target. The number of fast electrons N_f is estimated as:

$$N_f = \frac{\eta_{L\rightarrow e}E_L}{k_BT}, \tag{6.5}$$

where $\eta_{L\rightarrow e}$ is the laser-to-fast electron energy conversion efficiency and E_L is the laser pulse energy within the FWHM ($\sim$ 50 J). $\eta_{L\rightarrow e}$ was set to 30%, as inferred from bremsstrahlung spectrometer data on a similar laser system [152] (E_L =50 J, τ_L =1.5 ps, λ_L =1.054 µm). Substituting Equations 6.3, 6.4, 6.5 and 6.6 into Eq. 6.2 results in E_{max} being given by:

$$E_{max} = \sqrt{\frac{2}{ce\epsilon_0}}\sqrt{\frac{\eta_{L\rightarrow e}E_L}{A\tau_L}}. \tag{6.6}$$

For our laser-pulse parameters, $E_{max} \sim 0.9$ TV m^{-1}. With the electric field known, the acceleration of the protons, a_p, with mass m_p follows as:

$$a_p = q\frac{E_{max}}{m_p}. \tag{6.7}$$

The acceleration length of the cold target L_c is therefore given by

$$L_c = \frac{1}{2}a_p t_p^2, \tag{6.8}$$

where

$$t_p = \frac{v_p}{a_p} \tag{6.9}$$

is the time taken for the ions to reach the maximum velocity, v_p:

$$v_p = c\sqrt{1 - \left(\frac{\varepsilon_p}{m_p c^2} + 1\right)^{-2}}. \tag{6.10}$$

Assuming the accelerating field remains constant over the extent of the sheath field, an acceleration length L_c of between 16 µm and 21 µm is required to observe the maximum proton energies measured experimentally for the unperturbed targets. The length is weakly dependent on the Target 1 material, with the range based on the error bars in Fig. 6.6a (corresponding to 15.6 MeV and 20.5 MeV measurements of ε_{max}). As the target expands with increasing t_{heat}, the position of X_{max} remains the same, as it is based on the amount of energy absorbed by the target. This does not change drastically due to the low temperature at the target front-side, as seen in Fig. 6.13. The expanding rear-surface hydrogen layer, however, moves closer to this point. This effectively decreases the length over which the protons are accelerated, resulting in a lower ε_{max} for an increasingly expanded target.

By measuring the reduction in ε_{max}, the expanded length L_s is found simply by subtracting the acceleration length required for the ε_{max} of a heated target, L_h, from that of the cold target length L_c:

$$L_s = L_c - L_h, \tag{6.11}$$

L_h is computed the same way as L_c, with the only difference being in Eq. 6.10 where ε_p is reduced to the measured value shown in Fig. 6.6a. This method is effectively similar

to keeping the distance fixed and instead decreasing the electric field, E_0, by a factor of L_c/L_s.

Figure 6.16 displays the simulations results alongside the calculated L_s from the experimental data as a function of t_{heat}, for both values of the target separation L. Four graphs are shown corresponding to four different simulation results: Al and the H-Al-H targets, for both values of ε_{min}. In all cases, the H-layered Al target shows better agreement with the calculations, based on the experimental data, compared to the simple Al case. Figure 6.16d, showing the layered target with $\varepsilon_{min} = 0.5$ MeV, shows slightly better agreement than (c), where $\varepsilon_{min} = 1$ MeV. The difference at lower values of t_{heat} is small, due to the late arrival time of the lowest energy protons (as seen in Fig. 6.3). To absolutely determine whether (c) or (d) show better agreement, further data-points are required for the $L = 1.2$ mm case at $t_{heat} > 150$ ps, where the two trends would diverge more apparently. It is expected that protons of $\varepsilon_{min} \sim 0.5$ MeV will be contributing to the heating in the experiment (as discussed in section 6.3), however the absolute number of $\varepsilon_p < 1$ MeV is based on extrapolating the measured spectra in Fig. 6.2a. In future experiments this should be more accurately characterised. It is therefore likely that Fig. 6.16d provides the most accurate comparison between the experimental datasets and the HELIOS simulations.

After arrival of the lowest energy protons (55 ps for $L = 0.7$ mm; 90 ps for $L = 1.2$ mm), the expansion velocity should remain roughly constant. The expansion velocity, calculated for the experimental data points with t_{heat} above these values, is shown in Table 6.1 for both values of L. Results from the HELIOS simulations corresponding to $\varepsilon_{min} = 0.5$ MeV are also shown (results from Fig. 6.16d). It should be noted that, if considering the HELIOS simulations with $\varepsilon_{min} = 1$ MeV (i.e. Fig. 6.16), the experimental velocities show better agreement with the simulations. This is misleading for a number of reasons. Firstly, as the measured ε_{max} approaches zero, the accuracy of the expansion measurement reduces. Low energy protons are expected to be accelerated far from where the central point of the electrostatic sheath field is generated, due to lateral transport of the hot electrons [153, 154] in addition to the refluxing of electrons within the target [155]. This results in a space-charge field at radii larger than the lateral position of E_{max} (also where the highest concentration of heating is present), leading to the acceleration of ions. This field can be observed in the 2 ps time-frame in Fig. 5.2, Chapter 5. In this image, clear deflection of the probing protons can be seen

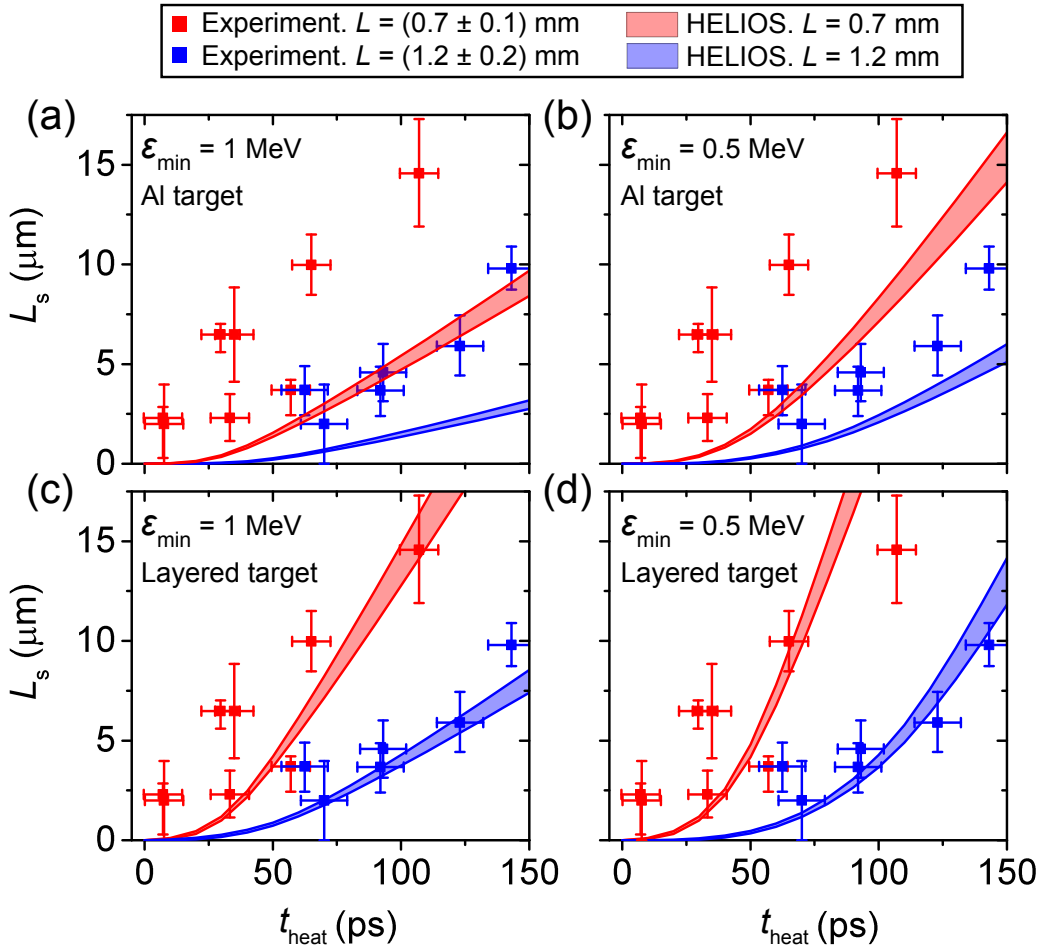

Figure 6.16: Plasma expansion length, L_s, as a function of heating time for the experimental data (squares) and simulations (shaded regions). (a) Al simulations with $\varepsilon_{min} = 1$ MeV; (b) same with $\varepsilon_{min} = 0.5$ MeV; (c) Mixed simulations with $\varepsilon_{min} = 1$ MeV; (d) Same with $\varepsilon_{min} = 0.5$ MeV. The vertical error bars in the experimental data points are a result of the uncertainty in determining the maximum proton energy. The horizontal error bars are uncertainty in the beam timing, which is a combination of uncertainty in target placement and the relative beam timings. The simulation boundaries are from the maximum and minimum dose used as inputs for the simulations, shown in Fig. 6.2.

	Velocity (µm ps^{-1})	
Separation (mm)	Experiment	HELIOS
0.7 ± 0.1	0.3 ± 0.1	0.42 ± 0.05
1.2 ± 0.2	0.11 ± 0.02	0.20 ± 0.02

Table 6.1: Calculated velocity of the expanding plasma from the experimental measurements and from simulations, for both target separations. The velocities are calculated from the data points after the lowest energy protons have arrived, where it should be a constant velocity.

$\sim$200 µm from the lateral position of E_{max}, implying a strong electric field is present. The expansion is assumed highest at the location of E_{max}, as this is the axial position from where the heating protons are generated. Outwith this region, a lesser-degree of heating will occur, resulting in less hydrodynamic expansion and a potentially longer accelerating gradient than where E_{max} is located - depending on the heating profile induced.

From the expansion length L_s calculated using HELIOS, the expected energy lost by ε_{max} can be found by rearranging Eq. 6.11. The simulations are shown along with the experimental measurements in Fig. 6.17. Good agreement is observed, particularly in Fig. 6.17b where the fractional energy lost is shown as a function of t_{heat}. This is a more accurate description of the energy loss as it takes into account the energy lost by the proton beam as it traverses Target 1. Detailed discussion regarding the effects of Target 1 can be found in section 6.4.1 and Appendix B. The boundaries delimiting the simulation curves take into account both the errors associated with the heating proton beam, in addition to the errors present in measuring the accelerated cold Target 2 beam.

6.7 Discussion

Here, future developments of the experimental technique, for improved accuracy as well as the possibility of diagnosing target temperature of heavy materials are discussed. An example of a more accurate simulation approach is also demonstrated. Further discussion of the implication of these results on PFI is presented, in addition to a discussion of proton focusing using expanded targets.

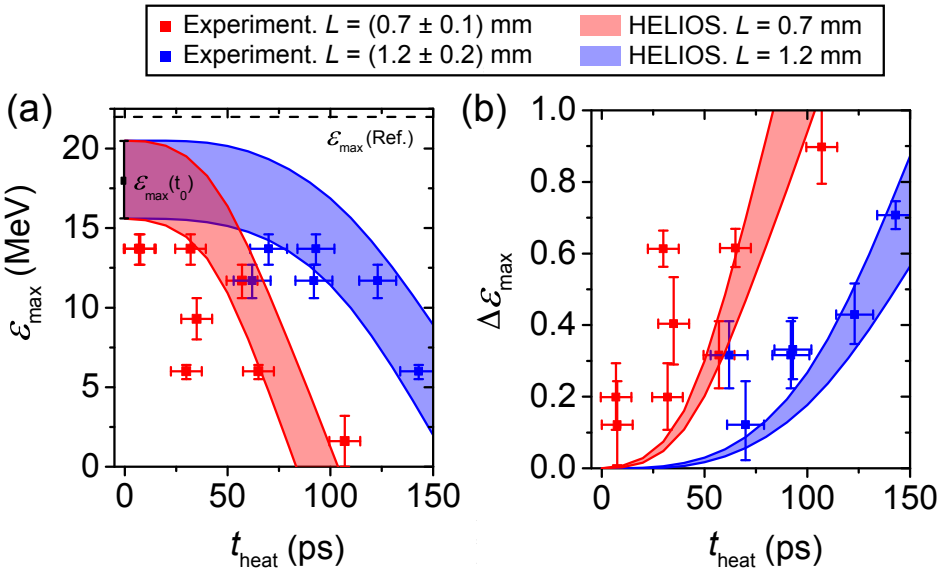

Figure 6.17: (a) Variation of the maximum proton energy, ε_{max}, as a function of heating time, t_{heat}, for both values of target separation L. Calculations based on the HELIOS simulations are also shown. The dashed black line refers to the ε_{max} of the reference beam, while $\varepsilon_{max}(t_0)$ represents the maximum proton energies measured in the cold Target 1 cases. (b) The energy lost, as a fraction of initial energy with reference to the corresponding $\varepsilon_{max}(t_0)$. A value of one corresponds to no proton signal.

6.7.1 Future developments

Experimental

There are several improvements that would increase the accuracy of the experimental measurements. Firstly, a characterisation of the cold proton beam (i.e. no Beam 2) for each laser shot would be extremely beneficial. This could be achieved by splitting the pulse using a double mirror system, such as in Aurand *et al.* [67], resulting in two spatially separate pulses. Care should be made to have both focused to precisely the same spot size, and a check made to verify that the same amount of energy is contained within each focal spot on a full-power shot. By using these two pulses to irradiate two identical targets, one of which is proton heated, and measuring the proton beam spatial distribution from both, a reference of the cold proton beam would be obtained for each shot.

This approach of diagnosing the expansion length could be extended beyond simply measuring the velocity of the protons originating on the target surfaces. By measuring the velocity of the heavy target ions (i.e. by using a Thomson Parabola spectrometer to determine the amount of energy lost by the heavy ions in the heated case), the

rate of expansion of the heavy ion front could be determined. Heavy materials could be investigated, and by incorporating the changes detailed in the previous paragraph, accurate measurements obtained. These measurements could be used to infer the temperature of the material with aid from radiation-hydrodynamic simulations.

Depending on the thickness and density of the material and the temperature gradient required, the incident proton beam parameters must be tuned. For example, a thick high-density target requiring an even temperature gradient would require a high energy beam, ideally with a small number of low energy protons, to uniformly heat the target. In the case studied here, we had the opposite (low maximum proton energy and a high flux of low energy protons); which resulted in a very high front surface temperature (relative to where the proton beam was incident). Other ion acceleration schemes, such as that proposed in the Chapter 4, could be used to further increase the range of applicability of this potential method for diagnosing target temperature, by using the high-energy beams measured to uniformly heat high-density targets.

Simulations

The 1-D dimensionality of the simulations is an issue, especially when considering spatial changes to the proton beam that are believed to be a consequence of the annular beam profile. As previously mentioned in section 6.7.1, the possibility of modelling a 2-D expansion profile is discussed with some preliminary attempts at this shown. This requires a 2-D temperature map, which can be generated in HELIOS by first sub-sampling the heating proton beam dose distribution, followed by running multiple 1-D simulations for each of these regions. An example of how to extract this information is shown in Fig. 6.18.

The beam in this example was accelerated from the rear-surface of an $\ell = 20\,\mu\text{m}$ Au target, with $L = 1.1$ mm. The size of the sampled regions were $1.7\,\text{mm} \times 1.7\,\text{mm}$, and were taken along the vertical 0° axis, from -16° to 16° (with respect to the target normal axis). The energy derived from each region was used as an input in HELIOS, with multiple heating profiles obtained for an $\ell = 200\,\mu\text{m}$ Si target for each region. Three example temperature profiles from three regions are shown in Fig. 6.19(a-c). A 2-D interpolation was performed on the nine outputs, converting the multiple 1-D profiles into a 2-D map. HELIOS does not take into account angular effects, so an

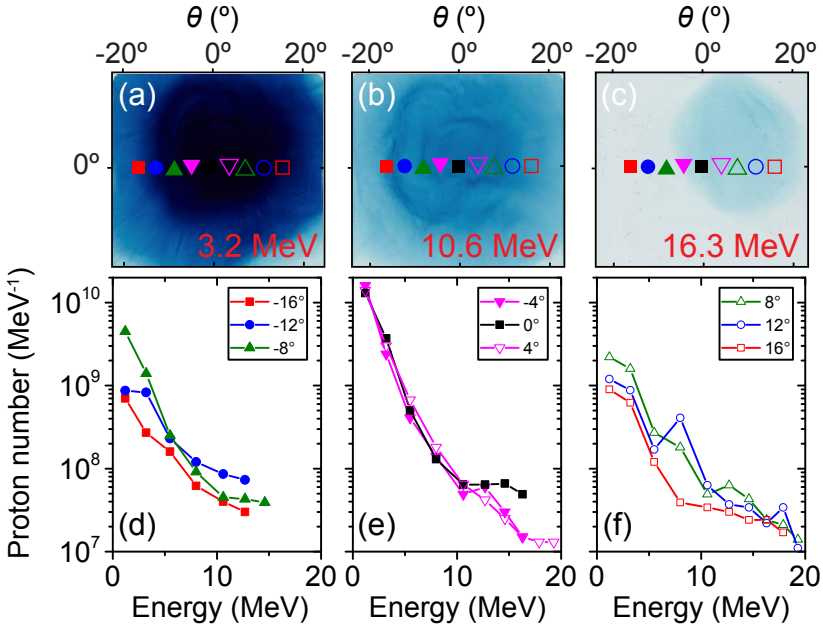

Figure 6.18: (a-c) Example dosimetry film (RCF) layers at stated proton energies that were sub-sampled, areas of which are indicated by the coloured shapes. (d-f) Proton energy spectra for each of the nine sub-sampled regions, split into three graphs for clarity. The symbols indicate the corresponding positions in the RCF images.

anti-clockwise rotational matrix calculation is performed:

$$\begin{pmatrix} \delta_r \\ T_r \end{pmatrix} = \begin{pmatrix} \cos(\theta(t)) & -\sin(\theta(t)) \\ \sin(\theta(t) & \cos(\theta(t)) \end{pmatrix} \begin{pmatrix} \delta \\ T \end{pmatrix} \tag{6.12}$$

such that each region is incident at the correct angle. δ_r represents the new depth position after rotation, T_r is the position of the corresponding temperature, θ is the angle of the proton beam with respect to the Si target normal (taking into account the proton beam divergence and the target angle of incidence), δ is the initial depth and T the initial temperature position (i.e. at normal incidence). The change in beam flux and temporal delay, due to the rotational angle, is also accounted for. An example of the resulting 2-D temperature maps are shown in Fig. 6.19(d-e).

The sharp temperature gradient along the transverse dimension, Y, demonstrates the importance of generating the sheath field at the intended position. By irradiating a position $\sim$100 µm away from where the peak temperature is located, the temperature drops by a factor of two. This suggests that accurate alignment of not only the laser focus but also the lateral position of the beam is crucial, and most likely attributes to the lack of agreement between some of the experimental data points and those calculated in

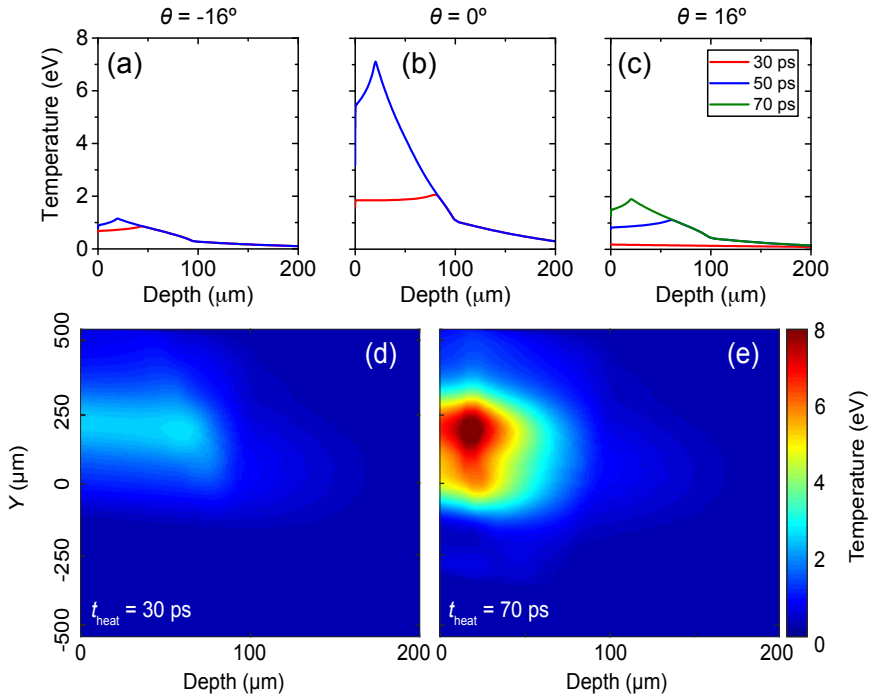

Figure 6.19: (a-c) Three example 1-D temperature maps from HELIOS (corresponding to $-16°$, $0°$ and $16°$ with respect to the target normal axis), for heating times (t_{heat}) of 30, 50 and 70 ps. (d-e) 2-D temperature profiles, as a result of interpolating the nine 1-D temperature profiles obtained in HELIOS, for t_{heat} = 30 ps and 70 ps.

HELIOS. This temperature gradient could manifest in a non-uniform proton beam, due to the expansion at one point along Y differing when compared to another. If the sheath field is set over this region, a non-symmetrical sheath field could result. Additionally, due to lateral electron transport, low energy protons will be accelerated along the entire rear-side of the target. It is likely that this explains some of the non-uniform structures observed in the RCF images, such as for later times in Fig. 6.4. It may also explain why some of the experimental data points lie outwith the region delimiting the HELIOS results in Fig. 6.17b; particularly in the high flux case ($L = 0.7$ mm), where a steeper gradient will be present due to the smaller area over which heating occurs. In future experiments, the use of mass-limited targets [156] (with limited lateral dimensions) would prove beneficial, as a lateral temperature gradient could be minimised - provided the target is small enough and the heating proton beam is large enough.

6.7.2 Implications for proton fast ignition

Some of the spectral effects observed here have been reported previously in Fuchs *et al.* [131]. In their manuscript, they irradiated the rear-surface of a 25 μm Al foil

with a $\tau_L = 350$ fs, $\omega_L = 50\,\mu$m, $I_L = 4{\times}10^{16}$ W cm^{-2} 2ω laser pulse, shortly before laser-irradiating the front surface of the foil and measuring the accelerated proton beam downstream. They observe that for an increasing time-delay between the two pulses, resulting in an increasing expansion of the target rear-surface, the maximum proton energy and overall proton number steadily decreases. They observe no effect on the beam spatial profile, contrary to what we observed. The method presented here is advantageous in that the whole target rear is irradiated (i.e. ~ 1 mm), leading to expansion of the whole target and not just where the peak sheath field is located. Additionally, in the study by Fuchs *et al.*, the number of low energy protons (~ 2 MeV) remain constant through their entire temporal scan. This is because most of low energy protons are accelerated from outwith this 50 µm laser-heated region, and are unaffected by the longitudinal expansion at this point. Using the proton heating technique, where a large area is irradiated, spectral and spatial changes to the entire proton beam are observed, for heating times as low as $t_{heat} = 10$ ps.

This poses an issue regarding proton fast ignition (PFI), as seen from Fig. 6.20a. The scale length expected for a beam used for PFI is of the order 5 µm (assuming a laser to proton conversion efficiency of 10%), and from the results in Fuchs *et al.* (Fig. 6.20b) this does not change the spectral parameters of the mid-low energy components of the proton beam. However, a clear reduction is observed in the results presented here. The green series in Fig. 6.7a corresponds to a calculated (from the maximum energy drop) scale-length of $\sim 5\,\mu$m. A drop in the overall proton number by a factor of ~ 5 is measured for the 1 MeV components. Our results provide a more accurate picture of a realistic PFI scenario, due to our larger area of heating. A similar area of heating at the target rear is expected due to the fast electrons accelerated by the leading edge of the pulse, driven by the 200 µm laser focal spot in PFI. In addition, we have diagnosed the degree of expansion based on the measured maximum energy decrease. In their paper, they do not experimentall measure the expansion.

6.7.3 Proton focusing

In our experiment, the heating proton beam (for the low-mid energy components) has a ring-like profile, with a low-density central point surrounded by a high-density population of protons. At early times, this would induce a greater degree of expansion around the central point of the target than in the centre, illustrated in Fig. 6.12.

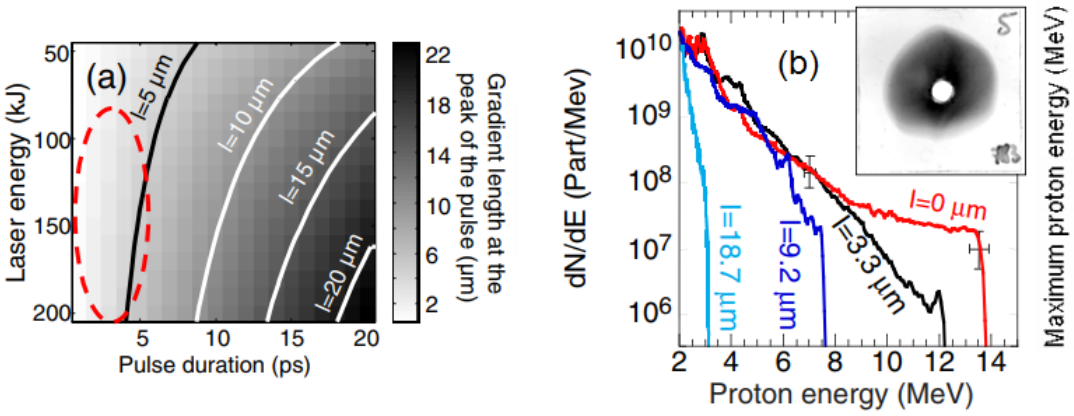

Figure 6.20: (a) Modelling of the heating of a target rear surface as a function of laser energy and pulse duration for a laser irradiating the target's front surface. I is the plasma scale length expected at the rear of the target due to the hot electrons accelerated by the leading edge of the laser pulse. The circled red area represents the parameter-space relevant for proton fast ignition. (b) Proton spectra from Fuchs *et al.* [131] for various rear surface plasma scale lengths, induced by laser heating. Both plots are reprinted from [131].

Assuming the peak of the electrostatic sheath field is located at the central point of the annulus, this leads to a curving of the sheath field, resulting in focusing of some of the lower energy components. This results in a proton spatial distribution with a pronounced circular region of high signal on the RCF. Other methods have been used to manipulate the spatial distribution of the proton beam, as described in section 6.1. However, none involve using a secondary proton beam to induce a plasma gradient. As the target expands further, the plasma longitudinally diffuses, creating a more even distribution which results in a smooth, collimated beam (Fig. 6.11).

This technique results in the collimation of a desirable range of spectral components, with applications in many areas that require a reduced beam divergence, high flux and narrow energy range. Potential applications of such a beam include fast ignition [16] and the production of high-energy density matter [17], which all require a high flux beam of low energy protons. Focusing of select spectral components of a laser-generated ion beam has been previously achieved using a laser-driven micro-lens [157], which provides tunable, simultaneous focusing and energy selection of multi-MeV proton beams. However, for the focusing of higher energy ions it requires increasingly high laser intensities of the secondary beam, and so becomes unfeasible for applications with high energy ions. Other approaches, such as the more traditional electrostatic or magnetic lensing [158], have several drawbacks, including large geometrical sizes, slow switching

times and beam aberrations.

An interesting future experiment may be achieved by using two targets that are much closer together, such that plasma profile due to the annular ring has a much higher gradient, which would in theory induce far more focusing at early times.

6.8 Conclusion

In summary, experimental measurements of sheath-accelerated protons from increasingly heated targets has been used to develop a simple analytical model describing the expansion behaviour. This model calculates the expansion length of the rear-surface proton layer, as a function of flux and time after irradiation – based on the drop of the maximum proton energy. A series of detailed radiation-hydrodynamic simulations (using the measured parameters of the input proton beam) with the 1-D HELIOS code support these findings. From the experimental results, it is possible to determine the temperature of the expanding ion layer by matching the calculated plasma expansion lengths to the simulations, providing a new technique for determining target temperature. This novel diagnostic could be further improved upon through using a more careful target alignment methodology, and constant monitoring of a reference proton beam. Additionally, with a time-resolved measure of the target temperature, these results could be coupled with the expansion measurements to gain insight of the heated material's properties. Scope exists for using this technique to diagnose the expansion of heavy ion species by using a Thomson parabola spectrometer.

The results have implications for proton fast ignition (PFI), where we measure a factor of ~ 5 decrease in proton number for 1 MeV protons for a similar plasma scale length expected in a realistic PFI scheme.

For a small plasma scale length, a clear focused component is observed in the proton beam. This is believed to be a consequence of the non-uniform heating proton beam, presenting a potential new method of inducing proton focusing. Implications of such a beam range from PFI to the generation of high-energy density matter.

Chapter 7

Physics underpinning proton focusing via curved and conical targets

This chapter addresses the physics underpinning high-current proton acceleration and focusing using novel conical targets with the Orion laser system at AWE plc [90]. The experiment was performed primarily to explore physics related to the development of proton fast ignition (PFI) and high energy density (HED) physics. The experiment was proposed by a proton fast ignition consortium, formed during the fast ignition workshops in 2014/2016. This chapter reports on the analysis of the experimental data and some preliminary simulation data.

Firstly, investigations of proton focusing were performed through using multiple conical target types. This was to develop our understanding of proton focusing and measure the effects that conical attachments have on the laser-to-proton energy conversion efficiency. Clear proton beam focusing is observed for certain target configurations, with little variation in the conversion efficiency. Proton radiography was implemented, using a second short pulsed laser-driver, to investigate the electromagnetic fields surrounding the conical structures that are responsible for the focusing.

Secondly, the influence of a plasma surrounding the cone on proton focusing was examined. Multiple long pulse beams were used to induce plasma expansion before the arrival of the short pulse beam. The effects of a long scale-length plasma effectively quenches any focusing effects, whilst also reducing the overall flux of protons and the maximum energy of protons accelerated.

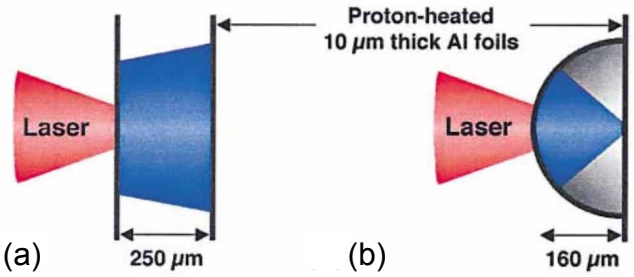

Figure 7.1: (a) Set-up for a flat and (b) focusing target used to heat a secondary foil target. The blue beam represents the accelerated protons. Figure reprinted from [17].

Lastly, the beam of accelerated protons was used to heat copper samples, with the X-ray emission imaged. This heating is found to deflect the accelerated protons, with the peak field strength around the cone estimated based on the amount of deflection experienced by the highest energy protons.

7.1 Introduction

The potential to isochorically heat materials using a beam of MeV laser-accelerated protons was discovered upon the emergence of ultra-high intensity, ultra-short pulsed laser systems [15]. Patel *et al.* [17] demonstrated that by irradiating a thin-foil target with ~ 1.5 MeV protons, accelerated from the rear of a second foil following its interaction with an intense laser pulse, the secondary foil was heated to several eV over the duration of the proton beam. In the same study, the team also used a hemi-spherically curved foil target (in order to generate a beam of focusing protons) as the proton driver, demonstrating that the heating could be localised to a far smaller spot when compared to the use of a flat foil. With this configuration, they achieved temperatures in excess of 20 eV. A schematic from this study illustrating how a curved target induces proton focusing is shown in Fig. 7.1.

Shortly after the initial demonstration of proton focusing, Foord *et al.* [159] observed that the subsequent isentropic expansion of the target could yield measurements of the equation of state (EOS) of the expanding material. Such measurements of difficult-to-construct WDM states are highly sought after for the modelling of inertial fusion plasmas [160], astrophysical plasmas and planetary cores [161]. Therefore, a high intensity proton beam that is capable of producing such matter is extremely valuable.

In the results detailed here, hemi-spherically curved foil targets are used in conjunc-

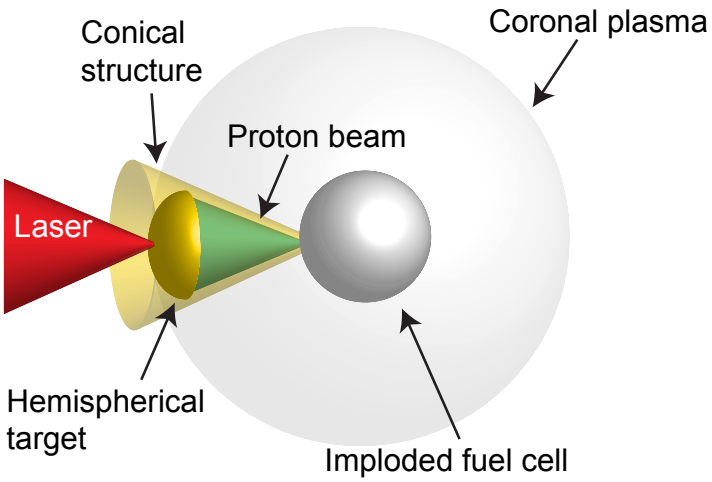

Figure 7.2: Schematic illustrating cone-guided proton fast ignition. The fuel cell is first imploded by uniformly irradiating the pellet with multiple long pulse beams. This results in a dense, hot fuel pellet surrounded by a coronal plasma. A short-pulsed laser then irradiates the hemispherical target, with the accelerated protons focused by both the curvature of the hemispherical target and the electromagnetic fields surrounding the gold cone. The short burst of energy deposited by the protons ignites the fuel cell.

tion with a surrounding cone structure [18]. The conical structure, similar to the one proposed for electron FI [162, 163], serves two purposes. Firstly, it acts to protect the hemispherical target from the intense soft X-ray radiation that would be emitted by an imploding target in a FI scenario. Secondly, the cone-attachment aids in focusing the proton beam. Figure 7.2 schematically illustrates this concept. Previous experiments using either self-guiding structures [164] or shaped targets [165] demonstrate proton focusing, however by combining both a significantly smaller focal spot can be achieved [166]. Particle-in-cell simulations [167], modelling the proton acceleration, show that the fields surrounding the cone structure and the fields due to the surrounding plasma play an important role in determining the focusing characteristics of the beam. A more systematic study utilising hybrid-PIC simulations [168] modelling the complete physical picture, from the fast-electron production through to the transient acceleration and thermal expansion/focusing of the proton beam is reported in [168].

As mentioned previously, one of the main motivations behind this study is to investigate the physics relevant to PFI [16], which has the potential for higher gains and smaller driver energy requirements than the more conventional central hot spot approach to ICF. PFI differs in that the compression and ignition stages are separate, with a beam of focused protons used to deliver the energy to the fuel core in a rapid

burst to achieve ignition. Hydrodynamic simulations by Temporal *et al.* [169] provide a baseline for the conditions required for ignition, with the required energy dependant on the beam temperature (assuming a Maxwellian-like beam spectrum typical of TNSA) and distance between the proton source and fuel pellet. For a beam temperature of 5 MeV and a separation of 500 µm, an energy of approximately 12 kJ is required.

Due to the required parameters, two key issues for PFI must be addressed. The first is the laser-to-proton energy conversion efficiency. In Chapter 4, the target thickness was optimised such that the conversion efficiency was $11 \pm 2\%$. Hybrid PIC modelling shows that with a high electron temperature and a low target areal density coupled with a rich proton layer on the target rear, up to 50% of the electron energy can be converted to proton kinetic energy [170]. The second key issue is proton focusing. Building on the work of Patel *et al.* [17], a recent Trident experiment by Bartal *et al.* [166] demonstrated focusing of the protons to a diameter of 40 µm using 350 and 600 µm diameter hemispheres. In the same work, Bartal *et al.* also demonstrate focusing by using self-charging structured targets.

The first goal outlined in this chapter is the investigation of proton focusing using various conical targets, to study the effects that different cone structures have on the measured proton beam's spectral and spatial characteristics in addition to the conversion efficiency. It is observed that for a conical target with an open tip, a beam of accelerated protons appears focused in the spectral window of (20 ± 10) MeV; appearing annular at high energies (> 45 MeV) and circular at low (> 10 MeV) energies. The maximum proton energy remains roughly constant regardless of the conical attachment used, as does the proton flux, with a conversion efficiency equal to $5 \pm 1\%$. Additionally, the coupling of the hemispherical target to the cone structure was changed by separating them, thereby limiting the fraction of electrons responsible for inducing the focusing electric field.

In the context of PFI, the required energy could potentially be reduced (by $\sim 50\%$) if the proton beam is applied in two consecutive bursts [171, 172]. In this scheme, the first beam has an annular distribution, which compresses the hot spot by inducing an inward-travelling radial symmetric shockwave. The second, focused beam then interacts with the compressed fuel. As mentioned in the previous paragraph, the beam accelerated from a hemi-open cone arrangement features both an annular distribution at high energies (i.e. early times) and a focused beam at mid energies. Such a beam

could potentially eliminate the need for two distinct proton beams.

To better understand the electromagnetic fields responsible for inducing focusing around the conical target, an auxiliary laser-accelerated proton beam is used to probe the fields forming around the target. This charged particle probe is used in conjunction with the main proton beam diagnostics, enabling a direct comparison to be made between the imaged fields and the accelerated protons from the conical targets.

To close in on a realistic PFI scenario, the second goal addresses the question: what influence does a plasma surrounding the conical structure have on the recirculation of electrons and the onset of the focusing fields. In a FI experiment the cone is surrounded by a dense plasma, and it is not well understood to what extend the presence of this plasma affects the build-up of the fields surrounding the cone structure. By using conical targets that have been uniformly irradiated with four long pulse laser beams, a plasma is produced around the outside of the cone. Changes in the accelerated proton beam are observed, with the beams possessing a lower maximum energy and no indication of focusing.

Lastly, copper samples with various densities were irradiated by the accelerated protons, with the primary motivation to characterise the proton heating of the secondary sample by imaging the emitted X-rays. This also provides a measure of the proton beam size and density within the Cu sample. Previous studies of proton focusing that have attempted to characterise these proton beam parameters have incorporated a mesh shadow imaging technique, providing an indirect measurement of the proton beam. The method presented here is advantageous, as the XUV imaging will provide a direct measurement of the degree of heating induced by the focused proton beam at the focal spot.

Preliminary simulations were also performed, involving both a closed and open cone, using the hybrid-PIC code LSP [173, 174]. These simulations were undertaken in order to model the electromagnetic fields present in the conical target, due to a moving population of fast electrons. Some differences were observed between the open and closed cone cases. In the following section the experiment set-up is outlined.

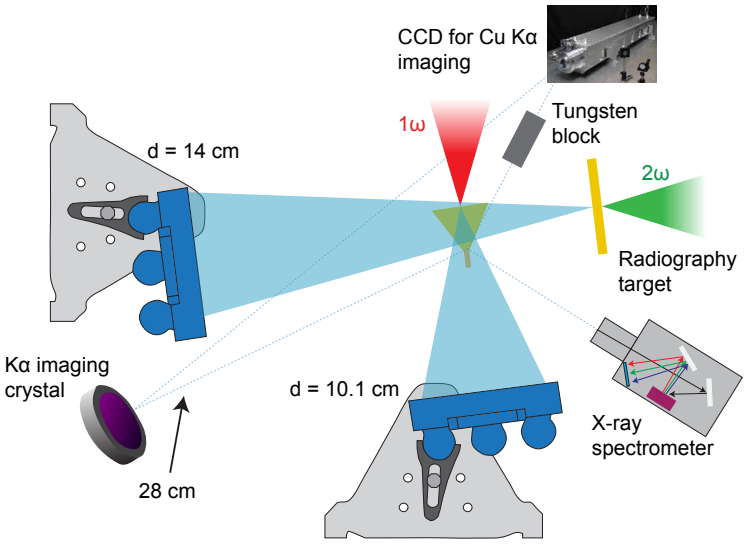

Figure 7.3: Schematic showing the experiment set-up, operating in the proton heating (X-ray imaging) mode. The transparent blue cones represent the accelerated protons.

7.2 Experiment set-up

The experiment was conducted in two parts: the first (four days) in January and the second (three days) in July, 2017. Two short-pulse lasers were used (SP1 and SP2), which were separately compressed to temporal durations (τ_L) of 0.5 ps. Both pulses were p-polarised, with wavelength (λ_L) equal to 0.527 µm in the SP1 case and 1.053 µm in the SP2 case (2ω and 1ω, respectively). SP1 was used to irradiate a planar foil target, with the accelerated protons acting as a transverse proton probe of the main, conical target irradiated by SP2. A detailed description of the proton probing technique is given in Chapter 3. Figure 7.3 shows a schematic of the experiment set-up, operating in the X-ray imaging mode. Figure 7.4 displays an in-chamber view of a typical shot configuration, with the main elements of the set-up indicated.

Both laser pulses were focused using two separate $f/3$ off-axis parabolic mirrors to spot sizes of around $\phi_L = 5$ µm (FWHM). The total estimated energy on-target for SP1 was $E_L = (200 \pm 10)$ J and SP2 $E_L = (490 \pm 20)$ J (provided by AWE). This corresponds to a peak intensity of $I_L = (6.0 \pm 0.5) \times 10^{20}$ Wcm^{-2} for SP1 and $I_L = (1.5 \pm 0.1) \times 10^{21}$ Wcm^{-2} for SP2, within the focal spot. The relative timing of the two beams was characterised using an X-ray streak camera, measuring the temporal separation to within an uncertainty of ±25 ps.

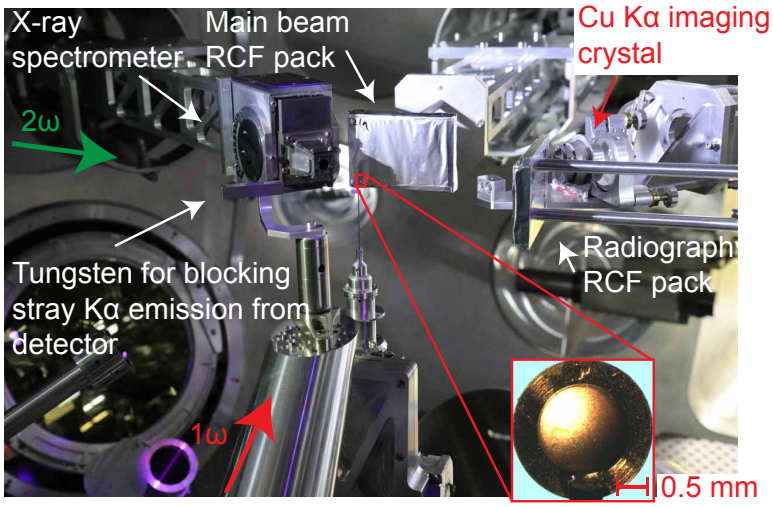

Figure 7.4: In-chamber photograph showing a typical shot-configuration for the proton heating mode.

For the second objective, where plasma expansion was induced around the conical target, between two and four long pulse beams where used (LP1, LP2, LP7, LP8). LP2 and LP8 came from the right hand side of the schematic, and irradiated the left hand side of the cone with respect to the SP2 propagation axis. LP1 and LP7 came from the left hand side of the schematic. LP1 and LP2 came from below the target and irradiated the lower portion of the conical targets, while LP7 and LP8 irradiated the top of the targets. The energy of the long pulse beams was equal to (50 ± 10) J, with $\tau_L = 2$ ns. The beams were delivered in a square pulse (temporally), with a 0.2 ns rise-time. Phase plates were incorporated such that the beam profile was uniform on the cone surface, inducing a longitudinally uniform plasma expansion. This enabled the expansion to be accurately modelled using 1-D radiation-hydrodynamic simulations. The spot size for all of the long pulse beams was equal to 300 µm. When used, the leading edge of the pulse was incident 2.2 ns prior to the arrival of the short pulsed beams.

Both the hemi-cone proton beam and the radiography beam were measured using separate dosimetry film (RCF) stacks, providing spectral and spatial information. Details of the ion-beam diagnostic can be found in Chapter 3. Both targets were irradiated at an angle of 8°, with the two RCF stacks angled perpendicular to their respective target-normal (TN) axes. The radiography stack (SP2) was placed 14 cm away from the foil target, in order to prevent geometrical clashes with the long pulse beams. This large distance also resulted in a high magnification, at the cost of a lower proton beam density on the film. The SP1 stack was positioned 10 cm downstream from the hemi-cone

target.

Multiple conical configurations were used, in order to investigate the effects of proton focusing as a function of target geometry. Additionally, several types of Cu (of various densities) were attached to hemi-closed cones, to observe the changes in deposited energy of the protons. All of the target types used in the SP2 interaction, including those with a Cu attachment, are shown in Figure 7.5. The thickness of the hemispherical targets was equal to 10 µm, with a curvature of 30° and a transverse length of 1.35 mm. The distance from the apex of the hemisphere to the rear of the cones was 800 µm. The cone tips were 300 µm in diameter, with either the whole tip closed or open depending on the cone configuration used. The thickness of the cone walls was equal to 15 µm. For the separate stalk targets, the gap between the hemisphere and cone was $\sim$ 200 µm, resulting in a hemi-to-cone tip distance of $\sim$1 mm. The proton driver targets used to accelerate the charged particle probe were $\ell = 20$ µm Au planar foils. Each target was individually manufactured and assembled, resulting in some small variation in the target geometries. These differences were minimal, however each target was carefully metrologised before insertion into the target chamber, such that the centre of the hemisphere was irradiated in each case. Retro-imaging was used to align the targets, however, this technique could not enable accurate location of the centre of the hemisphere and instead is only useful in moving the target into the focal plane of the laser.

For the Cu-attached target, the conical geometries remained the same. The horizontal Cu foams were 900 µm in length and 250 µm in diameter. The vertical foams had the opposite dimensions. The Cu foam disks were 525 µm in length and 300 µm in diameter. Finally, the solid Cu blocks were 110 µm in length and 140 µm in diameter.

A monochromatic X-ray Imager (MXI) was used to image the emitted K_α radiation from the heated Cu targets. The MXI was centred on 8.048 keV, with a bandwidth of 6 eV. A CCD was used to record the imaged radiation. A temperature measurement of the heated Cu samples was also attempted, by using a high-energy X-ray spectrometer (HEX-ID/TITAN), with four crystals directing the emitted X-rays towards four pieces of image plate. In order to acquire a measure of the target temperature, the ratio of signal between the K_α and K_β lines is required. Unfortunately, only one of these lines was present so a temperature measure cannot be deduced. Further analysis is required to determine if any useful information from this diagnostic can be extracted. Further information regarding the target diagnostics used on the Orion laser system can be

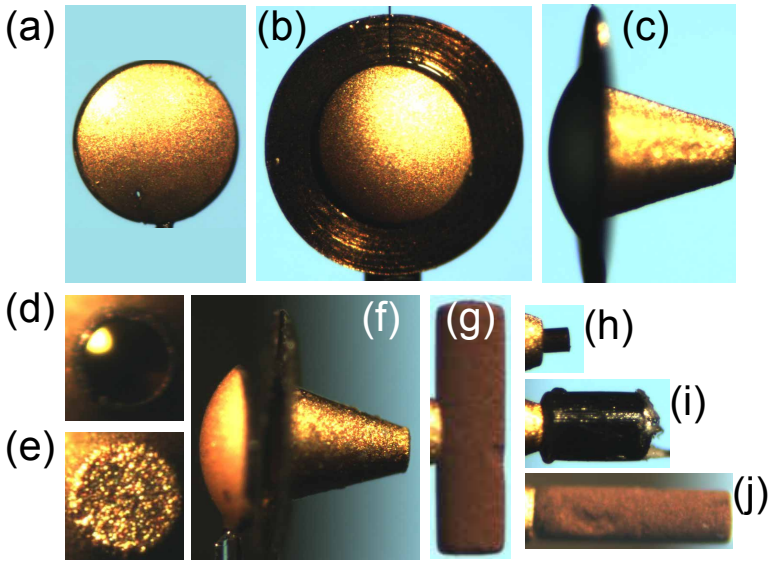

Figure 7.5: The main targets used on the experimental campaign. (a) Hemispherical target (face) with no cone; (b) hemi-cone target (face); (c) hemi-cone target (side-view); hemi-cone target with an (d) open tip; (e) closed tip; (f) hemi-cone target with separate stalks. The four remaining images feature Cu attachments: (g) vertical foam; (h) solid Cu block; (i) Cu-doped CH; (j) horizontal Cu foam. Note that the spatial scale changes between images.

found in the following references: [175, 176].

7.3 Experimental results

7.3.1 Effects of target geometry on proton focusing

The first objective of the experiment was to investigate the effects that various types of conical target attachments have on proton focusing and conversion efficiency. Several RCF slices are shown in Fig. 7.6 for three target types: hemisphere, hemisphere with a closed cone attachment and a hemisphere with an open cone attachment. The variation in the maximum proton energy, ε_{max}, was minimal between this particular data scan (55 ± 6 MeV), regardless of the target type used. Several differences in the spatial structure of the beams are observed. By far, the most prominent effect is the appearance of an annular structure in the open cone case at high proton energies (ε_p). In the same location as the centre of this annulus, at low values of ε_p (10 - 30 MeV), exists a region of high proton signal. Figure 7.7 displays additional RCF slices for the open cone arrangement to illustrate this more clearly. Another clear difference when comparing the cone targets with the hemisphere-only case is the disappearance of most of the non-

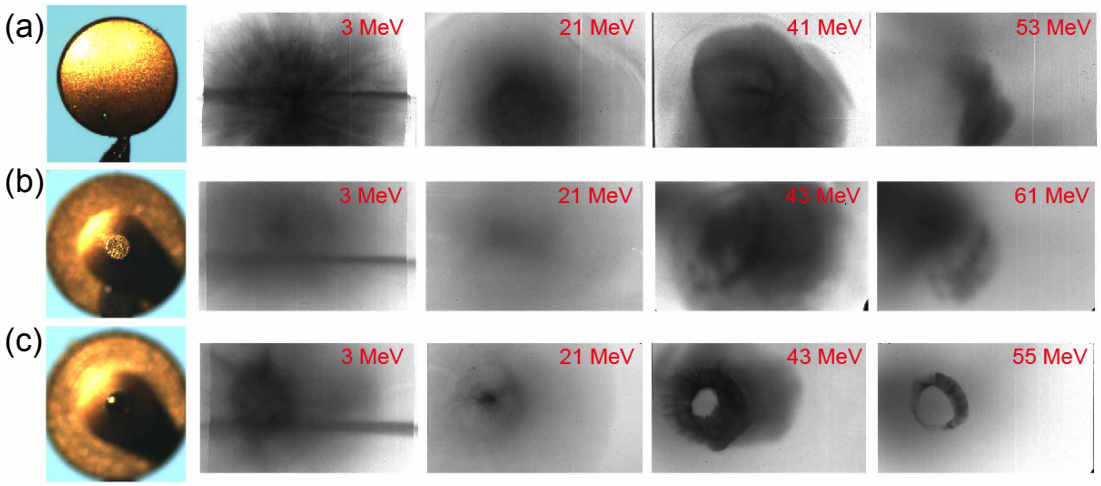

Figure 7.6: RCF slices for several target geometries. (a) Hemispherical target without the cone attachment; (b) hemi-cone with closed tip; (c) hemi-cone with open tip. The RCF images were all independently scaled for spatial clarity and are not representative of relative dose.

uniform structure observed at low energies ($\varepsilon_p < 5$ MeV), present in the hemisphere-only case. This is likely due to the fields present in the cone-cases effectively washing out these small modulations resulting from a non-uniform target rear surface. Note that in the closed cone with a spatially separate hemispherical target, the beam profile is near-identical to the connected version.

In the open-cone case, one interpretation of the changing beam structure is as follows. The highest energy ($\varepsilon_p = 55$ MeV) protons take around 8 ps to reach the rear of the cone, which is the position where the transverse (i.e. focusing) electric field is strongest. At 8 ps the field is relatively high, and acts to over-focus these protons, resulting in an annular structure when detected downstream. The lower energy protons arrive later, and experience a lower field than protons with an energy of ε_{max}. Protons with ε_p equal to 20 MeV take 13 ps to reach the rear of the cone, and it is suspected that the field strength has decayed enough such that the protons appear focused on the diagnostic plane. The spectral window over which the protons appear focused is large (20 ± 10 MeV). The reason for this large (spectrally) focused beam component is likely due to a combination of the field decaying with time, in addition to protons with a lower energy arriving at later times. The deflection scales linearly with the electric field, with lower energy protons experiencing a higher degree of deflection compared to those with a higher energy (by the same electric field). For the lowest energy protons ($\varepsilon_p < 10$ MeV; $t > 18$ ps) the field strength has decayed such that the protons are no longer

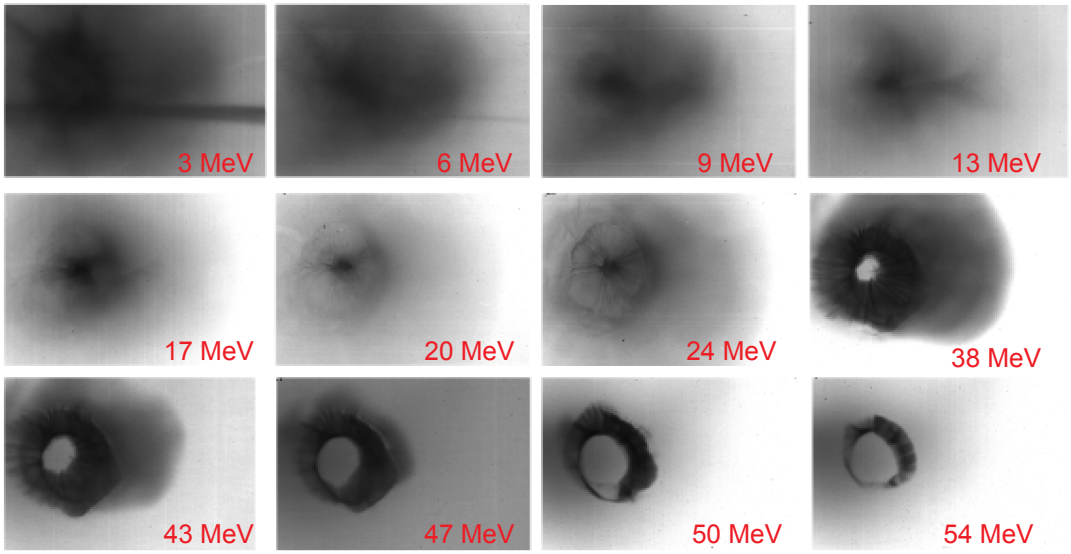

Figure 7.7: RCF slices for the hemi-cone target with an open tip (same as Fig. 7.6c). The clear focused component is evident between 10 MeV and 30 MeV, with a prominent annular structure observed at the highest proton energies. The RCF images were all independently scaled for spatial clarity and are not representative of relative dose.

focused/collimated, and diverge according to their initial trajectory. Another hypothesis regarding the annular structure observed is that the induced magnetic fields, due to the circulating electrons, near the cone walls counteracts the focusing at early times, when the field is strongest. This is discussed further in section 7.5.

A proton beam with a similar profile has been seen previously on the Titan laser facility [166], albeit with lower proton energies ($\varepsilon_{max} = 30$ MeV; collimated beam at 10 ± 2 MeV). In our experiment, $\varepsilon_{max} = 55$ MeV with a focused component in the energy range (20 ± 10) MeV. This factor of five higher in spectral range for the focused component is advantageous, and is likely a result of the higher electric fields present in our case acting to focus the protons over a larger time-window.

The laser-to-proton energy conversion efficiency was determined from the RCF data for the three target configurations shown in Fig. 7.6. Very little change in the overall spectral profile of the beam is observed, with the only difference being in the closed tip case where the low energy ($\varepsilon_p \sim 1$ MeV) proton number was lower; likely due to stopping/scattering in the tip. The efficiency calculated using each target was $(5 \pm 1)\%$. From simulations [168] and previous experimental data [166] it was previously thought that a reduction in efficiency would be expected in the conical case, due to electron transport from the region near the laser spot to the surrounding structure. This is likely

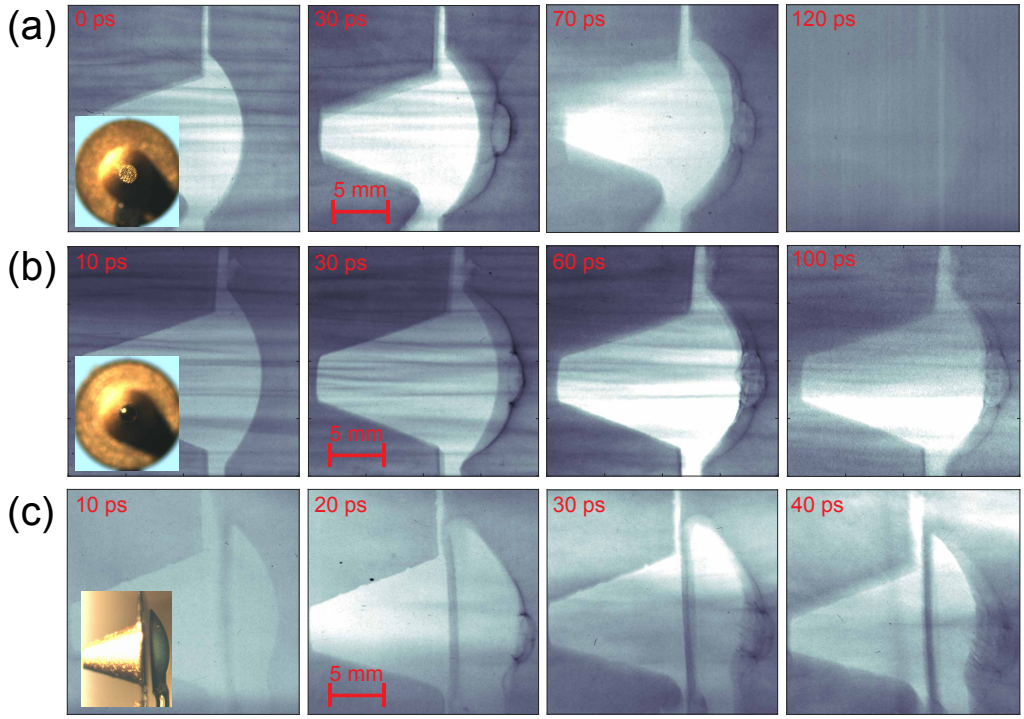

Figure 7.8: Proton radiography of several hemi-cone targets. (a) closed tip; (b) open tip; (c) closed tip, separate hemisphere and conical structure ($\sim$ 200 µm). Scale shown is that of the diagnostic plane and time is relative to the arrival of SP2 as determined by an X-ray streak camera.

due to the electrons escaping into the walls of the cone, instead of acting to accelerate protons. Some electrons must travel into the cone walls, as it is the only explanation that would result in a focused beam in the open cone case. Additionally, as will be seen in section 7.3.3, the electrons travel into the Cu attachments and deflect the accelerated protons from the SP2 (main) interaction, so some must escape into the cone walls. The conversion efficiency may instead be preserved due to the electrons contributing to the accelerating field being confined for a longer time by the charged conical structure. Fewer electrons will be contributing to the accelerating field, however, due to the longer confinement time the result is that no net change in conversion efficiency is observed. The time over which the electrons are confined will change depending on the target geometry used, which may explain why previous experimental measurements (with different target geometries than presented here) resulted in a reduction, while in our case no measurable change was observed.

To investigate the electromagnetic fields responsible for proton focusing, SP1 was

used to irradiate a planar Au foil; with the accelerated protons used as a transverse particle probe of the cone-target, in order to image the electric fields induced by the electrons. The results provided information regarding the structure and life-time of the fields present. Several example radiographs are shown in Fig. 7.8 for the hemi-closed cone, hemi-open cone and the separate stalk targets (with a closed cone). Very clear field structures surrounding the hemispherical target-face are observed, and appear most clearly at $t = (30 \pm 25)$ ps (second column). In the case of the hemi-open cone the field structure appears most uniform, and remains for tens of picoseconds before breaking up. Note that the Au conical target is thick enough to fully stop the probe protons (all spectral components < 10 MeV) and therefore no information pertaining to the field structures within the target is obtained.

The deflection along the front of the hemispherical target is likely to be the result of the front surface electrostatic sheath field, which is strongest at the position of the laser focal spot resulting in a greater degree of deflection at this point. Note than in Fig. 7.8c, the highest strength region appears near the bottom of the hemisphere. This is because the laser was focused slightly lower than in the other cases relative to the apex of the hemispherical target, such that the irradiated region lined up transversely with the middle of the cone (the cone and hemisphere for this target were not well aligned). By misaligning the laser such that it no longer irradiated the centre of the hemisphere, a less uniform field distribution is observed in (c) compared to the other two cases. Additionally, the field structure in (c) appears to break up roughly twice as quickly when compared to the other two cases. This may be an effect of the separate stalks, where the electrons are less effectively contained and do not recirculate back into the hemisphere.

Figure 7.9a quantifies the distance the protons were deflected from the front surface of the hemisphere (ΔX) in the open-cone case at $t = 30$ ps. Figure 7.9b displays an image of the region analysed. From ΔX, the average electric field experienced by the probe protons can be calculated (using Eq. 3.3, Chapter 3). A uniform field structure is observed, which peaks at the central point where the laser was incident ($Y = 0$ cm). The field appears convex, which will act to accelerate protons from the front surface in the positive X dimension with a larger divergence than from a flat planar foil target. This field is indicative of a focusing, concave field structure on the rear surface of the hemisphere. When comparing Fig. 7.8a and b, the field structure present

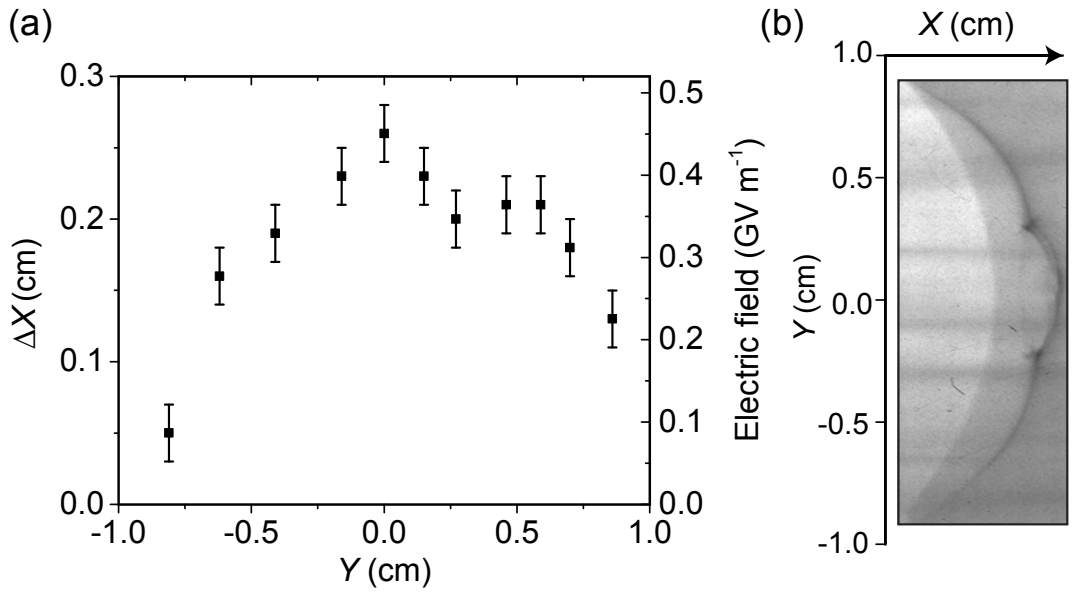

Figure 7.9: (a) Deflection of the probe protons (ΔX) due to the electric fields present on the front surface of the hemispherical target with an open cone attachment. The protons comprising this thin region of increased signal are assumed to originate from the target front surface, with the error bars based on the thickness of this dense belt of proton signal. The corresponding average field strength required to induce this degree of deflection is shown on the right vertical axis. Both are plotted as a function of lateral distance (Y) from the laser focus. (b) Radiography image from which the distances in (a) are measured, rotated 90° with respect to (a).

in b is far more symmetrical. It is unclear whether or not this is an effect of having an open tipped cone. These images illustrate that a focusing field structure on the rear surface of the hemispherical target will be present, and that the electrostatic field surrounding the cone exists over a long period of time. It also shows that without the cone attachment, the field decays more rapidly (as seen in Fig. 7.8c). Note that radiographs of a hemispherical target with no cone attachment were obtained, however no field structure was present on the hemispherical target-face. This further supports the argument that the conical attachment is necessary to allow these fields to exist over tens of picoseconds.

An additional effect observed in the radiographs is the apparent decrease in size of the target at later times. Two reasons exist which may account for this apparent decrease in size. One concerns the fields surrounding the cone. If they exist for a relatively long time after the interaction, the lower energy protons may be deflected around the cone, making it appear smaller. A second reason may be due to the large source size of the lower energy protons. If the source size is very large, the shadow

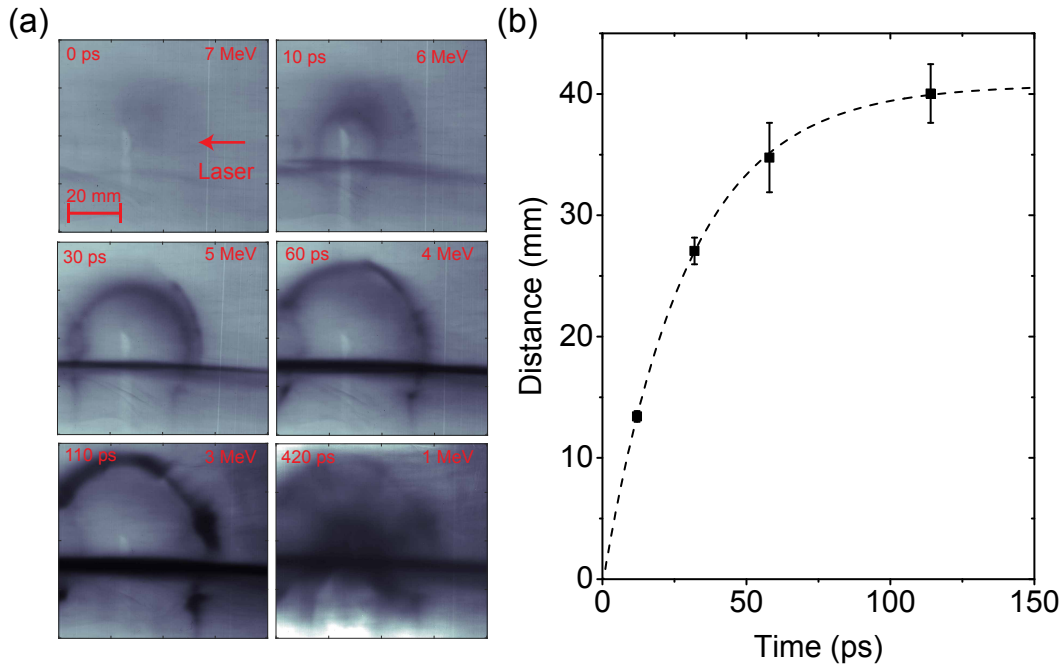

Figure 7.10: (a) Dosimetry measurements showing the apparent expansion of a charge wave from a hemispherical target. Multiple time-slices, relative to the approximate arrival of the laser pulse, are shown. (b) Distance from the hemisphere at the detector plane, as a function of time, of the deflected protons due to the charge wave.

of the object may blur, creating a large penumbra and a small true umbra. For some of the images, such as in Fig. 7.8a, the shadows do not appear sharp at late times, meaning this is the most likely explanation in these cases. In Fig. 7.8c, however, for $t > 10$ ps, the width of the cone appears to decrease whilst the image still remains sharp. This indicates that in this instance first reason is the most likely explanation. Another interesting feature of Fig. 7.8c, at $t = 20$ ps, is the apparent increase in longitudinal size of the hemispherical target (a factor of ~ 1.5 increase); likely due to the electrical charging of the target acting to deflect the protons close to the hemisphere.

Another effect, possibly distinct from the previous one detailed, is observed at late times, after the front-surface field structure appears to break-up. It appears as a pronounced circular deflection of the probe protons at very late times, indicating that is not due to electrical charging. RCF images of a hemispherical target showing this deflection are shown in Fig. 7.10a. Note that this effect is also observed in the hemi-cone configurations, however the timing for these data-scans was optimised for diagnosing the earlier (in time) field structures, shown in Fig. 7.8. This resulted in a maximum of two time-slices where the expanding feature was present.

Several interesting features are present in these images. Firstly, the velocity of the expanding front appears to decrease at later times, as seen in Fig. 7.10b. Secondly, the expansion appears semi-circular, with the bottom half of the circle (for $t > 10$ ps) disappearing. The first effect is likely due to the expanding spherical shock front. After $t > 0$ ps the shock front should have a constant velocity, with the amount of charge contained within this front being constant. As the shock is expanding spherically, the charge density will be falling with the expansion distance ($\sigma \propto r^{-3}$). By performing a first-order power fit to the expansion distances (also including the distance corresponding to $t = 420$ ps which is not plotted), the dependence is $t^{0.30}$. By performing a power fit to the data points shown in Fig. 7.10b, a square-root dependence results. The confidence of fit for both is of the order $R^2 \sim 0.7$. This discrepancy of the trends, and the relatively poor fits, is believed to be a product of two things. Firstly, as there is a systematic timing off-set of ± 25 ps, earlier times will be far less accurate (relative to time zero) than later times. Secondly, as the proton energy decreases, the deflection due to the fields increases linearly with the energy drop. The latter effect will be the main contributing factor to the poor power fits. Unfortunately, it is not possible to calculate the expansion velocity of the shock front, as both the velocity of the shock front and charge contained within the front are unknown.

The second observation, where the expansion is non-symmetric around the base of the target for $t > 10$ ps, may be due to the charge flow from the target stalk to the hemisphere. As electrons are expelled from the target, the target is left positively charged. Electrons from the stalk are attracted to the now-positive target, with this strong current flow resulting in a magnetic field surrounding the stalk. This magnetic field would act to deflect the probing protons vertically - possibly beyond the detector, explaining their absence in the radiographs. At the earliest time-slice where expansion is present ($t = 10$ ps), the expanding shock front appears symmetrical. At this time, it is likely that the target is not as strongly charged as it is at later times, therefore resulting in a lower drawn current from the target stalk and a lesser degree of vertical deflection.

From the experimental data presented here, it remains unclear why using an open cone attachment results in an annular beam at high values of ε_p, and a focused beam at mid-range values. Multiple closed cone targets were tested, with none of them exhibiting a focused beam, therefore it is unlikely it is due to fluctuations in the laser

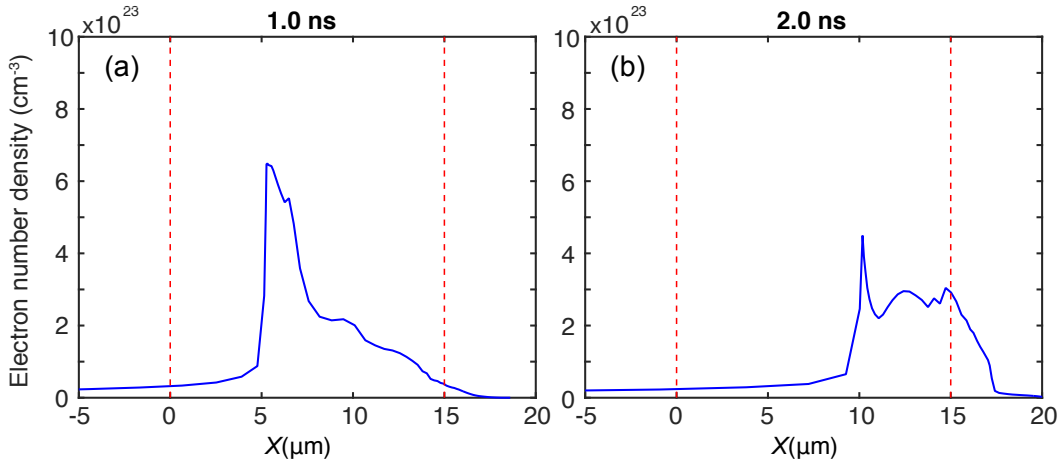

Figure 7.11: Shock propagation through the target for $t = 1$ ns and $t = 2.0$ ns relative to the arrival of the long pulse beam. The energy of the laser beam is equal to 50 J and the pulse duration is equal to 2 ns (i.e. the configuration used on the experiment). The red boundaries indicate the target surfaces.

parameters and positioning of the laser focus (the latter of which is extremely important). Simulations were performed (discussed in section 7.4) which potentially explain some of the differences observed in the two cases.

7.3.2 Effects of plasma expansion

The effects that a plasma surrounding the cone has on proton focusing was investigated, by irradiating the sides of the cone with either two or four long pulse beams. In preparation for the experiment, simulations were performed using the 1-D radiation-hydrodynamic code HELIOS [110], to ascertain the optimal laser parameters required for inducing a long scale-length plasma. The target was initialised as a 1-D slab of Au with a thickness $\ell = 15\,\mu$m. The laser had a linear rise-time of 0.2 ns and was flat for the labelled pulse duration. Further details of HELIOS can be found in Chapter 3. Phase plates were implemented on the experiment, to ensure a uniform beam profile on the cone walls. This enabled the expansion to be more accurately modelled in 1-D.

It is important that the hydrodynamic shock does not break through the inner cone wall before the acceleration of the protons from the SP2 interaction, which would disrupt the sheath field, as discussed in Chapter 2. Several snapshots in time are shown in Fig. 7.11 for the laser parameters chosen, showing the propagating ion density front through a 15 µm-thick target. Several example plasma profiles are shown in Fig. 7.12 for various laser parameters at the time (t_s) of shock break-through. From this figure, it's

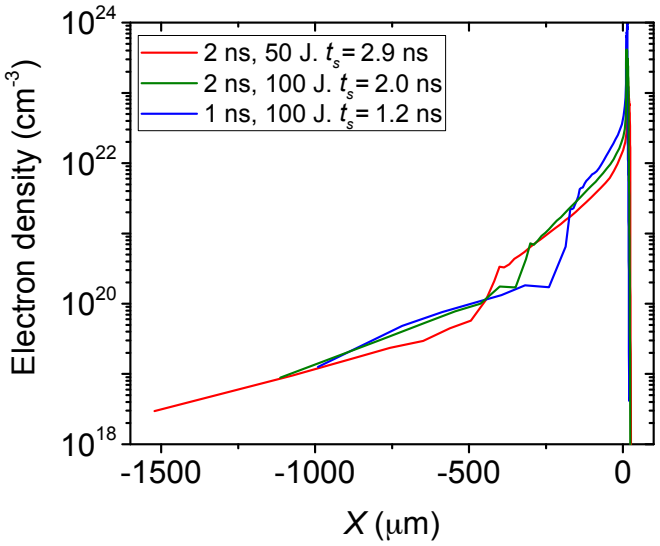

Figure 7.12: Several plasma density profiles for various laser parameters as a function of distance, X, with respect to the target rear (at position $X = 0$). t_s refers to the time the shock broke through the target rear.

clear that a 50 J, 2 ns pulse gives the most favourable plasma in terms of scale-length and density gradient before shock break-through. Note that other parameters were simulated (higher E_L, longer/shorter τ_L), resulting in an even less desirable plasma than the cases not shown in Fig. 7.12. To allow for any fluctuations in laser parameters, the LP beams were timed 2 ns prior to the short pulse beams.

Figure 7.13 shows the RCF slices for data, with and without long pulses, for both open and closed cone attachments. The use of long pulses beams, in the case of the open cone, completely inhibited any observed focusing of the accelerated protons. In both the open and closed cone cases, the maximum proton energy decreases by ~ 20 MeV when a surrounding plasma is present. Note that when irradiating the open conical structures, the long pulse beams had to be positioned 300 µm closer to the hemispherical front. In the first instance this translation was not performed, resulting in an almost complete suppression of the proton beam ($\varepsilon_{max} \sim 3$ MeV). This drop in signal is likely due to the rear-surface sheath field being disrupted, by either the surrounding plasma entering the open tip or by some stray laser light entering the cone and irradiating the rear of the hemispherical target, inducing expansion.

In the case of the closed cone with long pulse beams, the beam profile appears more circular and uniform. In the case of the open cone with long pulse beams, the beam appears less uniform and is likely due to the rear-surface field being affected in some

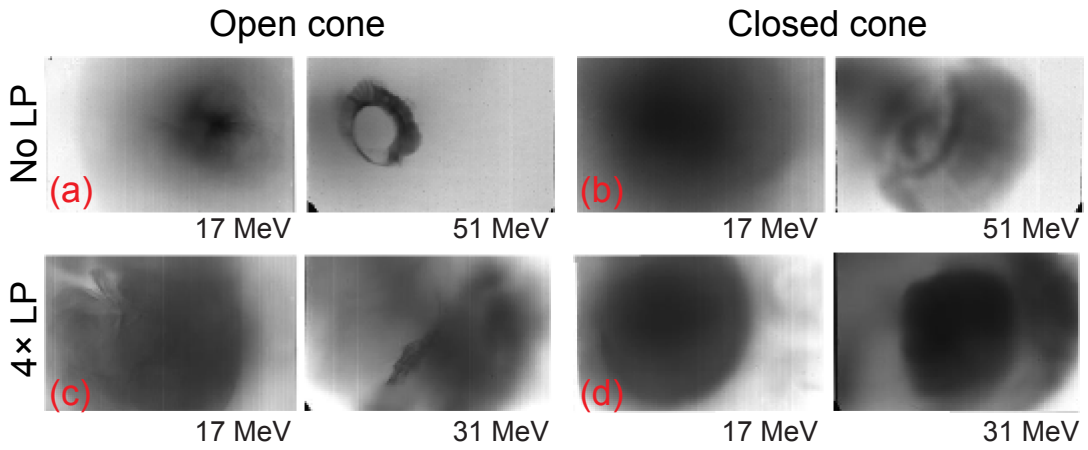

Figure 7.13: Dosimetry film (RCF) data comparing the accelerated protons from open and closed conical targets with and without four long pulse (LP) beams irradiating the cone walls. (a) and (b) correspond to the RCF data for open and closed cone with no long pulse beams, respectively; (c - d) same with four long pulse beams. Contrast of the images is scaled for clarity and is not representative of dose.

way by the expanding plasma entering the cone tip. This poses an issue for PFI, where an open cone is required to produce a focused proton beam. As seen from these results, the presence of a plasma results in no observable focusing, likely due to some of the plasma entering through the cone tip. Possible modifications to the open cone to resolve this issue are discussed in section 7.5.

In one case, the laser energy of one long pulse beam was far in excess of that modelled ($\sim$ 80 J). At this energy, the shock is expected to have broken through the cone wall before the arrival of the short pulse beam. Figure 7.14 displays several RCF slices diagnosing the accelerated protons. A region void of all proton signal is observed, and is likely the result of plasma expansion inhibiting the accelerating field on the rear of the hemispherical target at the position near the point of shock break-through. Note that, over the time-scales of proton acceleration (tens of picoseconds within the conical target), the expansion can be considered static, hence the size of the bubble-feature does not change.

7.3.3 Proton heating of Cu attachments

The MXI is a powerful visualisation tool for spatially resolving the proton beam directionality, by collecting K_α emission images. Figure 7.15a displays the imaging data for the vertical foam, showing the reference image along with the imaged Cu K_α emission. Figure 7.15b shows a line-out along the longitudinal position corresponding

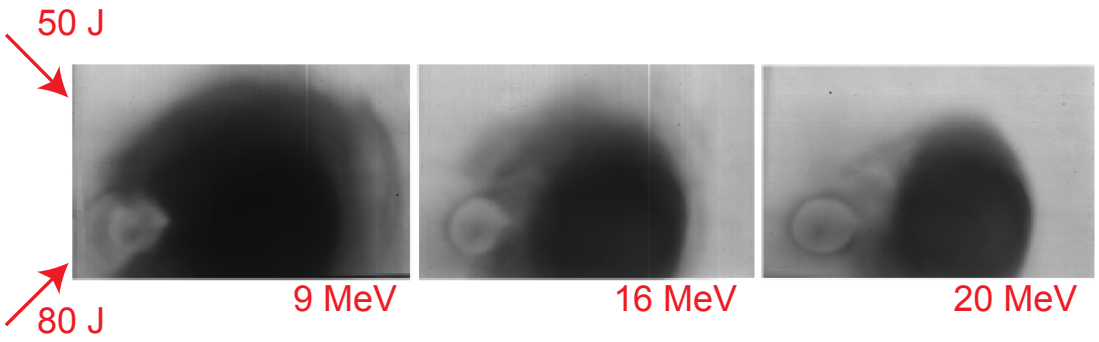

Figure 7.14: Processed dosimetry film (RCF) data diagnosing the accelerated protons from a hemi-closed cone target with two long pulsed beams irradiating the side of the cone (indicated by the red arrows). One of the long pulsed beams had significantly higher energy, which induced a faster shock through the cone than predicted which reached the cone interior some time prior to the arrival of the short pulsed beam, resulting in a void region in the proton signal.

to the central point of the proton heating. This is the only example where a noticeable decay over the longitudinal dimension was present, with a near-uniform temperature distribution obtained in every other case.

A two decay-pattern is visible, indicating energy deposition by two different types of radiation. The first term is likely due to energy deposition by protons, indicative by the sharp temperature gradient peaking near the front surface of the Cu foam as expected by heating with a Maxwellian-like (i.e. TNSA) proton beam. Such a temperature gradient was seen in Fig. 6.13, Chapter 6, where a front surface TNSA proton beam irradiated a 1-D slab of Al. The second, more gradual decay is likely due to either the fast electrons preceding the proton beam or by the emitted X-rays.

The reason why the vertical foam was the only example displaying a proton heating signature is at present unclear. The simplest explanation is that the other Cu attachments were getting much hotter than the vertical foam, and the emission was moving out of the working MXI spectral bandwidth. The maximum proton energy detected through the vertical foam was 15 MeV, whereas for the majority of the other Cu-attached data-set $\varepsilon_{max} \sim 40$ MeV was achieved. Therefore, it would be expected that the other Cu samples would reach a higher temperature than the vertical foam. Some other data-sets, however, had a similarly low proton energy; with the uniform signal still present.

A second hypothesis concerns the focusing of the protons. In the hemi-closed cone cases with no Cu attachment, proton focusing was not evident in any of the RCF images.

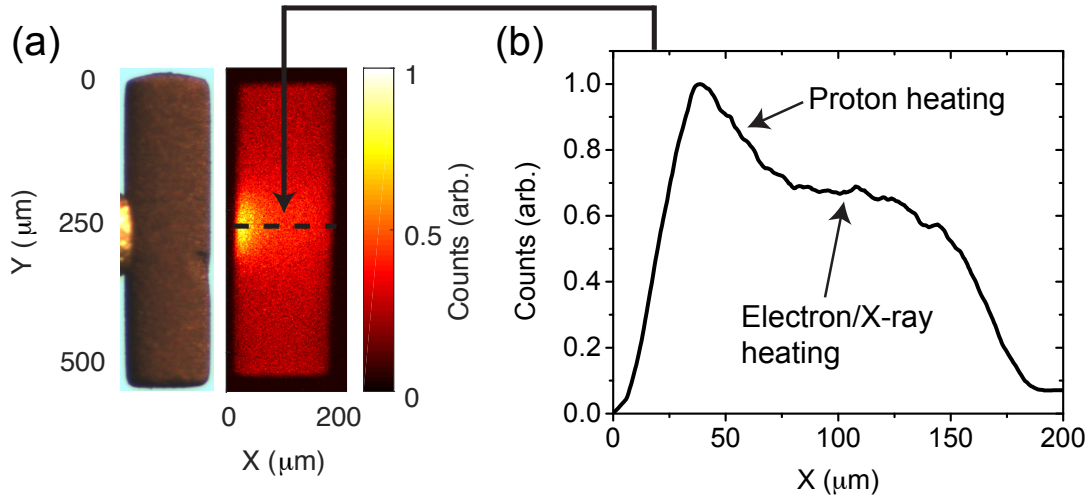

Figure 7.15: (a) Monochromatic X-ray Imaging data (right) for the vertical Cu foam attachment, imaging the Cu K_α X-ray emission. A reference picture of the foam is shown on the left. (b) 1-D line-out along the X dimension where the highest K_α signal is detected, indicated by the dashed black line. Two decay terms are present and are likely to result from proton heating and electron/X-ray heating.

Therefore, it is reasonable to assume that by attaching some form of Cu to the closed tip the outcome of this does not change. The vertical foam is the only example where the vertical size of the attachment is much greater than the cone tip, which may affect the circulating electrons travelling through/along the cone walls. A third hypothesis is that the type of cone tip used does not affect the focusing, and it instead relies on very accurate alignment of the focal spot to the apex of the hemisphere, which is difficult to achieve. As stated previously however, this is unlikely as more than five closed conical targets were irradiated, with none indicating any form of focusing.

The protons accelerated from the hemispherical target were affected by the Cu attachments, far more than simply stopping in matter could explain. Figure 7.16 displays some example RCF images for the three Cu species used in a horizontal orientation. Clear effects due to the Cu are observed. Note that from SRIM [94] calculations, a proton with an energy equal to 25 MeV would only lose $\sim$ 1 MeV travelling through a typical solid Cu attachment used (110 µm in length). The Cu sample is expected to be heated, however from the calculations in Appendix B a heated sample would only marginally increase the stopping power of a material. Therefore, stopping in the material is negligible. The reason for the change in profile observed is likely due to the circulating electrons around the cone travelled into the Cu, acting to charge it. The resulting field deflects the accelerated protons around the Cu, resulting

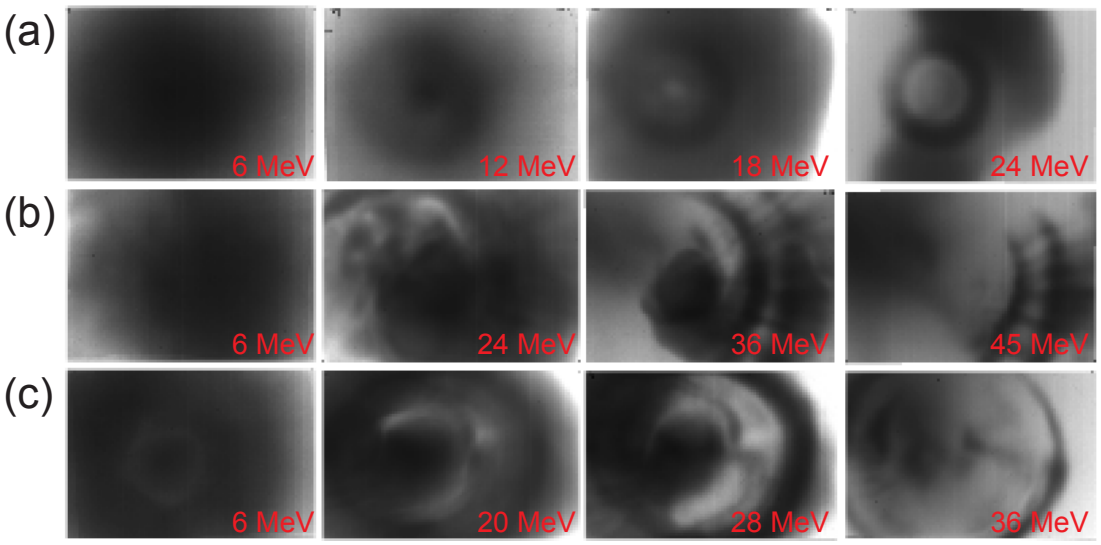

Figure 7.16: Several layers of dosimetry film (RCF) diagnosing the protons accelerated from a hemi-closed cone arrangement with a (a) solid Cu block; (b) CH-doped Cu; (c) Cu foam attachment on the rear of the cone tip. Contrast of the images is scaled for clarity and is not representative of dose.

in an annular beam density profile. The only case where this deflection is not observed is in the vertical foam case.

From Eq. 3.3 in Chapter 5, the peak electric field strength (E_{max}), averaged over the propagation distance, can be calculated assuming the protons deflected to the inner boundary (by a distance dx) of the annulus were deflected from the centre of the Cu attachment. Table 7.1 displays the variables used in Eq. 3.3, corresponding to the geometries of each Cu attachment, in addition to E_{max}. Each term is explained in the table caption. The distance over which the protons experience the peak field, b, is assumed as the length of the Cu attachment. It is valid to make this assumption for the smaller Cu block. However, as the length is increased (such as in the case of the Cu foam) the protons will begin deviating from the central region of the foam whilst still travelling through the length of the foam, resulting in a lower calculated E_{max}. Note that for each case the RCF piece sampled was the highest energy component, as it showed the clearest deflection. It is not expected that the type of Cu attachment used (due to the difference in density) would significantly affect the spectral profile of the proton beam, as the areal density is similar for all three. The change in the spectral profile of the beam is instead attributed to changes in the laser-drive parameters or inaccurate target alignment. Additionally, it should be expected that the smaller Cu attachments would reach a higher average field strength than the larger ones.

Type	ε_p (MeV)	dx (cm)	b (µm)	E_{max} (TV m^{-1})
Block	24	2.6	110	0.05
CH-doped	45	5.2	525	0.05
Foam	36	7.0	900	0.03

Table 7.1: The peak electric field, E_{max}, calculated from Eq. 3.3, responsible for the deflection of the protons seen in Fig. 7.16. The variables used in the calculations, from the target geometries, are also shown. ε_p is the proton energy corresponding to the layer analysed, dx is the distance from the centre of the annulus to the inner boundary of the ring on the diagnostic plane (10 cm downstream from the target) and b is the length of the Cu attachment.

7.4 Simulations

Preliminary simulations were performed using the self-consistent hybrid PIC code LSP [173, 174], which simulated the complete physical process concerning the electromagnetic fields surrounding the conical structure in 2-D. These simulations were performed by J. Kim, UCSD, CA, US. A population of fast electrons, the properties of which are based on the laser-drive parameters in the experiment, are directly injected at the apex of the hemispherical target. Simulating the laser in LSP is computationally expensive, hence why the electrons were directly injected. The injected electrons are defined as kinetic, like in PIC simulations, while the target electrons and ions are considered fluid. Both an open and closed cone were simulated, with the results at several time-steps shown in Fig. 7.17. Figure 7.17(a) Displays the electron density for the open cone (a near identical distribution was present in the closed cone case); Fig. 7.17(b-c) the transverse electric field (E_x) of the open and closed cone, respectively; Fig. 7.17(d-e) the longitudinal electric field (E_z) at $t = 6$ ps for the open and closed cone, respectively and Fig. 7.17(f-g) the B_y field at $t = 6$ ps for the open and closed cone, respectively.

From Fig. 7.17(a-b), it takes roughly 6 ps for the fast electrons to reach the cone tip. At this time, the highest energy protons are still contained within the conical structure. Comparing Fig. 7.17(b-c), the fields in both cases appear similar overall. Some differences exist. In the open cone case, the E_x field appears slightly stronger near the tip of the cone. This is the field responsible for focusing the accelerated protons, and has a larger effect on the tip than at any other location due its proximity (transversely) to the proton beam. The magnitude of the E_x field is of the order 0.1 TV m^{-1}, which

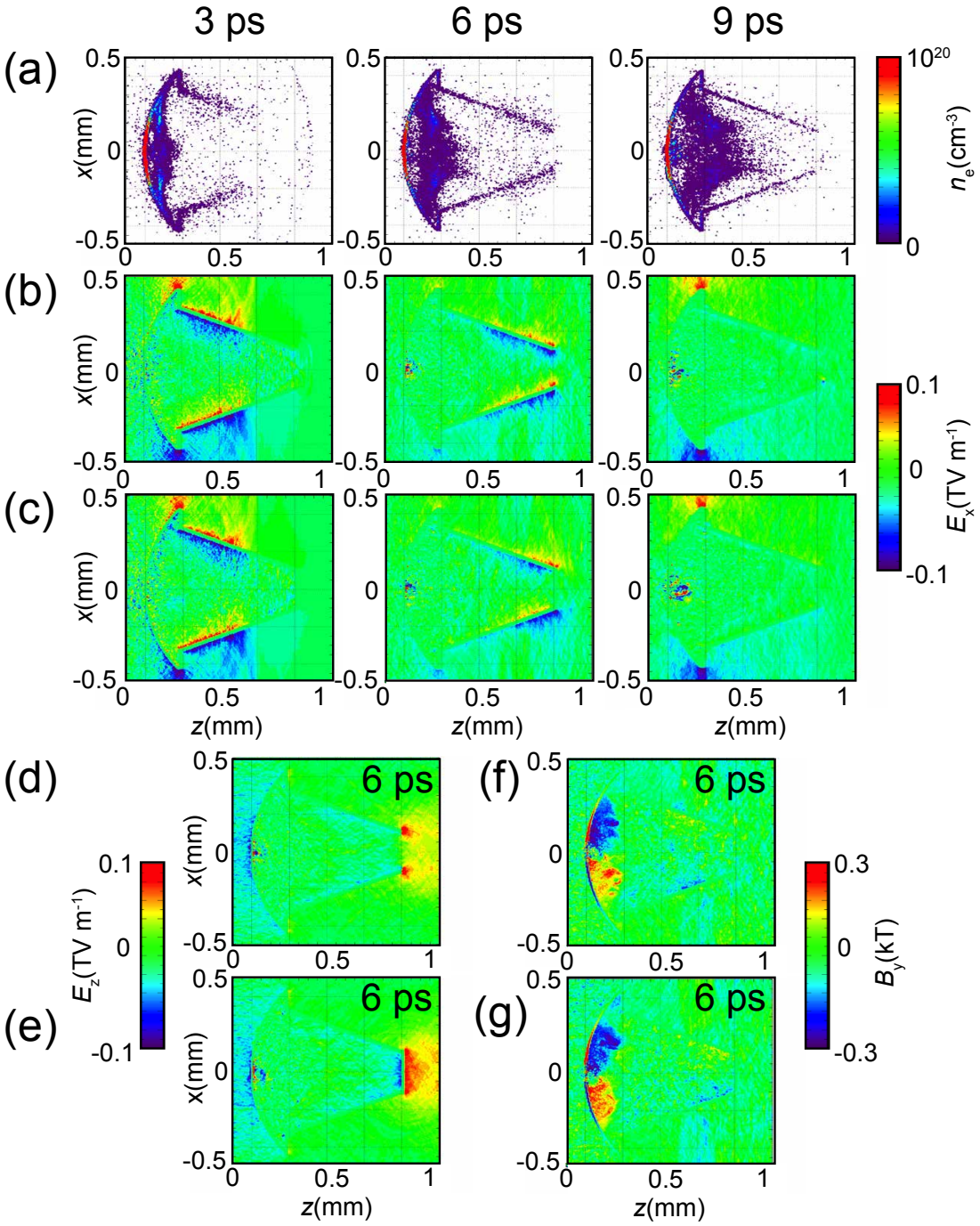

Figure 7.17: LSP simulations for open and closed-tip cones at several snapshots in time. (a) The electron density for an open tip cone. (b-c) The transverse electric field (E_x) for an open (b) and closed (c) tip cone. (d-e) Longitudinal electric field (E_z) at $t = 6$ ps for an open (d) and closed (e) tip cone. (f-g) B_y field for an open (f) and (g) closed tip cone at $t = 6$ ps. Simulations courtesy of J. Kim, UCSD, CA, US.

is close to the value calculated from the measurements of deflected protons in the experiment (~ 0.5 TV m^{-1}).

One other difference concerns the E_z field, Fig. 7.17(d-e), which builds up on the cone tip and would act to accelerate the protons slightly more along the longitudinal direction. While unlikely, due to the relatively low strength of the E_z field, in the open cone case this could act to boost the energies of protons in an annular ring. In the closed cone case it would simply boost the entire beam. The B_y field in both cases is almost identical, and is relatively strong on the rear-side of the hemispherical target. This field would act to counter the focusing induced by the E_x field, particularly at early times, and may result in an annular proton distribution of the high energy (i.e. early time) components.

After 10 ps the field starts to decay rapidly. As it takes around (14 ± 4) ps for the protons that appear focused ($\varepsilon_p = (20 \pm 10)$ MeV) to reach the rear of the cone tip in the open cone case, it seems unlikely that the fields produced in the LSP simulations would focus the protons within these time scales. From Fig. 7.8, clear field structures are observed at late times ($t = 60 \pm 25$ ps) which are not present in the simulations at these times. Therefore, the simulations should only be used as a guide of the physical picture; to illustrate the general field structure and strength expected in the experiment.

7.5 Discussion

At present, it is still unclear why the open cone appears to be more-suited for proton focusing that the closed cone. From the LSP simulations, it's expected that the electron current flowing along the cone walls is responsible for proton focusing, and acts like an electrostatic lens which appears to focus protons within the energy range of (20 ± 10) MeV in the plane of the detector. From the simulations, the transverse field appears slightly stronger at the tip of the cone in the open cone case, acting to focus the protons more than in the closed cone case. Two hypothesis exist that may explain the annular structure observed in the open cone case. The first explanation concerns the current of electrons inducing a strong magnetic field near the cone walls, acting to counteract the focusing. Another explanation is that at early times the transverse electric field is strong enough that it over-focuses the fastest protons, resulting in an annular beam profile on the detector plane.

The ion beam shown in Fig. 7.7 is interesting for PFI, where it starts as a hollow beam for high energies and then closes into a focused beam at lower ion energies, for which the proton number density increases. In one scenario of the PFI concept, two proton beams are used: the first to generate a radial shockwave, requiring a hollow ion beam, and the second to cause ignition (as described in section 2.6). The beam measured in the open-cone case would effectively eliminate the requirement for two separate beams, fulfilling both requirements. It is noteworthy that the beam presented here appears focused over such a large spectral window.

7.6 Conclusions and further work

Initial steps towards investigating the underlying physics of high-current proton acceleration and focusing using novel conical targets were addressed. Multiple conical target species were used, in order to further our understanding of proton focusing and the effects that the structures had on the laser-to-proton conversion efficiency. Clear focusing was only observed in the open-cone arrangement, with little variation in the laser-to-proton conversion efficiency through the entire data-set. At high energies (> 40 MeV), the beam appeared annular. At energies around (20 ± 10) MeV a clear focused component was observed. Proton radiography of the conical targets was also performed, with the fields surrounding the front surface characterised.

The influence of a plasma surrounding the cone on proton focusing was also investigated, by using four long pulse beams to uniformly induce plasma expansion before the arrival of the short pulse beam. The resulting plasma quenched any focusing effects observed, whilst also reducing the overall flux of protons and maximum energy of the protons accelerated by ~ 20 MeV.

Lastly, the beam of accelerated protons was used to heat several types of copper, with the X-ray emission imaged. The Cu samples appeared to deflect the accelerated protons, with the peak field strength of the cone estimated based on the degree of deflection experienced by the highest energy protons. Fields of the order ~ 0.05 TV m^{-1} were calculated for all of the Cu samples used, and showed good agreement with those calculated in the simulations (~ 0.1 TV m^{-1}).

7.6.1 Further work

From this proof-of-principle experiment, further work on optimising the target geometries for proton focusing should be performed, by altering the hemispherical curvatures and cone angles. By using RCF to diagnose the main beam measurements in conjunction with deflectometry, the optimum field arrangement for the purposes of proton focusing can be achieved.

As stated in section 7.1, one of the key challenges PFI faces is the high conversion efficiency required. New target manufacturing techniques altering the hemispherical surface are anticipated to lead to greater conversion efficiency and/or maximum energy. This is based on an experiment at the CLF (conducted by Roth *et al.*, currently unpublished) using micro-structured targets [177]. In addition, as seen in simulations and in previous experiments, the imprint of the laser focal spot strongly influences the TNSA sheath field and is vital to the focusing capability. For PFI, where the superposition of multiple kJ short pulse lasers is required, the resulting focal spot and electron source size is large. The effects of a large focal spot on conversion efficiency and final proton focal spot quality should thus be investigated.

From the results presented here, the open cone arrangement is the only configuration that demonstrates proton focusing. The introduction of a plasma, however, appears to counteract this focusing and disrupts the beam. In PFI a plasma will exist around the cone and so it is imperative this issue is addressed. A likely factor contributing to the disruption is plasma flow into the cone tip. By closing the tip off with an insulating material, the effects of plasma flow into the tip will be inhibited. Also, provided the conductivity is low enough (such that the insulating material does not behave like the closed Au tip), the effects that a closed Au tip have on the focused beam should be avoided.

The key physics of proton heating to produce states of WDM could also be achieved, using a very similar experiment set-up as the one used in this chapter. By using the MXI operating in streaked absorption mode ($\sim$ 10 ps resolution), with an X-ray backlighter driven by a long pulse beam, opacity and volume measurements of expanding materials heated by the focused protons can be achieved. Next, by inducing a 1-D shock through these materials with a long pulse driver, and performing the same MXI measurement as before, the shock transit time can be measured. A final interesting measurement would

be to compress the samples with long pulse beams, and heat the sample with a focused beam of protons. For all of these WDM measurements the temperature of the samples could be measured using streaked optical pyrometry.

Chapter 8

Conclusions and future prospects

Laser-driven ion beams have applications in the laboratory, including the probing of highly transient electromagnetic fields [100], as demonstrated in Chapters 5 and 7, and the creation of warm dense matter [17], as accomplished in Chapter 7. Societal applications, such as hadron therapy [113] and the fast ignition approach to inertial confinement fusion [16] require several key physics issues to be addressed. These include higher maximum ion energies, an increase of the laser-to-proton conversion efficiency, and the ability to control the spectral and spatial profile of the resultant ion beam.

The work in this thesis addresses some of this physics, and is the result of three experimental campaigns using the Vulcan and Orion high-power laser facilities. Significant advances in the understanding of the physics of ion acceleration were made, with each chapter focusing on a key issue or process that must be addressed to realise these prospective, real-world applications. In addition to the three experimental programs of work, simulations were performed in order to provide additional insight into the physics underpinning the dynamic processes investigated.

Chapter 4 reports on an investigation of a hybrid RPA-TNSA scheme for proton acceleration, with energies boosted by a RIT-driven jet of super-thermal electrons. Efficient acceleration of protons with a cut-off energy in excess of 94 MeV was achieved; the highest published proton energy resulting from a laser-plasma interaction to date. In Chapter 5, the electrodynamic sheath field driving TNSA is characterised, with the dynamics responsible for laser-driven ion acceleration in this regime directly observed; providing the most detailed measurement of its kind to date. For the same experimental campaign as that reported in Chapter 5, Chapter 6 reports on the effects that an increasingly expanded target has on ion acceleration. Finally, in Chapter 7, initial

steps towards investigating the physics underpinning proton focusing using novel conical targets is addressed.

Conclusions from each of these chapters are outlined in the following sections.

Ion Acceleration via a laser-driven transparency-enhanced hybrid acceleration scheme

The work presented in Chapter 4 reports on an experimental and simulation investigation of proton acceleration in the interaction of ultra-intense, linearly polarised laser pulses with ultrathin foils. The work is published in Ref. [5]. Efficient acceleration ($10 \pm 2\%$) of protons with energies exceeding 94 MeV is demonstrated, for plastic targets with an optimal thickness between 75 - 90 nm. Simulation results show that the acceleration occurs via a dual-peaked electrostatic field, produced via a combination of the RPA and TNSA mechanisms. RIT enhances the fields and produces a magnetically confined and directional jet of super-thermal electrons that drives higher proton energies over a relatively narrow angular range. Experimental measurements of both the critical surface velocity and transmitted laser light confirm that both RPA and RIT occur for targets at the optimal thickness.

It is demonstrated that by controlling the onset of RIT, it is possible not only to enhance the maximum proton energy in the RPA-TNSA hybrid acceleration regime, but also to manipulate the directional properties of the final proton beam. The range of parameters over which this hybrid scenario is valid are discussed, as are the implications on ion acceleration driven by next-generation, multi-petawatt laser facilities, such as the Extreme Light Infrastructure [26, 27], Apollon [28] and XCELS [29]. By extrapolating the results via analytical and PIC modelling, RIT is expected to play a key role for relatively long ($\sim$picosecond) pulses over a wide range of laser intensities. By changing the target thickness, and potentially the rising edge intensity profile, it is possible to transition between hybrid schemes with different dominating mechanisms; effectively altering the properties of the resulting proton beam.

These results are an important step towards the use of hybrid acceleration schemes to tune the spectral and spatial properties of the resulting proton beams, and are accessible during the early stages of operation of next-generation multi-PW laser facilities.

Investigation of the electrodynamic sheath field driving proton acceleration

TNSA is the most widely investigated, robust, laser-driven ion acceleration process to date; capable of accelerating ions with laser intensities as low as $\sim 10^{17}$ Wcm^{-2}. In the work detailed in Chapter 5, a laser-driven proton beam is used to diagnose the evolution of the highly transient field responsible for ion acceleration in the TNSA scheme. Temporally-resolved measurements, with sub-picosecond resolution, are reported. Two key features of the sheath field are diagnosed. The first distinct feature, from our interpretation of the radiographs, is the rear-surface electron plasma. Detailed information regarding the dynamics of this plasma are diagnosed and discussed, including the near-static longitudinal extent of the cloud and how it evolves transversely.

The second feature appears as deflections of the probe beam, due to the magnitude of the sheath field. Based on these measurements, the average field strength of the Guassian-like sheath field and the peak field strength are estimated. These are ~ 0.06 TVm^{-1} and ~ 1 TVm^{-1}, respectively. A detailed comparison is made between the experimental measurements and the electric fields determined from 2-D PIC simulations. A charged particle tracker is used to simulate the propagation of a probe proton beam through the field structures obtained, with excellent agreement found, confirming that the sheath field is responsible for the measured deflections.

As outlined previously, the use of ion beams for the detection of transient electromagnetic fields is one of their most promising applications, due to their short temporal duration, spatial quality and high-degree of laminarity. Scaled-up simulations were also performed, to gauge the diagnostic's response to higher laser intensities. The magnitude of deflection scales as expected, further confirming proton deflectrometry works for a wide variety of parameters. These results, in addition to diagnosing the sheath field to a higher accuracy than previously accomplished [58] at early times relative to the interaction, demonstrate the effectiveness of using a laser-driven proton beam to probe such a field structure.

Investigating target expansion dynamics via ion acceleration

In Chapter 6, the effects that an increasingly expanded target have on the acceleration of ions via TNSA is investigated. An aluminium target is heated using a secondary laser-accelerated proton beam, irradiating the entire rear surface. For an increasingly expanded target the maximum proton energy, overall number of accelerated protons and the size of the proton beam consistently decreases. A simple analytical model describing the expansion behaviour is developed, based on the 1-D plasma expansion model detailed in the work by Mora [61], which enables the plasma expansion length to be calculated, based on the decrease in maximum proton energy as a function of proton flux and time after irradiation.

A series of radiation-hydrodynamic simulations, using measured parameters derived from the input proton beam, support these findings. The simulations provide key insights into the heated target dynamics, indicating that it is the expanding hydrocarbon layer that results in the reduced maximum proton energy. From the experimental results, it is possible to determine the temperature of the expanding hydrocarbon layer by matching the calculated plasma expansion lengths to the simulations.

These results have implications for proton fast ignition (PFI). A factor of ~ 5 decrease in proton number for 1 MeV protons is observed for a expanded layer equal to $\sim 5\,\mu m$, which is the degree of expansion expected in a realistic PFI scenario. This is different from previous measurements [131] that used a defocused laser pulse to induce expansion. In the work detailed in Fuchs *et al.* [131], the small focal spot size relative to the size of the electrostatic sheath field would result in the low energy protons largely being unaffected for a small degree of expansion. Therefore, our technique of inducing expansion is advantageous, and provides a more accurate picture of the changes to the resulting proton beam for an expanded target rear surface.

By inducing a small amount of target expansion, a clear focused component is observed in the spatial-intensity distribution of the proton beam at low energies. From our interpretation, this is likely a consequence of the non-uniform radial heating profile induced by the proton beam. Such a beam may be well-suited for applications in PFI and the generation of high-energy density matter.

Physics underpinning proton focusing via curved and conical targets

In Chapter 7, initial steps towards the investigation of proton focusing and laser-to-proton conversion efficiency for the purposes of PFI using novel conical targets is addressed. Clear focusing is only observed for the open cone arrangement, with little variation of the laser-to-proton conversion efficiency through the entire data set. At high energies (> 40 MeV) in the open cone case, the beam appears annular. At energies around (20 ± 10) MeV, a clear focused component is observed. Proton radiography using an auxillary laser-driven proton beam enabled the fields surrounding the targets to be characterised. The field is long-lived (~ 50 ps), with clear deflection of the probe protons due to the fields present approximately two orders of magnitude after the drive pulse has gone.

To close in on a realistic PFI scenario, the influence of a plasma surrounding the cone on proton focusing was investigated. Four long pulse beams were used to uniformly induce plasma expansion, before the arrival of the short pulse beam. The induced plasma effectively quenched any focusing effects observed, whilst also reducing the overall flux of protons and the maximum energy of the protons by ~ 20 MeV.

Lastly, the beam of accelerated protons was used to heat several types of copper of varying densities, with the resultant X-ray emission imaged. The Cu samples appeared to deflect the accelerated protons, with the peak field strength of the Cu attachments (based on the degree of deflection experienced by the highest energy protons) calculated. Fields of the order ~ 0.05 TV m^{-1} were calculated for all of the Cu samples used, and showed good agreement with those determined from the simulations.

8.1 Future work

The results presented in this thesis are an important basis for future research into laser-driven ion acceleration.

A key theme of each chapter is the investigation of a fundamental aspect of ion acceleration physics. The main focus of current research in laser-driven ion acceleration is to increase the maximum energy of the ions accelerated, decrease the energy spread, increase the laser-to-proton conversion efficiency, and to control the spatial-intensity

profile of the ion beam. This thesis addresses aspects concerning all of these issues. A number of routes may be taken to achieve these goals, and from an experimental point of view there are several clear areas that may be developed.

The precise control of the experimental conditions is a challenging aspect of conducting experiments in the field of high power laser-plasma interactions, with fluctuations in the laser parameters that are often difficult to quantify. Additionally, due to the laser shot repetition rate common for high energy lasers (30 - 60 mins), it is difficult to obtain statistics of the data obtained. The limiting factor, from the external users end, is often due to opening the target chamber to replace the dosimetry film (RCF) stacks and solid targets, in addition to the time required to align the targets - requiring micrometer precision along the laser axis. This is a particular problem when using 40 fs laser systems, that are capable of generating pulses with a 10 Hz repetition rate. These limiting factors may be reduced. For example, transitioning to an active proton diagnostic would greatly increase the repetition rate. Efforts concerning auto-alignment techniques, in addition to using liquid crystal targets that are produced directly in the target chamber (using a sharp blade that slides across an aperture on a metal frame) [178], would massively increase the repetition rate from a target point of view. A detailed summary of the target requirements for high repetition laser facilities can be found in Ref. [179].

As ever, the current state of the art is progressing. Future investigations of ion acceleration using next generation, multi-PW laser facilities that are presently under development will open up an entirely new regime in the field. The results presented in Chapter 4 are particularly important for these developments, as the facilities are expected to produce pulses of light with intensities up to 10^{23} Wcm^{-2}. This would render near-solid density foils relativistically transparent, thus increasing the role of RIT-driven processes. Additionally, due to the difficulties of converting the inherently linearly polarised light to circular polarisation (due to the large diameter of the collimated beam), linearly-polarised hybrid acceleration schemes are likely to prevail. The modelling presented in Chapter 4 suggests that, within the range of parameters expected for next-generation laser facilities, the choice of target thickness can be optimised for either high proton energies or for the production of a narrow-band spectral peak.

The work presented in Chapter 6 illustrates the importance of increasing the laser-to-proton conversion efficiency for PFI. For a presently achievable $\sim$10%, the high laser

drive energies required result in significant expansion of the target rear surface, due to the fast electron population generated by the leading edge of the pulse. This results in an inhibition of the accelerated protons in the spectral bandwidth necessary for PFI. Therefore, schemes particularly suited for the optimisation of the conversion efficiency, such as those outlined in Chapter 4, should be implemented.

The work presented in Chapter 7 provides an initial investigation into the physics of PFI, with applications concerning the study of high energy density physics (e.g. the creation of WDM). By changing the angle and size of the conical structure, it may be possible to optimise the focusing effect for different spectral components of the proton beam, allowing non-uniform heating gradients to be induced within the irradiated samples. It was also discovered in Chapter 6 that an annular expansion profile resulted in a focused component in the beam profile. By altering this profile, it may be possible to tune the spectral components that appear focused. WDM, generated by these proton heating techniques, may be characterised by temporally resolving the X-ray emission, with opacity and volume measurements possible through the use of an X-ray backlighter. Scope to conduct an experiment diagnosing WDM in this way exists using a dual short pulse laser system, such as Orion or TAW.

Appendix A

Characterising the on-shot abberations on Vulcan

The implications for the resulting proton beam due to the defocus present on Vulcan is detailed. This appendix is relevant to the discussions presented in Chapter 4. Defocus is a lower-order wavefront abberration, and results in the focal position of the Vulcan laser fluctuating. The wavefront on-shot is characterised using a HASO Shack-Hartmann wavefront sensor (SHWFS), which provides information regarding the aberrations present in the laser beam. The sensor is based on an aperture array, developed by J. F. Hartmann in 1900 [180], for the purpose of tracing individual rays of light through the optical system of a telescope to test the quality of the image. The sensors used now operate using an array of lenslets [181]. A schematic illustrating the operational principles of a SHWFS is shown in Fig. A.1. The main aberration which causes issues on the Vulcan laser system is the defocus (Zernike mode Z_2^0). In our case, this resulted in a maximum defocus (longitudinally with respect to the laser propagation axis) of a distance approximately equal to the Rayleigh range (i.e. $\sim$40 µm). The Rayleigh range is defined as the position, from focus, where the beam waist increases by a factor of $\sqrt{2}$. This translates to an intensity decrease of a factor of two. By quantifying the level of defocus present on any one shot, a telescope lens is used to correct for the defocus, such that the subsequent laser-shot will be closer to best focus position. At present, it is unclear where the defocus originates from, which is likely a thermal lensing effect. However, it does appear to have a dependence on the number of laser-shots taken on a given day. The Vulcan laser group are investigating this at present.

Figure A.2 displays the maximum proton energy, ε_{max}, as a function of the peak

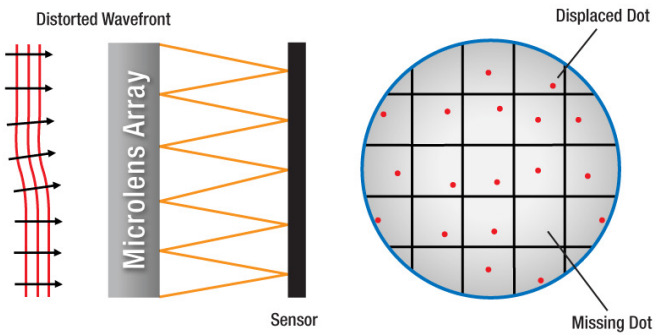

Figure A.1: Schematic of a microlens array focusing a distorted wavefront. When a wavefront enters the lenslet array, a spotfield is created on the sensor. The spot is then characterised in terms of its intensity and position. Figure reprinted from [182].

laser intensity, I_L, for two plastic target thicknesses. Figure A.2a shows the value of I_L without accounting for the level of defocus present, which is compared to Fig. A.2b which accounts for the defocus. Clearly, the defocus has a significant effect on the resulting proton beam. The calculations in Fig. A.2 also take into account the energy on-target, the energy contained within the FWHM and the size of the focal spot at best focus (characterised before each shot). For all laser-shots above $\sim$ 400 J (pre-compressor) the auto-correlator (AC) trace was saturated. However, several shots with a lower laser energy were performed, with the AC consistently measuring a pulse duration equal to 1.0 ps. This is used to calculate all of the intensities presented. Comparing the two graphs, some of the intensity points increase in the case shown in (b). This is because the energy contained within the FWHM is slightly higher at certain longitudinal positions away from best focus. This was characterised by imaging the focal spot with a CCD camera at various longitudinal positions, over a series of low-power shots.

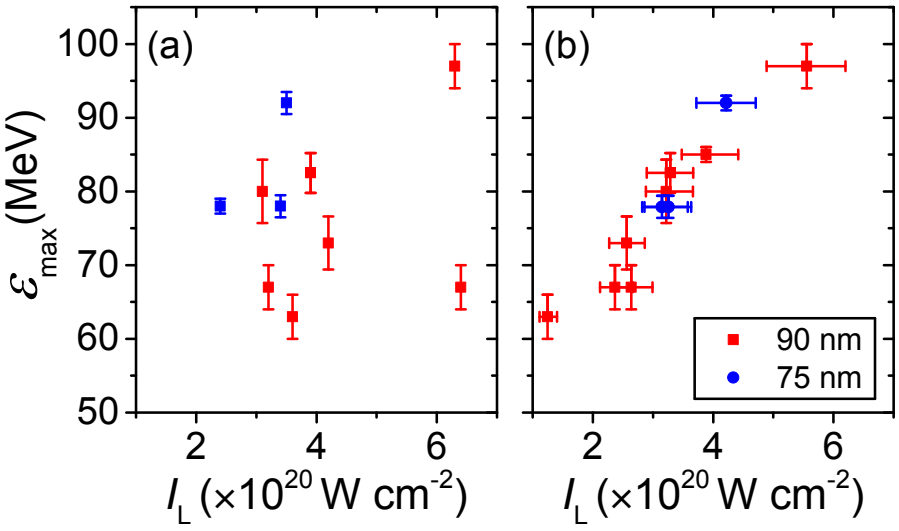

Figure A.2: Maximum proton energy (ε_{max}) as a function of laser intensity (I_L), illustrating the importance of accounting for the inherent defocus present on the Vulcan laser in TAP. (a) Without accounting for the level of defocus; (b) accounting for the level of defocus. The level of uncertainty in (b) is explained in the main text.

Appendix B

Proton stopping

This appendix details the simulations, modelling and calculations concerning proton stopping in Chapter 6. Two effects were investigated. Initially outlined are the effects due to the electromagnetic fields generated in the laser-Target 1 interaction, and the possible effects this would have on proton transit in the time-scales considered. Secondly, the effects due to proton stopping in the target bulk are outlined. Both cold and hot matter are considered.

Laser-generated electromagnetic fields

The effects due to proton energy loss as a result of the electromagnetic fields generated in the Beam 1-Target 1 interaction are discussed here. The magnitude, spatial extent and temporal dependence of the electrostatic fields on the surface of Target 1 were investigated using the fully relativistic, 2-D EPOCH PIC code [109] (detailed in Chapter 3). The target was initialised as a solid density 2 µm Si^{12+} slab, neutralised with an appropriate number of electrons, with initial temperature equal to 10 keV. The simulation box was 57 µm × 60 µm, with a mesh cell size equal to 5 nm × 10 nm. All simulation boundaries were defined as free-space. The laser was incident normal to the target, with Gaussian temporal and spatial profiles (FWHM equal to 100 fs and 6 µm respectively) and $I_L = 2 \times 10^{20}$ Wcm^{-2}. The simulation ran for 2.2 ps, in order to accurately determine the rate of decay of the electromagnetic fields. Data outputs were taken every 0.2 ps.

The results of the simulation are shown in Figure B.1. Figure B.1a shows the evolution of the peak electric field in the longitudinal (laser) direction ($E_{\mathrm{x,\ max}}$); located around 1 µm from the rear of the target. $E_{\mathrm{x,\ max}}$ decays linearly, and upon interpolation

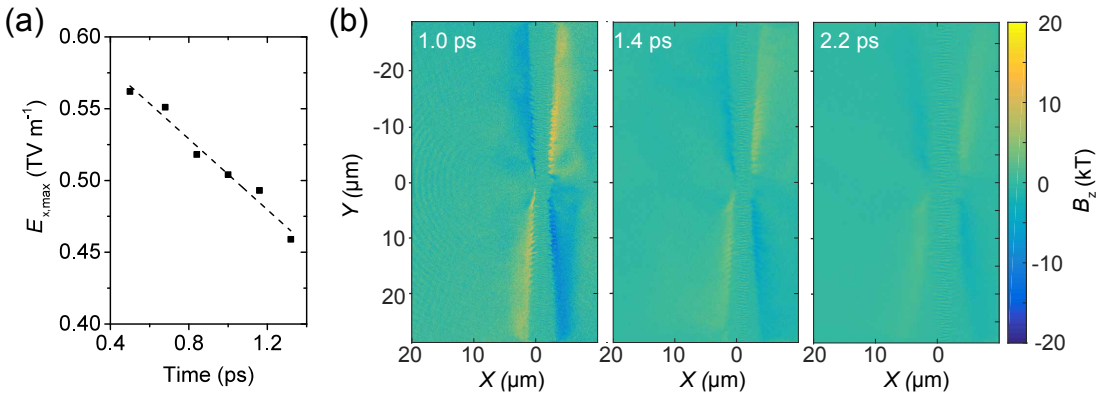

Figure B.1: 2-D EPOCH simulations showing the field evolution as a function of time after laser irradiation. (a) Peak electric field ($E_{\mathrm{x,\,max}}$) in the longitudinal dimension X. (b) B_{z} field at 1, 1.4 and 2.2 ps. The front surface of the target is located at X = 0 µm.

of the linear trend the field decays to zero at ∼6 ps. A 1-D line-out of the E_{x} field along the X dimension shows that it decays rapidly from the rear of the target, down to ∼ 25% of the peak value at 5 µm. Figure B.1b displays the evolution of the transverse (relative to the laser) magnetic field, B_{z}, over several times. B_{z} also decays rapidly, decreasing from around 20 kT to < 5 kT over 1.2 ps. Owing to the relatively short (relative to t_{heat}) life-times of the electromagnetic fields of Target 2, the effects due to the electrical charging of Target 1 from Beam 1 can be neglected as having an effect on the protons accelerated from Target 2 in the temporal window discussed in Chapter 6.

Proton stopping in heated matter

The effects due to proton energy loss in the bulk material of Target 1 are addressed here. Charged particle stopping in cold matter occurs primarily through Coulombic interactions between the particle and material's electrons, through the ionisation and excitation of the electron cloud surrounding the material's atoms. From relativistic quantum mechanics, stopping power (i.e. the mean rate of energy loss) is well described by the Beth-Bloch theory [133, 134], which treats the energy loss of the incident particle to the target nuclei as scattering of a charged particle from an isolated atom. For a uniform elemental medium with electron density n_e and atomic number Z, this is given by [183]:

$$-\frac{dE}{dx_b} = \frac{4\pi {k_B}^2 Z^2 e^4 n_e}{m_e c^2 \beta^2}\left(\ln\frac{2m_e c^2\beta^2}{I_e(1-\beta^2)} - \beta^2\right), \tag{B.1}$$

where k_B is Boltzmann's constant, Z is the atomic number of the charged particle, e is the magnitude of the electron charge, n_e is the number of electrons bound to an atomic nucleus per unit volume in the material, m_e is the electron mass, c is the speed of light in vacuum, β is the speed of the particle relative to c and I_e is the mean excitation potential per electron of the material. Additional terms are included in Fano's works [184], however these are near negligible for the parameter-space investigated. I_e is estimated following approximate empirical formulae, calculated using the quantum mechanical approach or measured experimentally. For an element with atomic number Z this can be approximated by:

$$I_e \approx \begin{cases} 19.0 \text{ eV} & Z = 1 \\ 11.2 \text{ eV} + (11.7 \times Z) \text{ eV} & 2 \leq Z \leq 13 \\ 52.8 \text{ eV} + (8.71 \times Z) \text{ eV} & Z > 13. \end{cases} \tag{B.2}$$

In this formulation, the velocity of the ion is taken to be fast relative to the orbital velocity of the atomic electrons. Also, any energy loss to nuclear reactions between the particle and target nuclei are ignored. A comprehensive summation of the Bethe-Bloch cold-stopping theory can be found in the review article by Ziegler [183].

In the experiment detailed in Chapter 6, the effects due to the heating of Target 1 by Beam 1 must be considered. Laser-irradiation leads to ionisation, therefore I_e must be scaled to account for the degree of ionisation of the target. This scaling takes the form:

$$I'_e = I_e \frac{Z^2}{(Z - Z_i)^2}, \tag{B.3}$$

where Z_i is the ionisation charge state. As discussed earlier, protons primarily lose their energy due to Coulomb interactions with electrons. Additional free electrons increase this stopping, which is captured in the equation [185]:

$$\frac{dE}{dx_f} = \frac{-4\pi e^4 n_{fe}}{m e v_p^2} L_{fe}, \quad L_{fe} = \ln \frac{2 m_e v_p^2}{\hbar \omega_p}, \tag{B.4}$$

which describes the stopping power of free electrons for fast protons in a plasma. This formula is based on work by Larkin [132]. In Eq. B.4: n_{fe} is the free electron density (i.e. the total electron density minus n_e), v_p is the proton velocity, L_{fe} is the Coulomb logarithm, $\hbar$ is the reduced Planck's constant and $\omega_p = (4\pi n_{fe} e^2 / m_e)^{1/2}$ is the plasma

frequency. Note that Eq. B.4 is in Gaussian cgs formalism. The total stopping of Target 1 is therefore a combination of the corrected bound stopping and free stopping terms:

$$\frac{dE}{dx_{tot}} = \frac{dE}{dx_b} + \frac{dE}{dx_f}. \tag{B.5}$$

The calculations were performed for solid Al, assuming a nearly fully-stripped nucleus ($Z_i = 11$). This is the highest charge state expected with our experimental parameters, and is the ionisation state Al is normally initialised in PIC simulations. For these patameters the individual stopping components were implemented into a MATLAB routine, with an iterative while loop incorporated to continually calculate the new stopping power of the sample proton such that the energy drop of the subsequent time-step could be determined. The spatial resolution was 1 µm, and the calculations were performed until the proton energy dropped below 0.1 MeV.

Figure B.2 displays the results of the calculations incorporating Eq. B.5 for several initial proton energies. Figure B.2a shows the proton energy as a function of depth, with the inset enlarging the region of interest (based on our experimental parameters). The solid lines are for a 'cold' material, with no free electrons, while the dashed line is for $Z_i = 11$. Figure B.2b displays the stopping power as a function of depth, for the same modelled parameters. The 'cold' penetration depths were benchmarked against those obtained using the SRIM software package [94], and showed excellent agreement for the parameters studied.

From Fig. B.2, it's clear that for the thicknesses involved in our experiment, the differences between a hot and cold target are near negligible, especially considering the maximum stopping case possible was considered in the modelling ($Z_i = 11$) for the entire target. Some energy loss can be attributed to cold stopping, however all of the calculations in section 6.6 are made with reference to the cold target with no Beam 1, thus taking this into account.

Density effects were also investigated, as in the modelling above the target is assumed to be isochorically heated, with no hydrodynamic expansion. A 16 MeV proton was modelled for a target at half-solid density, with the proton traversing exactly twice the distance compared to solid density in the cold case, meaning it is an areal density effect and that an increasingly expanded target results in no additional stopping.

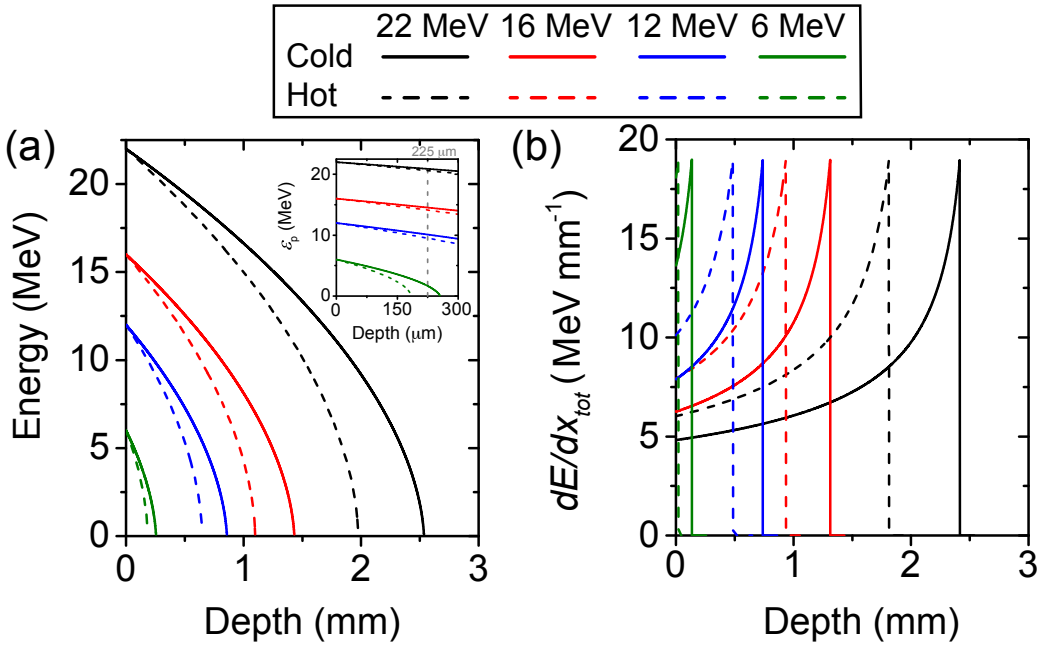

Figure B.2: Proton stopping in Target 1, for several initial proton energies. The black series corresponds to the maximum proton energy measured (22 MeV). (a) Proton energy remaining as a function of depth. Inset: region of interest, based on the experimental parameters. (b) Corresponding total stopping power, calculated from Eq. B.5, as a function of depth.

Bibliography

[1] R. Wideröe. Über ein neues prinzip zur herstellung hoher spannungen. *Archiv für Elektrotechnik*, 21:387 – 406, 1928.

[2] P.W. Lisowski *et al.* The Los Alamos national laboratory spallation neutron sources. *Nuclear Science and Engineering*, 106:208–218, 1990.

[3] W.I. Linlor. Ion energies prodiuced by laser giant pulse. *Applied Physics Letters*, 3:210–211, 1963.

[4] D. Strickland and G. Mourou. Compression of amplified chirped optical pulses. *Optics Communications*, 56:219 – 221, 1985.

[5] A. Higginson *et al.* Near-100 MeV protons via a laser-driven transparency-enhanced hybrid acceleration scheme. *Nature Communications*, 9:724, 2018.

[6] U. Amaldi and G. Kraft. Radiotherapy with beams of carbon ions. *Reports on Progress in Physics*, 68:1861, 2005.

[7] R.R. Wilson. Radiological use of fast protons. *Radiology*, 47:487–491, 1946.

[8] J.H. Lawrence. Proton irradiation of the pituitary. *Cancer*, 10:795, 1957.

[9] A.R. Smith. Vision: Proton therapy. *Medical Physics*, 36:556–568, 2009.

[10] S.V. Bulanov, T.Z. Esirkepov, V.S. Khoroshkov, A.V. Kuznetsov, and F. Pegoraro. Oncological hadrontherapy with laser ion accelerators. *Physics Letters A*, 299:240 – 247, 2002.

[11] U. Linz and J. Alonso. What will it take for laser driven proton accelerators to be applied to tumor therapy? *Physical Review Accelerators and Beams*, 10:094801, 2007.

[12] P. Antici *et al.* A compact post-acceleration scheme for laser-generated protons. *Physics of Plasmas*, 18:073103, 2011.

[13] S. Atzeni and J. Meyer ter Vehn. *The physics of intertial fusion.* Oxford University Press, 2004.

[14] M. Tabak *et al.* Ignition and high gain with ultrapowerful lasers. *Physics of Plasmas*, 1:1626–1634, 1994.

[15] R.A. Snavely *et al.* Intense high-energy proton beams from petawatt-laser irradiation of solids. *Physical Review Letters*, 85:2945–2948, 2000.

[16] M. Roth *et al.* Fast ignition by intense laser-accelerated proton beams. *Physical Review Letters*, 86:436–439, 2001.

[17] P.K. Patel *et al.* Isochoric heating of solid-density matter with an ultrafast proton beam. *Physical Review Letters*, 91:125004, 2003.

[18] M.H. Key *et al.* Proton fast ignition. *Fusion Science and Technology*, 49:440–452, 2006.

[19] M. Borghesi *et al.* Proton imaging: a diagnostic for inertial confinement fusion/fast ignitor studies. *Plasma Physics and Controlled Fusion*, 43:A267, 2001.

[20] A. Macchi, M. Borghesi, and M. Passoni. Ion acceleration by superintense laser-plasma interaction. *Reviews of Modern Physics*, 85:751–793, 2013.

[21] M. Koenig *et al.* Progress in the study of warm dense matter. *Plasma Physics and Controlled Fusion*, 47:B441, 2005.

[22] D. Riley. Generation and characterisation of warm dense matter with intense lasers. *Plasma Physics and Controlled Fusion*, 60:014033, 2018.

[23] S. Ichimaru. Strongly coupled plasmas: high-density classical plasmas and degenerate electron liquids. *Reviews of Modern Physics*, 54:1017–1059, 1982.

[24] G.J. Tallents *et al.* Measurements of opacity and temperature of warm dense matter heated by focused soft X-ray laser irradiation. *High Energy Density Physics*, 5:110 – 113, 2009.

[25] A.L. Kritcher *et al.* Ultrafast X-ray Thomson scattering of shock-compressed matter. *Science*, 322:69–71, 2008.

[26] B. Rus *et al.* Outline of the ELI-Beamlines facility, 2011.

[27] N.V. Zamfir. The ELI-nuclear physics project. *Journal of Physics: Conference Series*, 366:012052, 2012.

[28] H.B. Zhuo *et al.* Quasimonoenergetic proton bunch generation by dual-peaked electrostatic-field acceleration in foils irradiated by an intense linearly polarized laser. *Physical Review Letters*, 105:065003, 2010.

[29] A.V. Bashinov, A.A. Gonoskov, A.V. Kim, G. Mourou, and A.M. Sergeev. New horizons for extreme light physics with mega-science project XCELS. *The European Physical Journal Special Topics*, 223:1105–1112, 2014.

[30] D. Suter. *The physics of laser-atom interactions.* Cambridge University Press, 1997.

[31] A.V. Borovsky, A.L. Galkin, O.B. Shiryaev, and T. Auguste. *Laser physics at relativistic intensities.* Springer, 2003.

[32] W.L. Kruer. *The physics of laser plasma interactions.* Westview Press, 2003.

[33] P. Gibbon. *Short pulse laser interactions with matter.* Imperial College Press, 2005.

[34] L.V. Keldysh. Ionisation in the field of a strong electromagnetic wave. *Journal of Experimental and Theoretical Physics*, 47, 1964.

[35] M.V. Ammosob. Tunnel ionization of complex atoms and of atomic ions in an alternating electromagnetic field. *Journal of Experimental and Theoretical Physics*, 64:1191 – 1194, 1986.

[36] F. Cattani, A. Kim, D. Anderson, and M. Lisak. Threshold of induced transparency in the relativistic interaction of an electromagnetic wave with overdense plasmas. *Physical Review E*, 62:1234 – 1237, 2000.

[37] V.A. Vshivkov *et al.* Nonlinear electrodynamics of the interaction of ultra-intense laser pulses with a thin foil. *Physics of Plasmas*, 5:2727 – 2741, 1998.

[38] S. Palaniyappan *et al.* Dynamics of relativistic transparency and optical shuttering in expanding overdense plasmas. *Nature Physics*, 8:763, 2012.

[39] S. Palaniyappan *et al.* Efficient quasi-monoenergetic ion beams from laser-driven relativistic plasmas. *Nature Communications*, 6:10170 EP –, 2015. Article.

[40] J.D. Lawson. Lasers and accelerators. *IEEE Transactions on Nuclear Science*, 26:4217 – 4219, 1979.

[41] J.R. Davies. Laser absorption by overdense plasmas in the relativistic regime. *Plasma Physics and Controlled Fusion*, 51:014006, 2009.

[42] Y. Ping *et al.* Absorption of short laser pulses on solid targets in the ultrarelativistic regime. *Physical Review Letters*, 100:085004, 2008.

[43] R.J. Gray *et al.* Enhanced laser-energy coupling to dense plasmas driven by recirculating electron currents. *New Journal of Physics*, 20:033021, 2018.

[44] F. Brunel. Not-so-resonant, resonant absorption. *Physical Review Letters*, 59:52 – 55, 1987.

[45] W.L. Kruer and K. Estabrook. $\mathbf{J}\times\mathbf{b}$ heating by very intense laser light. *The Physics of Fluids*, 28:430 – 432, 1985.

[46] M.I.K. Santala *et al.* Effect of the plasma density scale length on the direction of fast electrons in relativistic laser-solid interactions. *Physical Review Letters*, 84:1459 – 1462, 2000.

[47] A.R. Bell, J.R. Davies, S. Guerin, and H. Ruhl. Fast-electron transport in high-intensity short-pulse laser - solid experiments. *Plasma Physics and Controlled Fusion*, 39:653, 1997.

[48] H. Alfvén. On the motion of cosmic rays in interstellar space. *Physical Review*, 55:425 – 429, 1939.

[49] Y. Sentoku, T.E. Cowan, A. Kemp, and H. Ruhl. High energy proton acceleration in interaction of short laser pulse with dense plasma target. *Physics of Plasmas*, 10:2009 – 2015, 2003.

[50] P. McKenna *et al.* Lateral electron transport in high-intensity laser-irradiated foils diagnosed by ion emission. *Physical Review Letters*, 98:145001, 2007.

[51] E.S. Weibel. Spontaneously growing transverse waves in a plasma due to an anisotropic velocity distribution. *Physical Review Letters*, 2:83 – 84, 1959.

[52] H. Daido, M. Nishiuchi, and A.S. Pirozhkov. Review of laser-driven ion sources and their applications. *Reports on Progress in Physics*, 75:056401, 2012.

[53] A. Macchi. A review of laser-plasma ion acceleration. *arXiv*, 2017.

[54] E.L. Clark *et al.* Measurements of energetic proton transport through magnetized plasma from intense laser interactions with solids. *Physical Review Letters*, 84:670 – 673, 2000.

[55] A. Maksimchuk, S. Gu, K. Flippo, D. Umstadter, and V.Y. Bychenkov. Forward ion acceleration in thin films driven by a high-intensity laser. *Physical Review Letters*, 84:4108 – 4111, 2000.

[56] S.C. Wilks *et al.* Energetic proton generation in ultra-intense lasersolid interactions. *Physics of Plasmas*, 8:542 – 549, 2001.

[57] M. Allen *et al.* Direct experimental evidence of back-surface ion acceleration from laser-irradiated gold foils. *Physical Review Letters*, 93:265004, 2004.

[58] L. Romagnani *et al.* Dynamics of electric fields driving the laser acceleration of multi-MeV protons. *Physical Review Letters*, 95:195001, 2005.

[59] N.P. Dover *et al.* Buffered high charge spectrally-peaked proton beams in the relativistic-transparency regime. *New Journal of Physics*, 18:013038, 2016.

[60] J. Fuchs *et al.* Laser-driven proton scaling laws and new paths towards energy increase. *Nature Physics*, 2:48, 2005.

[61] P. Mora. Plasma expansion into a vacuum. *Physical Review Letters*, 90:185002, 2003.

[62] M. Roth and M. Schollmeier. Ion accelerationtarget normal sheath acceleration. *CERN Yellow Reports*, 1:231, 2016.

[63] L. Robson *et al.* Scaling of proton acceleration driven by petawatt-laser-plasma interactions. *Nature Physics*, 3:58, 2006.

[64] F. Wagner *et al.* Maximum proton energy above 85 MeV from the relativistic interaction of laser pulses with micrometer thick ch_2 targets. *Physical Review Letters*, 116:205002, 2016.

[65] M. Borghesi *et al.* Fast ion generation by high-intensity laser irradiation of solid targets and applications. *Fusion Science and Technology*, 49:412–439, 2006.

[66] T. Esirkepov *et al.* Highly efficient relativistic-ion generation in the laser-piston regime. *Physical Review Letters*, 92:175003, 2004.

[67] B. Aurand *et al.* A setup for studies of laser-driven proton acceleration at the Lund Laser Centre. *Laser and Particle Beams*, 33:5964, 2015.

[68] A.P.L Robinson *et al.* Relativistically correct hole-boring and ion acceleration by circularly polarized laser pulses. *Plasma Physics and Controlled Fusion*, 51:024004, 2009.

[69] A. Macchi and C. Benedetti. Ion acceleration by radiation pressure in thin and thick targets. *Nuclear Instruments and Methods in Physics Research Section A: Accelerators, Spectrometers, Detectors and Associated Equipment*, 620:41 – 45, 2010.

[70] A.P.L. Robinson. Production of high energy protons with hole-boring radiation pressure acceleration. *Physics of Plasmas*, 18:056701, 2011.

[71] C.A.J. Palmer *et al.* Monoenergetic proton beams accelerated by a radiation pressure driven shock. *Physical Review Letters*, 106:014801, 2011.

[72] A.A Andreev, K.Y. Platonov V.I. Chestnov, and A.E. Petrov. Dynamics of ultrathin laser targets with optimal parameters. *Optics and Spectroscopy*, 117:276 – 286, 2014.

[73] S. Kar *et al.* Ion acceleration in multispecies targets driven by intense laser radiation pressure. *Physical Review Letters*, 109:185006, 2012.

[74] A. Henig *et al.* Radiation-pressure acceleration of ion beams driven by circularly polarized laser pulses. *Physical Review Letters*, 103:245003, 2009.

[75] C. Scullion *et al.* Polarization dependence of bulk ion acceleration from ultrathin foils irradiated by high-intensity ultrashort laser pulses. *Physical Review Letters*, 119:054801, 2017.

[76] O. Klimo, J. Psikal, J. Limpouch, and V.T. Tikhonchuk. Monoenergetic ion beams from ultrathin foils irradiated by ultrahigh-contrast circularly polarized laser pulses. *Physical Review Accelerators and Beams*, 11:031301, 2008.

[77] L. Yin, B.J. Albright, B.M. Hegelich, and J.C. Fernandez. GeV laser ion acceleration from ultrathin targets: The laser break-out afterburner. *Laser and Particle Beams*, 24:291298, 2006.

[78] L. Yin *et al.* Monoenergetic and GeV ion acceleration from the laser breakout afterburner using ultrathin targets. *Physics of Plasmas*, 14:056706, 2007.

[79] B.J. Albright *et al.* Relativistic buneman instability in the laser breakout afterburner. *Physics of Plasmas*, 14:094502, 2007.

[80] B.J. Albright *et al.* Theory of laser acceleration of light-ion beams from interaction of ultrahigh-intensity lasers with layered targets. *Physical Review Letters*, 97:115002, 2006.

[81] B.M. Hegelich *et al.* Laser-driven ion acceleration from relativistically transparent nanotargets. *New Journal of Physics*, 15:085015, 2013.

[82] X.Q. Yan, T. Tajima, M. Hegelich, L. Yin, and D. Habs. Theory of laser ion acceleration from a foil target of nanometer thickness. *Applied Physics B*, 98:711 – 721, 2010.

[83] F. Mako and T. Tajima. Collective ion acceleration by a reflexing electron beam: Model and scaling. *The Physics of Fluids*, 27:1815 – 1820, 1984.

[84] H.W. Powell *et al.* Proton acceleration enhanced by a plasma jet in expanding foils undergoing relativistic transparency. *New Journal of Physics*, 17:103033, 2015.

[85] C.N. Danson *et al.* Vulcan petawattan ultra-high-intensity interaction facility. *Nuclear Fusion*, 44:S239, 2004.

[86] I.N. Ross, P. Matousek, M. Towrie, A.J. Langley, and J.L. Collier. The prospects for ultrashort pulse duration and ultrahigh intensity using optical parametric chirped pulse amplifiers. *Optics Communications*, 144:125 – 133, 1997.

[87] C. Thaury *et al.* Plasma mirrors for ultrahigh-intensity optics. *Nature Physics*, 3:424, 2007.

[88] I. Musgrave *et al.* Review of laser diagnostics at the Vulcan laser facility. *High Power Laser Science and Engineering*, 3:e26, 2015.

[89] M. Galimberti *et al.* The new fast ignitor oriented target area in the Vulcan laser at the CLF. *AIP Conference Proceedings*, 1209:35 – 38, 2010.

[90] N. Hopps *et al.* Comprehensive description of the Orion laser facility. *Plasma Physics and Controlled Fusion*, 57:064002, 2015.

[91] Orion laser. `http://www.awe.co.uk/what-we-do/science-engineering-technology/orion-laser-facility/orion-publications/`. Accessed: 11/04/2018.

[92] M. Roth. The diagnostics of ultra-short pulse laser-produced plasma. *Journal of Instrumentation*, 6:R09001, 2011.

[93] O. Ettlinger, J.S. Green, D. Neely, D. Parker, and S. Green. A comparison of different radiochromic film types. *CLF Annual Report*, 2012.

[94] J.F. Ziegler, M.D. Ziegler, and J.P. Biersack. SRIM – the stopping and range of ions in matter. *Nuclear Instruments and Methods in Physics Research Section B: Beam Interactions with Materials and Atoms*, 268:1818 – 1823, 2010.

[95] A.M. Koehler. Proton radiography. *Science*, 160:303 – 304, 1968.

[96] C.W. Mendel and J.N. Olsen. Charge-separation electric fields in laser plasmas. *Physical Review Letters*, 34:859 – 862, 1975.

[97] O. Jäckel *et al.* All-optical measurement of the hot electron sheath driving laser ion acceleration from thin foils. *New Journal of Physics*, 12:103027, 2010.

[98] M. Borghesi *et al.* Multi-MeV proton source investigations in ultraintense laser-foil interactions. *Physical Review Letters*, 92:055003, 2004.

[99] T.E. Cowan *et al.* Ultralow emittance, multi-MeV proton beams from a laser virtual-cathode plasma accelerator. *Physical Review Letters*, 92:204801, 2004.

[100] M. Borghesi *et al.* Electric field detection in laser-plasma interaction experiments via the proton imaging technique. *Physics of Plasmas*, 9:2214 – 2220, 2002.

[101] Bakerian lecture — rays of positive electricity. *Proceedings of the Royal Society of London A: Mathematical, Physical and Engineering Sciences*, 89:1 – 20, 1913.

[102] K. Harres *et al.* Development and calibration of a Thomson parabola with microchannel plate for the detection of laser-accelerated MeV ions. *Review of Scientific Instruments*, 79:093306, 2008.

[103] H. Padda. *Intra-pulse dynamics of laser-driven ion acceleration in ultra-thin foils.* PhD thesis, University of Strathclyde, 2017.

[104] Y. Amemiya and J. Miyahara. Imaging plate illuminates many fields. *Nature*, 336:8990, 1988.

[105] I. Spencer *et al.* Laser generation of proton beams for the production of short-lived positron emitting radioisotopes. *Nuclear Instruments and Methods in Physics Research Section B: Beam Interactions with Materials and Atoms*, 183:449 – 458, 2001.

[106] A.P. Fews. Fully automated image analysis of etched tracks in CR-39. *Nuclear Instruments and Methods in Physics Research Section B: Beam Interactions with Materials and Atoms*, 71:465 – 478, 1992.

[107] P. McKenna, D. Neely, R. Bingham, and D.A. Jaroszynski. *Laser-plasma interactions and applications.* Springer, 2013.

[108] C.K. Birdsall and A.B. Langdon. *Plasma physics via computer simulation.* Taylor and Francic, New York, 2004.

[109] T.D. Arber *et al.* Contemporary particle-in-cell approach to laser-plasma modelling. *Plasma Physics and Controlled Fusion*, 11:113001, 2015.

[110] J.J. MacFarlane, I.E. Golovkin, and P.R. Woodruff. HELIOS-CR a 1-D radiation-magnetohydrodynamics code with inline atomic kinetics modeling. *Journal of Quantitative Spectroscopy and Radiative Transfer*, 99:381 – 397, 2006.

[111] L. Volpe *et al.* Proton radiography of laser-driven imploding target in cylindrical geometry. *Physics of Plasmas*, 18:012704, 2011.

[112] B. Dromey *et al.* Picosecond metrology of laser-driven proton bursts. *Nature Communications*, 7:10642, 2016.

[113] S.V. Bulanov *et al.* Feasibility of using laser ion accelerators in proton therapy. *AIP Conference Proceedings*, 740:414 – 429, 2004.

[114] A.P.L. Robinson, M. Zepf, S. Kar, R.G. Evans, and C. Bellei. Radiation pressure acceleration of thin foils with circularly polarized laser pulses. *New Journal of Physics*, 10:013021, 2008.

[115] I.J. Kim *et al.* Radiation pressure acceleration of protons to 93 MeV with circularly polarized petawatt laser pulses. *Physics of Plasmas*, 23:070701, 2016.

[116] B. Qiao *et al.* Dominance of radiation pressure in ion acceleration with linearly polarized pulses at intensities of 10^{21} W cm^{-2}. *Physical Review Letters*, 108:115002, 2012.

[117] B. Gonzalez-Izquierdo *et al.* Optically controlled dense current structures driven by relativistic plasma aperture-induced diffraction. *Nature Physics*, 12:505, 2016.

[118] B. Gonzalez-Izquierdo *et al.* Towards optical polarization control of laser-driven proton acceleration in foils undergoing relativistic transparency. *Nature Communications*, 7:12891, 2016.

[119] M. King, R.J. Gray, H.W. Powell, R. Capdessus, and P. McKenna. Energy exchange via multi-species streaming in laser-driven ion acceleration. *Plasma Physics and Controlled Fusion*, 59:014003, 2017.

[120] J.P. Zou *et al.* Design and current progress of the Apollon 10 PW project. *High Power Laser Science and Engineering*, 3:e2, 2015.

[121] Macchi A and S. Veghini F. Pegoraro. "Light Sail" acceleration reexamined. *Physical Review Letters*, 103:085003, 2009.

[122] T.C Liu *et al.* Generation of quasi-monoenergetic protons from thin multi-ion foils by a combination of laser radiation pressure acceleration and shielded Coulomb repulsion. *New Journal of Physics*, 15:025026, 2013.

[123] H. Padda *et al.* Intra-pulse transition between ion acceleration mechanisms in intense laser-foil interactions. *Physics of Plasmas*, 23:063116, 2016.

[124] R.J. Gray *et al.* Azimuthal asymmetry in collective electron dynamics in relativistically transparent laserfoil interactions. *New Journal of Physics*, 16:093027, 2014.

[125] M. Chen, A. Pukhov, T.P Yu, and Z.M. Sheng. Radiation reaction effects on ion acceleration in laser foil interaction. *Plasma Physics and Controlled Fusion*, 53:014004, 2011.

[126] M. Tamburini, F. Pegoraro, A.D. Piazza, C.H. Keitel, and A. Macchi. Radiation reaction effects on radiation pressure acceleration. *New Journal of Physics*, 12:123005, 2010.

[127] R. Capdessus and P. McKenna. Influence of radiation reaction force on ultraintense laser-driven ion acceleration. *Physical Review E*, 91:053105, 2015.

[128] M. Borghesi *et al.* Measurement of highly transient electrical charging following high-intensity lasersolid interaction. *Applied Physics Letters*, 82:1529 – 1531, 2003.

[129] A.J. Mackinnon *et al.* Proton radiography as an electromagnetic field and density perturbation diagnostic (invited). *Review of Scientific Instruments*, 75:3531 – 3536, 2004.

[130] S.J. Gitomer *et al.* Fast ions and hot electrons in the laserplasma interaction. *The Physics of Fluids*, 29:2679 – 2688, 1986.

[131] J. Fuchs *et al.* Laser-foil acceleration of high-energy protons in small-scale plasma gradients. *Physical Review Letters*, 99:015002, 2007.

[132] A.I. Larkin. Passage of particles through a plasma. *Soviet Physics JETP*, 37:186 – 191, 1959.

[133] H. Bethe. Zur theorie des durchgangs schneller korpuskularstrahlen durch materie. *Annalen der Physik*, 397:325 – 400, 1930.

[134] F. Bloch. Zur bremsung rasch bewegter teilchen beim durchgang durch materie. *Annalen der Physik*, 408:285 – 320, 1933.

[135] A.B. Zylstra *et al.* Measurement of charged-particle stopping in warm dense plasma. *Physical Review Letters*, 114:215002, 2015.

[136] J. Kim *et al.* Self-consistent simulation of transport and energy deposition of intense laser-accelerated proton beams in solid-density matter. *Physical Review Letters*, 115:054801, 2015.

[137] A.J. Mackinnon *et al.* Effect of plasma scale length on multi-MeV proton production by intense laser pulses. *Physical Review Letters*, 86:1769 – 1772, 2001.

[138] P. McKenna *et al.* Effects of front surface plasma expansion on proton acceleration in ultraintense laser irradiation of foil targets. *Laser and Particle Beams*, 26:591596, 2008.

[139] H. Azechi and the FIREX Project. Present status of the FIREX programme for the demonstration of ignition and burn. *Plasma Physics and Controlled Fusion*, 48:B267, 2006.

[140] F. Wagner *et al.* Pre-plasma formation in experiments using petawatt lasers. *Optics Express*, 22:29505 – 29514, 2014.

[141] W. Bang *et al.* Visualization of expanding warm dense gold and diamond heated rapidly by laser-generated ion beams. *Scientific Reports*, 5:14318, 2015.

[142] M. Roth *et al.* Energetic ions generated by laser pulses: A detailed study on target properties. *Physical Review Accelerators and Beams*, 5:061301, 2002.

[143] C. Brabetz *et al.* Laser-driven ion acceleration with hollow laser beams. *Physics of Plasmas*, 22:013105, 2015.

[144] F. Lindau *et al.* Laser-accelerated protons with energy-dependent beam direction. *Physical Review Letters*, 95:175002, 2005.

[145] D.A. MacLellan. *Effects of Electrical Resistivity on Fast Electron Transport in Relativistic Laser-Solid Interactions.* PhD thesis, University of Strathclyde, 2014.

[146] A. Manči ć *et al.* Picosecond short-range disordering in isochorically heated aluminum at solid density. *Physical Review Letters*, 104:035002, 2010.

[147] D.A. MacLellan *et al.* Tunable mega-ampere electron current propagation in solids by dynamic control of lattice melt. *Physical Review Letters*, 113:185001, 2014.

[148] D.C. Carroll *et al.* Active manipulation of the spatial energy distribution of laser-accelerated proton beams. *Physical Review E*, 76:065401, 2007.

[149] M. Gittings *et al.* The RAGE radiation-hydrodynamic code. *Computational Science and Discovery*, 1:015005, 2008.

[150] W. Bang *et al.* Linear dependence of surface expansion speed on initial plasma temperature in warm dense matter. *Scientific Reports*, 6:29441, 2016.

[151] J.E. Crow, P.L. Auer, and J.E. Allen. The expansion of a plasma into a vacuum. *Journal of Plasma Physics*, 14:6576, 1975.

[152] B. Westover *et al.* Fast electron temperature and conversion efficiency measurements in laser-irradiated foil targets using a bremsstrahlung X-ray detector. *Physics of Plasmas*, 18:063101, 2011.

[153] D.W. Forslund and J.U. Brackbill. Magnetic-field-induced surface transport on laser-irradiated foils. *Physical Review Letters*, 48:1614 – 1617, 1982.

[154] F. Amiranoff *et al.* The evolution of two-dimensional effects in fast-electron transport from high-intensity laser-plasma interactions. *Journal of Physics D: Applied Physics*, 15:2463, 1982.

[155] A.J. Mackinnon *et al.* Enhancement of proton acceleration by hot-electron recirculation in thin foils irradiated by ultraintense laser pulses. *Physical Review Letters*, 88:215006, 2002.

[156] S. Buffechoux *et al.* Hot electrons transverse refluxing in ultraintense laser-solid interactions. *Physical Review Letters*, 105:015005, 2010.

[157] T. Toncian *et al.* Ultrafast laser-driven microlens to focus and energy-select mega-electron volt protons. *Science*, 312:410 – 413, 2006.

[158] M. Szilagyi. *Electron and ion optics.* Plenum Press, New York, 1988.

[159] M.E. Foord, D.B. Reisman, and P.T. Springer. Determining the equation-of-state isentrope in an isochoric heated plasma. *Review of Scientific Instruments*, 75:2586 – 2589, 2004.

[160] J. Nuckolls, L. Wood, A. Thiessen, and G. Zimmerman. Laser compression of matter to super-high densities: Thermonuclear (CTR) applications. *Nature*, 239:139, 1972.

[161] B.A. Remington, D. Arnett, R.P. Drake, and H. Takabe. Modelling astrophysical phenomena in the laboratory with intense lasers. *Science*, 284:1488 – 1493, 1999.

[162] P.A. Norreys *et al.* Experimental studies of the advanced fast ignitor scheme. *Physics of Plasmas*, 7:3721 – 3726, 2000.

[163] R. Kodama *et al.* Fast heating of ultrahigh-density plasma as a step towards laser fusion ignition. *Nature*, 412:798, 2001.

[164] S. Kar *et al.* Dynamic control of laser-produced proton beams. *Physical Review Letters*, 100:105004, 2008.

[165] S. Kar *et al.* Ballistic focusing of polyenergetic protons driven by petawatt laser pulses. *Physical Review Letters*, 106:225003, 2011.

[166] T. Bartal *et al.* Focusing of short-pulse high-intensity laser-accelerated proton beams. *Nature Physics*, 8:139, 2011.

[167] M.E. Foord *et al.* Proton trajectories and electric fields in a laser-accelerated focused proton beam. *Physics of Plasmas*, 19:056702, 2012.

[168] B. Qiao *et al.* Dynamics of high-energy proton beam acceleration and focusing from hemisphere-cone targets by high-intensity lasers. *Physical Review E*, 87:013108, 2013.

[169] M. Temporal, J.J. Honrubia, and S. Atzeni. Numerical study of fast ignition of ablatively imploded deuteriumtritium fusion capsules by ultra-intense proton beams. *Physics of Plasmas*, 9:3098 – 3107, 2002.

[170] M.E. Foord *et al.* MeV proton generation and efficiency from an intense laser irradiated foil. *High Energy Density Physics*, 3:365 – 370, 2007.

[171] M. Temporal. Fast ignition of a compressed inertial confinement fusion hemispherical capsule by two proton beams. *Physics of Plasmas*, 13:122704, 2006.

[172] M. Temporal, R. Ramis, J.J. Honrubia, and S. Atzeni. Fast ignition induced by shocks generated by laser-accelerated proton beams. *Plasma Physics and Controlled Fusion*, 51:035010, 2009.

[173] D.R. Welch, D.V. Rose, B.V. Oliver, and R.E. Clark. Simulation techniques for heavy ion fusion chamber transport. *Nuclear Instruments and Methods in Physics Research Section A: Accelerators, Spectrometers, Detectors and Associated Equipment*, 464:134 – 139, 2001.

[174] D.R. Welch, D.V. Rose, M.E. Cuneo, R.B. Campbell, and T.A. Mehlhorn. Integrated simulation of the generation and transport of proton beams from laser-target interaction. *Physics of Plasmas*, 13:063105, 2006.

[175] C.D. Bentley *et al.* Orion laser target diagnostics. *Review of Scientific Instruments*, 83:10D732, 2012.

[176] Orion target diagnostics. `http://www.awe.co.uk/what-we-do/science-engineering-technology/orion-laser-facility/target-diagnostics/`. Accessed: 05/04/2018.

[177] D. Khaghani *et al.* Enhancing laser-driven proton acceleration by using micro-pillar arrays at high drive energy. *Scientific Reports*, 7:11366, 2017.

[178] P.L. Poole *et al.* Moderate repetition rate ultra-intense laser targets and optics using variable thickness liquid crystal films. *Applied Physics Letters*, 109:151109, 2016.

[179] I. Prencipe *et al.* Targets for high repetition rate laser facilities: needs, challenges and perspectives. *High Power Laser Science and Engineering*, 5:e17, 2017.

[180] J. Hartmann. *Bemerkungen über den Bau und die Justirung von Spektrographen.* Julins Springer, Berlin, 1900.

[181] R.V. Shack. Production and use of a lenticular Hartmann screen. *Journal of the Optical Society of America*, 61:648 – 697, 1971.

[182] Shack-Hartmann wavefront sensors. `https://www.thorlabs.com/newgrouppage9.cfm?objectgroup_id=2946`. Accessed: 11/04/2018.

[183] J.F. Ziegler. Stopping of energetic light ions in elemental matter. *Journal of Applied Physics*, 85:1249 – 1272, 1999.

[184] U. Fano. Penetration of protons, alpha particles, and mesons. *Annual Review of Nuclear Science*, 13:1 – 66, 1963.

[185] A. Golubev *et al.* Dense plasma diagnostics by fast proton beams. *Physical Review E*, 57:3363 – 3367, 1998.